Towards a network perspective on the nonlinear dynamics of mechanical structures

Vom Promotionsausschuss der
Technischen Universität Hamburg

zur Erlangung des akademischen Grades

Doktor-Ingenieur (Dr.-Ing.)

genehmigte Dissertation (kumulativ)

von
Charlotte Geier

aus
Göttingen

2026

Tag der mündlichen Prüfung: 04.11.2025

Gutachter: Prof. Dr. rer. nat. habil. Norbert Hoffmann
Prof. Dr. Sebastian Trimpe

ORCID: https://orcid.org/0000-0002-9918-1707
DOI: https://doi.org/10.15480/882.16616

Acknowledgements

This thesis is not only the result of my work, but also of the support and encouragement of many wonderful people around me. I am deeply grateful to all who have accompanied me on this path.

First and foremost, I would like to thank my supervisor, Norbert, for being the best mentor I could have wished for. Thank you for your guidance, the freedom to pursue my own ideas, and your unwavering support. I have learned, and continue to learn, so much from you. I also want to thank Prof. Trimpe for kindly agreeing to serve as my second examiner, and Prof. Grabe for his interest and engagement as the chair of the oral examination.

I am thankful to my colleagues at the Dynamics Group, especially to Mathies, for your support with all things technical and your dedicated proofreading of my manuscripts. I deeply enjoyed our traditional Market Fridays. Special thanks go to Merten, whose supervision of my Master's thesis sparked my interest in unconventional approaches to mechanical dynamics that laid the foundation for this work, and who helped secure the funding that made this project possible. Part of my research was conducted in collaboration with colleagues at Centrale Lille and Hitachi Astemo in France – thank you for many fruitful discussions and for hosting us during memorable visits.

Throughout this work, I had the pleasure of meeting many people from mechanics, dynamics, and network science at conferences and workshops. I cherish the openness and sense of community I encountered, and I am grateful to everyone who showed interest in my research and who contributed to my personal and professional growth. Sonja, initiating the Women* in GAMM networking event with you has been one of my proudest achievements.

This work would not have been possible without proper nourishment, which, admittedly, often consisted mainly of coffee. My thanks go to the staff at Café ZessP for the delicious lunches and the warm atmosphere, to the people at the Harburg farmers market for always sharing a laugh, and to Café Rennkoppel, where a large part of this thesis was written.

To all who attended my defense, in person or in spirit: thank you for raising a glass with me and making that day absolutely unforgettable. All my friends, my parents, and everyone I might have forgotten to mention: I feel truly fortunate to have you all in my life. Especially, I want to thank Laura and Mareike for always believing in me and encouraging me to follow my own path, and Kerstin for countless coffee dates and the same. Thank you to the *usual suspects*, who were a great team throughout our university years and made long days in the library fun.

And finally, Malte, my favorite person – your support means more than I can say. Thank you for sharing this journey with me and for making me laugh in the most unlikely situations.

Abstract

The study of the nonlinear dynamics of mechanical structures presents significant challenges in engineering today, particularly as these structures become more intricate and environmental conditions grow increasingly unpredictable. A deeper understanding and reliable modeling schemes are required for efficient design and safe operation of these systems. Where physics-based modeling and system identification techniques reach their limits, data-based methods such as machine learning have emerged, leveraging the increasing quality and availability of measurement data. However, some aspects of the structural dynamics, such as transient motion, nonlinearities, or the intricate interaction mechanisms between different components, remain difficult to grasp. Network science offers a new perspective on these phenomena. By studying networks composed of nodes connected via edges, this interdisciplinary field provides fresh approaches to time series analysis and the study of systems with many interacting parts. For example, network science offers methods for detecting and understanding the functional relationships between system components beyond their geometrical connections. This work explores and compares different perspectives on the dynamics of mechanical structures, studying the balance between interpretability and generalizability. A series of case studies demonstrate different methodologies, emphasizing the distinct insights that can be gained from each perspective. A particular focus point of this thesis is the applicability and potential of network-based methods for analyzing mechanical structures by drawing parallels with other scientific disciplines.

Contents

List of Figures

List of Symbols

This list of symbols summarizes the notation employed throughout the main part of this thesis. The notation within the articles may occasionally deviate slightly.

Preliminaries

x	small symbols: scalar values
$\mathbf{x}$	small symbols in bold font: vector valued quantities
$\mathbf{X}$	capital symbols in bold font: matrix valued quantities
$\dot{x}, \ddot{x}$	one or two overdots: first and second order temporal derivatives
$\Re\{\cdot\}$	real part of $\{\cdot\}$
$\mathrm{eig}(\cdot)$	eigenvalues of $(\cdot)$

Indices

$[\,]_{\mathrm{c}}$	coupling
$[\,]_{\mathrm{ex}}$	external excitation
$[\,]_i$, $[\,]_j$	the i-th or j-th entry of vector $[\,]$
$[\,]_{i,j}$	entry in the i-th row and j-th column of matrix $[\,]$
$[\,]_{\mathrm{in}}$	in-degree
$[\,]_{\mathrm{int}}$	internal
$[\,]_{\mathrm{l}}$	linear
$[\,]_{\mathrm{nl}}$	nonlinear

Greek notation

α, β	scaling factors in network setup
ε	recurrence threshold
τ	embedding delay

Latin notation

$\mathbf{A}$	state matrix in Chapter 2, network adjacency matrix in Chapter 4
$\mathbf{b}$	input vector
$\mathbf{C}$	output matrix
d	damping
dim	embedding dimension
$\mathbf{D}$	damping matrix
$\mathbf{f}$	force
G	transfer function
i	iteration index
k	stiffness
$\mathbf{K}$	stiffness matrix
m	mass
$\mathbf{M}$	mass matrix
n	node or oscillator
N	system dimension
s	complex variable
t	time
w	ordinal window size
$\mathbf{x}$	state vector
x	state
$\mathbf{y}$	observable states
z	node degree

List of Abbreviations

CEA	complex eigenvalue analysis
dof	degrees of freedom
DMD	dynamic mode decomposition
ECG	electrocardiogram
EEG	electroencephalogram
HAVOK	Hankel alternative view of Koopman
LASSO	least absolute shrinkage and selection operator
PDE	partial differential equation
SCC	strongly connected components
SINDy	sparse identification of nonlinear dynamical systems
SHAP	Shapley additive explanations
PINN	physcs-informed neural network

1 Introduction

The dynamics of large-scale mechanical structures arise from the interplay of many interacting parts [1, 2]. The analysis of the entire system is often a complicated endeavor [3], even more so as structures become more sophisticated and the environmental conditions of their deployment become more volatile. Reliable models that can be queried for prediction and analysis are thus indispensable for the safe design and control of these systems while also necessary in striving towards energy efficiency and sustainability [4]. Mechanical engineering can draw from a large arsenal of physics-based approaches for acquiring and analyzing these models [4]. However, these methods often reach their limits when applied to real-world systems: Many techniques require linearity assumptions [3], which are problematic since slender structures, such as the shaft and blades of a wind turbine, are prone to exhibit geometrical nonlinearities [5, 6]. Steady-state measurements are often required for model fitting but are challenging to obtain from systems that are subjected to transient loading scenarios, such as offshore wind turbines, robots, or antennas. "Classical" methods are mostly limited to time or frequency domain and analyze structure and dynamics separately [4], for example, via finite element methods or lumped mass models. This separation of structural and dynamical perspectives on mechanical structures results in models that are very good in their respective applications but do not offer a general framework for a more holistic modeling scheme. For example, functional relationships that describe the dynamical interrelations between structural components beyond their geometric proximity have not yet been studied in detail, even though nonlinear interaction mechanisms likely play a tremendous role in the entire system dynamics [7, 8].

Dynamical systems with mathematical descriptions similar to those of mechanical structural vibrations exist across various scientific disciplines. Contrary to mechanical engineering, many of these fields do not have the physical knowledge of their systems in terms of governing laws a priori. Within these sciences, different data-based techniques have evolved, some of which, such as neural network-based modeling, are already established tools in engineering. Others, such as network science, are only just gaining a foothold. Network science is a method popular across many fields for studying the interaction between system components [9], thereby addressing some of the challenges in dynamical systems from an alternative angle. For example, network approaches are used to identify coupling relationships in climate data [10–12], to study the collective interaction of fish swarms [13, 14], and to represent human collective decision-making behavior [15]. At the same time, networks provide an intuitive approach to emergent phenomena, describing the appearance of high-level dynamics that cannot be characterized entirely by adding up the contributions of individual components [9, 13, 16, 17]. It has been proposed that understanding these

phenomena requires a novel perspective that can be found in interdisciplinary research only, where universal patterns may be recognized without the bias of a specific application [18].

It is the aim of this work to develop novel perspectives on the nonlinear dynamics of mechanical structures composed of many interacting parts by leveraging methods from other scientific disciplines. The questions addressed in this thesis are the following: First, can a new, networks-based perspective provide complementary insights into the functional dependencies within a mechanical system, and capture the interplay between structure and dynamics? Second, is the shift from generalizing, physics-based descriptions towards more phenomenon-based approaches advantageous? Third, how can these approaches be leveraged for the better design, analysis, and operation of mechanical systems? The presented methods are data-based, acknowledging the current trend towards data-centered schemes that arise with the increasing availability of data and computational power [19, 20]. This work demonstrates different aspects of inferring structure from data, illustrating how distinct modeling perspectives facilitate specific intuition and analyses of the underlying system. Parallels and differences of these approaches are highlighted, both in their application within mechanical vibrations and in their applicability to a range of dynamical systems. The potential benefits of interdisciplinary exchange for understanding structural vibrations are demonstrated, encouraging greater integration and application of methodologies from diverse scientific disciplines.

This work is structured as follows. The introduction is followed by an overview of complex mechanical vibrations and physics-based perspectives in Chapter 2. Exemplary phenomena are presented along with the challenges that arise from them. Physics-based approaches to modeling and analyzing these aspects are introduced. The focus on the different possibilities and intuitions that each perspective provides motivates the development of novel, complementary views throughout this work. Chapter 3 provides insight into data-driven perspectives on nonlinear dynamics, which have become the state-of-the-art in many disciplines. The description distinguishes between statistical approaches that aim at obtaining low-order interpretable models from data, and machine learning methods, that focus on accurate models and predictions. The application of methods from each field is demonstrated with exemplary case studies. Chapter 4 introduces networks as novel perspectives on the nonlinear dynamics of mechanical structures. This chapter highlights the different possibilities network-based approaches hold for analyzing structural dynamics, focusing on complementing state-of-the-art approaches. Particularly, a case study demonstrates the possibilities of studying the functional relationships between different components beyond their geometric connections and shows that this approach can be used to detect imminent localized vibrations. An in-depth discussion of the different approaches, resulting models, and possibilities for analysis is given in Chapter 5. Parallels and differences of the perspectives are examined in this chapter, along with the placement of the studies in the larger field of complexity science and structural dynamics in general, and potential benefits for structural mechanics in particular. An outlook on further research directions concludes this chapter. The work is completed with some final remarks in Chapter 6.

2 Complex mechanical dynamics

This work studies the dynamics of mechanical systems with many interacting components, such as a wind turbine, a robot, or a car. Such a system is generally composed of multiple components that interact and move to fulfill a given task. Besides the desired motion, unwanted or even harmful vibrations often also come into play, resulting in a rich and diverse set of dynamical phenomena. Structural mechanics aims at understanding, modeling, and predicting the dynamics resulting from the complex interactions between numerous components. The field has a long history rooted in first principles of physics. Several different, physics-based perspectives on nonlinear machine dynamics exist, each one specializing in the analysis and interpretation of a specific aspect of the dynamics. Despite significant progress in the field, the demand for heightened energy efficiency, the growing complexity of machines, and the increasingly challenging environments such as space, deep sea, and offshore locations continue to pose new challenges to the design and analysis of machines. These challenges include the elevated significance of nonlinearities due to geometric deformation and material properties [21], as well as transient environmental loads. Additionally, as these systems become more sophisticated, the interactions within them become more complex. Consequently, analyzing system stability and functional relationships gains importance, especially given unresolved issues such as noise, data sparsity, and uncertainties, as the efficient and safe operation and design of machines remain critical concerns [21].

This chapter offers an introduction to the dynamics of mechanical systems and to corresponding physics-based modeling approaches and perspectives, motivating the development of novel, complementary views. Section 2.1 addresses multiple phenomena in the structural dynamics of mechanical systems using the example of a wind turbine and a robot, and explains why they pose challenges to current modeling approaches. The classical, physics-based model perspective is presented in Section 2.2. Section 2.3 focuses on various views on system dynamics and illustrates how each of them yields an intuition for a different aspect of the underlying system. Diverse dynamical phenomena are not yet completely understood within the available toolbox, providing a motive for broadening the view with complementary perspectives from the data-driven and networks sciences.

2.1 Structural dynamics

Mechanical structures, such as machines with numerous interacting components, exhibit rich dynamical behavior. These behaviors can be decomposed into specific phenomena, some of which are not entirely understood until today. This section highlights key aspects relevant to the subsequent work, explaining the challenges they pose to physics-based modeling

approaches. Figure 2.1 illustrates the different aspects using an offshore wind turbine and a humanoid robot as sample systems, acting as the guiding examples throughout this section.

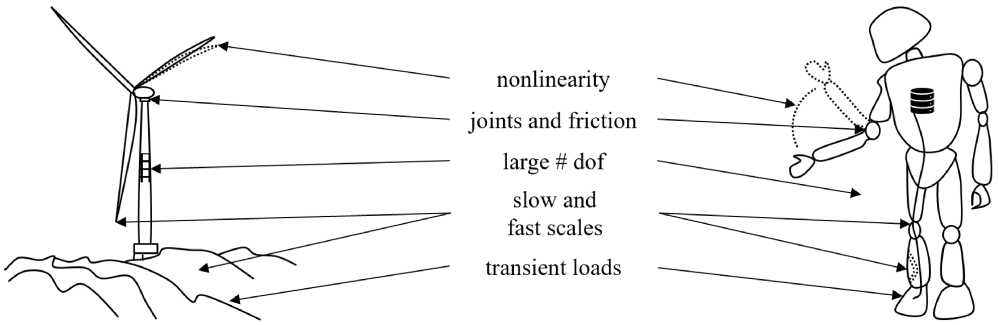

FIGURE 2.1: Exemplary mechanical structures exemplifying related phenomena. Nonlinearities, one of the primary challenges in dynamical systems today, can occur due to large deformations (left) or extensive rotatory motion (right). Joints and connections introduce friction and damping. Large numbers of degrees of freedom (dof) stem from finite element meshing (left) or a large number of individual components (right), often resulting in high modeling costs and low efficiency. The combination of fast and slow time scales poses difficulties to numerical solvers. Examples include the slow excitation through water waves versus the high-frequency wind-induced vibrations (left) or the slow varying temperature versus high-frequency friction-induced joint vibrations (right). Transient loads, for example, through unsteady waves (left) or rough surfaces (right), challenge modeling and analysis schemes that often require steady-state assumptions.

Large systems: Models of real-world mechanical systems typically exhibit a large number of degrees of freedom, as seen in the finite element meshing of a wind turbine's wing or the intricate interactions within robotic assemblies (see Figure 2.1). These large models pose significant challenges, as they require a lot of storage and computational power, often resulting in high cost and low efficiency [22, 23]. To address these issues, the entire structure is either divided into sub-systems through substructuring techniques, or reduced to lower dimensions using model order reduction techniques. In dynamic substructuring, structural systems are analyzed component-wise, breaking a large complex analysis into several smaller, manageable parts [24–26]. On the other hand, model order reduction, seeks to efficiently capture the most relevant system properties with fewer variables, utilizing methods like the harmonic balance approach [21, 27, 28] and proper orthogonal decomposition [29, 30]. Both strategies, substructuring and model order reduction, align with the reductionist idea which suggests that a complex system can be broken down into simpler, constituent elements [9]. However, ongoing developments in complexity science suggest these reductionist methods might not always hold true, resulting in a shift towards more holistic approaches [9].

Nonlinearities: Nonlinear dynamics [31] are ubiquitous in real-world systems and pose one of the central challenges to modeling approaches today [32, 33]. In mechanical structures, nonlinearities can emerge from intrinsic material properties [34–36], large deformations, especially of light-weight structures [6, 21, 37], and the complex interactions within joints [38]. Figure 2.1 illustrates examples of significant deformation of the slender wing of a wind turbine, extensive rotation of a robot extremity, or nonlinear interaction mechanisms within joints.

Nonlinearity can drive phenomena such as chaos, multistability, and localized vibrations, which significantly complicate the analysis and prediction of system behavior. Multistability describes the existence of multiple attractors for the same model parameters, with initial conditions determining which state the system will eventually reach. The basin of attraction defines all initial conditions leading to the same attractor dynamics. Localized vibrations refer to high-amplitude oscillations in one component or a small subset of components. These vibrations can arise from nonlinearities or symmetry-breaking manufacturing imperfections (mistuning) and are notoriously difficult to predict [39–41]. Mechanical engineering typically tries to avoid these high-amplitude vibrations, as they might induce high cycle fatigue [42], potentially leading to system failure. Even small manufacturing imperfections within manufacturing tolerances can significantly impact on the dynamics of periodic structures like wind turbines or ship hulls [42, 43]. Synchronization involves the temporal coordination of two or more states [44], in terms of phase, frequency, amplitude, or all of these dimensions. Though not a phenomenon unique to nonlinear systems, synchronization is relevant in this context due to the complex interactions and behaviors that nonlinear dynamics can induce.
A key challenge in dealing with nonlinear systems is the failure of the superposition principle, which renders many conventional reductionist approaches ineffective. Local linearization is a common strategy for addressing this issue, approximating nonlinear dynamics by a linear system around specific points of interest, but it often fails to capture the full spectrum of the system's properties [45]. Despite these advances, a comprehensive framework for the global analysis of nonlinear dynamical systems remains elusive [4]. At the same time, there is a growing industrial demand for tools capable of addressing large-scale nonlinear dynamics as the focus shifts from circumventing to leveraging these phenomena [45].

Joints: Joints play an important role in shaping the dynamics of mechanical systems [8, 46–48]. Figure 2.1 illustrates the omnipresence of joints in the robot, whose dynamics may be governed by the joints properties. In the dynamic interaction between the support structure and the rotor of an offshore wind turbine [49], damping plays an important role. In general, joints represent a considerable source of nonlinearity [39, 50, 51] and uncertainty [46, 52], as well as damping [49, 51, 53]. These characteristics pose a bottleneck for developing precise predictive models of machines [25]. Friction and the resulting self-excitation frequently occur at contact surfaces and joints, often leading to friction-induced vibrations [48, 52].
The properties of joints depend on the contact parameters [25], which are rarely accessible to non-intrusive measurements. Additionally, the dynamics is highly sensitive to small parameter variations and load history effects, meaning that the future behavior of the system does not just depend on the current state, but on prior (historic) events as well. This limited accessibility and repeatability of experimental results present significant challenges to accurately analyzing and modeling these phenomena [25, 46]. Consequently, accurate descriptions of these dynamics commonly rely on costly experimental methods. This observation calls for continued innovative modeling strategies or alternative methods to better capture the nuanced behaviors of joints and contact surfaces in mechanical systems.

Transient dynamics: Many real-world engineering systems exhibit transient dynamics. In the case of chaotic systems, this occurs due to their inherently transient nature. Transients

can also appear as a response to transient loads or excitations like wind and water waves or movements over uneven surfaces [54–56] (compare Figure 2.1). These transient dynamics pose significant challenges to contemporary modeling and system identification techniques, which frequently depend on steady-state assumptions. Despite the focus on steady-state analysis, it is becoming increasingly evident that a system's transient behavior may reveal more about its underlying mechanisms than the steady-state response alone. This realization highlights the need for developing advanced methodologies capable of capturing and analyzing transient phenomena to provide deeper insights into system characteristics and enhance model accuracy.

Emergence: The overall system dynamics emerge from the intricate interplay of its components, aligning with the complex systems maxim that "the whole is more than the sum of its parts." This concept dates back to Anderson's seminal work in 1972 [57], which contrasted the reductionist view with a constructionist perspective, highlighting phenomena such as broken symmetries and the emergence of different laws at various scales. Anderson's work challenged the traditional reductionist approach by proposing that the system's behavior could not be fully understood merely by examining its individual components, as new laws or dynamics might arise at a higher level of organization. Interestingly, contemporary research suggests that the global dynamics of a system could also be less than the sum of its parts, influenced for example by equalizing interactions. Although largely overlooked in engineering analyses, this perspective encourages the development of more holistic approaches that account for emergent properties within complex mechanical systems.

Multi-scales: Multi-scale dynamics exemplify this complexity, for example by uniting dynamics at slow and fast time scales within a single system. Solving these systems often poses difficulties for current computational solvers. Examples for multi-scale dynamics include the interaction between slow-varying temperatures in the robots environment and high-frequency friction induced vibrations within its joints, or slow excitation of the wind turbine shaft through water wave in contrast to high-frequency wind-induced vibrations. These phenomena motivate the pursuit of holistic modeling approaches that can accommodate diverse scales.

Data sparsity and noise: In addition to the inherent complexities of the mechanical system itself, practical considerations such as the sparsity of measurement data or noise contamination play a vital role in the analysis and modeling of dynamical systems. Measurement data may be sparse for several reasons. First, the number of physical sensors can be limited, as some locations may be impractical or impossible to monitor, for example, due to extreme environmental conditions or limited available space, resulting in incomplete system state measurements and spatial data sparsity. Second, data acquisition via experiments can be time-consuming and costly, limiting the number of measurements and causing parameter and temporal data sparsity. The case studies in Sections 3.1.2 and 3.2.2 provide solutions to address data sparsity.
While noise is a common issue across scientific fields and not the primary focus of this work, the case studies examine the noise robustness of the methods, albeit at a low level. In practical scenarios, noise in real-world data is often managed using filtering techniques.

2.2 Physics-based modeling

Dynamical systems offer a mathematical framework for describing the complex interactions and co-evolution of quantities over time, providing critical insights into the natural world. The study of dynamical systems encompasses the analysis, prediction, and comprehension of the behavior of systems governed by differential equations or iterative mappings, which capture how a system's state evolves. Mathematical models are a crucial tool for describing and analyzing real-world systems across various scientific disciplines. In mechanical engineering, these models often build upon a well-established foundation of physics-based knowledge that has been developed over centuries. Fundamental laws of physics are typically expressed through differential equations. Recently, data-driven methods, particularly those leveraging neural networks, have emerged to enhance traditional "top-down" with a "bottom-up" strategies. Hybrid approaches aim to integrate physics-based knowledge with the strengths of high-dimensional neural networks. Digital models, as abstractions of real-world systems, allow for the efficient querying of system properties, thereby saving time and resources compared to costly and labor-intensive experimental methods. This chapter will primarily focus on physics-based modeling and analysis, the increasingly popular data-driven perspectives will be presented in subsequent chapters.

There are several objectives that guide the modeling process, particularly in fields like engineering, physics, and data science. Based on general modeling strategies, there are four primary goals to consider [4]:

Prediction aims at forecasting the future state of the system, for new initial conditions or system parameters, or its reaction to different environmental conditions. The behavior of the dynamical system is predicted based on past and present data.

Optimization helps improve the efficiency, performance and stability of a structure and its dynamics, especially during the design process.

Control focuses on approximating the full system state from sparse measurement data to actively control the underlying system. In control-oriented models, the aim is to estimate the state of the entire system from sparse measurement data to develop control strategies that achieve the desired behavior.

Understanding concentrates on obtaining interpretable models. The objective is gaining additional understanding of the inner workings of a dynamical system, possibly discovering new physical laws in the process.

Each of these objectives requires different modeling techniques and approaches. The choice of a modeling strategy often depends on the specific goals, available data, and the complexity of the system being studied. This thesis is particularly concerned with analyzing system state and understanding the interplay between different system components.

The global *state* of a dynamical system describes its response to a set of initial conditions or an external excitation. Differently shaped attractors determine the behavior of the system, for example, fixed points, (periodic) orbits, or strange attractors. The *stability* of a state determines its resilience to small perturbations, describing whether the system will return to

the original attractor if perturbed. Many real-world dynamic systems show multi-stability, see Section 2.1. For a linear system, the eigenvalues of the state matrix determine the state and stability of the oscillations. An oscillatory mode is stable if the corresponding eigenvalue lies in the left half of the complex plane. These linear and local stability concepts are limited to point and limit cycle attractors [58]. Basin stability provides a more global approach to the stability of nonlinear systems, essentially measuring the volume of a basin of attraction of a given attractor [58, 59]. However, understanding the often intricate mechanisms that lead to multi-stability and predicting which specific state a system will arrive at remains an active area of research. Brake squeal is an example of a multi-stability phenomenon from engineering that is not entirely understood until today. Data from brake squeal experiments is used in case studies in Publication I and Publication II. These high-frequency oscillations depend on many parameters and their interplay [60–62], and are sensitive to small parameter variations [63–65]. The limited repeatability of experimental results [62, 64] poses an additional challenge, as expensive experiments [61, 62] are still required for analysis and verification of models. In industry, complex eigenvalue analysis (CEA) is commonly employed to study brake squeal of a given system [66, 67]. The method computes complex mode shapes to determine the stability of the dynamical system; however, its applicability is inherently restricted to linear systems. This limitation underlines the need for innovative perspectives and approaches that can extend state or stability analysis to nonlinear systems.

The second key area of interest in this work focuses on the *functional relationships* governing the interactions between different components of a machine, extending the concept beyond mere geometric proximity. Machine components are connected through various means such as welds, bolts, screws, gears, or friction surfaces. Describing these connections is difficult due to the limited accessibility of interfaces, the sensitivity of dynamics to minuscule parameter variations, and the changes in parameters throughout experiments, which often cannot be replicated. As a result, data tends to be sparse, as previously described in Section 2.1. Although the theoretical points of contact might be describable, quantifying the actual functional relationships between components proves to be difficult. Apart from the difficulties in describing the interconnections, interaction mechanisms beyond mere geometric proximity play an important role in the emerging dynamics of the entire system. State-of-the-art methods such as transfer path analysis [68] and operational deflection shape analysis [69] are employed to study the dynamics of composed structures. The accuracy of these methods heavily relies on precise measurements and suitable sensor placement to ensure that appropriate data is collected for analysis [70].

In the strive for a better understanding of the system states and the intricate component relationships that give rise to the system dynamics, this work develops novel perspectives beyond the *classical description*, which is given by

$$\mathbf{M}\ddot{\mathbf{x}} + \mathbf{D}\dot{\mathbf{x}} + \mathbf{K}\mathbf{x} + \mathbf{f}_{\mathrm{nl}}(\mathbf{x}) = \mathbf{f}_{\mathrm{ex}}(t), \tag{2.1}$$

describing the dynamics of a mechanical system in terms of inertia $\mathbf{M}\ddot{\mathbf{x}}$, damping $\mathbf{D}\dot{\mathbf{x}}$, spring forces $\mathbf{K}\mathbf{x}$, excitation forces $\mathbf{f}_{\mathrm{ex}}(t)$, and nonlinearities $\mathbf{f}_{\mathrm{nl}}(\mathbf{x})$. For a single nonlinear component i within a system with nearest-neighbor coupling, the equation of motion is

described by

$$m\ddot{x}_i + d\dot{x}_i + k_\mathrm{l}x_i - k_\mathrm{c} \cdot (x_{i-1} + x_{i+1} - 2x_i) + f_\mathrm{nl}(x_i) = f_{\mathrm{ex},i}(t), \tag{2.2}$$

where $\ddot{x}_i, \dot{x}_i, x_i$ describe the acceleration, velocity and displacement of the oscillator, m its mass, d its damping, k_l and k_c the related linear and coupling spring constants, and $f_\mathrm{nl}(x_i)$ the nonlinear spring forces, and $f_{\mathrm{ex},i}(t)$ defines the external forcing.

System identification aims at fitting a mathematical model to data from a real-world dynamical system. The standard system identification process can be divided into three main steps. First, a model structure is chosen based on model requirements and prior knowledge of the underlying system. The decision could for example be based on first principles of physics, such as symmetries and conservation laws [71]. Second, the model parameters have to be estimated from the data. For example, the inertia and stiffness properties of a rotating system can be read off a Bode plot that describes the system amplification over a given frequency range. Third, the model is validated, for example by comparing measurement data to time series predicted by the model. The model is accepted if the reconstruction error is sufficiently small. A detailed overview of current trends in system identification can be found in [72], while [45, 73] focus on nonlinear system identification.
Many of the "classical" system identification methods rely on characteristic spectral properties of the system and steady-state measurements [3, 74]. While it is suggested that identifying higher-dimensional models with strong nonlinearities is within reach – primarily through the expansion of linear identification techniques to nonlinear systems – nonlinear system identification remains a challenging task [45]. Furthermore, the traditional approaches often require some understanding of the underlying physics driving the dynamics, which may not always be available [71]. These limitations motivate the development of purely data-driven or observation-based approaches, such as those involving equation and machine learning, which are discussed in the next Chapter 3.

2.3 Perspectives on mechanical dynamical systems

In response to the various phenomena and modeling goals in mechanical dynamics, various perspectives on nonlinear dynamical systems have evolved. Each of these views is suited to the study of a specific phenomenon and providing its own intuition on the underlying dynamics. Some perspectives have already been introduced, for example, the ordinary differential equation in time domain in Equations 2.1 and 2.2, that can be solved for time series data, which in turn represent the vibratory movement of the individual parts. While the equation allows for mathematical manipulation, the time series data allows for an intuitive understanding of the movements: is there a repeated harmonic motion, does the motion decay? At the same time, none of these two views allow for an intuitive understanding of the frequency content of the dynamics, which requires an additional perspective. Figure 2.2 provides an overview of selective perspectives on nonlinear dynamics. The subsequent parts of this section explain these perspectives and the transformations connecting them. While this overview is not exhaustive and does not encompass every possible viewpoint –

an undertaking that would by far exceed the scope of this work – it is intended to illustrate a range of potential perspectives. The purpose of this section is to convey the notion that diverse perspectives on the same dynamical system can lead to fundamentally different analytical approaches, thereby encouraging the development of new, complementary viewpoints.

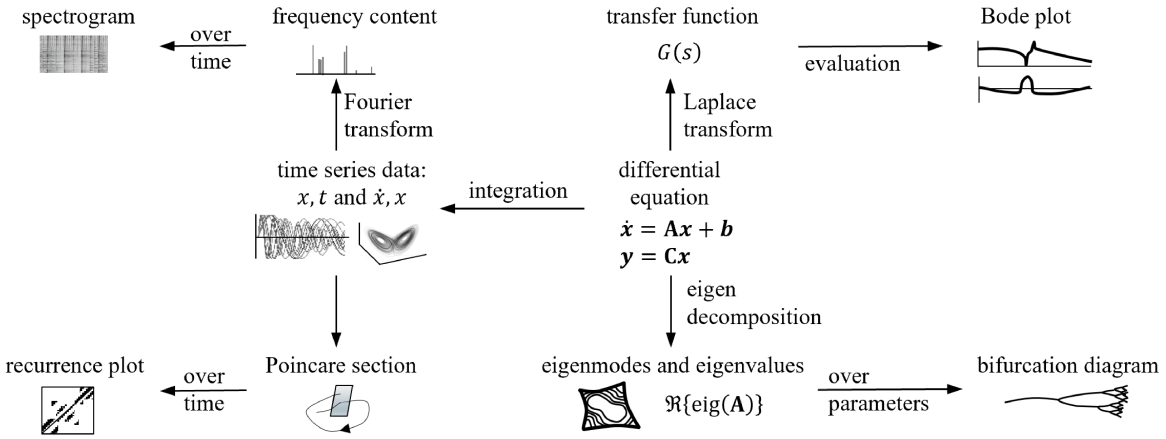

FIGURE 2.2: Different perspectives on the dynamics of mechanical structures. Differential equations, the baseline mathematical formulation, can be decomposed into eigenmodes and eigenvalues, which provide insight into system stability and default patterns of deformation or motion. A bifurcation diagram illustrates the change in dynamics over a specific system parameter. A Laplace transform of the time-domain differential equations yields a transfer function, the classical control systems perspective that relates system input and output, from which the Bode plot can be derived. Time series data can be obtained from the differential equations via integration, or directly from a system via measurements. The frequency content of a time series can be assessed using a Fourier transform, which yields a statistic of the frequency content, or a short-term Fourier transform, which results in a spectrogram that represents the frequency content over time. A Poincaré section provides an intermediate step towards the recurrence plot of a time series, which can help classify the dynamic properties of the time series. This representation is an incomplete one, which merely serves to illustrate how different perspectives can yield different intuitions about a dynamical system.

Analytical equations. Equations are great: their (mostly) compact formulation in terms of mathematical operators has made them a fundamental component in the expression of core physical laws, such as Newtons laws of motion or the Navier-Stokes equations. Their representation via mathematical operators facilitates clear identification of various elements within a system, such as coupling terms that illustrate interactions between components, or inertial forces (compare Equations 2.1 and 2.2). Additionally, equations allow for an intuitive recognition of diverse effects, including damping phenomena and nonlinearities. Depending on the quantities of interest, equations can be formulated in different domains, such as time, frequency, or Laplace domain, as illustrated in Figure 2.2. Transformations between the domains are possible through mathematical operations. Despite their various advantages, it has to be noted that equations, as models of real-world systems, contain assumptions and approximations, which can impact their applicability and accuracy.

Transfer function and Bode plot. The transfer function is a perspective developed in control theory. The description in Laplace domain, derived from continuous-time systems through

a Laplace transform, provides an equation-based perspective of the input-output relation of a dynamical system. A pole-zero plot shows the poles and zeros of the equation in the complex plane, from which system properties such as stability can be read off. The Bode plot can be obtained via evaluation of the transfer function. It consists of a magnitude and a phase plot, describing the amplification and phase shift of the systems response for a given frequency. The evaluation of the Bode plot for model parameters during system identification is a common tool in electrical engineering, as has been referred to in Section 2.2.

Modal decomposition, eigenmodes, and bifurcation diagram. Through the eigendecomposition of the state matrix $\mathbf{A}$, the eigenmodes and eigenvalues of the system can be identified. These eigenmodes, along with their corresponding eigenvalues, provide homogeneous solutions to the analytical equations of the linear system and describe the response shape of the unforced system. Eigenvalues are crucial for assessing system stability and oscillatory properties through their location in the complex plane, see Section 2.2.
These mode-based analyses are typically limited to linear systems. Extensions to nonlinear systems, such as nonlinear normal modes [75–78], offer an alternative by providing a more nuanced understanding of the system's inherent dynamics. Critical transitions between regimes or qualitatively different dynamic behaviors can be effectively represented using bifurcation maps [33, 63]. Variations in the parameters of a dynamical system can cause attractors to be created or destroyed. These phase transitions are depicted in a bifurcation diagram which shows co-existing attractors together. These diagrams are a common tool in the analysis of nonlinear dynamical systems, for example, to illustrate routes to chaos.

Time series. In the framework of Figure 2.2, time series data is derived through integration of the governing equations, but it could also be obtained from direct measurements of a real-world system. This data consists of successive observations of a quantity at known time intervals, describing its evolution over time. For example, it may depict displacement over time or, in a state space representation, the interplay of velocity and displacement, essentially forming a multi-dimensional time series. While factors like coupling and system mass might not be immediately apparent from a time series, it provides intuitive insights into the oscillatory behavior of a system, revealing characteristics such as whether it is damped or oscillatory. In a state space context, multi-dimensional patterns can emerge, such as periodic orbits. Analogous to analytical equations, time series can be analyzed in domains, for example, time, frequency, or Laplace.

Frequency content and Fourier transform. The Fourier transform offers a method to transform time series data into harmonic frequency components. This transformation allows for the assessment of individual frequency contributions to the time series and the examination of their evolution over time through the spectrogram. Such analyses help understand the frequency-dependent characteristics of the system.

Poincaré section and recurrence analysis. A Poincaré section, derived from time series data, serves as a tool for understanding the system's dynamics by providing a cross-section of its state space trajectories. Originally introduced by Eckmann et al. in [79] recurrence plots expand on this concept by adding a temporal dimension. Building on principles described by Poincaré to identify patterns and transitions through recurrence quantification analysis,

recurrence plots can distinguish between periodic, quasi-periodic, and chaotic motions, as well as determine laminarity and determinism [3]. An overview of recurrence quantification analysis can be found in [80], and its application to mechanical systems is tested in [3]. Recurrence analysis is one of the underlying methods for the network analyses in Chapter 4.

In summary, phenomena such as nonlinearities and transients from different sources, combined with a large number of degrees of freedom and often sparse real-world data pose significant challenges to our modeling approaches today. It is therefore often difficult to study things such as functional relationships between components, or system stability, within this context. This chapter has provided a concise overview of the dynamics of machines composed of numerous interacting components, highlighting the challenges associated with modeling and analyzing these systems. It has demonstrated that various perspectives have evolved to study different phenomena, thereby motivating the development or integration of additional perspectives to address phenomena that remain difficult to understand.

The subsequent chapters will introduce innovative, data-driven perspectives and approaches to tackle some of the challenges in nonlinear structural dynamics. Chapter 3 provides an overview on state-of-the art data-based methods: First, Section 3.1 presents statistical learning approaches and a case study of a novel approach to nonlinear structures with limited observability by developing a linear reduced-order model from an equation-based perspective. Second, Section 3.2 provides insights into neural network-based methods, with a case study examining system states and stability from sparse measurement data to create a comprehensive map of system states across a broad range of parameters. Chapter 4 introduces a novel perspective by applying network science to study functional relationships within mechanical systems.

3 Data-driven methods

The increased availability and quality of measurement data, along with the development of higher computational power, has led to a rise in data-driven approaches to modeling and analyzing complex dynamical systems [81–83]. Data-based methods can be split into two main fields [4, 32]: statistical learning and machine learning. Statistical learning focuses on obtaining interpretable low-order models that generalize and can be queried for extrapolations [84], fostering understanding and fast and efficient modeling. Machine learning approaches concentrate on accurate predictions, interpolation, and complex mechanisms, accepting large models that are not necessarily (human) interpretable. Mixed methods have also been developed, for example, methods that employ neural networks to learn low-dimensional models from data.

This chapter gives an overview of advances, advantages, and shortcomings in both fields. Section 3.1 is dedicated to describing statistical and equation learning methods, which are closely related to reduced-order modeling approaches, and introduces Koopman operator theory, a concept popular in the equation learning context. Section 3.1.1 provides some background to the case study presented in Publication I, discusses results, and points out the contribution of the work to the fields of statistical learning and nonlinear structural dynamics. Section 3.2 introduces the developments in machine learning and neural network-based methods, with a focus on their application in the engineering context. A case study in Publication II presents a method for mapping out the state of a dynamical system from sparse measurement data using a neural network-based approach, providing a more phenomenon-based perspective on the dynamics of the underlying system. Section 3.2.1 discusses the results, contributions, and possible further research directions of the second case study.

3.1 Statistical learning

Statistical learning aims at generating reduced-order models from measurement data. These low-dimensional models allow for fast and efficient modeling and are often interpretable in terms of physical quantities. Inferring fundamental laws directly from data is a constant motivator in scientific research, especially in cases where little to no prior knowledge related to the underlying first principles of physics is available [71, 82]. Equation learning algorithms, which distill models in the form of differential equations automatically from measurement data while requiring little to no prior knowledge of the underlying system, form a significant advancement towards this goal. One popular equation learning method is the sparse identification of nonlinear dynamical systems (SINDy) algorithm [82] and its

variants, which utilize sparse regression techniques to derive differential equations from time series data. The efficacy of this algorithm for mechanical model system data is explored in [74, 85]. SINDy uncovers familiar states and structures from uni- and multivariate time series data, often in the form of nonlinear models. The resulting models in the form of differential equations are popular for their interpretability, and possibility to be studied for physical properties of the underlying system. Since nonlinear models are not necessarily suited to the analysis with classical methods, which often require linearity, Koopman operator theory has been suggested as a tool for obtaining linear models from data. The Hankel alternative view of Koopman HAVOK algorithm combines equation learning and Koopman operator theory to generate a forced, linear, low-order model from sparse measurement time series data.

This section will give a brief overview on statistical learning methods that generate reduced-order models from data and provide some background on Koopman operator theory. The application of the HAVOK algorithm in the context of mechanical vibrations is discussed in Section 3.1.1, based on a case study in Publication I that highlights the advantages, possibilities, and pitfalls of the HAVOK algorithm.

One of the first methods developed to discover equations from data is the eigensystem realization algorithm [86], which uses a Hankel matrix and singular value decomposition to detect a minimum order representation of a dynamical system in the form of mode shapes, modal damping rates, and frequencies. Automated symbolic regression [87, 88] sets up a library of candidate symbolic models to fit recorded measurement data and iteratively evaluates these models based on their response to new sets of initial conditions, simplifying and restructuring candidate models throughout the process. In SINDy, a library of candidate nonlinear function terms is built up from the available measurement data. Sparse regression, such as the least absolute shrinkage and selection operator (LASSO) [89], or, in this case, sequential thresholded least squares, is used to obtain a model description with as few terms as possible. The l1-penalization of the number of active model coefficients within the regression yields parsimonious models [4]. The SINDy algorithm has been employed across the scientific fields to study fluid dynamics [90, 91], biological networks [92], atmospheric chemistry [93, 94], and active matter [95]. In engineering, SINDy has been applied for example to models of low-dimensional oscillators [74] and cantilever beams [85], and to power grid dynamics [96]. Several variants and extensions of the algorithm have been developed, such as the probabilistic ensemble-SINDy (E-SINDy) [93] or statistical Z-SINDy [97] approaches that focus on uncertainty quantification, combinations with time delay embedding for sparse data scenarios [74], inclusion of higher-order derivatives [98], and integration with model predictive control schemes [99], adaptations for data with large noise (weak SINDy or WSINDy) [100], or the discovery of partial differential equations (PDE-FIND) [101]. In [90], physical constraints and symmetries are integrated into the method, while several variants connect to machine learning approaches, for example, using autoencoders [71, 102, 103], shallow neural networks [104, 105], or reinforcement learning [106].

The discovery of differential equations from data marks significant progress in the strive for interpretable models from data. However, the resulting models are often nonlinear and therefore not amenable to analysis with classical linear methods [32]. Koopman operator

theory has been named as a promising tool to resolve this issue, as a system identification method that simultaneously identifies a suitable set of coordinates [32]. By translating the system states into the Hilbert space of function of the state, capturing the nonlinearities within new system states, a nonlinear system can be transformed into a linear one. This method offers a linear perspective on a nonlinear dynamical system by incorporating the nonlinearities into the transformed system states, typically trading finite dimensions for infinite ones. This facilitates the analysis of the underlying dynamical system with linear tools, without the need for approximation through linearization tools.

Koopman operator theory was introduced in 1931 by Koopman [107] and has gained popularity in the last two decades with works by Mezic et al. [108, 109], due to its strong connection to data-based methods [32]. The key challenge in Koopman operator theory is the tendency of the operator to be infinite, therefore the search for a suitable closed-form approximation is one of the primary concerns in related research endeavors [32, 110]. With the development of dynamic mode decomposition (DMD) [111–113], a purely data-driven method for approximating the Koopman operator from data has evolved. DMD unites the spatial dimensionality reduction capabilities of the singular value decomposition with the advantages of the discrete Fourier transform to detect spatiotemporal structures in time series data. The connection between the DMD and Koopman mode decomposition has been made in throughout the literature [112, 114, 115], and the method has evolved to be one of the standard methods for obtaining the Koopman operator from data. Other approaches include autoencoders [116]. As estimating the Koopman operator from data is a similar task to equation learning, several approaches combine the two procedures, for example, featurized Koopman mode decomposition [117], or the sparse EDMD, which combines a SINDy-type sparse regression with a DMD-approach [118].

More details on Koopman operator theory are given in Publication I and is available in review articles [32, 119, 120]. The following section discusses a case study on an equation learning algorithm that makes use of Koopman operator theory. The case study can be found in Publication I.

3.1.1 Koopman-based interpretable models from sparse data

The HAVOK algorithm [110] combines SINDy-type equation learning and Koopman operator theory to derive a linear representation of the underlying system from sparse measurement data. The resulting model is a forced, low-order state space representation, a familiar form that is well understood. Consequently, the entire model is, in principle, amenable to analysis using standard linear tools, and interpretable in terms of physical laws and quantities. A case study applying HAVOK to the nonlinear vibrations of mechanical structures is presented in the subsequent Publication I. This section gives a brief introduction to the HAVOK algorithm and the results of the case study, followed by a discussion of the article and its contribution to the field. The section concludes with a brief outlook on further research directions in this context.

Sometimes called HANKEL-DMD [115] or delay-DMD [121], the HAVOK algorithm [110] unites the three aims of system identification, linearization, and reduced-order modeling into a single, data-driven method. It combines Koopman operator theory, time delay embedding, and model reduction to generate a forced linear low-dimensional state space model from sparse measurement data, and can thus be interpreted as a version of SINDy for sparse data scenarios. Similar to approaches taken in the eigensystem realization algorithm [86] or dynamic mode decomposition [121], HAVOK starts by stacking the available measurement data into a Hankel matrix. A singular value decomposition of the Hankel matrix determines a suitable model rank and a SINDy-type sparse regression is employed to set up a state space system. A forcing term in the state space model captures elements not captured by the linear approximation. The theoretical foundations of the algorithm have been explored in [114, 115, 122]. In the original work, the algorithm was applied to discover models from several chaotic systems, such as the Lorenz or Rössler systems, and real-world data from different fields. Publication I illustrates the applicability of the algorithm to synthetic and real-world mechanical systems.

Summary of the case study
Publication I provides a more detailed description of the HAVOK algorithm. The study describes hyper-parameters, tuning knobs, and the inner variables of the algorithm, along with their interconnections and mutual influences. The applicability in the context of mechanical vibrations is assessed via variations of a classical model in structural dynamics, the Duffing oscillator, and real-world data from a friction brake system. The application to the well-known mechanical oscillator system allows for the comparison of the resulting model with the true underlying description, for example in terms of model and matrix structure, dimensionality, system eigenvalues, stability, and predictive quality. While the HAVOK model generally reproduces the observed dynamics well, the quality of the remaining discovered properties is highly dependent on the underlying system. The dimensionality of the HAVOK model is related to the number of frequency components in the underlying dynamics. Systems with a low number of frequency components, such as linear systems forced with a finite number of harmonics, result in an unforced HAVOK model that accurately captures stability properties. Increasing nonlinearity and an increasing number of frequency components in the forcing of the underlying system result in larger and more forcing-intense HAVOK models. With the increasing importance of the forcing term, more of the properties of the underlying system are not represented in the state matrix of the HAVOK model, decreasing its interpretability in terms of physical quantities. While the system dimension, stability, and dominant frequency components are discovered correctly for systems with a low number of frequency components, these properties can no longer be discovered as the number of frequency components goes to infinity, for example, in excitation with a frequency sweep. The application of the algorithm to real-world friction brake system data results in good reconstruction of the dynamics and discovers models of similar dimensions to those discovered in other literature.

Discussion and contribution to the field
The case study provides an in-depth application study of HAVOK and its hyper-parameters. By demonstrating how the choice of parameters affects the remaining algorithm steps and ultimately the result, the study unravels the inner workings and dependencies within the

method and hopefully helps future users to choose suitable parameter settings for their studies. To the author's knowledge, the study represents the first application of the HAVOK algorithm to mechanical oscillators with a focus on the extraction of physically meaningful properties from the resulting model, such as stability and damping. This focal point aligns with one of the key questions in Koopman operator theory, which asks how properties from the nonlinear model carry over to the Koopman model [32]. The results of the study agree with the findings in [123], where the SINDy and HAVOK algorithms are used to discover nonlinear multiscale systems. The authors in [123] show that the unforced HAVOK model correctly encodes the dynamics of weakly nonlinear systems, but fails with chaotic dynamics, which require the forcing term. This work also draws a connection between the new system coordinates found by the singular value decomposition of the Hankel matrix and the Fourier modes, underlining the dependence of the resulting HAVOK model on the number of frequency components in the underlying system. It has been shown that the quality of the approximation of the Koopman operator with the HAVOK algorithm is highly dependent on the number of frequency components in the underlying system. It is a well-known phenomenon that no homeomorphic coordinate transform from a multiple fixed points to a single fixed point system exists [32]. Compared to standard linearization techniques, which linearize the dynamics of a system within a small region around the fixed points [32], the Koopman operator provides a linearization of the system for an entire basin of attraction of a fixed point [124]. It cannot, however, provide a complete linearization of a system with multiple fixed point, which is why the HAVOK model requires a forcing term. Therefore, a significant amount of the dynamics is hidden in the forcing term of the resulting state space model, resulting in a non-autonomous model that is highly dependent on the input forcing for its predictive capabilities. Extensions of the algorithm that aim at approximating the forcing for better predictions include learning from the prediction error [125] or the employment of a second Hankel matrix [126].

From a mechanical engineering perspective, the HAVOK algorithm provides a data-driven method for identifying a linear reduced-order model from sparse measurement data, without requiring any prior knowledge of the underlying dynamical system. The case study and its insights regarding the interpretability of the results illustrates the possibilities and limitations of the algorithm, especially in the context of mechanical structural vibrations, guiding as to whether the method is a good choice for a given scenario. The article demonstrates that the choice of input data is crucially important, as the resulting model can capture only the observed and observable dynamics. For example, a large amount of transient dynamics might distort the results and conceal the underlying system. While the first point, the crucial dependence on the input data, is inherent to all data-based methods, the second underlines that this equation learning algorithm faces similar challenges as standard system identification methods described in Chapter 2. This might not be surprising, since the two approaches share the goal of correctly identifying models in the form of differential equations.

Outlook

The discovery of differential equations directly from measurement data with little or no prior knowledge of the underlying dynamical system remains an active area of research. In the HAVOK algorithm, the coordinates for the linear model are obtained within the quite rigid

framework of the singular value decomposition of the Hankel matrix. Perhaps a more open definition of Koopman eigenfunctions would facilitate a more suitable approximation of the Koopman operator in some cases. Another important development direction in equation learning is the inclusion of uncertainty quantification into the algorithms [32], which would help to assess the model quality in real application scenarios where the true dynamics are unknown.

In summary, this chapter has studied a method for deriving a linear, low-order model from sparse measurement data of a nonlinear dynamical system. This approach utilizes a Koopman-inspired technique that transforms the coordinate space into a nonlinear function space, aiming to capture all nonlinearity in the system states. However, some aspects of the nonlinearity remain unresolved due to the nature of the approximation. While the method accurately reproduces a linear system, it faces challenges when handling systems with infinite frequency components, such as systems with transients or strong nonlinearities. If the resulting state space model is not autonomous and requires a forcing term, its predictive and interpretative capabilities are limited since much of the system information is moved into the forcing instead of the states or state matrix.

Among the methods proposed in this work, the equations perspective is the most closely aligned with the "classical" physics-based framework. The model, expressed as a linear state space representation with nonlinear forcing, allows for conventional analyses, for example, of linear system stability via its eigenvalues. Although this approach is very promising in principle, it becomes evident that the highly constrained structure of a linear low-order model might not be suitable for capturing all aspects of nonlinear machine dynamics, even when the model is defined in a nonlinear function space. The following Section 3.2 and Chapter 4 explore alternatives beyond state space models and move from the all-encompassing equations to a more phenomenon-focused perspective on system stability and functional relationships.

3.1.2 Publication I: Data-driven reduced order modeling for mechanical oscillators using Koopman approaches

C. Geier, M. Stender, and N. Hoffmann. "Data-driven reduced order modeling for mechanical oscillators using Koopman approaches". *Frontiers in Applied Mathematics and Statistics* 9 (2023). DOI: 10.3389/fams.2023.1124602

frontiers | Frontiers in Applied Mathematics and Statistics

TYPE Original Research
PUBLISHED 28 April 2023
DOI 10.3389/fams.2023.1124602

OPEN ACCESS

EDITED BY
Benjamin Unger,
University of Stuttgart, Germany

REVIEWED BY
Jonas Kneifl,
University of Stuttgart, Germany
Camilo Silva,
Technical University of Munich, Germany

*CORRESPONDENCE
Charlotte Geier
✉ charlotte.geier@tuhh.de

RECEIVED 15 December 2022
ACCEPTED 06 April 2023
PUBLISHED 28 April 2023

CITATION
Geier C, Stender M and Hoffmann N (2023) Data-driven reduced order modeling for mechanical oscillators using Koopman approaches. *Front. Appl. Math. Stat.* 9:1124602. doi: 10.3389/fams.2023.1124602

Data-driven reduced order modeling for mechanical oscillators using Koopman approaches

Charlotte Geier[1]*, Merten Stender[1,2] and Norbert Hoffmann[1,3]

[1]Dynamics Group, Department of Mechanical Engineering, Hamburg University of Technology, Hamburg, Germany, [2]Cyber-Physical Systems in Mechanical Engineering, Technische Universität Berlin, Berlin, Germany, [3]Imperial College London, Department of Mechanical Engineering, London, United Kingdom

Data-driven reduced order modeling methods that aim at extracting physically meaningful governing equations directly from measurement data are facing a growing interest in recent years. The HAVOK-algorithm is a Koopman-based method that distills a forced, low-dimensional state-space model for a given dynamical system from a univariate measurement time series. This article studies the potential of HAVOK for application to mechanical oscillators by investigating which information of the underlying system can be extracted from the state-space model generated by HAVOK. Extensive parameter studies are performed to point out the strengths and pitfalls of the algorithm and ultimately yield recommendations for choosing tuning parameters. The application of the algorithm to real-world friction brake system measurements concludes this study.

KEYWORDS

structural dynamics, system identification, state-space models, state-space embeddings, sparse measurement data, modal analysis

1. Introduction

The growing availability and quality of data in many fields of science throughout the last decades [1, 2] causes the emergence of data-driven techniques for understanding and analyzing dynamical systems [1–3]. In order to facilitate accurate and fast predictions of system dynamics, efficient reduced order models (ROM) are required [4]. Currently, many system identification methods that aim at generating ROM are limited to linear models or require prior information on the model structure [5, 6]. While neural network-based techniques are very popular, they are limited in their applicability to dynamical tasks [2] and often lack interpretability [7, 8]. Several deep-learning based reduced order modeling methods have evolved, such as deep learning based reduced order model (DL-ROM) [9], where autoencoders are applied for generating ROM of non-linear parameter-dependent partial differential equations, or its expansion using proper orthogonal decomposition (POD) to avoid an expansive training stage, called POD-DL-ROM [10]. However, these methods might also lack interpretability and have limited generalization capability beyond the time and parametric domain contained in the training data set [4]. In the pursuit of generating data-based models that generalize well, data-based reduced order modeling techniques which try to extract governing equations or laws of physics from measurement data gain popularity [6]. For example, an adaptive approach for inference of dynamics from time series data is presented in [11], a method for quantification of the reliability of the model learned from data is given in [12], and an algorithm for identifying non-linear dynamical

system from data is proposed in [13]. Methods such as symbolic regression [14], which can be applied to determine the structure of the underlying dynamics from data remain computationally expensive [6]. Other equation-free or data-based reduced order modeling methods include dynamic mode decomposition (DMD) [15, 16] for periodic or quasi-periodic systems, its extension EDMD to non-periodic systems [17], or the Hankel-DMD algorithm [18]. The sparse identification of non-linear dynamics (SINDy) algorithm [6] used sparse regression for the identification of governing equations from data, exploiting the fact that most dynamical systems can be described by only a few non-linear terms [6]. This method has been widely applied for identifying linear, non-linear, and chaotic oscillators as well as fluid flows [6]. As the initial version of SINDy requires measurements of the full state space of a dynamical system, several extensions for sparse measurements have evolved. Here, sparsity is meant as a limitation in system observability, i.e., measuring only a fraction of all degrees of freedom is possible. A version using higher order derivatives is developed in [19]. Other variations deploy autoencoders to learn suitable coordinate transformations in combination with the SINDy method to obtain a low-dimensional model that generalizes well [4, 8, 20]. The HAVOK (Hankel Alternative View of Koopman) algorithm [1] can also be interpreted as an extension of the SINDy algorithm for sparse data. The relation to Koopman operator theory [2, 21] has also been made for DMD and EDMD [16, 22], and autoencoders have previously been applied for learning Koopman eigenfunctions [23]. From one univariate measurement time series of a dynamical system, the HAVOK-algorithm retrieves a low-order model in the form of a forced state-space system by combining time-delay embedding, Koopman analysis, and sparse regression. The resulting state-space model is not a black-box system, but a system of equations comparable to classical analytical descriptions for dynamical systems. In the original study by Brunton et al. [1], the algorithm was applied to chaotic systems such as the Lorenz and Rössler system, the double pendulum, and real-world measurements such as electroencephalogram and electrocardiogram data, just to name a few.

In this study, the potential of HAVOK for identifying low-rank models for mechanical oscillators is investigated, starting from small analytical systems to measurement data from a real-world friction brake system. The main focus lies in the interpretation of the resulting state-space models, and how these relate to those models that one would achieve through a physics-based modeling approach using first principles. Extensive studies of the effects of tuning parameters of the algorithm and changes in model parameters on the resulting HAVOK models are performed. These yield insights as to the information of the underlying dynamical system that can be gathered from a HAVOK model, as well as the conditions under which those can be obtained. Chances and pitfalls of the application of the HAVOK-algorithm to mechanical oscillators are pointed out, along with recommendations concerning the optimal choice of tuning parameters.

2. Methods

The HAVOK-algorithm presented by Brunton et al. in [1] combines Koopman operator theory, embedding techniques, and sparse regression into a data-driven system identification approach that facilitates the recovery of a low-order state-space system from a given measurement time series. This study is concerned with dynamical systems in the form

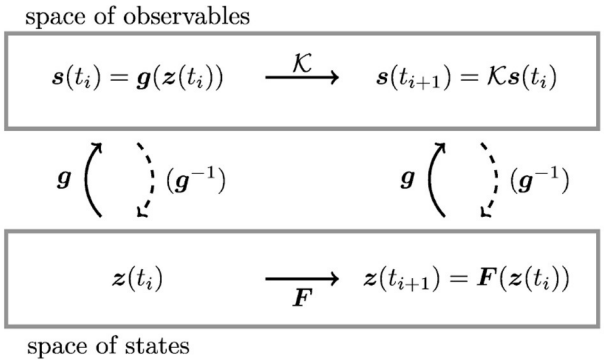

FIGURE 1
Illustration of Koopman operator theory. A finite, non-linear system described by states $z \in \mathbb{R}^n$ and a non-linear function $F : \mathbb{R}^n \to \mathbb{R}^n$ can be transformed into an often infinite-dimensional, linear system described by observables $s \in \mathbb{R}^{\mathcal{K}}$ and Koopman operator $\mathcal{K} : \mathbb{R}^{\mathcal{K}} \to \mathbb{R}^{\mathcal{K}}$. The measurement functions $g : \mathbb{R}^n \to \mathbb{R}^{\mathcal{K}}$ and their inverse counterparts $g^{-1} : \mathbb{R}^{\mathcal{K}} \to \mathbb{R}^n$ link between the two spaces.

$$\frac{d}{dt}\boldsymbol{x}(t) = \boldsymbol{F}(\boldsymbol{x}(t)), \forall t \in I, I \in (0, \tau), \tau > 0 \tag{1}$$

where I defines a time interval and $\boldsymbol{F} : \mathbb{R}^n \to \mathbb{R}^n$ is a time-invariant flow map. In the following, a multi-variate time series is denoted as $\boldsymbol{x}(t) \in \mathbb{R}^n, \forall t \in I$ and uni-variate time series as $x(t) \in \mathbb{R}, \forall t \in I$. This section is dedicated to presenting the HAVOK-algorithm and its parameters. Where possible, ways to compute optimal values of the parameters are pointed out. To illustrate the relation of the algorithm with Koopman operator theory, a short introduction to said theory will be given first.

2.1. Koopman operator theory

First introduced in 1931 by Koopman in [24], the Koopman operator faces a growing interest in recent years [2] as a method for learning dynamical systems from data [2, 25]. A detailed description of the Koopman operator and its history can be found in [2, 21]. The basic idea of Koopman analysis is illustrated in Figure 1. Koopman analysis is the transformation of a non-linear system described by a discrete, time-invariant, non-linear flow map $\boldsymbol{F} : \mathbb{R}^n \to \mathbb{R}^n$ and states $\boldsymbol{z} \in \mathbb{R}^n$ into a linear system by considering observables $\boldsymbol{s} \in \mathbb{R}^{\mathcal{K}}$ defined by measurement functions of the states $\boldsymbol{g}(\boldsymbol{z}) : \mathbb{R}^n \to \mathbb{R}^{\mathcal{K}}$ instead of the states $\boldsymbol{z}$ themselves. In the space of observables, the dynamics propagate in time through the linear Koopman operator $\mathcal{K} : \mathbb{R}^{\mathcal{K}} \to \mathbb{R}^{\mathcal{K}}$. The measurement functions $\boldsymbol{g}$ which link the space of states $\boldsymbol{z}$ with the space of observables $\boldsymbol{s}$ can be any functions from the Hilbert space of functions of the state [1]. In specific cases, inverse measurement functions $\boldsymbol{g}^{-1} : \mathbb{R}^{\mathcal{K}} \to \mathbb{R}^n$ may exist, which allows for a transform from the Koopman space $\mathbb{R}^{\mathcal{K}}$ back into the space of states $\mathbb{R}^n$. The relationship between

the Koopman operator $\mathcal{K}$ and the functions $\boldsymbol{F}$ can be described by

$$\mathcal{K}\boldsymbol{g}(\boldsymbol{z}(t_i)) = \boldsymbol{g}(\boldsymbol{F}(\boldsymbol{z}(t_i)) = \boldsymbol{g}(\boldsymbol{z}(t_{i1})) = \boldsymbol{s}(t_{i+1}), \tag{2}$$

where $\boldsymbol{z}(t_i)$ and $\boldsymbol{s}(t_i)$ denote the system state or respective observables at a discrete point t_i in time.

For most systems, the Koopman operator is infinite-dimensional, as illustrated in [21], but in some cases, a finite-dimensional representation can be found, as an example in [6] shows. Essentially, the Koopman operator exists, if one can find a transformation of the non-linear system $\boldsymbol{F}$ into a linear one using the measurement functions $\boldsymbol{g}$. The main challenge in Koopman operator theory is, thus, identifying a set of functions $\boldsymbol{g}$ for which the Koopman operator is finite [1, 21]. Many approaches to this challenge have been developed [2, 26], such as (Empirical) Dynamic Mode Decomposition (DMD) [17], Hankel-DMD [18], and the HAVOK-algorithm [1], which is the object of this study. If a finite-dimensional representation of the dynamical system at hand can be found, Koopman operator theory facilitates the identification of a global linear representation of the given non-linear system [1]. As the toolset and theoretical basis for linear system analysis are much larger and more robust, one would in many cases prefer a linear system description over a non-linear one. Even if an exact and finite-dimensional representation may not exist for a given system, the approximation of a finite-dimensional Koopman operator can still yield accurate system state-space models.

2.2. Time series similarity measures

Throughout this study, it is often necessary to estimate the accuracy of a model or an algorithm by comparing a ground truth time series x_{true}, typically the one measured, to the approximated time series x_{approx}, typically the one generated by HAVOK. To do so, the normalized mean absolute error is used, which is defined as

$$\text{nMAE} = \frac{1}{l}\sum_{t_i=1}^{l}\left|\frac{x_{\text{true}}(t_i) - x_{\text{approx}}(t_i)}{\max(|x_{\text{true}}|)}\right|, \tag{3}$$

where $x(t_i) \in \mathbb{R}^n$ is one uni-variate measurement within a time series x at time t_i. Each time series contains l different measurements at l different points t_i in time. This equation results in an error measure that is normalized to both the number of sampling points, i.e., the time series length, and the maximum amplitude of a time series. This choice is beneficial for measuring similarity across oscillatory time series of different lengths.

2.3. HAVOK and its parameters

After the basics of Koopman operator theory and the error measure have been explained, the HAVOK-algorithm [1] and its parameters will be described in the following. Figure 2 shows a flow chart of the HAVOK-algorithm, illustrating the six steps from data generation via the setup of the Hankel matrix, singular value decomposition, differentiation, sparse regression using the SINDy algorithm [6], to the compilation of the state-space system. The parameters of each individual step are marked on the left-hand side of the diagram.

2.3.1. Data acquisition

The input to the HAVOK-algorithm is a one-dimensional time series $x(t)$ of length t_l and sampled with frequency f_s. In theory, any measurement from a deterministic dynamical system could be used, as long as the dynamics are observable through that time series, as will be shown in detail later on. For the purpose of understanding the inner workings of the algorithm and its parameters, this study uses synthetic data generated through the integration of a known system of equations $\dot{\boldsymbol{x}} = \boldsymbol{f}(\boldsymbol{x}(t))$ in the first part, and measurement data from a real-world brake system in the second part. An exemplary time series is shown in the top right of Figure 2.

The data acquisition step has three parameters: the time series length t_l, the sampling frequency f_s, and the choice of degree of freedom from which the measurement is taken, although in practice, the latter two might be fixed by the sensor location. Naturally, those parameters will have an effect on the state-space model that is identified in the final step of the algorithm.

2.3.2. Time embedding

In a second step, the time series data $x(t)$ is stacked with q time-shifted copies of itself into a Hankel matrix $\boldsymbol{H} \in \mathbb{R}^{q\times p}$, where the second dimension p is computed from the number of input samples l minus the embedding dimension q, such that $p = l - q$. Generally, the adaptive parameter of this step, i.e., the embedding dimension q is chosen such that $q << p$. Figure 2 shows the resulting time series segments $x^{(q)}(t) \in \mathbb{R}, t \in [0, t_q], t_q > 0$ and $x^{(p)}(t) \in \mathbb{R}, t \in [0, t_p], t_p > 0$ which are contained in a column and a row of the Hankel matrix, respectively.

The procedure of using time-delayed observable as approximations of the Koopman operator was first introduced by Mezić and Banaszuk in [27] and is based on Takens' embedding theorem [28], which states that the state-space of a deterministic system can be uncovered from measurements in only one point. The relation of the Hankel matrix to the Koopman operator becomes apparent when rewriting the Hankel matrix $\boldsymbol{H}$ with the Koopman operator $\mathcal{K}$ to

$$\boldsymbol{H} = \begin{bmatrix} x(t_1) & x(t_2) & x(t_3) & \dots & x(t_p) \\ x(t_2) & x(t_3) & x(t_4) & \dots & x(t_{p+1}) \\ \vdots & \vdots & \vdots & \ddots & \vdots \\ x(t_q) & x(t_{q+1}) & x(t_{q+2}) & \dots & x(t_l) \end{bmatrix} = \begin{bmatrix} x(t_1) & \mathcal{K}x(t_1) & \mathcal{K}^2x(t_1) & \dots & \mathcal{K}^{p-1}x(t_1) \\ \mathcal{K}x(t_1) & \mathcal{K}^2x(t_1) & \mathcal{K}^3x(t_1) & \dots & \mathcal{K}^{p}x(t_1) \\ \vdots & \vdots & \vdots & \ddots & \vdots \\ \mathcal{K}^{q-1}x(t_1) & \mathcal{K}^{q}x(t_1) & \mathcal{K}^{q+1}x(t_1) & \dots & \mathcal{K}^{l-1}x(t_1) \end{bmatrix}, \tag{4}$$

such that the states are propagated in time by the Koopman operator $\mathcal{K}$. Reordering the resulting matrix to

$$\boldsymbol{H} = \begin{bmatrix} | & | & | & | \\ x^{(q)}(t) & \mathcal{K}x^{(q)}(t) & \dots & \mathcal{K}^{p-1}x^{(q)}(t) \\ | & | & | & | \end{bmatrix}, \tag{5}$$

$$\text{where } x^{(q)}(t) = \begin{bmatrix} x(t_1) \\ \mathcal{K}x(t_1) \\ \mathcal{K}^2x(t_1) \\ \vdots \\ \mathcal{K}x^{q-1}x(t_1) \end{bmatrix} = \begin{bmatrix} x(t_1) \\ x(t_2) \\ x(t_3) \\ \vdots \\ x(t_q) \end{bmatrix}$$

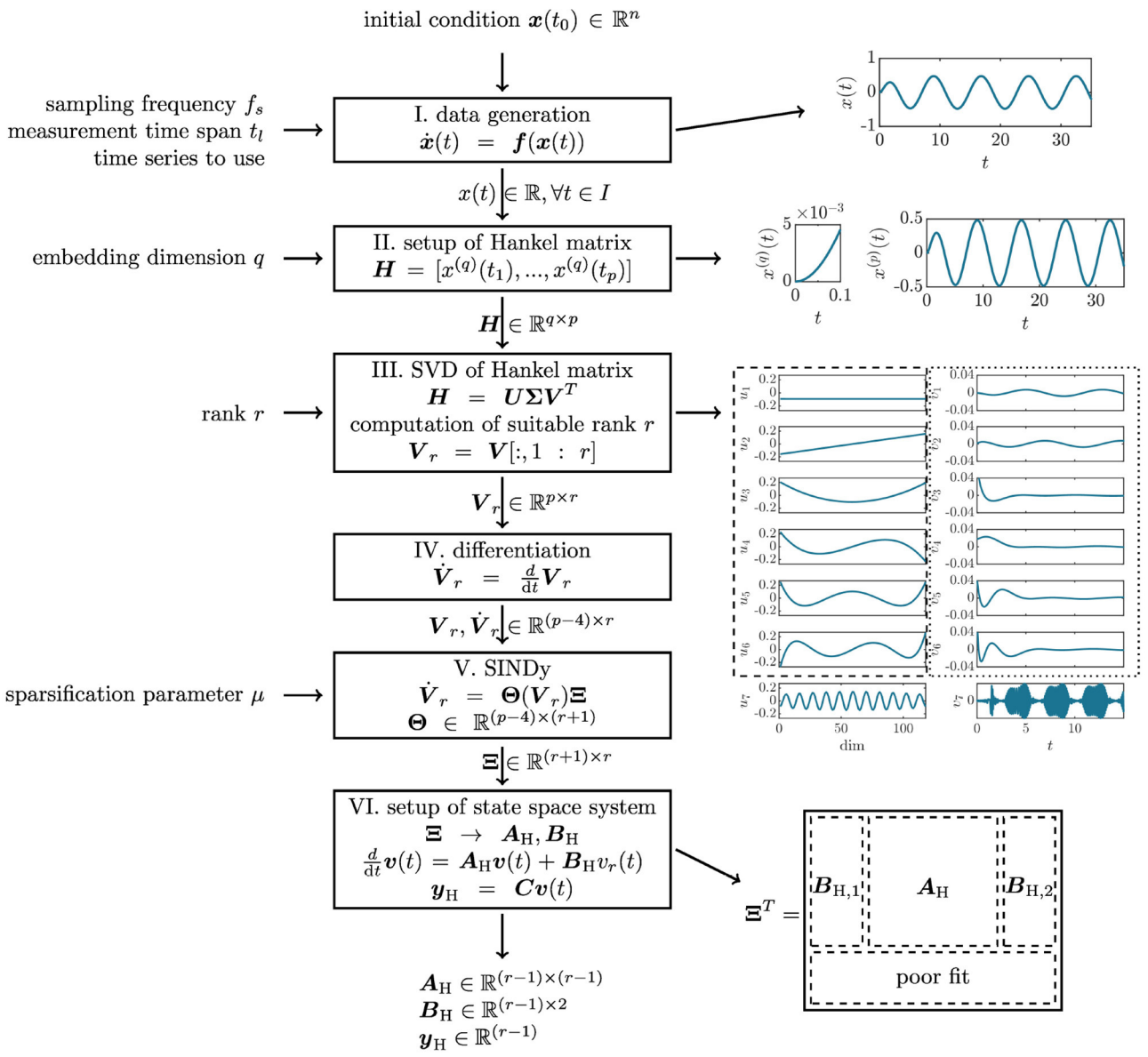

FIGURE 2
The six steps of the HAVOK algorithm, the parameters, and exemplary images of the data processed in each step. The vertical flow-chart illustrates the six steps data-generation, setup of the Hankel matrix, singular value decomposition (SVD) of the Hankel matrix, differentiation, sparse regression using the SINDy algorithm, and finally the setup of the state space system. On the left, the tuning parameters for each step are introduced. The images on the right-hand side of the figure illustrate the data each step is concerned with. From top to bottom. (1) The time series $x(t)$ generated is the first step. (2) The time series sections $x^{(q)}(t)$ and $x^{(p)}(t)$ that form a column and a row of the Hankel matrix $\boldsymbol{H}$, respectively. (3) The results of the SVD, represented by columns $\boldsymbol{u}_j$ and $\boldsymbol{v}_j$ of the matrices $\boldsymbol{U}$ and $\boldsymbol{V}$. The $\boldsymbol{u}_j$ represents a coordinate system, while the $\boldsymbol{v}_j$ represents the evolution of these coordinates in time t. (4) The state space matrices $\boldsymbol{A}_\mathrm{H}$ and $\boldsymbol{B}_\mathrm{H}$ are setup by dividing up the matrix of sparse coefficients $\boldsymbol{\Xi}$. The bottom row of $\boldsymbol{\Xi}$ is dropped as it represents a poor fit. Each step is described in detail in the respective section of the methods part of this study.

shows that the matrix $\boldsymbol{H}$ consists of p time series sections $x^{(q)}(t) \in \mathbb{R}$, which could be interpreted as q-dimensional snapshots of the system. In the next step, a singular value decomposition is performed on the Hankel matrix in order to determine a q-dimensional function basis for these system snapshots.

2.3.3. Singular value decomposition

A singular value decomposition (SVD) is performed on the Hankel matrix $\boldsymbol{H}$ in the third step, which yields both a function basis for the snapshots $x^{(q)}(t)$ and a description of the observed dynamics in the determined function space. The SVD decomposes the Hankel matrix $\boldsymbol{H} \in \mathbb{R}^{q \times p}$ into three matrices

$$\boldsymbol{H} = \boldsymbol{U}\boldsymbol{\Sigma}\boldsymbol{V}^T, \tag{6}$$

where $\boldsymbol{U} \in \mathbb{R}^{q \times q}$, $\boldsymbol{\Sigma} \in \mathbb{R}^{q \times p}$, and $\boldsymbol{V} \in \mathbb{R}^{p \times p}$. The orthonormal columns of the unit matrices $\boldsymbol{U}$ and $\boldsymbol{V}$ form a basis for the column- and row-space of the Hankel matrix $\boldsymbol{H}$, respectively. The matrix $\boldsymbol{\Sigma}$ contains q so-called singular values σ_j on the main diagonal,

which can be interpreted as representing the relative importance of the respective columns in $\boldsymbol{U}$ and $\boldsymbol{V}$ for representing the data in $\boldsymbol{H}$. The singular values are ordered from largest to smallest, and, accordingly, the columns of $\boldsymbol{U}$ and $\boldsymbol{V}$ are ordered by their importance for representing the data in $\boldsymbol{H}$. For a more detailed description of the SVD, see for example [21].

In the context of the HAVOK-algorithm, the columns $\boldsymbol{u}_j \in \mathbb{R}^{q\times 1}$ of the matrix $\boldsymbol{U}$ form a basis for the column space of $\boldsymbol{H}$ and, thus, for the snapshots $x^{(q)}(t)$, representing the Koopman observables $\boldsymbol{s}(t_i) = \boldsymbol{g}(x^{(q)}(t))$ as introduced in Figure 1. The vectors $\boldsymbol{u}_j$ provide a Koopman invariant subspace for the non-linear dynamics in the Hankel matrix. The time evolution of each $\boldsymbol{u}_j$ is described by the respective column $\boldsymbol{v}_j \in \mathbb{R}^{p\times 1}$ of the matrix $\boldsymbol{V}$. The vectors $\boldsymbol{v}_j$ can thus be interpreted as time series in the new coordinate system formed by the vectors $\boldsymbol{u}_j$. Note that the transformation $\boldsymbol{H} = \boldsymbol{U}\boldsymbol{\Sigma}\boldsymbol{V}^T$ is unique up to simultaneously switching the signs of a column in $\boldsymbol{U}$ and $\boldsymbol{V}$. Some exemplary observables $\boldsymbol{u}_j$ and new dynamics $\boldsymbol{v}_j$ are shown in Figure 2.

In [1], it was shown that only a small number of the columns of $\boldsymbol{U}$ and $\boldsymbol{V}$ are necessary to describe the dynamics of the different systems at hand. The model rank r, which also defines the size of the final state-space model, is determined from the singular values σ_j. Depending on the dynamical system at hand, the singular values may form an elbow curve, clearly separating more important columns from less important ones. In the original paper by Brunton et al. [1], the optimal rank $r_{\text{opt,GD}}$ is computed by hard-thresholding the singular values with a method proposed in [29], where the threshold is computed as a function of the Hankel matrix dimensionality ratio q/p as

$$\sigma_{\text{thresh}} = \left(0.56\left(\frac{q}{p}\right)^3 - 0.95\left(\frac{q}{p}\right)^2 + 1.82\left(\frac{q}{p}\right) + 1.43\sigma_{\text{thresh}}\right) \cdot \text{median}(\sigma_j). \tag{7}$$

However, it was found in the course of this study that this method often fails to locate the elbow in the curve, which is usually easy to determine visually. Figure 3 shows the singular values obtained with data from the double mass oscillator presented in Section 3.1. The rank $r_{\text{opt,GD}} = 51$ is located far away from the elbow. For the purpose of this study, the $r_{\text{opt}} = 7$, which is located at the elbow or kink of the curve, is used.

Implementing an elbow-finding algorithm such as the one proposed in [30] would help the automation of the HAVOK-algorithm at this point but is beyond the scope of this study. For the course of this study, the rank r for each system is chosen manually. Independent of which algorithm is chosen for the computation of the model rank, we recommend analyzing the singular values to confirm the choice of model rank for each new system.

With the obtained rank r, a matrix $\boldsymbol{V}_r = \boldsymbol{V}[:, 1{:}r]$ is set up using the first r columns of $\boldsymbol{V}$. The matrix $\boldsymbol{V}_r \in \mathbb{R}^{p\times r}$ is a representation of the dynamics in the space of observables $\boldsymbol{u}_i$ and can be interpreted as an approximation of the Koopman operator in a Koopman-invariant subspace. In the remaining steps of the algorithm, a state-space system representing the dynamics in $\boldsymbol{V}_r$ is sought.

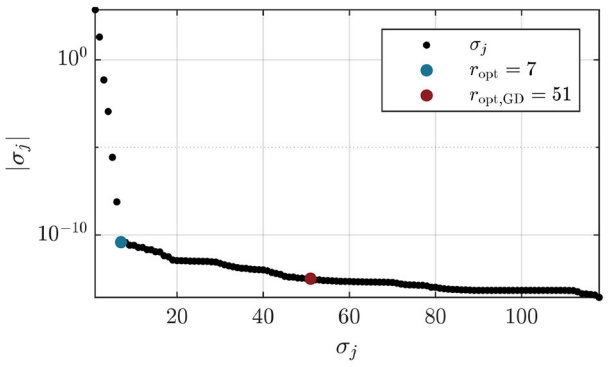

FIGURE 3
Determination of model rank r for the double mass oscillator system introduced in Section 3.1. The absolute values of the σ_j form an elbow curve. The method proposed in [1] yields the rank $r_{\text{opt,GD}} = 51$ which is much higher than the suitable model rank $r_{\text{opt}} = 7$ determined visually.

2.3.4. Time differentiation

In this step, the time derivative $\dot{\boldsymbol{V}}_r$ of the matrix $\boldsymbol{V}_r$ is computed, which is required for the computation of the linear system representation in the next step. As suggested in [1], a fourth-order central difference method

$$\dot{f}(x(t_i)) = \frac{1}{12\Delta t}\big(f(x(t_i - 2\Delta t)) - 8f(x(t_i - \Delta t)) + 8f(x(t_i + \Delta t)) - f(x(t_i + 2\Delta t))\big) \tag{8}$$

is implemented, where $\Delta t = \frac{1}{f_S}$ denotes the time step size. The derivative $\dot{f}(x(t_i))$ of a state $x(t_i)$ at time t_i is computed using two past and two future steps. The resulting matrix $\dot{\boldsymbol{V}}_r \in \mathbb{R}^{(p-4)\times r}$ is, thus, slightly reduced in dimension.

2.3.5. Sparse identification of non-linear dynamics

A sparse linear system representing the system dynamics contained in $\boldsymbol{V}_r$ is recovered using the matrix $\boldsymbol{V}_r$ and the matrix of derivatives $\dot{\boldsymbol{V}}_r$ using the sparse identification of non-linear dynamics (SINDy) algorithm, which was introduced by Brunton et al. in [6]. *Sparse* denotes a system description that comprises only a small number of terms compared to the space of ansatz functions used in the regression, thus yielding a very compact and simple set of differential equations. The SINDy algorithm is an equation-free method for obtaining differential equations describing the observed dynamics of a system from measurement data. First, a library of candidate functions $\boldsymbol{\Theta}(\boldsymbol{V}_r) \in \mathbb{R}^{(p-4)\times(r+1)}$ is set up from the matrix of measurements $\boldsymbol{V}_r$, which for the HAVOK-algorithm is defined as

$$\boldsymbol{\Theta}(\boldsymbol{V}_r) = \begin{bmatrix} \boldsymbol{1} & \boldsymbol{V}_r \end{bmatrix}, \tag{9}$$

where $\boldsymbol{1} \in \mathbb{R}^{(p-4)\times 1}$ represents a bias matrix containing only entries of 1. SINDy will then identify the linear combination of those candidate functions that can represent the dynamics in $\boldsymbol{V}_r$. As the goal of the HAVOK-algorithm is identifying a linear system, only linear terms are included here, even though the SINDy algorithm would allow for including non-linear terms in the function library,

such as $\left(\boldsymbol{v}_{r,j}\right)^2$, where $\boldsymbol{v}_{r,j}$ denotes a column of the matrix $\boldsymbol{V}_r$. With this function library and the state derivatives, a system of equations

$$\dot{\boldsymbol{V}}_r = \boldsymbol{\Theta}(\boldsymbol{V}_r)\boldsymbol{\Xi} \tag{10}$$

is set up. The matrix $\boldsymbol{\Xi} \in \mathbb{R}^{(r+1)\times r}$ contains sparse vectors of coefficients $\boldsymbol{\xi}_j$ which are computed using a thresholded sequential least squares algorithm. The SINDy algorithm seeks to find a solution to this system of equations that minimizes the L^1-norm of the coefficients, promoting sparsity. Only a few terms in the coefficient vectors are non-zero for generating a sparse model $\dot{\boldsymbol{V}}_r = \boldsymbol{\Theta}(\boldsymbol{V}_r)\boldsymbol{\Xi}$ with as less terms as possible. The sparsification knob μ, which is another important parameter of the HAVOK-algorithm, is introduced. After an initial least-squares guess $\boldsymbol{\Xi} = \boldsymbol{\Theta}(\boldsymbol{V}_r)^+\dot{\boldsymbol{V}}_r$, all entries of $\boldsymbol{\Xi}$ smaller than μ are set to zero. The regression is performed again on the non-zero entries of $\boldsymbol{\Xi}$, and once again, the resulting entries in $\boldsymbol{\Xi}$ are set to zero if their values are below the sparsification threshold μ. This process is repeated until it converges to a final sparse matrix $\boldsymbol{\Xi}$, i.e., until no more small entries are set to zero within one iteration. The matrix $\boldsymbol{\Xi}$ now contains the few coefficients that govern the observed dynamics. With the final coefficients $\boldsymbol{\Xi}$, it is possible to describe the system dynamics in the form of

$$\dot{\boldsymbol{v}}_r = \boldsymbol{\Xi}^T(\boldsymbol{\Theta}(\boldsymbol{v}_r^T))^T, \tag{11}$$

where $\dot{\boldsymbol{v}}_r$ and $\boldsymbol{v}_r$ are no longer matrices containing time series measurement and their derivatives, but state vectors $\boldsymbol{v}_r = [v_1, v_2, ..., v_r]^T$ forming the dynamical system described in state-space form.

The challenge in this step is to identify a Pareto-optimal μ that balances model accuracy, which is achieved with a smaller μ (deleting fewer terms), and model sparsity, which is implied by a larger μ (deleting more terms). In the original study, the authors propose increasing the sparsification threshold for each column, such that $\mu_j = j\mu_0$ and $\mu_0 = 0.02$, while noting that $\mu = 0$ yields better results, even though sparsity is not ensured in that case. In this study, an additional function is implemented to identify optimal sparsification parameters μ_j. Each column of the SINDy regression is considered separately. A set of 100 candidate sparsification thresholds $\mu \in [0.0001, 1]$ is tested. The SINDy algorithm is applied using each threshold, such that 100 different versions of a vector or sparse coefficients $\boldsymbol{\xi}_j$ are obtained. As a measure for model accuracy, the approximated derivative

$$\dot{\boldsymbol{v}}_{\text{lin},j} = \boldsymbol{\xi}_j^T(\boldsymbol{\Theta}(\boldsymbol{V}_r^T))^T \tag{12}$$

is computed and compared to the original derivative $\boldsymbol{v}_{r,j}$

$$\text{nMAE}_j(\mu_1) = \text{nMAE}\left(\dot{\boldsymbol{v}}_{r,j}(\mu_1), \dot{\boldsymbol{v}}_{\text{lin},j}(\mu_1)\right), \tag{13}$$

using the normalized mean error. The result is a vector of normalized mean errors

$$\mathbf{nMAE}_{\mu,j} = [\text{nMAE}_j(\mu_1)\ \text{nMAE}_j(\mu_2)\ ...\text{nMAE}_j(\mu_{100})] \in \mathbb{R}^{1\times 100}. \tag{14}$$

As a measure for sparsity, the number of non-zero elements (NZE) in $\boldsymbol{\xi}_j$ normalized to the length $r+1$ of the vector is computed. By comparing these measures, nMAE for accuracy and NZE for sparsity, a suitable threshold value can be determined for each column of the sparsification. This procedure is repeated for each column separately, ultimately yielding a vector of threshold values $\boldsymbol{\mu}_{\text{opt}}$. The process would be rendered more exact by comparing the initial columns $\boldsymbol{v}_r$ with the HAVOK trajectories y_{H} instead of comparing the derivatives $\dot{\boldsymbol{v}}_{\text{lin},j}$ and $\dot{\boldsymbol{v}}_{r,j}$ for the error measure, thus taking the interplay of the different columns into account. However, this expansion drastically increases the number of necessary computations and renders the numerical cost too high. Both the evolution of nMAE and NZE for one exemplary column are shown in Figure 4A. The smaller the sparsification parameter μ, the more terms are included, and the better the fit. On the other hand, if too few terms remain for large μ, the fit is not satisfying anymore. An optimal selection of μ will balance both competing quantities. For each column, an optimal sparsification parameter μ is obtained as the largest μ to yield an nMAE below a threshold value $\text{nMAE}_{\text{thresh}}$. This hard-thresholding of the nMAE results in an optimal μ_i for each column i that will satisfy that heuristic goodness of fit, see Figure 4B. As the magnitude of the nMAE is different for each dynamical system, it is necessary to adjust the sparsification threshold μ_{thresh} for each new system. We recommend studying the resulting nMAE for each column and choosing a threshold $\text{nMAE}_{\text{thresh}}$ that is optimal for your individual purpose. A higher $\text{nMAE}_{\text{thresh}}$ results in a larger μ and thus in a less accurate, but more sparse result, and vice versa.

2.3.6. Construction of state-space representation

In the last step of the HAVOK-algorithm, a forced linear state-space system describing the system dynamics is set up from the matrix of sparse coefficients $\boldsymbol{\Xi}$ obtained through SINDy. To do so, the matrix $\boldsymbol{\Xi}^T$ is split into a state matrix $\boldsymbol{A}_{\text{H}} \in \mathbb{R}^{(r-1)\times(r-1)}$ and an input matrix $\boldsymbol{B}_{\text{H}} \in \mathbb{R}^{(r-1)\times 2}$ as illustrated in Figure 2. Precisely, the matrix $\boldsymbol{B}_{\text{H}}$ is set up from two sections of $\boldsymbol{\Xi}^T$, $\boldsymbol{B}_{\text{H},1}$ and $\boldsymbol{B}_{\text{H},2}$, each $\in \mathbb{R}^{(r-1)\times 1}$, such that $\boldsymbol{B}_{\text{H}} = [\boldsymbol{B}_{\text{H},1}, \boldsymbol{B}_{\text{H},2}]$. The result is a forced state-space system representation in the form of

$$\begin{aligned} \frac{\mathrm{d}}{dt}\boldsymbol{v}(t) &= \boldsymbol{A}_{\text{H}}\boldsymbol{v}(t) + \boldsymbol{B}_{\text{H}}\begin{bmatrix} 1 \\ v_r(t) \end{bmatrix} \\ \boldsymbol{y}_{\text{H}}(t) &= \boldsymbol{C}\boldsymbol{v}(t), \end{aligned} \tag{15}$$

with states $\boldsymbol{v}(t) \in \mathbb{R}^{(r-1)\times 1}$ and a square $r-1$-dimensional identity matrix $\boldsymbol{C}$. The output of the system is given by $\boldsymbol{y}_{\text{H}} \in \mathbb{R}^{(r-1)\times 1}$. The forcing $v_r(t)$ is given by the last column of the matrix $\boldsymbol{V}_r$. The forcing term is necessary for the reconstruction of the system dynamics when no closed-form representation of the Koopman operator can be found, i.e., to compensate for the approximation error. It was found by Champion et al. in [7], that a linear HAVOK model without forcing is sufficient to reconstruct the dynamics for quasi-periodic systems. For most cases, however, the forcing is necessary and the main drawback of this modeling approach as it is a priory only available for the time span t_l measured initially. There are different approaches to computing the forcing term beyond merely inserting the last column of $\boldsymbol{V}_r$, including learning a forcing u^{disc} from the prediction error [31] and modeling the forcing using a second Hankel matrix [32].

The setup of the state-space system concludes the description of the HAVOK-algorithm and its parameters, specifically the sampling

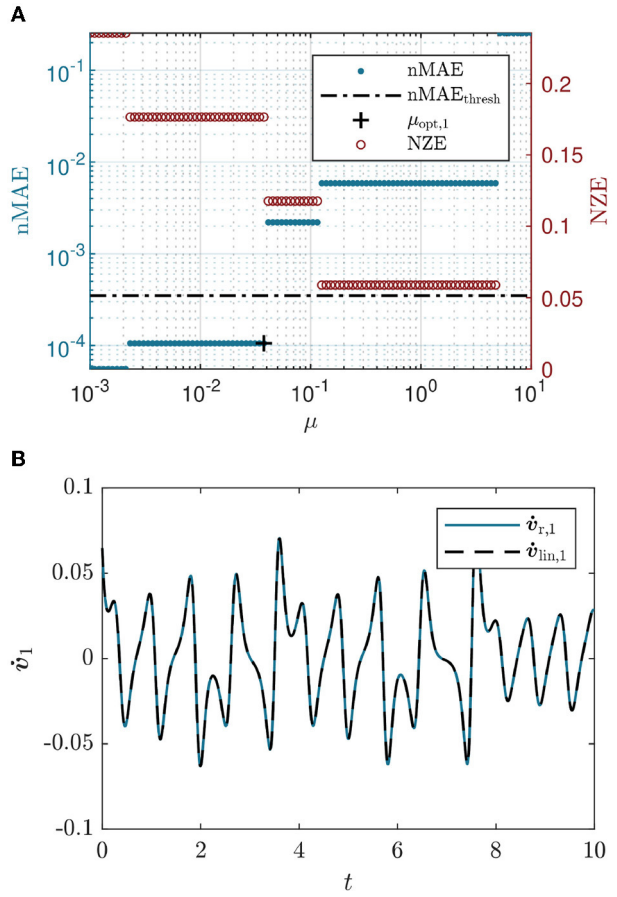

FIGURE 4
(A) Determination of an optimal sparsification threshold μ. The optimization is performed for each column of the sparse regression separately, the image shows the process for the first column only. The sparse regression is performed 100 times with different values of $\mu \in [0.0001, 1]$ to obtain 100 different versions of a vector of sparse coefficients $\boldsymbol{\xi}_j$. As a measure for accuracy, the nMAE of the resulting approximated derivative $\dot{\boldsymbol{v}}_{\text{lin},1}$ with its corresponding true derivative $\dot{\boldsymbol{v}}_{r,1}$ is computed for each variation of μ. The relative number of non-zero elements (NZE) in the vector of sparse coefficients is a measure for model sparsity. By hard-threshold the nMAE at a value nMAE$_{\text{thresh}}$, a suitable μ for the given column is chosen. **(B)** Results of the sparse regression. The approximated derivative $\dot{\boldsymbol{v}}_{\text{lin},1}$ obtained with the indicated $\mu_{\text{opt},1}$ compared to the corresponding true derivative $\dot{\boldsymbol{v}}_{r,1}$.

frequency f_s, measurement time span t_l, and chosen degree of freedom from the data acquisition step, the embedding dimension q, which is chosen during the setup of the Hankel matrix, the model rank r which has to be fixed after the SVD of the Hankel matrix, and the sparsification knob μ, which impacts the results of the sparse regression in the SINDy-step. Currently, the optimal selection, and the impact of a specific selection on the resulting model are unknown. In the previous paragraphs, possibilities for the computation of suitable values for these parameters have been introduced, sometimes beyond the original algorithm from [1]. In the next section, a deep dive into those parameters and how they influence each other will be taken.

2.4. Counter-intuitive action of embedding parameters

To illustrate the inner workings of the algorithm, several parameter studies have been performed that show how the parameters interact with each other and the final reduced-order model. In particular, some interrelations between parameters that are not obvious right away are pointed out here. These studies help to understand how the algorithm works and might thus help in choosing parameters for new systems.

First, it is important to note that the time spans contained in the rows and columns of the Hankel matrix, t_q and t_p, do not solely depend on the choice of the embedding dimension q, but also on the sampling frequency f_s. Essentially, more modes of vibration can be discovered if the sampling frequency is high. For a fixed embedding dimension q, a smaller sampling rate leads to less time series information in a column of the Hankel matrix $\boldsymbol{H}$, while a larger sampling rate leads to a larger time span $x^{(q)}(t)$. To cancel out the effect of the sampling frequency f_s on further results, it is prudent to define the time span in a column of $\boldsymbol{H}$, $x^{(q)}(t)$ instead of the embedding dimension q. For periodic motions, it is not necessary to use more than half a period of vibration in that column time span.

Second, the optimal rank r, i.e., the number of relevant modes $\boldsymbol{u}_i$ that results from the SVD, depends on the amount of information contained in $x^{(q)}(t)$. If little information is contained in $x^{(q)}(t)$, only a small number of basis functions are necessary to span the function space, but as the information in a column of $\boldsymbol{H}$ grows, so does the size of the space of basis functions, and thus the rank r. However, studies that were performed in the course of this study indicate that there is a maximum model rank r for a given system, which does not increase further even as $x^{(q)}(t)$ is increased. These findings agree with assertions in the literature [31].

The combination of these two observations leads to the (at first counter-intuitive) observation that decreasing the sampling frequency f_s yields a larger number of relevant basis functions $\boldsymbol{u}_j$ and a larger model. This is because a larger sampling frequency f_s, together with a fixed embedding dimension q, results in a larger time span in $x^{(q)}(t)$ and thus is a larger model rank r. If the time span $x^{(q)}(t)$ is kept constant instead of the embedding dimension q when varying f_s, the obtained model rank r becomes independent of the sampling frequency f_s, up to a value when the sampling frequency becomes too coarse to accurately represent the core dynamics of the system. In realistic settings, the sampling frequency will be fixed, and a limited time series measurement will be available. Our recommendations for an optimal embedding process are given in Section 4.2.2.

3. Results

In this section, the results of the application of the HAVOK-algorithm to different mechanical oscillators are presented. Starting with a linear double-mass oscillator, the analytical model and the low-dimensional HAVOK model will be compared with a focus on which information of the analytical model can be extracted from the HAVOK model. Moving on, the dependence of the results on

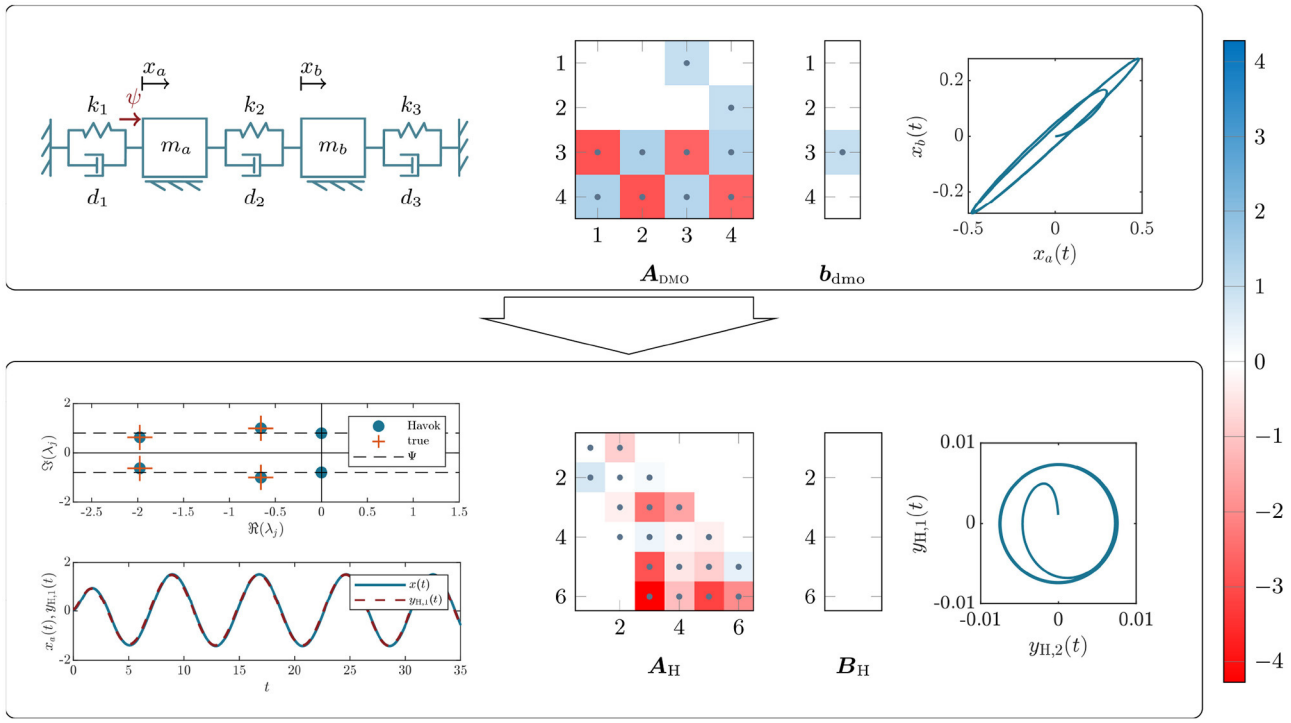

FIGURE 5
The HAVOK model (bottom) for a double mass oscillator compared to its analytical basis (top). The state matrix $\boldsymbol{A}$ and input matrices $\boldsymbol{B}$ are shown in color code where red, white, and blue squares denote negative, zero, and positive entries of the matrices, respectively. To ensure that small values don't get lost in the color scale, all non-zero entries are marked with gray dots additionally. The eigenvalues of the two systems match. State-space representations and the time series comparisons show that the reduced-order model reproduces the dynamics of the original system well, except for a difference in amplitude, which is visible in the state space plots. For better visualization, the time series data of both $x_a(t)$ and $y_{\mathrm{H},1}(t)$ is normalized to have zero mean and a standard derivation of one.

the algorithmic parameters is studied and the impact of varying model parameters such as initial conditions, damping, forcing type, and non-linearity is analyzed. These studies foster conclusions about which information of the *true* underlying dynamical system can be drawn from the data-driven reduced-order HAVOK model, and under which conditions this is possible. The exemplary application of HAVOK to real-world brake data, illustrating how parameters can be chosen for an unknown system, concludes this section.

3.1. Application to mechanical oscillators

The first step in the study of the application of HAVOK to mechanical oscillators is the double mass oscillator (DMO), which is shown in Figure 5. Two masses m_a and m_b are connected to each other and to the fixation points via spring-damper systems with linear spring constants $k_j, j \in \{1,2,3\}$ and damping parameters $d_j, j \in \{1,2,3\}$. The displacement of the two masses in the horizontal direction is denoted by x_a and x_b, respectively. A forcing ψ, which in this first study is considered to be harmonic such that $\psi(t) = \Psi\cos(\Omega t)$ with amplitude Ψ and frequency Ω. Initially, the parameters are considered to be homogeneous, i.e., $m_a = m_b = m$, $k_1 = k_2 = k_3 = k$, and $d_1 = d_2 = d_3 = d$. The equations of motion for this system are given by

$$\underbrace{\begin{bmatrix} m_a & 0 \\ 0 & m_a \end{bmatrix}}_{\boldsymbol{M}_{\mathrm{DMO}}} \underbrace{\begin{bmatrix} \ddot{x}_a(t) \\ \ddot{x}_b(t) \end{bmatrix}}_{\ddot{\boldsymbol{x}}_{\mathrm{DMO}}(t)} + \underbrace{\begin{bmatrix} 2d & -d \\ -d & 2d \end{bmatrix}}_{\boldsymbol{D}_{\mathrm{DMO}}} \underbrace{\begin{bmatrix} \dot{x}_1(t) \\ \dot{x}_2(t) \end{bmatrix}}_{\dot{\boldsymbol{x}}_{\mathrm{DMO}}(t)} + \underbrace{\begin{bmatrix} 2k & -k \\ -k & 2k \end{bmatrix}}_{\boldsymbol{K}_{\mathrm{DMO}}} \underbrace{\begin{bmatrix} x_1(t) \\ x_2(t) \end{bmatrix}}_{\boldsymbol{x}_{\mathrm{DMO}}(t)} = \underbrace{\begin{bmatrix} \psi(t) \\ 0 \end{bmatrix}}_{\boldsymbol{\psi}_{\mathrm{DMO}}(t)}, \quad (16)$$

where $\boldsymbol{M}_{\mathrm{DMO}}$ is the mass matrix, $\boldsymbol{D}_{\mathrm{DMO}}$ the damping matrix, and $\boldsymbol{K}_{\mathrm{DMO}}$ the stiffness matrix. The states and their time derivatives are given by the vectors $\boldsymbol{x}_{\mathrm{DMO}}$, $\dot{\boldsymbol{x}}_{\mathrm{DMO}}$, and $\ddot{\boldsymbol{x}}_{\mathrm{DMO}}$, respectively. The forcing vector is denoted by $\boldsymbol{\psi}_{\mathrm{DMO}}$. The damping is assumed to be in the form of Rayleigh damping, i.e., proportional to mass and spring stiffness

$$\boldsymbol{D}_{\mathrm{DMO}} = \alpha \boldsymbol{M}_{\mathrm{DMO}} + \beta \boldsymbol{K}_{\mathrm{DMO}} \quad (17)$$

with stiffness- and mass-proportional damping parameters α and β. The system parameters are chosen such that the first damped eigenfrequency $\omega_{\mathrm{d},1} = 1\,\mathrm{rad/s}$ and the mass $m = 1\,\mathrm{kg}$. The Lehr damping factors D_j [33] of the two eigenmodes of the DMO are $0 < D_j < 1$, such that both modes are weakly damped. The forcing frequency is chosen to lie in between the damped

TABLE 1 Default parameters and resulting properties of the double mass oscillator.

Parameter	Symbol	Value	Unit
Mass	m	1.0000	kg
Spring constant	k	1.4337	N/m
Proportional damping factor	α	0	1/s
Proportional damping factor	β	0.9187	s
1st undamped eigenfrequency	$\omega_{0,1}$	1.1894	rad/s
2nd undamped eigenfrequency	$\omega_{0,2}$	2.0739	rad/s
1st damped eigenfrequency	$\omega_{d,1}$	1.0000	rad/s
2nd damped eigenfrequency	$\omega_{d,2}$	0.6308	rad/s
1st damping factor	D_1	0.5500	
2nd damping factor	D_2	0.9526	
Forcing amplitude	F_0	1	N
Forcing frequency	Ω	0.8	rad/s

eigenfrequencies such that $\omega_{d,2} < \Omega < \omega_{d,1}$. The default parameters used with the DMO, the undamped eigenfrequencies $\omega_{0,j}$, damped eigenfrequencies $\omega_{d,j}$, and damping factors are listed in Table 1.

The state-space model of the analytical DMO is set up as

$$\underbrace{\begin{bmatrix} \dot{x}_a(t) \\ \dot{x}_b(t) \\ \ddot{x}_a(t) \\ \ddot{x}_b(t) \end{bmatrix}}_{\dot{\boldsymbol{x}}_{\mathrm{DMO}}(t)} = \underbrace{\begin{bmatrix} 0 & 0 & 1 & 0 \\ 0 & 0 & 0 & 1 \\ -\frac{2k}{m} & \frac{k}{m} & -\frac{2d}{m} & \frac{d}{m} \\ \frac{k}{m} & -\frac{2k}{m} & \frac{d}{m} & -\frac{2d}{m} \end{bmatrix}}_{\boldsymbol{A}_{\mathrm{DMO}}} \underbrace{\begin{bmatrix} x_a(t) \\ x_b(t) \\ \dot{x}_a(t) \\ \dot{x}_b(t) \end{bmatrix}}_{\boldsymbol{x}_{\mathrm{DMO}}(t)} + \underbrace{\begin{bmatrix} 0 \\ 0 \\ \frac{1}{m} \\ 0 \end{bmatrix}}_{\boldsymbol{b}_{\mathrm{DMO}}} \underbrace{F_0 \cos(\Omega t)}_{w_{\mathrm{DMO}}(t)} \tag{18}$$

$$\boldsymbol{y}_{\mathrm{DMO}}(t) = \boldsymbol{C}_{\mathrm{DMO}} \boldsymbol{x}_{\mathrm{DMO}}(t)$$

where $\boldsymbol{C}_{\mathrm{DMO}}$ is a 4×4 unitary matrix. Figure 5 shows a representation of the state matrix $\boldsymbol{A}_{\mathrm{DMO}}$ and the input vector $\boldsymbol{b}_{\mathrm{DMO}}$ in color-code: Red and blue squares mark negative and positive entries in the matrices, respectively. White squares denote zero entries, while gray dots mark all non-zero entries to ensure that no small entries are lost in the color scale. A state-space image of the dynamics of the system with $\boldsymbol{x}_0 = [0, 0, 0, 0]^T$ is also shown.

For this first study, the input to the HAVOK model is a time series of the x_1-coordinate, with an input time span $t_l = 5T$ which is five times the forcing period $T = \frac{2\pi}{\Omega}$ and the sampling frequency $f_s = 1\,\mathrm{kHz}$. The parameters of the algorithm are set to the embedding dimension $q = 118$, the model rank $r = 7$, and the sparsification threshold $\mathrm{nMAE}_{\mathrm{thresh}} = 3.5 \cdot 10^{-3}$, yielding a sparsification parameter $\boldsymbol{\mu} = [0.0044, 0.0196, 0.2915, 0.0236, 0.3854, 1.0723, 0]^T$. How changing those parameters affects the results will be studied in the next subsection. The resulting HAVOK model is shown in Figure 5, where the HAVOK state-space matrices $\boldsymbol{A}_{\mathrm{H}}$ and $\boldsymbol{B}_{\mathrm{H}}$ are depicted in the same color-code as previously, showing that the input matrix $\boldsymbol{B}_{\mathrm{H}}$ is completely empty. The state matrix $\boldsymbol{A}_{\mathrm{H}}$ has an almost block-diagonal shape, where the first two states are only connected to the rest of the states via two very small entries. The state-space formed by the first two states $\boldsymbol{y}_{\mathrm{H},1}$ and $\boldsymbol{y}_{\mathrm{H},2}$ of the HAVOK model resembles the state-space of the analytical model up to a scaling of the axes. The difference in scaling stems from the orthonormalization of the modes $\boldsymbol{v}_j$ during the SVD in the third step of the HAVOK algorithm, see Figure 2. The results from the SVD can be related to the input time series, both in terms of amplitude and dynamics, as the projection of the input time series onto a mode $\boldsymbol{u}_j$ fits the respective mode $\boldsymbol{v}_j$ multiplied with the singular value σ_j. Unfortunately, it is not as straightforward to regain this difference in amplitude for the final HAVOK model time series. Integrating a correction for this effect would be an interesting point for future research. The HAVOK eigenvalues match the *true* eigenvalues of the analytical model exactly, and an additional eigenvalue-pair on the imaginary axis matches the forcing frequency, as illustrated in Figure 5. For the linear DMO with harmonic forcing, the HAVOK-algorithm yields an unforced state-space model whose eigenvalues match the analytical eigenvalues exactly. This is an interesting finding, as we only observed a single degree of freedom, and did not specify the true dimensionality of the system, or any system parameters. Still, HAVOK is able to correctly identify the dynamic properties of the underlying system accurately (eigenvalues encode modal properties and stability).

3.1.1. Influence of HAVOK parameters

The results presented in the previous subsection are obtained with specific settings of parameters. In the following, the influence of the tuning parameters input time span t_l, input degree of freedom, model rank r, and sparsification parameter $\boldsymbol{\mu}$ on the resulting HAVOK model and the information which can be extracted from it, are studied. These studies yield important insights into how to choose those parameters in order to determine a good low-rank representation of the dynamics. Figure 6A shows the results of varying each of these tuning parameters separately, which will be discussed in the following.

The **measurement time length** $\{t_l \in \rho \cdot T | \rho \in \mathbb{N}, \rho \leq 10\}$ is varied in integer multiples of the forcing period. It controls the ratio of transient and steady state (periodic) motion that is contained in the input time span. The shorter the input time span, the larger the relative importance of the transient motion in the time series. Figure 6A shows the resulting state matrices $\boldsymbol{A}_{\mathrm{H}}$, and the respective eigenvalues for this variation. To visualize the variations of the matrix $\boldsymbol{A}_{\mathrm{H}}$, each matrix is represented as one column. For example, the left column in the Figure shows the matrix $\boldsymbol{A}_{\mathrm{H}}$ for the first variant of t_l row-by-row. The evolution of each matrix entry for parameter variations becomes clearly visible since the corresponding entries lie directly next to each other. The input matrix $\boldsymbol{B}_{\mathrm{H}}$ is not depicted as it remains all-zero over all variations. Only absolute values of the matrix entries are shown. It can be seen that as the input time span (and thus the relative importance of the periodic motion

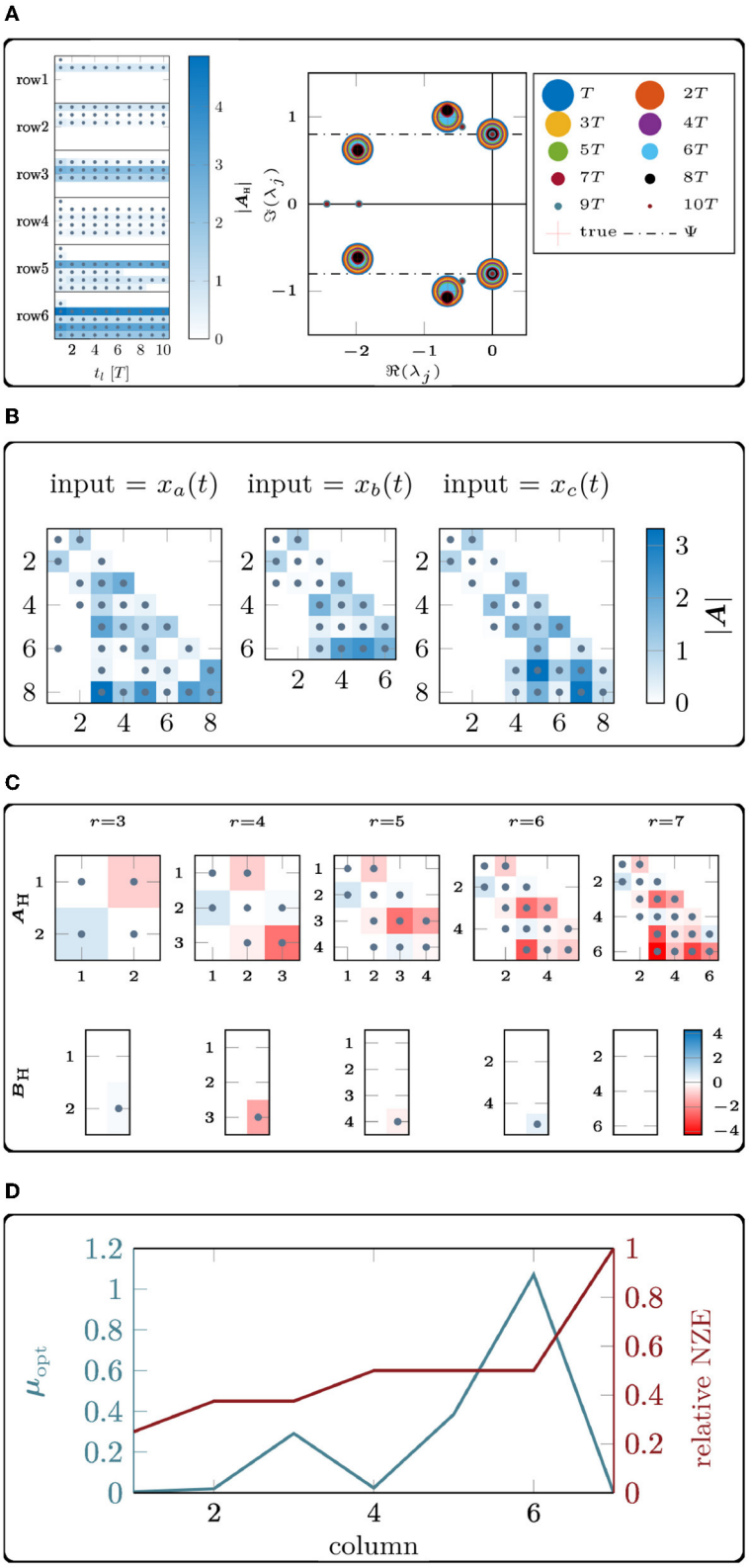

FIGURE 6
(A) HAVOK model results for variations of the algorithm parameters, studied by computing the model for a range of values. The state matrix $\boldsymbol{A}_{\mathrm{H}}$ and HAVOK model eigenvalues for different input time spans $t_l \in [T : 10T]$. In the figure, one column represents one matrix $\boldsymbol{A}_{\mathrm{H}}$, with the rows stacked on top of each other. This view allows for a direct comparison of the matrix entries. **(B)** HAVOK model results for variations of the algorithm parameters, studied by computing the model for a range of values. The state matrix $\boldsymbol{A}_{\mathrm{H}}$ obtained when using different input time series $x_a(t), x_b(t)$ or $x_c(t)$ from the 3MO illustrated that the model rank can depend on the choice of input degree of freedom. **(C)** HAVOK model results for variations of the algorithm parameters, studied by computing the model for a range of values. HAVOK model matrices $\boldsymbol{A}_{\mathrm{H}}$ and $\boldsymbol{B}_{\mathrm{H}}$ obtained when varying only the model rank $r \in [3 : 7]$, while using the $x_a(t)$ time series of the DMO. It is shown that the magnitude of the matrix entries do not change when increasing rank. **(D)** The sparsification parameter μ and NZE for each column of the sparse regression when using the $x_a(t)$ time series of the DMO and a model rank $r = 7$.

in the input time span) increases, the resulting state matrix becomes more sparse and for $t_l > 8T$, HAVOK no longer correctly identifies the system eigenvalues. The forcing-related eigenvalues are identified correctly for all variations of the input time span.

To visualize the impact of the **chosen measurement degree of freedom** on the resulting system, a three-mass oscillator (3MO) is considered. We study each state as input to HAVOK separately. The three-mass oscillator model has the same structure as the DMO seen before, but with one additional mass. This dynamical system has three eigenmodes, where in the second eigenmode, only the two exterior masses at the two sides move. For the three depicted state matrices in Figure 6B, the input time series was taken to be the displacement of each of the masses $x_a(t), x_b(t)$ and $x_c(t)$. The dynamical system obtained with the two exterior measurements $x_a(t)$ and $x_c(t)$ has rank $r = 8$, while the middle degree of freedom $x_b(t)$ results in a smaller $r = 6$ dimensional system. Analysis of the eigenvalues shows that while all models correctly contain the forcing frequency and the eigenvalues associated with the first and third eigenmodes, only the models obtained with $x_a(t)$ and $x_c(t)$ also contain the eigenvalue pair related to the second eigenmode, which is a physically consistent result with respect to the mode shapes.

The effect of varying the **embedding dimension** q, or time series section $x^{(q)}(t)$, has already been discussed in a previous section, but the question of how to choose an optimal embedding dimension for a given measurement time series remains. Here, a large range of q was tested and the evolution of singular values σ_j and coordinates $\boldsymbol{u}_j$ was observed. Finally, an embedding dimension was chosen such that the coordinates $\boldsymbol{u}_j$ resemble Legendre polynomials, and the singular values yield a suiting rank value.

A study of the impact of the **model rank** of the system, where the model rank is varied such that $\{r \in \mathbb{N} | 3 \leq r \leq 7\}$ demonstrates that the chosen rank does not affect the magnitude of the values in the state-space matrix A or the input matrix. Instead, the non-zero part of the state matrix remains constant when increasing the rank, only adding values that were previously observed in the input matrix, see Figure 6C. Concerning the eigenvalues, it was found that the HAVOK model first contains the eigenvalue pair on the imaginary axis, which is related to the forcing frequency, and then adds the system-related, that is damped, eigenvalues.

The determination of the **sparsification parameter** has been described in a previous section. Figure 6D shows the chosen optimal sparsification parameter $\boldsymbol{\mu}_{\text{opt}}$ for each column of the sparse regression along with the relative number of non-zero elements in the resulting matrix column. It shows that the sparsification parameter has an increasing trend with increasing column number and that its value is directly related to the sparsification process: For the last column, where $\mu_7 = 0$, the column appears fully populated, as no sparsification takes place. Physically speaking, the dynamics contained in the last column are too complex to be matched by the simple linear ansatz space, even when fully populated. In the case of the linear oscillator with monochromatic forcing, the last column of the sparse regression does not contain physically meaningful information, it is simply a relic of the algorithm. However, for more general systems, e.g., when including non-linearities, this column contains the more complex dynamics which cannot be matched by the linear ansatz.

3.1.2. Dependence on physical model properties

After the dependence of the HAVOK results on the tuning parameters of the algorithm has been established, this section explores the evolution of the HAVOK model as the parameters of the analytical model itself change. The aim is to explore the limits of the HAVOK-algorithm as a method for obtaining low-order models that correctly represent the properties of the underlying system. The sensitivity of the HAVOK model for the double mass oscillator to changes in initial conditions, damping, and different forcing types is explored as well as the HAVOK model for non-linear double mass oscillators. The results are shown in Figures 7A, 9.

To study the dependency of the HAVOK model on the initial conditions, five exemplary initial conditions along one trajectory starting from $\boldsymbol{x}(t_{0,1}) = [10, 10, 0, 0]^T$ are chosen, where the first $\boldsymbol{x}(t_{0,1})$ is quite far away from the steady-state motion and the last $\boldsymbol{x}(t_{0,5})$ lies exactly on the steady-state, as shown in Figure 7A. The measurement time span t_l is kept constant while varying the initial conditions, such that the initial conditions further away yield an input time series with a larger fraction of transient motion. The resulting matrices and eigenvalues shown in Figure 7A illustrate that the state matrix becomes more sparse as the initial conditions approach the steady-state. While the forcing frequency and the first eigenvalue pair are always identified correctly, the second eigenvalue pair is not detected correctly for the time series with large transients, which originate from the initial conditions further away.

For the study of the damping parameter, the proportional damping factor β is varied such that $\beta \in \{0.5\beta_0, 0.9\beta_0, \beta_0, 1.01\beta_0, 1.1\beta_0\}$. A variation of the damping factor changes the damped eigenfrequencies of the system and with it the damping factors for both eigenmodes. With increasing β, the damped eigenfrequencies ω_d decrease, while the respective damping factor D increases. For β_5, the damping factor $D_2 > 1$, indicates that this mode becomes strongly damped. The second panel of Figure 7B shows the evolution of the state matrix $\boldsymbol{A}_\text{H}$ and the eigenvalues for the changes in the damping parameter. For all values of β, $\boldsymbol{B}_\text{H}$ is all-zero. The bottom rows of the state matrix change slightly, but the overall structure of the matrix remains the same. HAVOK correctly identifies all eigenvalues, except for the second eigenvalue pair for the strongest damping factor, which has been noted to correspond to a strongly damped mode.

Thus far, only harmonic monochromatic forcing has been considered. To analyze the influence of the forcing on the HAVOK model, two different cases are considered. First, a frequency-sweep forcing with $\psi_1(t) = \Psi\cos(\Omega_0 \frac{t}{2} t)$, where $\Omega_0 = 0.8\,\text{rad/s}$ and second, a harmonic forcing with three superimposed frequencies given by $\psi_2(t) = \Psi(\cos(\Omega_1 t) + \cos(\Omega_2 t) + \cos\Omega_3 t))$, with $\Omega_1 = 8\,\text{rad/s}$, $\Omega_2 = 0.8\,\text{rad/s}$ and $\Omega_3 = 0.4\,\text{rad/s}$. The respective forcing and input time series are shown in Figures 7C, D along with the resulting HAVOK model matrices and eigenvalues. The HAVOK

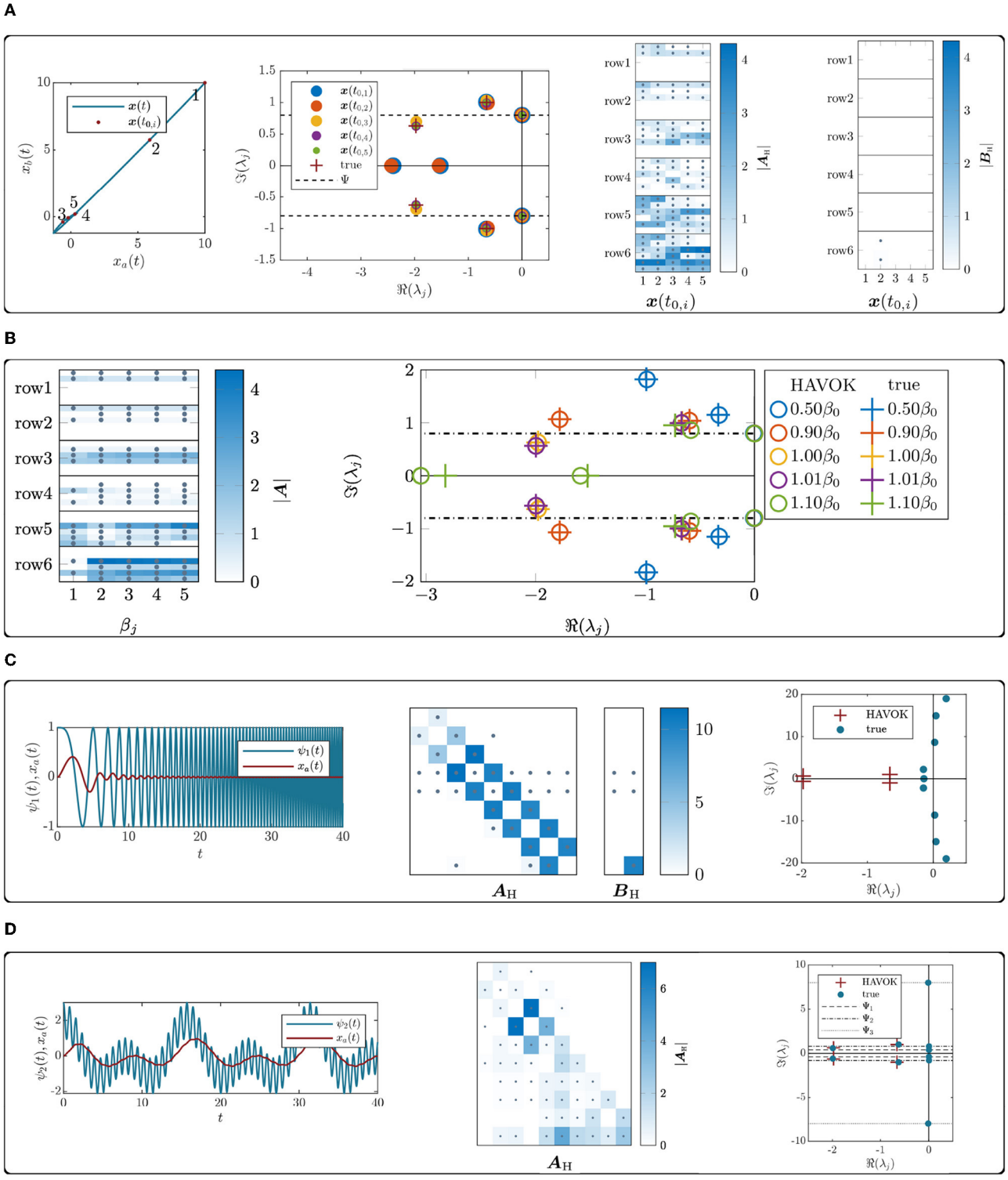

FIGURE 7
(A) Dependence of the HAVOK model on changes in the physical parameters of the analytical model. For each study, the double mass oscillator is used, varying one of the system parameters only. The HAVOK-DMO for different initial conditions along one trajectory result in different input time series. The resulting HAVOK model state and input matrices are show following the convention introduced in Figure 5. The respective model eigenvalues are compared to the forcing frequency and the eigenvalues of the underlying DMO system. **(B)** The HAVOK-DMO model for different damping values is illustrated by the state matrix. The all-zero input matrix is not represented. The eigenvalues for each model are shown in different colors, where circles represent the HAVOK model eigenvalues and crosses the true eigenvalues. One pair of HAVOK model eigenvalues lies on the imaginary axis for every model variation. **(C)** The application of HAVOK to a DMO forcing with a frequency-sweep type forcing shows entries on the sub-diagonal of the state matrix. In the representation of the eigenvalues, no forcing frequency is shown as it is varied continuously. **(D)** HAVOK-DMO model for a system that is forced with three superimposed sinusoids, where the HAVOK model catches both the system eigenvalues and the forcing frequency.

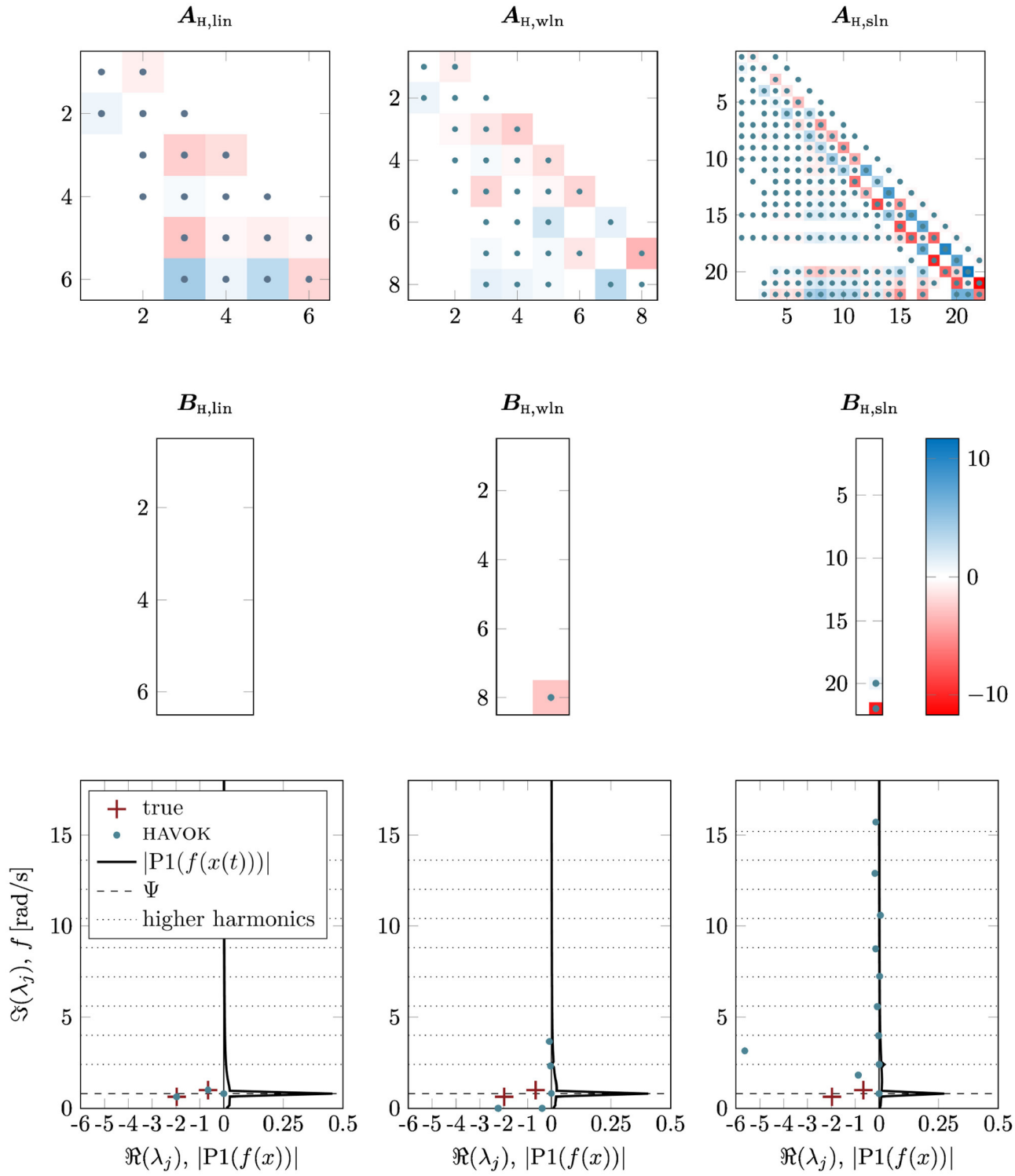

FIGURE 8
HAVOK models a linear, weakly non-linear, and strongly non-linear double mass oscillator. The state matrices $\boldsymbol{A}_{H,lin}$, $\boldsymbol{A}_{H,wnl}$, and $\boldsymbol{A}_{H,snl}$ are shown on top, with the input matrices $\boldsymbol{B}_{H,lin}$, $\boldsymbol{B}_{H,wnl}$, and $\boldsymbol{B}_{H,snl}$ below. The system eigenvalues λ_j of the true underlying DMO system, and the HAVOK model are shown on the bottom, along with a frequency spectrum of the input time series $P1|f(x(t))|$, the forcing frequency Ψ and its higher harmonics.

model for the system excited with three superimposed sinusoids is an unforced model with rank $r = 11$, and three eigenvalue pairs corresponding to the forcing frequencies on the imaginary axis. As before, HAVOK correctly identifies the eigenfrequencies of the system. The picture is very different for the frequency-forcing sweep excited model. Here, the structure of the resulting—now forced—state-space model of rank $r = 10$ is similar to the structure of the model that was identified for the chaotic Lorenz63

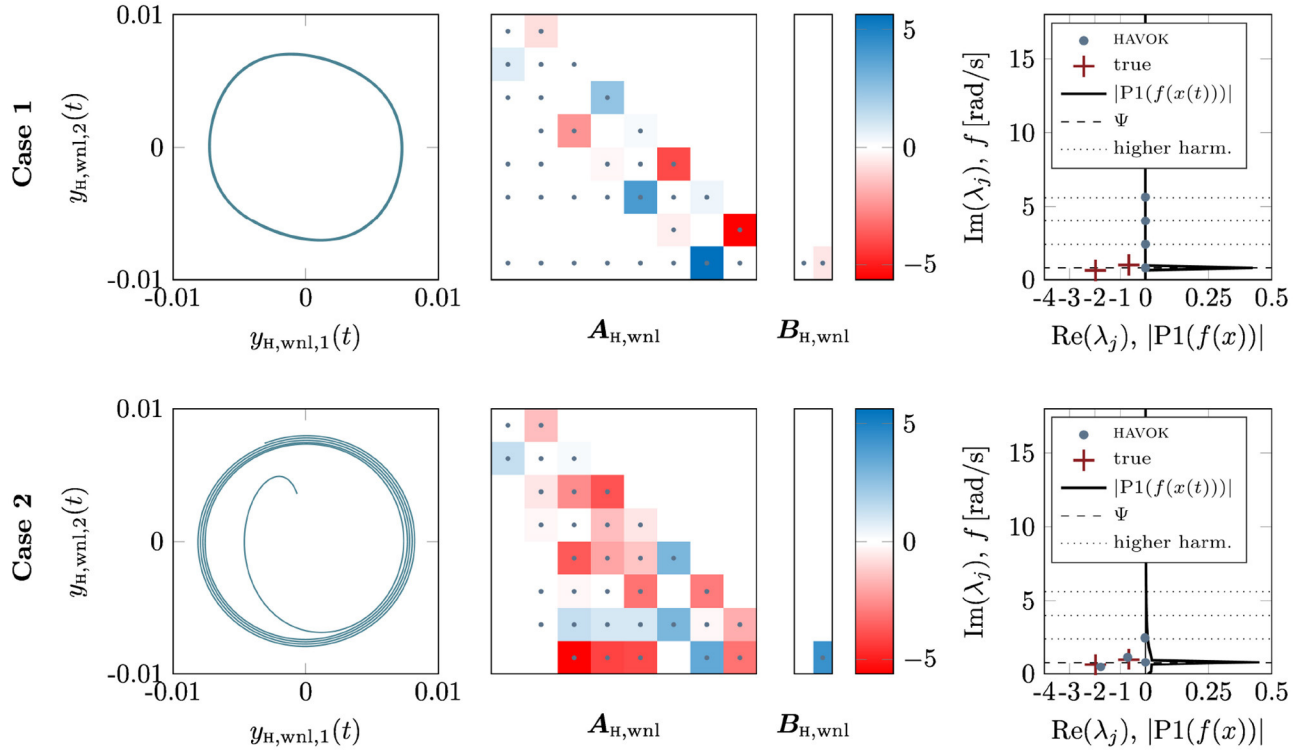

FIGURE 9
Case studies of the weakly non-linear double-mass-oscillator. **(Top)** The HAVOK model obtained when omitting all transient motion in the input time series. **(Bottom)** The HAVOK model for a DMO when the non-linearity is moved to the other end of the oscillator chain, away from the excitation and the input time series. For both systems, the state space resulting from the first two HAVOK trajectories $y_{\mathrm{H,wnl},1}$ and $y_{\mathrm{H,wnl},2}$ are shown, as well as the state and input matrices. On the right, the HAVOK model eigenvalues are compared to the true DMO system eigenvalues, the frequency spectrum $P1|f(x)|$ of the input time series and the forcing frequency.

[34] system in the original [1] article. The HAVOK eigenvalues do not correspond to the system eigenvalues but include unstable eigenvalue pairs.

Non-linearity is introduced into the system by adding a cubic spring stiffness k_{nl} to the first spring k_1. The equations of motion are now given by

$$\begin{aligned} m\ddot{x}_a(t) + 2d\dot{x}_a(t) - d\dot{x}_b(t) + 2kx_a(t) - kx_b(t) - k_{\mathrm{nl}}x_a^3(t) &= \psi(t) \\ m\ddot{x}_b(t) - d\dot{x}_a(t) + 2d\dot{x}_b(t) - kx_a(t) + 2kx_b(t) &= 0 \end{aligned} \tag{19}$$

with a non-linearity $k_{\mathrm{nl}}x_a^3$ in the first line. Two versions, a weakly non-linear model with $k_{\mathrm{nl},1} = 2k$ and a strongly non-linear model with $k_{\mathrm{nl},2} = 20k$, are considered. The resulting HAVOK models are shown in Figure 8. Here, $\boldsymbol{A}_{\mathrm{H,lin}}$, $\boldsymbol{A}_{\mathrm{H,wnl}}$, and $\boldsymbol{A}_{\mathrm{H,snl}}$ denote the system matrices of the linear, weakly non-linear, and strongly non-linear system, respectively. With a stronger non-linearity, the model rank increases, while the overall structure of the state matrix remains the same. As soon as a non-linearity is introduced, the HAVOK model becomes forced, i.e., $\boldsymbol{B}_{\mathrm{H}}$ is no longer all-zero. At the same time, the non-linearity seems to keep the algorithm from correctly identifying the eigenvalues of the system. Instead, the HAVOK eigenvalues correspond to the forcing frequency and its higher-order harmonics, marked in the Figure by dotted lines.

Two additional case studies with systems including non-linearity, the first neglecting all transient motion and the second moving the non-linearity to the spring k_3 on the other end of the oscillator chain, conclude the studies of parameter dependence. The resulting HAVOK models and their eigenvalues are both shown in Figure 9. The first two trajectories of the HAVOK model are shown as $y_{\mathrm{H,wnl},1}(t)$ and $y_{\mathrm{H,wnl},2}(t)$. The HAVOK model obtained from only the steady-state oscillation of the non-linear oscillator has a dominant off-diagonal structure, where the states as strongly coupled pair-wise. Its eigenvalues correspond to the forcing frequency and its higher harmonics on the imaginary axis, there is no signature of the linearized system's eigenvalues. For the model with the non-linearity away from the excitation and the measurement time series, the structure of the state matrix resembles the structure of previous state matrices, i.e., is less dominated by the diagonal. The eigenvalues of this system correspond closely to the eigenvalues of the analytical model, the forcing frequency, and one higher-order harmonic. Both these HAVOK models are forced, the same as the previous non-linear models.

3.2. Application to a real-world brake system

Thus far, the low-order HAVOK models obtained from synthetic data have been considered, which enabled the comparison of the true analytical model (generating the data) and the HAVOK

model. To round off this study, HAVOK is applied to real-world measurement data obtained with a microphone during the actuation of a friction disc brake system of a passenger car. For details regarding the experimental setup, see [35] and [36]. Friction brakes can exhibit squeal noises during braking, resulting from complex self-excited machine dynamics whose mechanisms have not yet been fully understood today [35]. There are two different prominent theories as to the process that yields brake squeal. Both of these theories are based on studying the silent (not squealing) and the squealing section of a brake stop separately and agree on a regime shift between the two dynamical states, which leads to qualitatively different dynamics in the two regimes. One theory states that the squealing, which is represented by a low-dimensional attractor, originates from the equilibrium-point dynamics in the non-squealing regime losing its stability [37], for example through a Hopf bifurcation. The other theory identifies 8–12-dimensional attractors in the silent regime, which transition toward a lower-dimensional attractor of 3–6 dimensions in the squealing regime [35, 38, 39]. These studies all agree on signs of chaotic dynamics in both the silent and the squealing regimes. As the realistic brake system is comprised of multiple components, actuation and a complex friction interface, the identification of a reduced order model using only measurement data is highly interesting, also to study the aforementioned root causes of the vibrations.

The microphone data was sampled at 51.2 kHz and bandpass-filtered with cutoff frequencies at 1 and 20 kHz. Two exemplary samples are taken from a single brake stop that is not squealing in the beginning and then exhibiting strong squeal events toward the end. To obtain a sufficient quality of the numerical derivatives during the application of HAVOK, it is necessary to upsample the data to 5,120 kHz for the silent and 512 kHz for the squealing region. The upsampling was performed using a Matlab spline interpolation function. The entire microphone signal and the two exemplary snippets are shown in Figure 10. Characteristic differences are visible in both time series.

The tuning parameters of the HAVOK algorithm are chosen as follows. For the input data, only the chosen time span t_l remains a flexible parameter, as the sampling frequency is fixed. Section lengths of 150,000 samples and 15,000 samples are taken from the silent and the squeal region, respectively, resulting in $t_l \approx 0.03$ s for both regimes. This time length was shown to yield consistent results with time delay embedding in [35]. As has been explained in the previous sections, the embedding dimension q and the model rank r are closely related, as the model rank is obtained from the results of the SVD, which depend on the embedding dimension q. To find an optimal embedding dimension and rank, the embedding dimension is initially set to $q = 100$ and varied over a large value range. The optimal values are determined based on the ability of the final HAVOK model to represent the measured dynamics, computed as the fit between the measurement data and the trajectory of the first HAVOK state $y_{\mathrm{H},1}(t)$. For the silent section, $q = 100$ and $r = 9$ are found, and $q = 1,000$ and $r = 4$ for the squealing section. Note that the time span $x^{(q)}(t)$ in a column of the Hankel matrix $\boldsymbol{H}$ is very different between the two regimes due to the different embedding dimensions. Figure 10 shows the first 100 singular values for each section which lead to the choice of model rank. For the squealing regime on the right, the choice of rank is obvious through the elbow-like formed curve. For the silent region, no clear kink in the curve is visible, making the choice of rank more heuristic. The sparsification parameter μ is set to zero for this initial study because the computational cost of obtaining an optimal μ is very high and was beyond the scope of this study. Due to this setting, no sparsification takes place in the SINDy regression, but a dominant structure of the state matrices is still clearly visible, see Figure 10. In the original study by Brunton et al. [1], where the algorithm was first introduced, the sparsification parameter μ was often kept at zero, too.

For both regimes, the HAVOK model reproduces the measured dynamics well except for a difference in amplitude which has been elaborated on in Section 3.1. Figure 10 shows the state matrix $\boldsymbol{A}_{\mathrm{H}}$ and the input matrix $\boldsymbol{B}_{\mathrm{H}}$ of the low-order HAVOK model as well as the attractors build from the first three states $y_{\mathrm{H},1}(t)$, $y_{\mathrm{H},2}(t)$ and $y_{\mathrm{H},3}(t)$ for the silent and squealing region, respectively. Both models are forced and a dominant structure with only a few large coefficients is visible in the matrices. The state matrix $\boldsymbol{A}_{\mathrm{H,nosq}}$ of the silent section exhibits a clear structure with dominant entries on the two sub-diagonals. This matrix structure resembles that of the HAVOK model for the chaotic Lorenz attractor presented in [1]. The much smaller model of the squealing section shows two states are strongly coupled, and a third is mainly driven by the forcing term. The resulting attractors are shown as black lines, where the forcing is small, and red lines, where the forcing is larger. In the silent regime, no clear structure of the attractor or forcing patterns is discernible. In the squealing regime, the dynamics form concentric circles around the $y_{\mathrm{H},3}$-axis, being tilted slightly with respect to the $(y_{\mathrm{H},1}, y_{\mathrm{H},2})$-plane. The forcing marks the transitions of the system from one radius to another.

4. Discussion

The results presented in the previous section show that the HAVOK algorithm can be used to obtain low-order state-space models that are able to reproduce the dynamics of the measured system well. The studies with the double mass oscillator reveal that the amount of system properties that can be extracted from the HAVOK state-space model depends on the type of underlying dynamical process, as will be discussed in detail in Section 4.1. Extensive studies of the effects of the HAVOK parameters on the resulting HAVOK model and the inner workings of the algorithm give rise to recommendations for choosing these parameters when applying HAVOK to a new model, as will be elaborated on in Section 4.2.

It has been shown how HAVOK can be applied to real-world measurement data where the type of underlying dynamics are still subject to discussion. Even for the complex dynamical system at hand, HAVOK is able to generate a model that reproduced the dynamics well. It becomes clear that the obtained model ranks for the silent $r = 9$ and squealing $r = 4$ section agree well with the theories presented in the literature. At the same time, the HAVOK models do not allow for much further information, for example on the damping properties of the system. Taking a step back and considering the results of the studies of the double and three-mass oscillators, these results are not surprising.

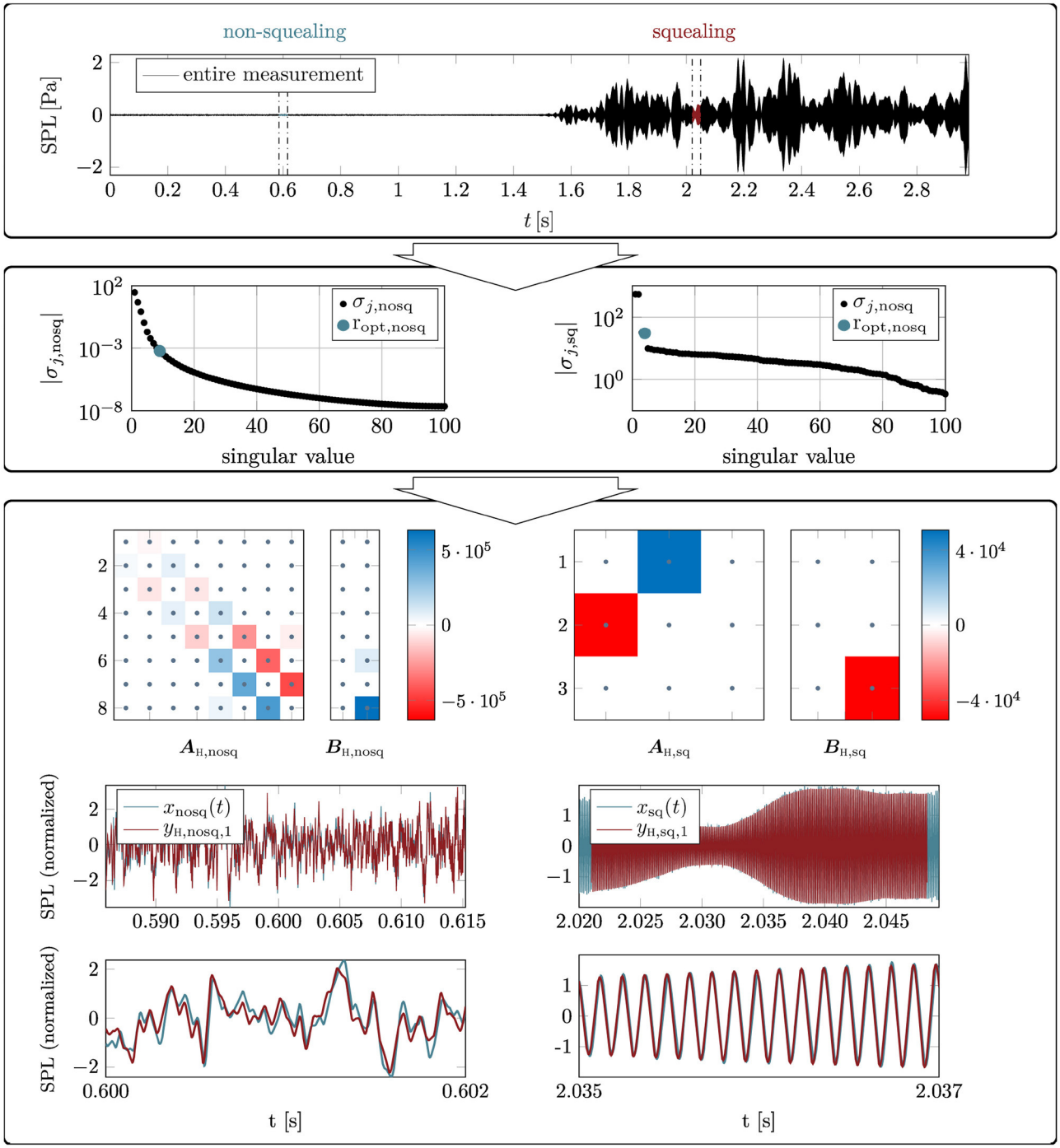

FIGURE 10
Application of the HAVOK algorithm to real-world measurement data. The sound pressure level (SPL) obtained with a microphone during the actuation of the friction brake of a passenger car is shown on the top. The dash-dotted lines indicate the sections from the silent and squealing regime used as input to the HAVOK algorithm. The singular values for each regime are visible in the center panel. In the bottom panel, the HAVOK model state matrices $\boldsymbol{A}_{\mathrm{H}}$ and the input matrices $\boldsymbol{B}_{\mathrm{H}}$ are shown, along with the resulting time series $y_{\mathrm{H},1}(t)$ compared to the input time series $x(t)$. As before, both time series are normalized to have zero mean and a standard derivation of 1.

4.1. Physical interpretability

The fundamental research question for the study at hand is: how much information can one obtain from a fully data-driven system identification process using HAVOK, and how can the resulting system description be linked with classical physics-based descriptions? For all of the considered models, the HAVOK algorithm generates state-space systems that are able to reproduce the observed dynamics well. The reconstructed state space trajectories $y_{\mathrm{H},j}$ of the HAVOK model

will most likely be distorted compared to the original one due to the orthonormalization that takes place during the SVD. Whether or not it is possible to accurately recover the original amplitude from the process remains subject to further studies.

HAVOK builds up a state-space system based on the frequency components in the input time series. Therefore, a closed-form representation of the Koopman operator, i.e., an unforced state-space system, is found for a dynamical system with a finite number of frequency components, such as the linear double mass oscillator with harmonic forcing. For this special type of system, the HAVOK model accurately captures the true eigenvalues and thus some of the properties of the original system. The dependency on the periodicity of the input signal is also emphasized by the fact that periodic dynamics can be represented by a more sparse model, as the studies with different initial conditions and input time series lengths illustrate. It has also been shown that the rank of the HAVOK model depends directly on the number of frequency components in the input data. Note that even though HAVOK captures the dynamics and the eigenvalues for dynamics with a finite number of frequency components, it cannot distinguish between system-inherent and forcing-related contributions in the data. Therefore, HAVOK yields an unforced state space model whenever possible, as no distinction between the different components is possible without additional information on the underlying system.

For general systems that include non-linearities or non-harmonic forcing, no closed-form representation of the Koopman operator can be found and the resulting HAVOK model is forced, as is to be expected. The forcing will collect all dynamics that cannot be represented by the linear Koopman operator. In these cases, a lot of information on the underlying dynamical system is moved into the forcing term of the HAVOK model and is not accessible for further analysis in the state matrix $\boldsymbol{A}_{\mathrm{H}}$. Some information on the dimensionality, stability, and main spectral components of the underlying dynamical system can still be found, but the extraction of principles, coupling between the states, or generalizations, remains difficult.

As with any data-driven method, the system identification potential of the HAVOK algorithm is limited by the fact that only observable dynamics can be represented in the final model, as the study with the three-mass oscillator showed. Measurements from a degree of freedom that does not move with a specific mode cannot be used to create a model that represents that mode. The same is true for strongly damped modes that do not affect enough oscillations to become visible in the measurement data and are thus not present in the HAVOK model.

4.2. Recommendations for choosing HAVOK parameters

From the numerous studies of the HAVOK algorithm with different mechanical oscillator models, we derive some recommendations for choosing suitable parameter settings in order to obtain the most meaningful HAVOK model possible.

4.2.1. Input data

The input data forms the basis for the HAVOK model and may be subject to several parameter choices during the first step of the algorithm. First, if a choice of potential input data is available, choose a time series $x(t)$ that contains rich information on the underlying dynamics and captures as many different modes as possible in order to get a more complete picture of the dynamics at hand. The sampling frequency f_s has to be high enough to represent the dynamics in the desired time scale. It is recommended to check the accuracy of the derivatives $\dot{\boldsymbol{V}}_r$ in the fourth step of the algorithm by reintegrating the obtained derivatives and comparing them to the original modes $\boldsymbol{V}_r$. If the differentiation error is larger than 1% nMAE, the input signal $x(t)$ should be upsampled using a suitable algorithm, until sufficient differentiation accuracy can be assured. The input time span t_l chosen from the measurement data is an important parameter that impacts the final HAVOK model. If the possibility of capturing both transient and steady-state dynamics is given, a mixture of both regimes was shown to yield robust and consistent results. Omitting the transient part completely prevents HAVOK from correctly capturing the system-related part of the dynamics (particularly damping), while large transients with strongly dissipative dynamics lead to an overestimation of the damping factors by the HAVOK algorithm. On the other hand, it seems that only transient motion, as in the case study with the frequency sweep function or the self-excited friction brake system, HAVOK cannot pick up the properties of the dynamical system itself in a fashion that is directly extractable, though it still yields a good reconstruction of the underlying dynamics and, in some cases, of the dimensionality of the system.

4.2.2. Embedding dimension and model rank

The embedding dimension q defines the amount of information that is contained in one column of the Hankel matrix $\boldsymbol{H}$ which is set up in the second step of the algorithm. The model rank r, which is chosen in the third step after the SVD of the Hankel matrix, marks the number of columns of the matrix $\boldsymbol{V}$ which are taken along for the sparse regression and ultimately defines the rank of the final model. Because the model rank r is generally chosen as the number of relevant components that are computed in the singular value decomposition, these two tuning parameters are closely connected. There are two approaches to deciding on an embedding dimension and model rank.

If the information on the desired model rank is available, either from prior knowledge of the system or from a fixed, desired output model rank, then the embedding dimension q can simply be varied until the singular value decomposition yields the desired number of relevant components. A larger embedding dimension q or, more accurately, a larger time span $x^{(q)}(t)$, yields more valid coordinates and thus a higher model rank r, while a smaller value of q yields a smaller rank r. A good initial guess for the model rank r is the number of frequency components of the model and its forcing times two.

If no specific model rank r can be expected or is desired, it is recommended to vary the embedding dimension q over a wide value range and observe how the resulting model rank evolves. A model rank can then be chosen as a larger value, if a high

model accuracy is desired, or a smaller value if a low-order model is wanted.

For the models studied in the course of this study, a variation of embedding dimension in the range of $q \in [50:1,000]$ was found to be sufficient. For periodic or quasi-periodic systems, a good starting point is an embedding dimension that yields a time span $x^{(q)}(t) = (q-1)\Delta t$ that matches one period of the system [7]. For any system, the embedding dimension has to capture enough of the oscillation. If q is too small, the Koopman observables or $\boldsymbol{u}_j$ obtained from the SVD are highly non-linear and do not form a good basis for the HAVOK model [7]. According to Dylewsky et al. in [31], the embedding dimension q can be too small, but not too large. Our studies showed that there is an upper limit to the model rank r that can be obtained for a given system through variation of embedding dimension, above which no reasonable results are achieved.

4.2.3. Sparsification threshold

The sparsification threshold μ is set to define the cutoff threshold for small coefficient entries in the sparse identification of non-linear dynamics in the fifth step of the HAVOK algorithm. The parameter does not impact the dominant structure of the resulting state matrices but induces the final state and input matrices $\boldsymbol{A}_\mathrm{H}$ and $\boldsymbol{B}_\mathrm{H}$ to be more sparse. Finding a Pareto-optimal μ between model sparsity and model accuracy requires large computational efforts when performed extensively. It is possible to compute the vectors of sparse coefficients for a range of sparsification thresholds and compare the resulting non-zero elements and model accuracy for each individual state [3], as presented in Section 2.3.5. From this, an optimal sparsification threshold for each state can be found. However, since the dominant structure is not affected by the sparsification, it may be sufficient to set the sparsification threshold $\boldsymbol{\mu} = 0$.

5. Conclusion

In this study, the steps of the HAVOK algorithm, its parameters, their interconnections, and the relation of the method to the Koopman operator theory have been presented. The studies were performed in Matlab. Several mechanical oscillator models, ranging from linear to non-linear, weakly to strongly damped, excited with different types of forces, and subjected to different initial conditions, have been subjected to the HAVOK algorithm. The resulting low-order HAVOK state-space models have been compared to the analytical physics-based models to determine which properties of the underlying dynamical systems can be extracted from the data-driven approach and under which conditions. For all of the considered systems, the obtained HAVOK models reproduce the measured dynamics well. Information on the underlying (i.e., the data-generating) system dimensionality, stability, and dominant frequency components can be obtained in most cases, but detailed information such as eigenvalues can only be identified correctly for systems with a low number of frequency components in our study. The HAVOK algorithm is, thus, a good choice if a low-order model is required for future state prediction or control purposes of a complex and unknown dynamical process. However, the method is of limited use as a system identification algorithm when system properties are to be identified in the classical sense of modal properties. Extensive studies of the effects of the algorithm's parameters yield valuable insights into the inner workings of the algorithm and give rise to recommendations for choosing those parameters when applying the method to new systems.

Data availability statement

The raw data supporting the conclusions of this article will be made available upon reasonable request.

Author contributions

MS and CG contributed to the conception and design of the study. CG performed the analysis and investigation and wrote the first draft of the manuscript. MS supervised the study. All authors contributed to the manuscript revision, have read, and approved the submitted version.

Funding

This research was funded by the German Research Foundation (Deutsche Forschungsgemeinschaft DFG) within the Priority Program 1897 calm, smooth, smart, grant number 314996260.

Conflict of interest

The authors declare that the research was conducted in the absence of any commercial or financial relationships that could be construed as a potential conflict of interest.

Publisher's note

All claims expressed in this article are solely those of the authors and do not necessarily represent those of their affiliated organizations, or those of the publisher, the editors and the reviewers. Any product that may be evaluated in this article, or claim that may be made by its manufacturer, is not guaranteed or endorsed by the publisher.

References

1. Brunton SL, Brunton BW, Proctor JL, Kaiser E, Kutz JN. Chaos as an intermittently forced linear system. *Nat Commun.* (2017) 8:19. doi: 10.1038/s41467-017-00030-8

2. Mezić I. Koopman operator, geometry, and learning of dynamical systems. *Not Am Math Soc.* (2021) 68:1087–105. doi: 10.1090/noti2306

3. Stender M, Oberst S, Hoffmann N. Recovery of differential equations from impulse response time series data for model identification and feature extraction. *Vibration*. (2019) 2:25–46. doi: 10.3390/vibration2010002

4. Conti P, Gobat G, Fresca S, Manzoni A, Frangi A. Reduced order modeling of parametrized systems through autoencoders and SINDy approach: continuation of periodic solutions. *arXiv*. (2022). doi: 10.48550/arXiv.2211.06786

5. Guckenheimer J, Holmes P. Global bifurcations. In: *Nonlinear Oscillations, Dynamical Systems, and Bifurcations of Vector Fields* (New York, NY: Springer) (1983). p. 289–352.

6. Brunton SL, Proctor JL, Kutz JN. Discovering governing equations from data by sparse identification of nonlinear dynamical systems. *Proc Natl Acad Sci USA*. (2016) 113:3932–7. doi: 10.1073/pnas.1517384113

7. Champion KP, Brunton SL, Kutz JN. Discovery of nonlinear multiscale systems: sampling strategies and embeddings. *SIAM J Appl Dyn Syst*. (2019) 18:312–33. doi: 10.1137/18M1188227

8. Bakarji J, Champion K, Kutz JN, Brunton SL. Discovering governing equations from partial measurements with deep delay autoencoders. *arXiv*. (2022). doi: 10.48550/arXiv.2201.05136

9. Franco N, Manzoni A, Zunino P. A deep learning approach to reduced order modelling of parameter dependent partial differential equations. *Math Comp*. (2023) 92:483–524. doi: 10.1090/mcom/3781

10. Fresca S, Manzoni A. POD-DL-ROM enhancing deep learning-based reduced order models for nonlinear parametrized PDEs by proper orthogonal decomposition. *Comput Methods Appl Mech Eng*. (2022) 388:114181. doi: 10.1016/j.cma.2021.114181

11. Daniels BC, Nemenman I. Automated adaptive inference of phenomenological dynamical models. *Nat Commun*. (2015) 6:8133. doi: 10.1038/ncomms9133

12. Atkinson S. Bayesian hidden physics models: uncertainty quantification for discovery of nonlinear partial differential operators from data. *arXiv*. (2020). doi: 10.48550/arXiv.2006.04228

13. Ribera H, Shirman S, Nguyen A, Mangan N. Model selection of chaotic systems from data with hidden variables using sparse data assimilation. *Chaos*. (2022) 32:063101. doi: 10.1063/5.0066066

14. Schmidt M, Lipson H. Distilling free-form natural laws from experimental data. *Science*. (2009) 324:81–5. doi: 10.1126/science.1165893

15. Schmid PJ. Dynamic mode decomposition of numerical and experimental data. *J Fluid Mech*. (2010) 656:5–28. doi: 10.1017/S0022112010001217

16. Rowley CW, Mezić I, Bagheri S, Schlatter P, Henningson DS. Spectral analysis of nonlinear flows. *J Fluid Mech*. (2009) 641:115–27. doi: 10.1017/S0022112009992059

17. Williams MO, Kevrekidis IG, Rowley CW. A data-driven approximation of the Koopman operator: extending dynamic mode decomposition. *J Nonlinear Sci*. (2015) 25:1307–46. doi: 10.1007/s00332-015-9258-5

18. Arbabi H, Mezić I. Ergodic theory, dynamic mode decomposition, and computation of spectral properties of the Koopman operator. *SIAM J Appl Dyn Syst*. (2017) 16:2096–126. doi: 10.1137/17M1125236

19. Somacal A, Barrera Y, Boechi L, Jonckheere M, Lefieux V, Picard D, et al. Uncovering differential equations from data with hidden variables. *Phys Rev E*. (2022) 105:054209. doi: 10.1103/PhysRevE.105.054209

20. Champion K, Lusch B, Kutz JN, Brunton SL. Data-driven discovery of coordinates and governing equations. *Proc Nat Acad Sci USA*. (2019) 116:22445–51. doi: 10.1073/pnas.1906995116

21. Brunton SL, Kutz JN. *Data-Driven Science and Engineering: Machine Learning, Dynamical Systems, and Control*. Cambridge: Cambridge University Press (2019).

22. Mezić I. Analysis of fluid flows via spectral properties of the Koopman operator. *Annu Rev Fluid Mech*. (2013) 45:357–78. doi: 10.1146/annurev-fluid-011212-140652

23. Lusch B, Kutz JN, Brunton SL. Deep learning for universal linear embeddings of nonlinear dynamics. *Nat Commun*. (2018) 9:4950. doi: 10.1038/s41467-018-07210-0

24. Koopman BO. Hamiltonian systems and transformation in Hilbert space. *Proc Natl Acad Sci USA*. (1931) 17:315–8. doi: 10.1073/pnas.17.5.315

25. Mezić I. Spectral properties of dynamical systems, model reduction and decompositions. *Nonlinear Dyn*. (2005) 41:309–25. doi: 10.1007/s11071-005-2824-x

26. Parmar N, Refai H, Runolfsson T. A survey on the methods and results of data-driven Koopman analysis in the visualization of dynamical systems. *IEEE Transact Big Data*. (2020) 8:1. doi: 10.1109/TBDATA.2020.2980849

27. Mezić I, Banaszuk A. Comparison of systems with complex behavior: spectral methods. In: *Proceedings of the 39th IEEE Conference on Decision and Control (Cat No00CH37187)* (Sydney). (2000) p. 1224–31.

28. Takens F. Detecting strange attractors in turbulence. In: *Dynamical Systems and Turbulence, Warwick 1980*, Vol 898 (Berlin: Springer). (1981). p. 366–81. doi: 10.1007/BFb0091924

29. Gavish M, Donoho DL. The optimal hard threshold for singular values is 4/sqrt(3). *IEEE Transact Inf Theory*. (2014) 60:5040–53. doi: 10.1109/TIT.2014.2323359

30. Branke J, Deb K, Dierolf H, Osswald M. Finding knees in multi-objective Optimization. In: *International Conference on Parallel Problem Solving From Nature* (Birmingham). (2004) p. 722–31.

31. Dylewsky D, Kaiser E, Brunton SL, Kutz JN. Principal component trajectories for modeling spectrally continuous dynamics as forced linear systems. *Phys RevE*. (2022) 105:015312. doi: 10.1103/PhysRevE.105.015312

32. Khodkar MA, Hassanzadeh P, Antoulas A. A Koopman-based framework for forecasting the spatiotemporal evolution of chaotic dynamics with nonlinearities modeled as exogenous forcings. *arXiv*. (2019). doi: 10.48550/arXiv.1909.00076

33. Lehr E. *Schwingungstechnik. Ein Handbuch für Ingenieure: Grundlagen. Die Eigenschwingungen eingliedriger System*. Berlin, Heidelberg: Springer Berlin Heidelberg (1930). p. 231–92.

34. Lorenz EN. Deterministic nonperiodic flow. *J Atmos Sci*. (1963) 20:130–41. doi: 10.1175/1520-0469(1963)020<0130:DNF>2.0.CO;2

35. Stender M, Oberst S, Tiedemann M, Hoffmann N. Complex machine dynamics: systematic recurrence quantification analysis of disk brake vibration data. *Nonlinear Dyn*. (2019) 97:2483–97. doi: 10.1007/s11071-019-05143-x

36. Stender M, Tiedemann M, Spieler D, Schoepflin D, Hoffmann N, Oberst S. Deep learning for brake squeal: brake noise detection, characterization and prediction. *Mech Syst Signal Process*. (2021) 149:107181. doi: 10.1016/j.ymssp.2020.107181

37. Oberst S, Lai JCS. Chaos in brake squeal noise. *J Sound Vib*. (2011) 330:955–75. doi: 10.1016/j.jsv.2010.09.009

38. Wernitz BA, Hoffmann NP. Recurrence analysis and phase space reconstruction of irregular vibration in friction brakes: signatures of chaos in steady sliding. *J Sound Vib*. (2012) 331:3887–96. doi: 10.1016/j.jsv.2012.04.003

39. Vitanov NK, Hoffmann NP, Wernitz B. Nonlinear time series analysis of vibration data from a friction brake: SSA, PCA, and MFDFA. *Chaos Solit Fractal*. (2014) 69:90–9. doi: 10.1016/j.chaos.2014.09.010

3.2 Machine learning

Machine learning is a large field of data-driven methods that obtains models in the form of neural networks which are trained on measurement data. In contrast to the methods presented in the previous section, neural network models mainly focus on providing accuracy over interpretability and are therefore often huge black boxes. The strength of these models lies in their ability to learn complex relationships that are beyond our current physical understanding using a high-dimensional embedding space. Their ability to perform efficient interpolations makes neural network models particularly suited to applications in scenarios where data is only available at specific points, for example, when experimental data collection is expensive. The resulting models are generally coined for a specific application and cannot generalize in the way the equations obtained in the previous Section 3.1 can, but provide a modeling possibility where physical laws remain elusive.

Machine learning has a long history of fluctuating popularity, dating back to cybernetics in the 1940-60s, and has become practical as the amount of available training data increased sufficiently [83]. Deep neural networks, or neural networks with hidden layers, had their breakthrough with the discovery of the backpropagation algorithm in the 1980s [83, 128–130]. Deep neural networks can learn on different layers of abstraction [130], such that different laws can emerge on different layers, a powerful parallel to the phenomenon of emergence in physical systems. Around 2006, deep feed-forward networks gained popularity with the introduction of greedy layer-wise pre-training methods for the hidden layers [131, 132]. Convolutional neural networks, designed for detecting patterns in array-formatted data, were introduced in the 1990s for document reading [133]. These networks later became widely popular in the 2010s [130] in speech recognition [134, 135], object detection, and face recognition [136]. Other popular methods include recurrent neural networks such as long short term memory networks [137, 138], which specialize in the prediction of sequential data such as text or speech [130]. Reservoir computing methods reduce the computational effort by using a fixed but random network structure and only training an output layer [139–142].

Today, neural network-based methods are almost omnipresent for prediction, classification, and optimization in all fields of science [83]. In engineering, applications include finding structure in high-dimensional data [130], which can be highly nonlinear [97]. Neural networks can be set up as predictors for sequential data when operated in a closed loop that feeds back predictions to the input [139]. These types of feedback applications can learn the long-term statistical behavior ("climate") of a chaotic dynamical system [139], act as predictors for systems with unknown dynamics [116, 138, 143, 144], or speed up simulation times in cases with computationally expensive physical laws, such as water wave propagation [145] or reconstruction [146]. A different approach uses deep convolutional autoencoders to learn model reductions [147, 148].

These examples illustrate that neural network-based modeling approaches are successful in cases where physical laws are unattainable, or computation times too large. At the same time, these models are limited in their abilities for generalization, extrapolation, and interpretation [71, 81, 97, 144, 149, 150], especially compared to equation-based models, which provide more universal insights and direct interpretability. To close this gap, methods

combining physics-based and neural network-based approaches evolve. These approaches include coupling physical and neural network models, or integrating physical knowledge, such as conservation laws, into the learning process via the loss function, for example, in physics-informed neural networks (PINNs) [151–153]. Some methods combine equation learning with neural network approaches, for example by learning equations from data using autoencoder networks [102], or by learning the Koopman operator using reservoir computing [154]. A different approach to obtaining insight into the physics that govern the dynamics of a structure from a neural network is presented in Publication II. In this work, a convolutional neural network is trained to pick up the intricate parametric relationships governing the system dynamics. This model can then be queried for the system state across a range of parameters, revealing the patterns that give rise to specific phenomena. The following Section 3.2.1 provides a short overview of the case study in Publication II, followed by a detailed discussion of the results and contribution to the field, and concludes with an outlook on future work.

3.2.1 Neural network-based state maps for mechanical dynamics

Publication II presents an approach to gaining physically interpretable information using neural networks by using the network to map out the system state over a range of parameter values. As discussed in Chapter 2, understanding the parametric relationships that result in the state or stability of an engineering system is of great interest when it comes to avoiding unwanted or potentially harmful vibrations. However, the system state might depend on a large number of different parameters or complex relationships between those parameters. Often, the physical laws underlying these phenomena are not yet known, and expensive experiments are required to detect these dependencies. The noise emission of friction brake systems is one example of a situation where only a limited number of experimental data is available, such that only a few discrete points on a state map are known.

Summary of the case study
In the process proposed in Publication II, a convolutional neural network is trained on measurement data from the real-world brake system. If the training is successful, the model has picked up some of the parameter relationships that give rise to the system state. In the next step, the original measurement data is expanded in a data augmentation process, where additional data is generated systematically from the original data in a physics-consistent manner. The trained network is then queried for the system state throughout the newly generated data, resulting in a fine-grained state map across a parameter range. The state map can be interpreted as mapping the system state over a chosen set of parameters, visualizing the parametric relationships from a new perspective.

The results of the case study indicate that the convolutional neural network has picked up some intricate mechanisms that give rise to break squeal from the training data. In the case study, maximum brake pressure and rotational velocities are chosen as the variables over which the system state is mapped. The resulting state maps depend on the base sample chosen for the data augmentation. The state maps differ if the qualitative evolution of the state variables varies within a sample, indicating that a more complex mechanism than

maximum brake pressure and rotational velocity is responsible for the noise occurrence. This finding does not contradict the consistency of the method, since state maps obtained from overall similar dynamics result in similar state maps. A probability state map is generated by averaging over state maps obtained with different base samples, illustrating predominant state patterns dependent on the two chosen variables.

Discussion and contribution to the field
From a machine learning perspective, the method presented in Publication II represents an approach to inferring a physical understanding of the underlying dynamical system from data. Instead of focusing on the internal structure of the trained neural network, which is difficult to analyze due to its high dimensionality, the entire method is set up such that the model itself provides information about the mechanisms it has picked up. In principle, the method is applicable to any dynamical system with several states, as long as there is sufficient labeled training data available. However, some knowledge of the underlying physics is required to keep the data augmentation physically consistent.

In the application presented in the case study, the data augmentation process is very rudimentary, focusing only on not violating any physics, which is validated using exemplary samples. However, more active leverage of physical laws, such as the conservation of energy, might be required when considering additional variables such as temperature, and yield additional insights. The quality of the model employed in the case study might be increased with additional input data, as training the model is difficult due to the class imbalance since actual squeal data is relatively sparse. Even though recurrent neural networks might seem the more obvious choice when dealing with time series data, the use of convolutional neural networks for detecting patterns in time series data is common [130]. Recurrent neural networks, especially in long short term memory configuration, are well suited for predictive modeling. In the application at hand, the neural network model is used for classification of time series samples rather than prediction of future behavior, making convolutional neural networks the more suitable technique.

From a structural mechanics perspective, the proposed method offers an alternative approach to mapping out the state of a dynamical system over a fine grid of parameters. The method offers the possibility to overcome data sparsity in parameter space, for example, when only a limited number of experiments can be performed. This type of data sparsity is different from the spatial data sparsity stemming from a limited number of measurements per experiment in Section 3.1.1. The approach to overcoming data sparsity through synthetic data augmentation could potentially help reduce cost and time consumption in the design and analysis of mechanical systems. The advantage of the neural network-based method over conventional methods is that it is not limited to the classical notion of stability or specific attractors, but the user can create their own labels, focusing on phenomena difficult to describe mathematically, such as the squeal/no-squeal labels in the case study. The state map generated in this context can thus be seen as a step away from conventional representations towards more phenomenon-based descriptions. The proposed approach to studying the system state, albeit of an uncommonly defined one, is closely related to bifurcation analysis. State-of-the-art physics-based methods for bifurcation analysis, which

provides a mapping of the system state over a single parameter, have been described in Chapter 2.

The phenomenon of brake squeal remains an actively researched topic. Due to the complex nature of the interplay of dynamics at many scales, and the underlying mechanisms remain poorly understood until today and no models with satisfying predictive quality have been found [155]. Unsurprisingly, the results of the case study indicate that the mechanisms resulting in brake squeal are more complex than a simple dependency on maximum velocity and pressure. The approach provides a complementary tool for analyzing the brake squeal phenomenon, paving the way for a novel perspective. Recent work [155] with experimental data in a highly instrumented pin-on-disc test setting indicates that a thermal measurement within the brake pad, which indirectly captures the macro- and microscopic contact scenario, might facilitate more accurate brake squeal predictions.

Outlook
Three main research directions follow from the case study in Publication II: First, the refinement of the probability state map, for example by introducing a confidence interval for each contributing state map. An area centered around the base sample, marking the decreasing influence of a single state map to the probability map as the parameter values are further from those of the base sample, includes the assumption that the obtained state maps are more reliable closer to the base sample they are generated from. Second, the expansion to higher-dimensional state maps, for example by adding temperature, derivative values, specific oscillatory patterns, or even parameter combinations. The extension is straightforward via the expansion of the data augmentation process to include the additional dimension. The only limit to unfolding the state map into further dimensions is the physical consistency of the data generation. A third research direction involves quantifying the information in the state map, for example, by fitting a function through the edges. The resulting description would contain less information than common studies on system stability as it only contains the information squeal/no squeal, but it focuses on the quantity of interest, possibly gaining accuracy concerning this specific quantity.

In summary, this chapter introduces a novel method for mapping the state space of a system across an entire parameter space based on sparse measurement data. Instead of building a physics-based model, a high-level embedding approach is employed to re-infer information. Verification is feasible due to the availability of partial ground truth via experimental data. The methodology can be extended easily to accommodate even higher dimensions, such as a three-dimensional parameter space. The model itself lacks interpretability. More explainable machine learning methods or interpretability approaches, such as the Shapley additive explanations (SHAP) [156], may be able to resolve this issue.

Similar to the approach in Section 3.1.1, the neural network-based state map method involves embedding measurement in a high-dimensional space and then inferring human-understandable information about the underlying system from that space. In the previous Publication I, the resulting information took the form of equations. In this Publication II, it takes the form of a two-dimensional map. While the equations can be queried for system stability and could potentially be used to infer a state map, the results in Chapter 3.1.1 have illustrated the limitations of the information that is captured in them. Since the neural

network-based approach makes close to no assumptions on model structure and provides a more flexible embedding space, this model can capture more complex relations, the results of which can be extracted. The subsequent Chapter 4 provides another phenomenon-specific perspective, studying functional relationships within a mechanical system from a network point of view.

3.2.2 Publication II: Machine learning-based state maps for complex dynamical systems: applications to friction-excited brake system vibrations

C. Geier et al. “Machine learning-based state maps for complex dynamical systems: applications to friction-excited brake system vibrations”. *Nonlinear Dynamics* 111.24 (2023), pp. 22137–22151. DOI: 10.1007/s11071-023-08739-6

Nonlinear Dyn
https://doi.org/10.1007/s11071-023-08739-6

ORIGINAL PAPER

Machine learning-based state maps for complex dynamical systems: applications to friction-excited brake system vibrations

Charlotte Geier · Saïd Hamdi · Thierry Chancelier · Philippe Dufrénoy · Norbert Hoffmann · Merten Stender

Received: 3 November 2022 / Accepted: 9 July 2023

Abstract In this work, a purely data-driven approach to mapping out the state of a dynamical system over a set of chosen parameters is presented and demonstrated along a case study using real-world experimental data from a friction brake system. Complex engineering systems often exhibit a rich bifurcation behavior with respect to one or several parameters, which is difficult to grasp using experimental approaches or numerical simulations. At the same time, the growing need for energy-efficient machines that can operate under varying or extreme environmental conditions also calls for a better understanding of these systems to avoid critical transitions. The proposed method combines machine learning techniques with synthetic data augmentation to create a complete state map for a dynamical system. First, a machine learning model is trained on experimental data, picking up hidden mechanisms and complex parametric relations of the underlying dynamical system. The model is then exploited to assess the state of the system for a set of synthetically generated data to obtain a state map over the complete space spanned by the chosen parameters. In addition, an extension of the concept to a probability state map is introduced. The results indicate that the proposed method can uncover hidden variables which drive dynamical transitions between different states of a system that were previously inaccessible.

Keywords Bifurcations · Data-driven models · Complex vibrations · Nonlinear dynamics · Convolutional neural network

C. Geier (✉) · N. Hoffmann · M. Stender
Dynamics Group, Hamburg University of Technology, Am Schwarzenberg-Campus 1, 21073 Hamburg, Germany
e-mail: charlotte.geier@tuhh.de

S. Hamdi · T. Chancelier
Hitachi Astemo France S.A.S., 126 rue de Stalingrad, 93700 Drancy, France

P. Dufrénoy
CNRS, Centrale Lille, - LaMcube - Laboratoire de Mécanique Multiphysique et Multiéchelle, University of Lille, 59000 Lille, France

N. Hoffmann
Department of Mechanical Engineering, Imperial College London, Exhibition Road, London SW7 2AZ, UK

M. Stender
Chair of Cyber-Physical Systems in Mechanical Engineering, Technische Universität Berlin, Straße des 17. Juni 135, Berlin 10623, Germany

1 Introduction

Real-world engineering systems typically consist of many components accompanied by a large number of parameters and degrees of freedom, which give rise to complex emergent dynamical behavior. The analysis of structural vibrations remains challenging in many fields of engineering today, not only because large-scale numerical methods exhaust the computational resources but also because nonlinear and damping phenomena [1] pose difficulties to our modeling and prediction capabilities [2,3]. The dynamics of these

Published online: 21 July 2023

machines often depend on a large number of parameters [4,5], such as loading conditions or uncertain components [6], whose change during the operation or the lifetime of the system can cause bifurcations or critical regime shifts [3,7]. It is crucial for the safe operation of complex machines to analyze and understand the mechanisms behind parametrically driven regime changes to prevent critical transitions into unwanted or even dangerous points of operation. In the following, we refer to parameters when reasoning about different external loads imposed by the operation and secondary changes to system component properties, such as reduced stiffness values resulting from higher temperatures caused by heavy loading conditions. Our approach is generically applicable to many high-dimensional nonlinear dynamical systems. In this paper, automotive disk brake systems and their rich friction-induced vibrations are taken as illustrative exemplary application case.

Today, the main approaches to understanding the rich nonlinear dynamics of machines are either of experimental nature or rooted in simulations based on first principles of physics [5]. Some engineering domains rely primarily on experimental tests for research and design purposes [3], which are often costly and time-consuming [8]. Since only a limited number of tests can be performed for some characteristic points of operation, the information on the state of the dynamical system in the high-dimensional parameter space is only available at specific points. This sparse experimental sampling of the parameter space could lead to unobserved phenomena in the system dynamics for unseen parameters. An example of this aspect is depicted in Fig. 1: The dynamical system under consideration exhibits unstable behavior for a given set of parameters that is not covered by experimental data. The second common approach to analyzing the dynamics of a sizable dynamical system is rooted in numerical simulation. High-dimensional numerical models and complex multi-scale, multi-physics simulations are often necessary to represent the dynamics. Large-scale multi-physics simulations of a system are computationally expensive and have a significant climate footprint. Because experimental tests are time-consuming and expensive, and numerical models are often computationally very costly, obtaining a finely-grained state map for a dynamical system is complex with current methods. Our research aims at providing a time- and cost-efficient way of generating a high-resolution state map as a post-processing technique for either experimental or numerical results. On the example of automotive disk brake systems, a detailed description of state-of-the-art methods, and our contribution, is given in the following.

Friction-induced vibrations (FIV) of vehicles, for example, automotive or aircraft braking systems, represent a family of complex dynamical systems [6,9,10] whose dynamics depend on many parameters and parameter inter-dependencies [9,11,12], as well as being sensitive to parameter variations [10,13]. Several mechanisms for explaining FIV have been proposed in [9,11,14,15], as friction brake systems have seen a rich research history in the last decades [9–12,15–17]. A detailed review of these can be found in [9] and [18]. However, FIV are notoriously difficult to grasp experimentally, because of the limited repeatability of results [9,13], which is likely due to the sensitive dependence of the system on small-scale parameter variations [7]. Still, expensive experiments [9,12] remain a crucial pillar in the analysis of brake systems and validation of simulation models. Because simplified models that neglect the effects of time-varying, uncertain parameters are often not accurate enough in their predictions [7,13,16,19], the brake system models often involve large-scale finite element models and elaborate computational schemes such as complex eigenvalue analysis [9,10,12,17] and transient analysis [10,11,14,17,20]. As complex eigenvalue analysis misses the effects of nonlinearities [9,10], a nonlinear transient analysis is often required to study the impact of parameter variations on the stability of the system [9,11,14,17,20]. In all these methods, considerable computational times remain an issue [9,11,14,16,17,20,21], which poses a challenge to performing extensive parameter studies [16] for realistic loading conditions seen during customer driving. Therefore, current research efforts focus on advancing methods to deal with uncertainties and nonlinear effects, increasing model accuracy and decreasing computation time, see [9–11,16,17,20].

As both experimental analysis and modeling of brake system remain challenging, obtaining a detailed state map for a brake system with state-of-the-art methods, for example, from measured data or numerical simulation alone, is currently very expensive. Therefore, the system state, in the simplest form given by the binary indication of the occurrence of high-amplitude vibrations, is only known for a few points of operation and unknown in most of the high-dimensional (loading) parameter space. In this work, we propose a purely

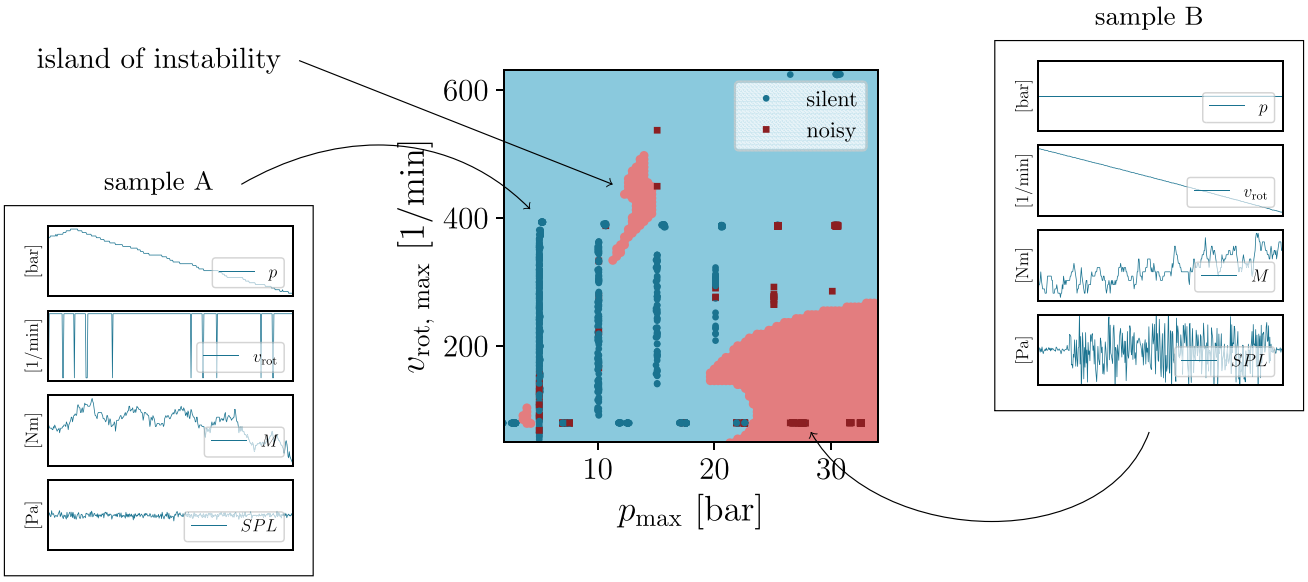

Fig. 1 Illustration of a data-based state map. A data-based state map for a complex dynamical system illustrates the system states within a space spanned by two predefined parameters. Each point on the map represents one data sample and is color-coded to the state of the system for a given sample. Darker colored dots mark the sparse information available from experiments; lighter colors represent a possible fill-in of the white spaces that will be obtained with the method proposed in this work. It is possible that "islands of instability" exist, which are not captured by the data gained from experiments

data-based approach to obtaining a fine-grained map, which is computationally less expensive and requires only a limited number of experimental results. Data-driven methods have recently evolved to complement conventional modeling methods [22]. Neural network models trained on large data sets do not rely on suitable reduced order modeling [23] or quasi-static dynamic observations and can interpolate within the input value range they have been trained in, making these models ideal candidates for the computation of state maps from sparse measurements.

In this work, we propose a new, data-driven approach for approximating the functional behavior of real-world machines using input–response relationships from experimental observations to generate a machine learning-based state map. First, a neural network model is trained with real-world measurement data to predict the system state in a specific loading and parameter configuration. If this data-driven modeling is successful, the neural network model has picked up complex parametric relations and hidden mechanisms that were activated during testing, but are not necessarily discernible to a human or accessible via classical system identification. The trained model can then be queried for the system state for new conditions and parameters beyond those tested experimentally. A set of synthetic input data is generated to fill the white spots in the parameter space and fed into the neural network model. The predictions of the model for these new points can be used to build a data-based state map over the "complete parameter space" in a very cost- and time-efficient manner, even if the parameter space was originally only sparsely sampled through measurement data, as illustrated in Fig. 1. The method is demonstrated with real-world experimental data from a friction brake obtained at Hitachi Astemo in Drancy, France. This complex system contains rich dynamical behavior that has not been fully understood until today [7,10,11,13,24], making it an interesting case study for the proposed method.

2 Methods

A novel and universal way of obtaining a state map illustrating the state of a dynamical system over a space spanned by a chosen set of parameters in a purely data-based fashion is proposed in this work. This section gives a schematic overview of the process, followed by more detailed presentations of the underlying real-world measurement data, the involved machine learn-

ing process, necessary data preparation, and the data augmentation procedure.

2.1 Schematic overview

The method proposed in this work can be split into two stages, namely a machine learning model training phase and a state map computation phase, as illustrated in Fig. 2. In the first phase, a neural network model is trained and validated using real-world experimental data from brake testing to predict the system state for a given set of input data. In the second phase, the model is queried for the system state using synthetically generated data to fill up the parameter space that is only sparsely sampled through the experimental data. Physics-consistent augmentation of the measurement data is the essential piece to this undertaking. This way, the model can be used to predict the state of the system over the entire range of parameter combinations, ultimately yielding a state map of the complete parameter space.

During the first phase, a neural network model is trained with experimental data obtained from a test rig at Hitachi Astemo France to represent complex input–output relationships between a set of measured quantities and a system state, here encoded in form of a binary squeal/no-squeal label. In preparation for the machine learning application, the raw data is processed using a sliding window method and split into a training and validation set for neural network model training and validation, as described in Sect. 2.2. During the data processing, binary squeal/no-squeal labels are assigned to each data sample from machine learning input/output data. A neural network model is then trained and validated with the processed real-world data, see Sect. 2.3. When the training is successful, the neural network model has learned complex parametric relations in terms of a mapping from input to output data that is based on features of the high-dimensional input data. These features can be any property of the input data or a combination thereof, and as these are not directly discernible to the user, they are referred to as "hidden." The model can predict whether or not a section of a braking is noisy for a given set of input parameters. Then, the obtained model can be deployed to predict the system state for parameter sets it has not seen before.

In the second phase, the trained model is exploited to compute state maps based on physics-consistent variations of the experimental data. The two-dimensional state map requires a featurization of the input samples with two basis parameters that form the two axes of the state map. As the parameter space spanned by the two chosen parameters is sampled only sparsely through the available measurement data, additional data has to be generated. The sparse measurement data is augmented in a physics-consistent manner to fill the parameter space, as described in Sect. 2.4. This synthetic data is fed into the machine learning model that outputs the system state in a binary label form, namely silent or noisy, for each new, synthetically generated data sample. These predicted labels are recorded in the two-dimensional parameter space, forming a purely data-based state map. The following sections are dedicated to describing the process in more detail.

2.2 Data acquisition

The data used in this work is real-world measurement data obtained from a dynamometer test rig at Hitachi Astemo. A standard disk brake system with prototype-material brake pads is tested. The test setup is depicted in Fig. 3, including the microphone location for recording the brake noise 50 cm away from the axle. The measurements are taken in a temperature- and humidity-controlled environment. The load on the brake system originating from the vehicle chassis is simulated by the surrounding structure.

The brake testing is performed according to the industry standard noise, vibration, and harshness (NVH) test procedure SAE-J2521 [25], which consists of a set of initial break-in and burnishing tests, after which several drag and stop brakings are carried out. The brake system is subjected to a series of temperature and velocity ramps to cover a wide range of braking scenarios. Figure 4 shows an overview of the SAE-J2521 data channels used in this work, namely brake pressure p, rotational velocity v_{rot}, brake torque M, friction coefficient μ, rotor temperature T_{rot}, ambient temperature T_{amb}, relative ambient humidity H_{rel}, and noise level. The friction coefficient μ is a derived quantity that is computed by the test bench directly using a Coulomb-type friction model assumption, i.e., the linear relationship between normal force and resulting friction force via the friction value. A total of 2498 brakings with

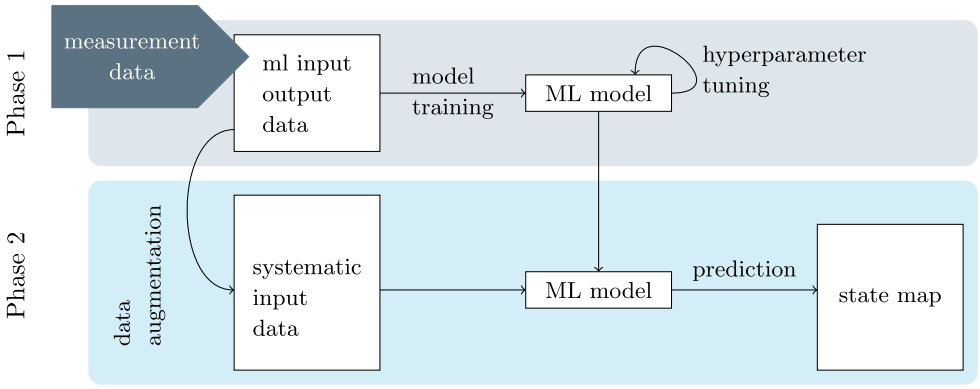

Fig. 2 Generation of a machine learning-based state map. A schematic overview of the method proposed in this paper, in which a two-dimensional state map representing the state of a dynamical system over a chosen set of features is computed in a purely data-driven way. The process can be split into two phases, a neural network model training phase, and a state map computation phase

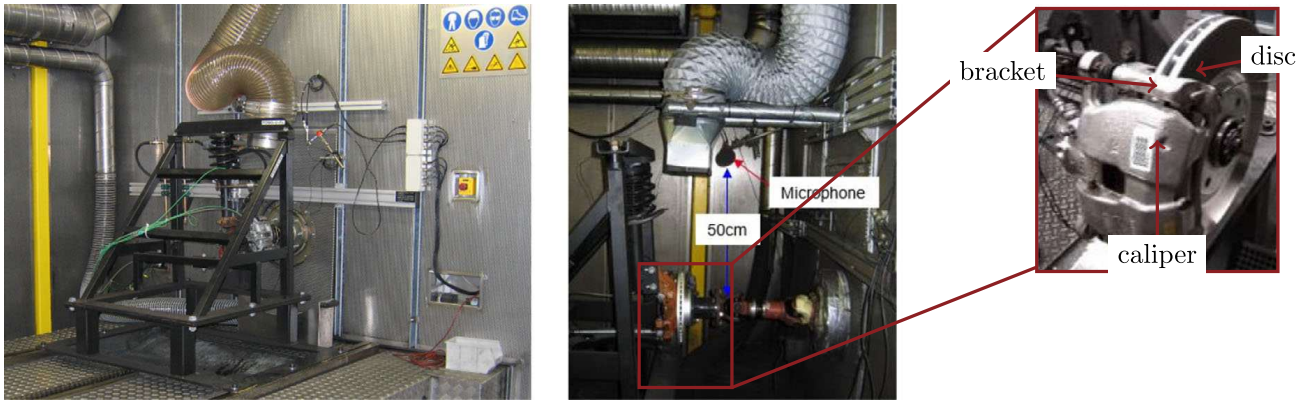

Fig. 3 Test rig. The dynamometer test rig at Hitachi Astemo France, which was used to record the data used in this work. A disk brake system consisting of disk, caliper, bracket, and brake pads is tested in a controlled environment, where the impact of the vehicle chassis is simulated by the surrounding structure. A microphone is located close to the disk for recording the brake noise. Additional verification of the noise is given by accelerometers located on the caliper

36 % noise occurrence are available. An overview of the measurement channels and value ranges is given in Table 1. The first seven measurement channels are recorded with a frequency of 100 Hz, while the sound pressure for the brake noise detection is recorded with a microphone and accelerometer at 51.2 kHz.

During the brake tests, noise detection is carried out with the microphone signal using a dBA threshold on the peak value of the sound pressure level (SPL) and the average spectrum. Tonal noises in the frequency range of 1 to 12 kHz and more than 70 dBA are labeled brake noises. The detected noise is validated using an additional accelerometer which measures the vibrations on the brake directly. Only if a noise is found in both signals, it is considered valid. For the purpose of this work, the noise start time and duration were recorded additionally to the standard time of maximum SPL for each braking. This procedure allows for more precise localization of the noise occurrence within a given braking and facilitates a straightforward label generation.

The recorded raw data is submitted to some preprocessing for the machine learning application, as illustrated in Fig. 5, for one exemplary braking with eight measurement channels. For each time instance, the system state is labeled either squealing or non-squealing, generating a time series of binary labels encoding the system state as 0—silent, or 1—noisy, which replaces the sound pressure level of the raw data. Additionally,

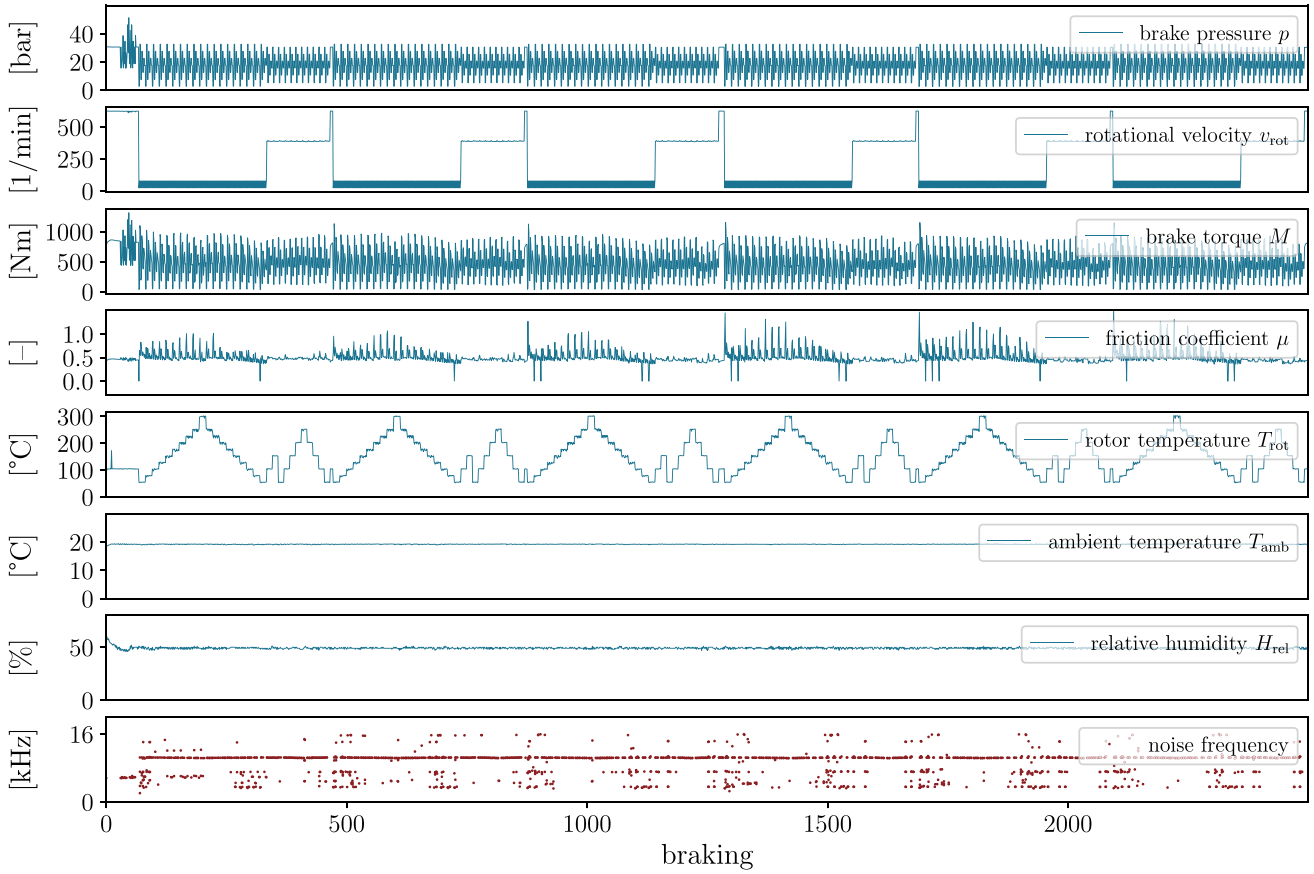

Fig. 4 Available data. Overview of the measurement data from 2498 brakings recorded with the industry standard SAE-J2521 [25] test procedure. The test protocol consists of a series of temperature ramps combined with different load cases, i.e., various velocity and brake pressure conditions. The recorded noise levels are also indicated. For clarity, maximum values are reported for the first five channels, and mean values for ambient temperature and relative humidity, while the noise-level information is limited to the number of available frequencies

Table 1 Summary of experimental data channels and value ranges

Data channel	Symbol	Unit	Min. value	Max. value
Maximum brake pressure per braking	p	[bar]	2.6	51.4
Rotational velocity at start of braking	v_{rot}	[1/min]	23.0	624.5
Maximum brake torque in braking	M	[Nm]	33.0	1317.0
Maximum friction coefficient in braking	μ	[-]	0.0	1.5
Maximum rotor temperature in braking	T_{rot}	[°C]	52.0	303.2
Mean ambient temperature in braking	T_{amb}	[°C]	18.5	19.5
Mean relative humidity in braking	H_{rel}	[%]	46	63

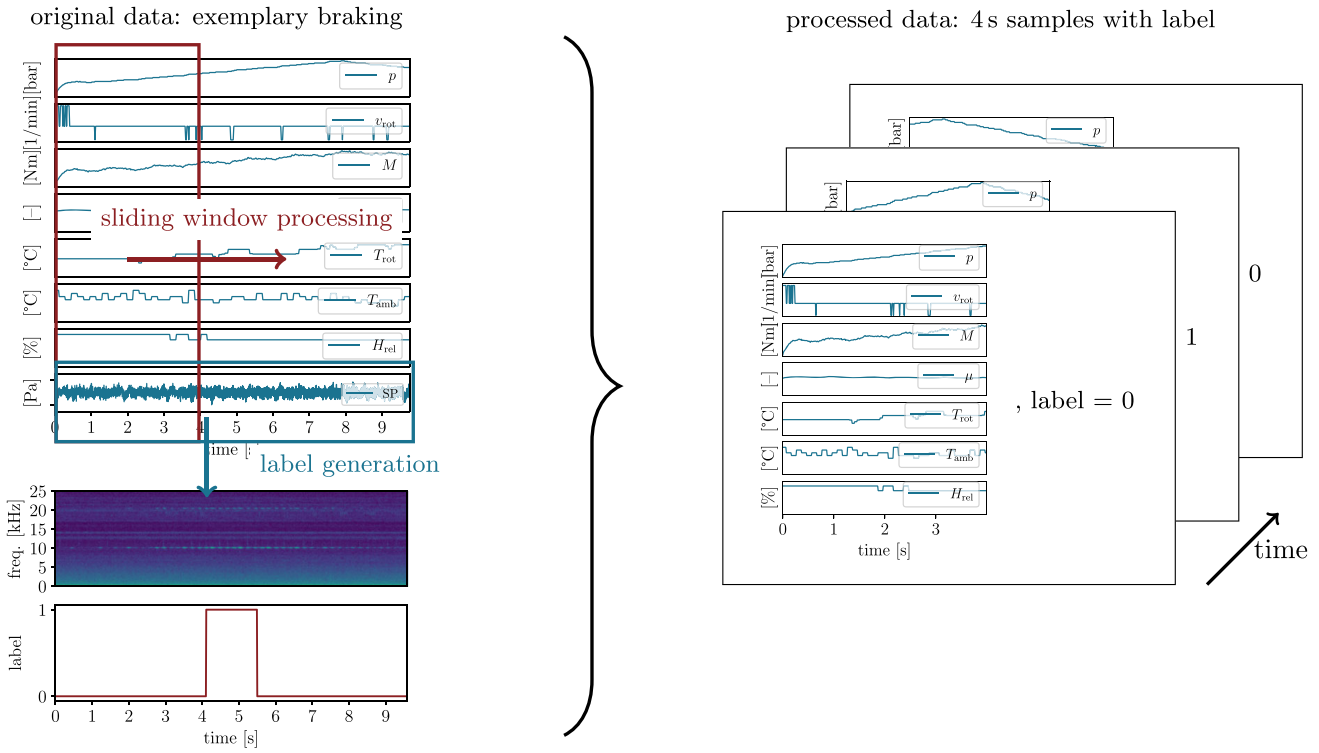

Fig. 5 Data processing. The data-processing procedure consists of generating a binary label classifying the system state as either "0" or "1" for silent or squealing, respectively, and a sliding window approach for generating equal-sized samples. The process is illustrated for one exemplary braking. The final input–output data for our machine learning models consists of 9896 samples, each of which is 4 s long and has a binary label denoting the system state as either squealing or non-squealing

the data is split into equally-sized windows using a sliding window approach with a window length of 400 time steps, or 4 s and an overlap of 50 %. To determine an optimal sliding window size, different variants in the range of 2 to 10 s were tested. The chosen option of 4-s samples was found to yield the best predictions results, balancing the number of generated samples, which here increases with a smaller sample size, with the time history included in each sample, which increases with a larger sample size. To avoid data leakage between the training and test set and a clean training procedure, the original set is split into five folds of training and test (validation) data at an 80–20 split before the sliding window is performed. A stratified split is implemented to ensure an equal class distribution between training and test data. The entire processed data consists of 9896 samples in total. In the final preparation step, the channel containing the time-distributed labels is condensed from 400 time steps down to one value. A sample is given the label "1" for noisy if a squeal is indicated within a given sample, that is, if there is a noisy section within the 4-s interval, or "0" otherwise. The final input/output data consist thus of sets of 4-s samples, seven channel samples input with a binary label output. The noise occurrence of 20 % in the processed data set of smaller samples differs from the original noise occurrence due to the sliding window processing.

An overview of the experimental data before and after the processing is given in Table 2, indicating the value range for each data channel. The fivefold 80:20 data split for the neural network modeling results in five training–test data pairs, where each training split contains 7975 samples and each test split consists of 1921 samples, each with a noise ratio of $20\,\% \pm 1\,\%$, respectively.

2.3 Neural network modeling

The neural network modeling task at hand is a binary classification task, where the neural network model classifies the system state in terms of a binary label of "0" or "1" for silent or noisy for a given input sample.

Table 2 Summary of processed data characteristics. The ratio of noisy samples varies from raw data to processed samples due to the slicing during the sliding window processing routine

	Raw data	Processed data
Total number of samples	2498	9896
Noise ratio	36 %	20 %

One input sample consists of 4 s or 400 time steps of a multi-variate time series with seven channels given by the recorded measurement channels brake pressure p, rotational velocity v_{rot}, brake torque M, friction coefficient μ, rotor temperature T_{rot}, ambient temperature T_{amb}, and relative ambient humidity H_{rel}. A convolutional neural network (CNN) is trained with the experimental data using a binary cross-entropy loss function. The neural network modeling is implemented in Python using the machine learning framework TensorFlow. Several hyperparameter studies are performed to obtain a suitable model for the given prediction task, for example, testing different numbers of hidden layers. Additionally, k-fold cross-validation with five folds is carried out for each set of hyperparameters to ensure model performance does not depend on a lucky training–test data split. It is also possible to retain a certain amount of data from the training for independent model evaluation, but since the experimental data set is already relatively small, k-fold cross-validation is deemed a more suitable method in this case. A 1D CNN with two hidden layers, 64 filters per layer, and a kernel size of 3 is found to attain the highest classification scores.

After the training is completed, the model is evaluated using the Matthews correlation coefficient (MCC) [26] to obtain a more tangible measure of model performance. The MCC is defined as

$$MCC = \frac{TP \cdot TN - FP \cdot FN}{\sqrt{(TP+FP)(TP+FN)(TN+FP)(TN+FN)}} \in [-1, 1], \tag{1}$$

where TP, TN, FP, and FN denote true positives, true negatives, false positives, and false negatives, respectively. This performance measure accounts for the class imbalance between silent and noisy samples and ranges from -1 to 1, indicating a perfect negative and perfect positive correlation between the true and the predicted labels, respectively. Due to its value range, the MCC is not usable directly as a loss function.

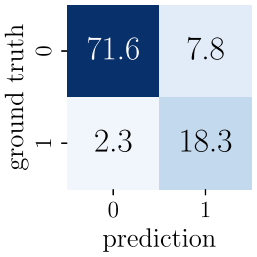

Fig. 6 Model training performance. The performance of the trained CNN, which is used for further computations, is illustrated by the confusion matrix on the test data set. The labels predicted by the CNN are shown against the ground-truth labels; values are given in % of the total number of samples in the test set. The model achieves a MCC = 0.73 ± 0.02 (accuracy of $90.6\,\% \pm 0.01$) for the test data set

The neural network model deployed for computation of the state map in the following achieves an MCC = 0.73 ± 0.02 (accuracy of $90.6\,\% \pm 0.01$) on the test data set. The confusion matrix obtained with the said model on the test data set is shown in Fig. 6, where the labels predicted by the CNN are plotted against the true labels. For better readability, the values are given in percent of the total number of samples in the test set.

2.4 Physics-consistent data augmentation

This work aims at generating a complete 2D state map that represents the system state over a space spanned by two chosen parameters to obtain a high measure of abstraction. The first step in the data augmentation process is thus the choice of an appropriate featurization of the data samples from a seven-dimensional time series into two parameters. This step is necessary to visualize the high-dimensional data set in a two-dimensional space. Here, the maximum rotational velocity $v_{\mathrm{rot,max}}$ and maximum brake pressure p_{max} per 4-s sample time series are chosen, which represent two characteristics of the macroscopic load conditions on the brake system. Any other measure of the samples, such as mean values, derivatives of the measurement time series, or values from the remaining measurement channels, for example, the temperatures, would be conceivable, as well as an extension to more than three dimensions. A purely measurement data-based state map results from this featurization. Figure 7 shows the result of the featurization of the test data set, illustrating that the

parameter space spanned by $v_{\mathrm{rot,max}}$ and p_{max} is only sparsely sampled by experimental data. Blue squares denote non-squealing samples, and red dots mark noisy samples.

To fill in the white spaces in this initial, very sparsely populated state map obtained from the measurement data, synthetic data samples are generated that fill up the 2D parameter space. The new data is fed into the machine learning model for state prediction. The additional data is generated from a base sample taken from experimental data, which is subjected to a physics-consistent data augmentation, as depicted in Fig. 7. To begin with, a base sample is chosen from the test data set of the processed experimental data, ensuring the neural network model predicted the system state for the base sample correctly during the model testing phase. The time-series values of this base sample are varied systematically by adding and subtracting constant values to the time series in the two featurized dimensions v_{rot} and p until the parameter space is filled up in a grid-like fashion. To remain consistent with the physics of the system, the brake torque M is varied along with the brake pressure p. All other parameters such as the friction coefficient μ, rotor temperature T_{rot}, ambient temperature T_{amb}, and relative ambient humidity H_{rel} are kept as in the original sample to ensure the state map represents the system stability over a variation of the chosen parameterization instead of other hidden variables.

The data augmentation process is performed carefully, with the laws of physics and information from the experimental data in mind. Nonetheless, there can be no guarantee that our newly generated data is physically meaningful, especially for points of the state map far away from the base sample. However, there are several points in favor of our data augmentation method being consistent, which we will be elaborated on in the following. First, the SAE-J2521 procedure is parameterized to contain repeating brakings with the same brake pressure and rotational velocity profiles, while systematically varying the overall pressure and velocity levels and the (initial) rotor temperature. The imposed temperature ramps are shown in Fig. 4. As a result, brakings with similar profiles but different value levels for each channel exist. Second, basic physical principles are accounted for in our data augmentation method since the brake torque is varied along with the brake pressure. The range of brake pressure and torque pressure is computed over the data set, and the torque is varied by the same relative amount as the pressure. The main physical effect underlying our data is therefore accounted for. Any secondary effects such as a greater rise in rotor temperature with a greater energy input due to a greater brake torque are negligible locally because the induced changes are small. There are data samples in our experimental data set that support this hypothesis, as shown in Fig. 8. Each subfigure shows two samples taken from our experimental data set. Figure 8a shows two samples with different rotational velocities, where all other measurement channels are very similar. Figure 8b shows two samples with different brake pressure, and, respectively, different brake torque, where all other channels remain similar. Figure 8c shows two samples for which both quantities are varied, but the remaining channels are similar. These three data samples illustrate that variations like the ones we are performing in our data augmentation process do in fact exist in our data set and that it is reasonable to believe that our approach is physically meaningful.

Nevertheless, it can be assumed that the augmented data is more meaningful closer to the base sample and that the resulting state map is more reliable the smaller the extent of the data augmentation. Improving the data augmentation process and including some measure of confidence in the final state maps are interesting and important points for further research.

A matrix of 100 by 100 augmented samples is generated using our data augmentation procedure, which densely fills up the parameter space spanned by the two chosen features maximum rotational velocity $v_{\mathrm{rot,max}}$ and maximum brake pressure p_{max}, as shown in Fig. 7. As the system state for these newly generated data samples is not known a priori, these are marked by gray dots. In theory, it is possible to choose an arbitrarily high number of samples to fill up the space arbitrarily densely; however, the computational cost involved has to be taken into consideration.

Finally, the trained CNN obtained in Sect. 2.3 is queried for the system state for each sample in the augmented data set. If the model has picked up the hidden underlying dynamic mechanisms correctly, it can predict the system state for these synthetically generated data samples, filling up the white spaces in the state map given by the experimental data alone. This way, a state map over the entire parameter space is generated, as illustrated in Fig. 2. The state map divides the parameter space into squealing and non-squealing sections according to the binary label defined in the initial pre-

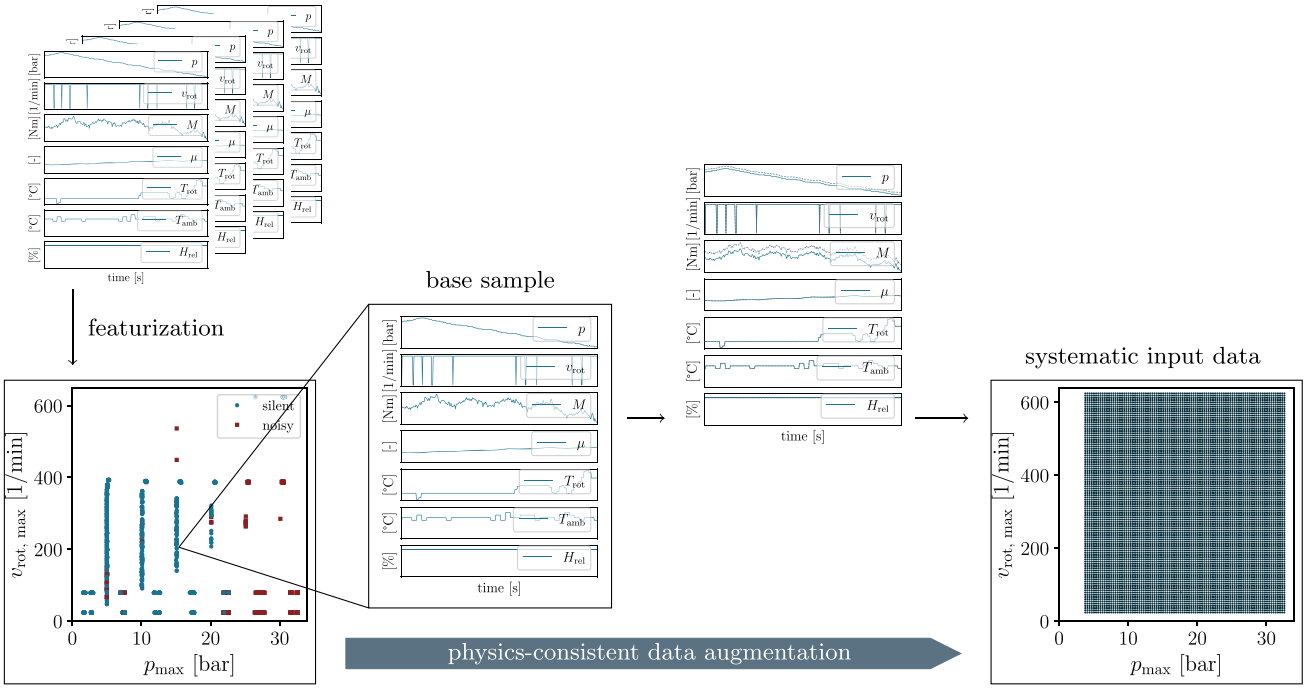

Fig. 7 Data augmentation. The physics-consistent data augmentation process forms the basis for the state map computation. First, a featurization of the full-scale data samples with two parameters is chosen. In this case, the maximum rotational velocity $v_{\mathrm{rot,max}}$ and maximum brake pressure $p_{\max}$ for a given 4-s sample. Plotting the system state in form of blue dots for non-squealing measurement samples and red squares for squealing samples over these two parameters yields a sparely sampled state map. To fill in the blank spaces, a systematic variation of the two parameters $v_{\mathrm{rot,max}}$ and $p_{\max}$ is performed from one base sample by adding constant values to the respective time series v_{rot} and p of the base sample. The other measurement channels are kept at their initial time series to separate out the two chosen parameters. However, to remain consistent with the physics of the system, the brake torque M is varied along with the brake pressure p. The result of the data augmentation process is a new, synthetic set of input data for which the system state is not yet known and thus illustrated by black dots in the right image

processing routine. Theoretically, it would be possible to validate the obtained results by comparing the predictions of the ML model for specific $v_{\mathrm{rot,max}}$ and $p_{\max}$ to the known system state for the same value range from the experimental data set. However, the results presented in the next section indicate that a proper validation requires the samples to match not only in terms of $v_{\mathrm{rot,max}}$ and $p_{\max}$, but also in terms of hidden variables, which makes finding appropriate samples hard if they even exist in the experimental database. Developing a sophisticated validation scheme is therefore left for future work. Exemplary results are shown in the following section.

The entire process from generating the augmented data set to obtaining the state map can be repeated for different base samples, generating as many state maps as there are samples in the measurement data. By averaging the binary system state overall computed state maps, a probability state map can be computed, which contains not only binary 0/1 labels but probability values between 0 and 1, which approximate the probability of the system state to be squealing for a given set of parameters, here $p_{\max}$ and $v_{\mathrm{rot,max}}$. This probability state map is also presented in the next section.

3 Results

As explained in the previous section, the content of the synthetically generated data set depends on the chosen base sample. From a given data set, it is thus possible to obtain as many state maps for a given system as there are different base samples available within this framework. It is found that the shape of the squealing/non-squealing areas within a binary state map depends heavily on the underlying base sample, as will be elaborated on in the following.

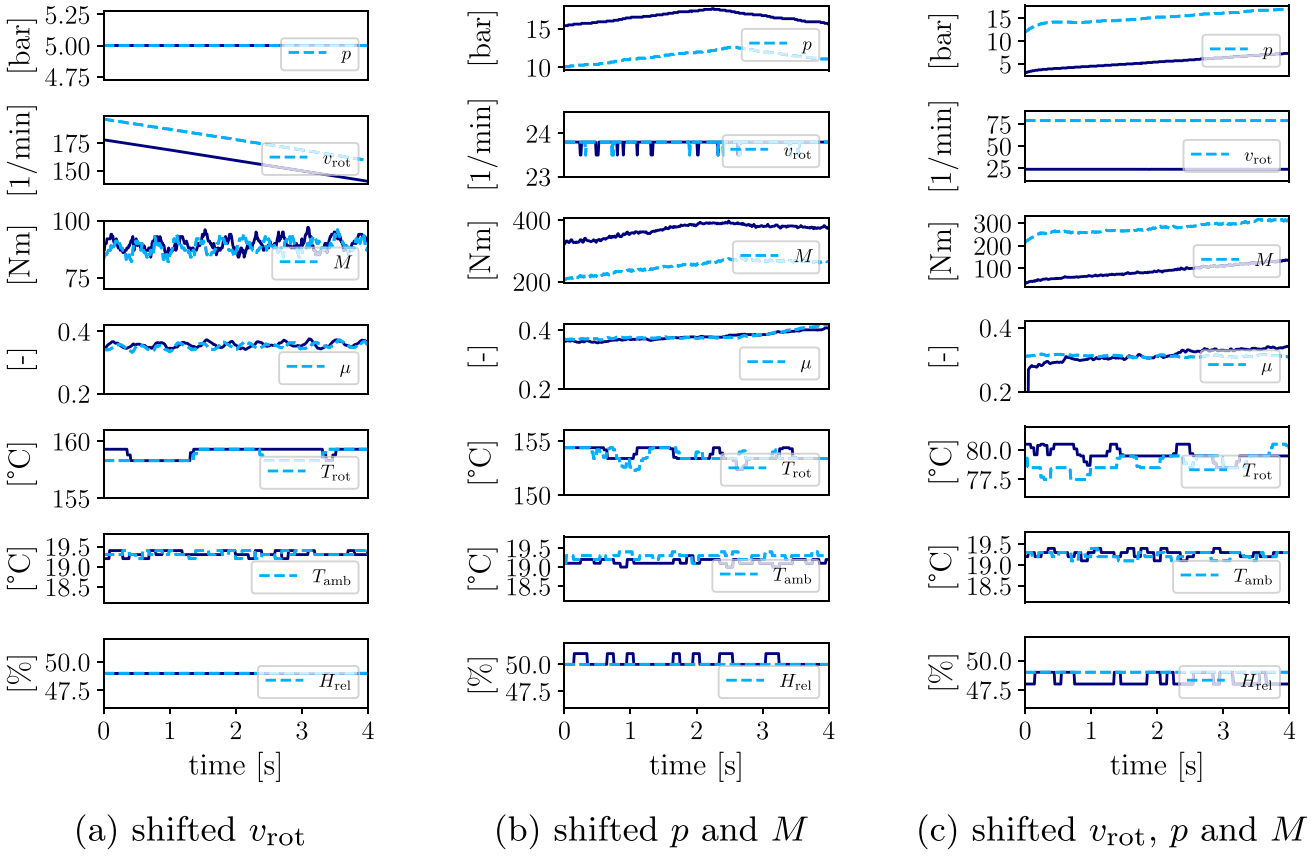

Fig. 8 Validation of the data augmentation procedure. Samples taken from the experimental data set underline the validity of the data augmentation method. In each subfigure, two experimental data samples are shown that differ only in 8a maximum rotational velocity $v_{\mathrm{rot,max}}$, 8b maximum brake pressure p_{max} and torque M_{max}, and 8c all of these dimensions, while the remaining variables are very similar

Figure 9 shows two state maps, 9a and 9b, which are generated from two base samples as indicated by black stars in each subfigure. At a first glance, the two base samples appear to be similar since they are located closely together on the state map with $p_{\mathrm{max},1} = 22.5\,\mathrm{bar}$, $p_{\mathrm{max},2} = 22.5\,\mathrm{bar}$, and $v_{\mathrm{rot,max},1} = 78.5\,\mathrm{l/min}$, $v_{\mathrm{rot,max},2} = 78.8\,\mathrm{l/min}$, and the system state for both given samples is non-squealing. However, the resulting state maps look different. While the first state map 9a shows only a small squealing area for high brake pressures and low rotational velocity, accompanied by another small squealing area around $p_{\mathrm{max}} = 15\,\mathrm{bar}$ and low rotational speed, the second one 9b not only connects these two areas but expands them to higher rotational velocities and a small, disconnected island of the squealing state appears at about $p_{\mathrm{max}} = 5\,\mathrm{bar}$ and $v_{\mathrm{rot,max}} = 100\,\mathrm{l/min}$. A closer look at the two base samples, see 9c, reveals that the qualitative dynamics of the system within the given 4-s intervals are different. While the brake pressure and brake torque decrease overall in sample one (illustrated by the dark blue line), these two parameters increase in total in the second sample (shown by the dashed light blue line), and the peaks of the respective channels, though reaching a similar maximum, are located at different times in each sample. Additionally, the gradients of both the friction coefficient and the disk temperature differ from one sample to the other. Considering the differences in the underlying hidden parameters in the two base samples, it is not surprising that the resulting state maps appear unalike. On the contrary, this observation indicates that the machine learning model has picked up some hidden variables and features in the training process and predicts the system state for a given sample based on a system understanding beyond a simple threshold on brake pressure and rotational velocity. Otherwise, the state maps would be the same for the same value range of p_{max} and $v_{\mathrm{rot,max}}$, independently

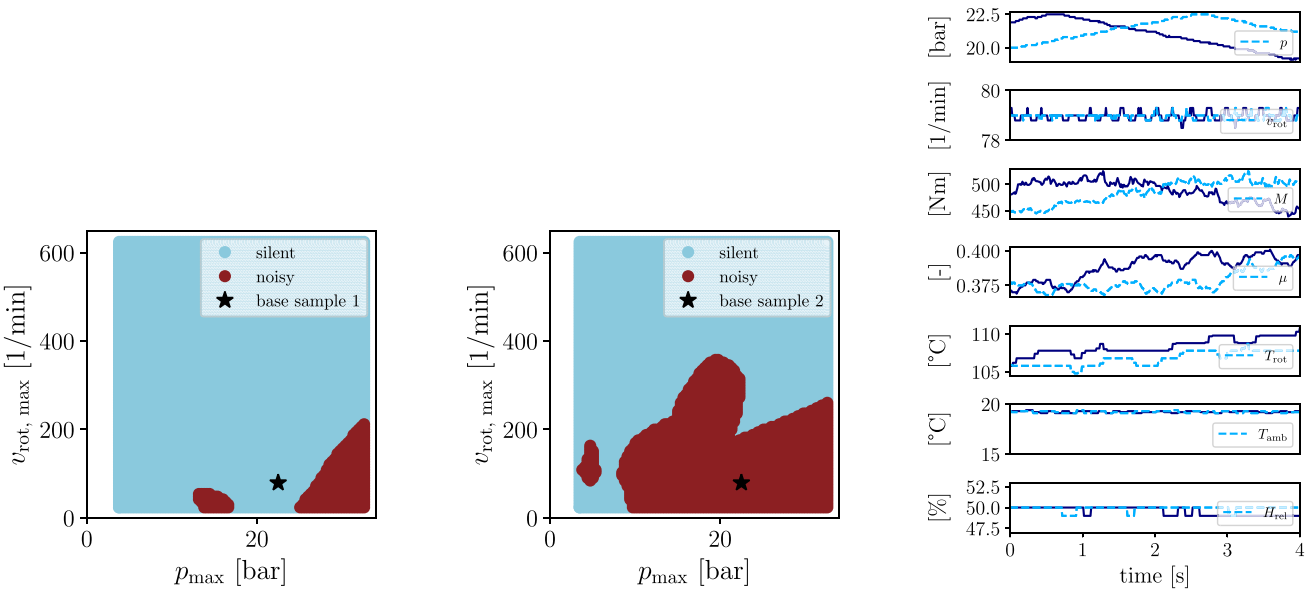

Fig. 9 State maps from base samples with similar $p_{\max}$ and $v_{\mathrm{rot,max}}$. Exemplary state maps (**a**) and **b** computed using two different base samples **c** in the data augmentation process. The location of the base sample in each state map is marked by a black star. Red areas indicate the system state as "squealing," while blue areas indicate a non-squealing state. The two state maps appear quite different, even though the base samples are located closely together in the $p_{\max}$ and $v_{\mathrm{rot,max}}$ parameter space. A closer look at the qualitatively very different dynamics between sample 1 (dark blue line) and sample 2 (light blue, dashed line) in (**c**) suggests that the neural network model has indeed picked up hidden mechanisms and predicts the system state based on a complex system understanding beyond a mere pressure and velocity threshold

of the remaining dynamics that may be prominent in the sample.

Following this reasoning, state maps generated with two similar base samples, namely samples that exhibit matching dynamics over time, should generate resembling state maps for our method to be consistent. Figure 10 shows that this is the case: The two base samples in 10c not only share almost identical maximum parameter values but also exhibit qualitatively very similar dynamics over all measurement channels, and the corresponding state maps in 10a and 10b match well. It can be concluded that our method yields congruent results, consistently exploiting hidden features from the input time series that are not directly accessible from the outside.

The results displayed in Figs. 9 and 10 illustrate that the state maps generated from different base samples with qualitatively different dynamics can be quite different. This distinctness is to be expected since it is well known that the appearance of brake squeal does not solely depend on a velocity or pressure threshold, but originates from a more intricate mechanism. It is reasonable to extend the concept of a binary state map to a probability state map, where the probability of the system operating in one state or the other for a given set of features is approximated within a value range from 0 to 1. As introduced in Sect. 2.4, such a probability state map can be obtained by computing a large set of binary state maps and averaging across the results. To obtain the probability state map shown in Fig. 11, $N = 1223$ binary state maps were calculated and combined. The resulting probability state map represents how likely it is that the dynamical system, here the friction brake, assumes one of the two states, non-squealing or squealing, for a given maximum brake pressure and maximum rotational velocity over a given time span. Since many different base samples with different hidden variables, such as other channels or derivative measures, underlie each binary state map, the individual state maps used to compute the probability state map may differ. In averaging over a large number of samples, the influence of the hidden parameters is smoothed out, and the prob-

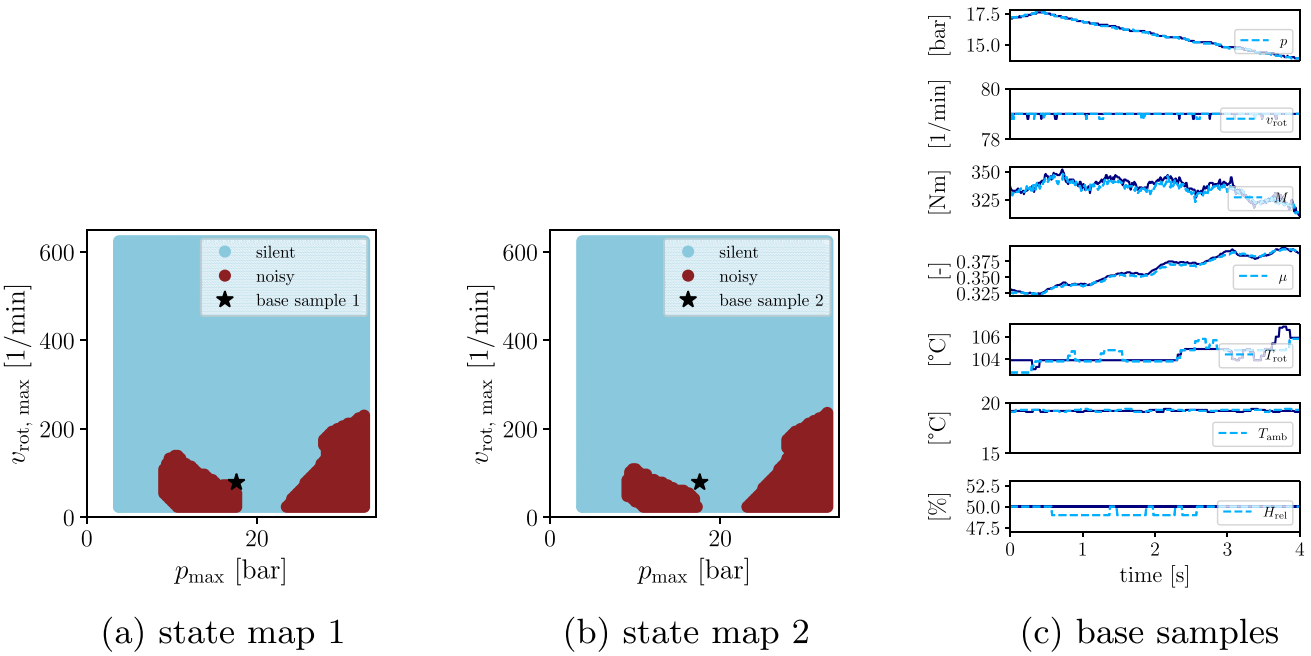

Fig. 10 State maps from base samples with similar p_{max} and $v_{\mathrm{rot,max}}$, and similar dynamics. For two base samples that not only match in terms of maximum values but also in terms of qualitative dynamic behavior (see (**c**)), the resulting state maps **a** and **b** appear very similar, illustrating the consistency of the method. State map 1 in **a** is generated based on sample one, shown by the dark blue line in (c), while state map 2 **b** is generated from sample 2, represented by the light blue dashed line in (**c**)

ability of different phenomena can be estimated. For example, it can be concluded from the probability state map in Fig. 11 that the island of the noisy state at low pressure and velocity visible in Fig. 9b rarely occurs for the given p_{max} and $v_{\mathrm{rot,max}}$ and its appearance is therefore highly dependent on the hidden variables.

4 Conclusion

A method for obtaining fine-grained maps representing the state of a dynamical system within a space spanned by operational conditions and high-dimensional parameters has been proposed in this work. Such a state map is difficult to obtain from numerical analysis or experimental data alone due to reasons including parameter uncertainties, numerical costs, and time consumption of experiments. Especially in the case of brake systems, where the system likely depends on small-scale parameter variations, existing measurements represent only sparse support in the parameter space. The presented method uses machine learning and physics-consistent data augmentation to generate state maps for the input samples in a time- and cost-efficient manner. By calculating many binary state maps using different base samples and averaging over them, probability state maps can be obtained

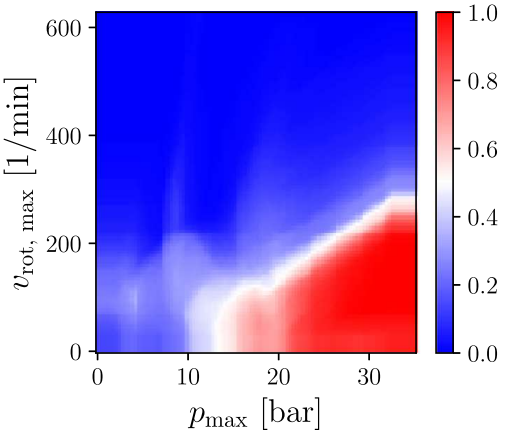

Fig. 11 Probability state map. A probability state map is obtained by computing binary stability maps for $N = 1223$ different basis samples and averaging over the results. The map thus encodes the probability of the brake system to operate in the squealing or non-squealing state, where 1 indicates a 100 % chance of operation in the squealing regime and 0 represents a 100 % chance of arriving in the non-squealing regime

that encode the probability of the dynamical system operating in one of two states. This way, only a limited number of real-world experiments are necessary to generate a full-scale and highly resolved state map. The method is shown to yield consistent results, exploiting the complex system representation picked up by a neural network during the training phase. The resulting state maps indicate the influence of the chosen parameters on the system state, while clearly illustrating that these are not the only relevant factors driving the system state. On the contrary, our results indicate that the chosen parameters, while providing an intuitive featurization for visualizing the data, cannot be taken as a single measure for reproducing the exact data labels. Testing different featurization or higher-dimensional state maps could yield additional insight into the driving mechanisms, which constitutes a starting point for future work.

Even nonlinear phenomena, such as multi-stability, become manageable through an appropriate choice of input data, i.e., by including the relevant initial conditions into the input data set. Choosing suitable parameters for the axes of the state map would make it possible to unfold even the hidden mechanisms driving the system through more than two states. The many interesting conceivable extensions to the proposed concept constitute additional possibilities for future work, including integrating a confidence interval into the computation of a probability state map such that the impact of each sample decreases radially around the initial feature values. An expansion of the method to higher-dimensional state maps by adding more parameters in the featurization is straightforward and might yield detailed insight into the mechanisms underlying dynamical regime changes.

This work hopes to contribute to a machine learning-driven system understanding beyond simple system representation and black-box modeling. As more and more real-world measurement data is available, data-based methods become increasingly valuable when it comes to analyzing dynamical systems. With a growing demand for sophisticated machines that can operate even under severe and changing environmental conditions, the need for a more detailed understanding of the underlying dynamics of a given system rises as well. The proposed method for data-driven state maps constitutes a significant step toward machine learning-based system understanding.

Author contributions CG and MS were involved in conceptualization, methodology, and writing—original draft preparation. SH and Thierry Chancelier were involved in data curation. CG was involved in formal analysis and investigation. CG, SH, TC, PD, and NH were involved in writing—review and editing. PD, NH, and MS were involved in funding acquisition. NH and MS were involved in supervision.

Funding Open Access funding enabled and organized by Projekt DEAL. This research was funded by the German Bundesministerium für Bildung und Forschung (BMBF) and the French Ministère de l'enseignement supérieur de la recherche et de l'innovation (MESR) within the project "Physics-informed artificial Intelligence for Cutting Brake Emissions from Electric Vehicles" (Pi-Cube). Merten Stender was supported by the German Research Foundation (Deutsche Forschungsgemeinschaft DFG) within the Priority Program 1897 "calm, smooth, smart," Grant Number 314996260.

Availability of data and materials The data sets generated and analyzed during the current study are available from the corresponding author upon reasonable request.

Declarations

Conflict of interest The authors have no competing interests to declare that are relevant to the content of this article.

Ethical approval Not applicable.

Consent to participate Not applicable.

Consent for publication Not applicable.

Code availability The code for reproducing the case studies can be made available upon reasonable request.

References

1. Strogatz, S.H.: Nonlinear Dynamics and Chaos: with Applications to Physics, Biology, Chemistry, and Engineering. Westview Press, Boulder (2015)
2. Stender, M., Di Bartolomeo, M., Massi, F., Hoffmann, N.: Revealing transitions in friction-excited vibrations by nonlinear time-series analysis. Nonlinear Dyn. **98**(4), 2613–2630 (2019). https://doi.org/10.1007/s11071-019-04987-7
3. Stender, M., Tiedemann, M., Spieler, D., Schoepflin, D., Hoffmann, N., Oberst, S.: Deep learning for brake squeal: Brake noise detection, characterization and prediction. Mech. Syst. Signal Process. **149**, 107181 (2021). https://doi.org/10.1016/j.ymssp.2020.107181
4. Kruse, S., Tiedemann, M., Zeumer, B., Reuss, P., Hetzler, H., Hoffmann, N.: The influence of joints on friction induced vibration in brake squeal. J. Sound Vib. **340**, 239–252 (2015). https://doi.org/10.1016/j.jsv.2014.11.016
5. Jahn, M., Stender, M., Tatzko, S., Hoffmann, N., Grolet, A., Wallaschek, J.: The extended periodic motion concept for fast limit cycle detection of self-excited systems. Comput. Struct. **227**, 106139 (2020). https://doi.org/10.1016/j.compstruc.2019.106139
6. Urbakh, M., Klafter, J., Gourdon, D., Israelachvili, J.: The nonlinear nature of friction. Nature **430**(6999), 525–528 (2004). https://doi.org/10.1038/nature02750
7. Butlin, T., Woodhouse, J.: Sensitivity of friction-induced vibration in idealised systems. J. Sound Vib. **319**(1), 182–198 (2009). https://doi.org/10.1016/j.jsv.2008.05.034
8. Fidlin, A.: Nonlinear Oscillations in Mechanical Engineering. Springer, Berlin (2005)
9. Ouyang, H., Nack, W., Yuan, Y., Chen, F.: Numerical analysis of automotive disc brake squeal: a review. Int. J. Veh. Noise Vib. **1**(3–4), 207–231 (2005). https://doi.org/10.1504/IJVNV.2005.007524
10. Sinou, J.-J.: Transient non-linear dynamic analysis of automotive disc brake squeal: on the need to consider both stability and non-linear analysis. Mech. Res. Commun. **37**(1), 96–105 (2010). https://doi.org/10.1016/j.mechrescom.2009.09.002
11. Denimal, E., Sinou, J.-J., Nacivet, S., Nechak, L.: Squeal analysis based on the effect and determination of the most influential contacts between the different components of an automotive brake system. Int. J. Mech. Sci. **151**, 192–213 (2019). https://doi.org/10.1016/j.ijmecsci.2018.10.054
12. Ouyang, H., Cao, Q., Mottershead, J., Treyde, T.: Vibration and squeal of a disc brake: modelling and experimental results. Proc. Inst. Mech. Eng. Part D J. Automob. Eng. **217**(10), 867–875 (2003)
13. Butlin, T., Woodhouse, J.: Friction-induced vibration: quantifying sensitivity and uncertainty. J. Sound Vib. **329**(5), 509–526 (2010). https://doi.org/10.1016/j.jsv.2009.09.026
14. Chevillot, F., Sinou, J.-J., Hardouin, N.: Nonlinear transient vibrations and coexistences of multi-instabilities induced by friction in an aircraft braking system. J. Sound Vib. **328**(4–5), 555–574 (2009)
15. Sinou, J.-J., Dereure, O., Mazet, G.-B., Thouverez, F., Jezequel, L.: Friction-induced vibration for an aircraft brake system-part 1: experimental approach and stability analysis. Int. J. Mech. Sci. **48**(5), 536–554 (2006)
16. Denimal, E., Sinou, J.-J., Nacivet, S.: Influence of structural modifications of automotive brake systems for squeal events with kriging meta-modelling method. J. Sound Vib. **463**, 114938 (2019). https://doi.org/10.1016/j.jsv.2019.114938
17. Coudeyras, N., Nacivet, S., Sinou, J.-J.: Periodic and quasi-periodic solutions for multi-instabilities involved in brake squeal. J. Sound Vib. **328**(4–5), 520–540 (2009). https://doi.org/10.1016/j.jsv.2009.08.017
18. Kinkaid, N.M., O'Reilly, O.M., Papadopoulos, P.: Automotive disc brake squeal. J. Sound Vib. **267**(1), 105–166 (2003). https://doi.org/10.1016/S0022-460X(02)01573-0
19. Butlin, T., Woodhouse, J.: Sensitivity studies of friction-induced vibration. Int. J. Veh. Des. **51**(1/2), 238–257 (2009)
20. Sinou, J.-J., Thouverez, F., Jezequel, L., Dereure, O., Mazet, G.-B.: Friction induced vibration for an aircraft brake system-part 2: non-linear dynamics. Int. J. Mech. Sci. **48**(5), 555–567 (2006)
21. Ouyang, H., Mottershead, J., Li, W.: A moving-load model for disc-brake stability analysis. J. Vib. Acoust. **125**(1), 53–58 (2003). https://doi.org/10.1115/1.1521954
22. Brunton, S., Kutz, J.: Data-Driven Science and Engineering: Machine Learning, Dynamical Systems, and Control. Cambridge University Press, Cambridge (2019). https://doi.org/10.1017/9781108380690
23. LeCun, Y., Bengio, Y., Hinton, G.: Deep learning. Nature **521**, 436–444 (2015). https://doi.org/10.1038/nature14539
24. Stender, M., Oberst, S., Tiedemann, M., Hoffmann, N.: Complex machine dynamics: systematic recurrence quantification analysis of disk brake vibration data. Nonlinear Dyn. **97**(4), 2483–2497 (2019). https://doi.org/10.1007/s11071-019-05143-x
25. SAE International: Disc and Drum Brake Dynamometer Squeal Noise Test Procedure J2521. https://www.sae.org/standards/content/j2521_202210/
26. Matthews, B.W.: Comparison of the predicted and observed secondary structure of t4 phage lysozyme. Biochimica et Biophysica Acta (BBA) - Prot. Struct. **405**(2), 442–451 (1975). https://doi.org/10.1016/0005-2795(75)90109-9

4 Network perspectives

Network science is an interdisciplinary field concerned with the study of systems described by nodes (vertices) and edges (links) [158]. While nodes might represent an individual entity, such as a part in a machine, a human in a social network, or a species in a food web, the edges encode the relationships between them, for example, via friction or gears, human contact, or predator-prey relationships. Due of its focus on component interrelations, network science is sometimes referred to as the *study of interactions* [9]. The field offers a novel perspective on the nonlinear dynamics of mechanical structures, complementing traditional physics-based methods such as those described in Section 2.2 and the machine learning techniques detailed in Chapter 3, thus investigating the dynamic properties of mechanical systems such as those illustrated in Section 2.1 from a new angle. For example, network-based methods offer new model order reduction techniques for managing high-order systems, provide phenomenon-focused procedures for handling nonlinearities and dynamical transitions in time series data, and propose different, high-level descriptions of joint dynamics by inferring interactions directly from data.

The study of real-world systems in network form dates back to Euler's treatment of the Königsberg Bridge Problem in 1736 [159], where bridges were defined as the edges of a network, connecting different city parts. Network science became popular in the 1950s, with Kruskal's algorithm [160] for finding the shortest spanning tree in a network to minimize the summed length of a power grid, Dijkstra's algorithm for shortest path finding, and the introduction of the theory of random graphs [161, 162]. Many fundamental questions have been studied using network science, such as whether a higher-dimensional system is more or less likely to be stable than a smaller one [163, 164] or the idea of small world graphs [165], which relate to the famous six degrees of separation theorem and graph growth via preferential attachment [166]. The investigation of the structure and dynamics of complex networks has emerged as an alternative approach to describing multiple complex systems from a statistical mechanics perspective [166, 167]. In the last two decades, network methods have also been employed for time series analysis [168]. Network science is a field closely related to the study of complex systems, and is thus popular across many fields [9, 18, 158, 166, 168–173] to study patterns that arise from the interplay of many interacting parts. Applications include social networks [15, 173–175], financial data [176, 177], biological networks [178–180], for example, fish swarms [181], bird flocks [182], food webs [9, 183], or the brain [9, 184–188], metabolic networks [189], gene regulatory networks [190–192], the genome [178] or human language [193], geophysical or climate networks [10–12, 167, 194–200], and fluid dynamics [201–207]. Applications related to engineering include the internet [9], power grids [208–212], or transportation networks [213], for example, natural gas pipelines [214].

Network science provides a range of perspectives on a real-world system, which can be split into three main groups. Figure 4.1 provides a schematic of the different methods. Depending on the approach taken, network nodes can encode, for example, a system state or a component, while the edges can, for example, represent the temporal ordering of states or interactions between the components.

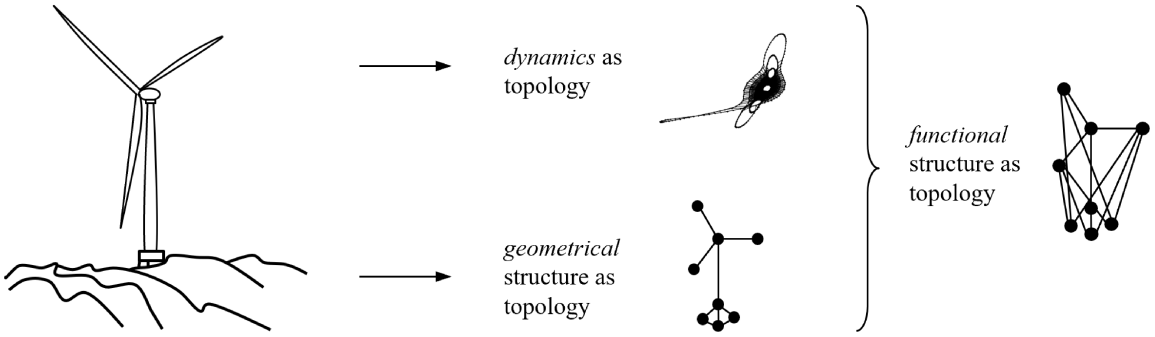

FIGURE 4.1: Diverse network perspectives on structural dynamics. The transformation of dynamic time series data into network topology allows the network structure to reflect the system's inherent dynamics. In this approach, each node corresponds to a measurement point in time, with connections established based on proximity or visibility measures. Alternatively, the geometrical structure can be interpreted as network topology, where nodes represent components and links denote physical connections. The third perspective integrates both approaches by using nodes as components connected according to their dynamic relationships, forming what is referred to as a "functional network."

One perspective is a dynamics-driven one, which translates dynamics in the form of time series into topology in the form of a network. In this setting, each network node is associated with a system state or a measurement point in time, and nodes are connected via proximity measures such as recurrence or mutual visibility/time series convexity or via temporal ordering. This approach is mainly used in the analysis of one-dimensional time series data and could be interpreted as a translation from a dynamical to a topological perspective. Section 4.1 gives an overview of different popular methods and showcases the application to time series from mechanical model systems. The second perspective, perhaps more intuitive, directs the focus onto geometrical aspects of the system. Each node represents a bounded element of a higher-dimensional system, such as a machine component, a neuron in a brain, or a species in a food web. In this case, an edge corresponds to a connection between two parts, for example, a physical connection, an information exchange, or a predator-prey relationship. These networks can be analyzed as static topologies or dynamical systems, where temporal dynamics are associated with nodes and edges. This view provides insight into the structural ordering of a system based on its geometric connectivity. While still clearly distinguishing between physical connections and dynamical properties, dynamical networks can capture the interplay between network topology and dynamics. Section 4.2 provides an overview of structural and dynamical networks, along with possible applications to mechanical structures. A third perspective is developed in Publication III, combining the two previous approaches. While each node is associated with a system component, the connections are inferred based on the functional relationships encoded in time series data instead of the geometrical connectivity, thus encoding dynamic relationships beyond purely geometrical proximity. Section 4.3 provides the background for the studies presented in

Publication III and adds more in-depth studies of the nonlinear dynamics of mechanical structures. Section 4.3 concludes with a discussion and an outlook on further research directions.

4.1 Networks for time series analysis

In network-based time series analysis, time series data is translated into network topology. To do so, a node is associated with a system state or section of a time series. The edges are inferred using proximity measures, mutual visibility criteria, or temporal succession. The networks resulting from the transformation of time series data have been shown to keep properties relating to the underlying dynamical system [182] and can thus provide information on the system complementing the insights gained through classical time series analysis [215]. For example, network-based approaches have been applied in paleoclimatology, where these methods are particularly advantageous for handling datasets that feature non-uniform sampling or uncertainties in age determination [194]. Network methods have been used to distinguish different dynamical patterns, differentiating stochastic from chaotic dynamics [216] and identifying deviations from the healthy state in medical data, aiding in diagnosing cardiovascular diseases [217, 218], and in the analysis of EEG [219–222] and ECG data [223, 224]. These approaches have also been employed to explore bifurcation scenarios in two-phase water-air flows [225], to distinguish various flow patterns in gas-liquid two-phase flow scenarios [226, 227], to investigate climate transitions [228], detect change points in oscillator dynamics [229], and assess time-reversal symmetry [230–232].

Zou et al. in [168] cluster the diverse methods for network-based time series analysis into three categories, namely proximity networks, visibility graphs, and transition networks. *Proximity networks* use the proximity of observations in an embedding space. *Visibility graphs* connect nodes based on the convexity of time series segments, in other words, the mutual visibility of nodes. *Transition networks* form links based on temporal succession. Each of these approaches results in a distinct network topology, allowing the study of different phenomena. Figure 4.2 illustrates the diverse methods and the resulting networks for qualitatively different time series. Four exemplary input time series, a periodic motion with $x_1 = \sin(\pi t)$ (S1), a damped trajectory with $x_2 = \sin(5t) \cdot e^{(-0.5t)}$ (S2), two sinusoids with $x_3 = \sin(5t) + 0.3\sin(15t)$ (S3), and the x-coordinate of a Lorenz 96 system in a chaotic parameter setting (S4), are shown on the left. All time series are sampled with a frequency of $dt = 0.02$ in the interval $t = [0, 10]$. The right-hand side presents networks generated from the four time series with three different methods, namely a proximity network (N1), a natural visibility graph (N2), and an ordinal partition network (N3). An in-depth review of various network approaches to nonlinear time series analysis can be found in [168], an overview is given in the following paragraphs.

Recurrence networks [172, 194, 234–236] were developed from cycle networks [237–239] and correlation networks [240] and are the principal representative of proximity networks today. To infer the network structure, a recurrence plot [20, 79, 80, 241, 242] is computed from the time series data, and the resulting recurrence matrix is interpreted as the adjacency

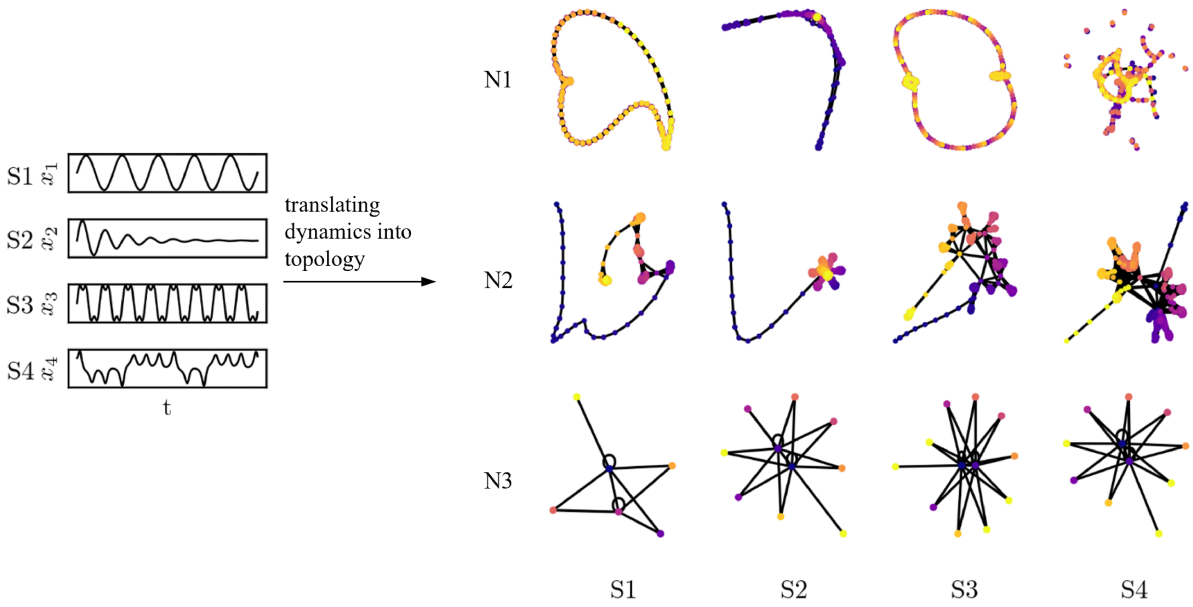

FIGURE 4.2: Different translations of dynamics into network structure. The dynamics of four different time series shown on the left, S1, S2, S3, and S4, are translated into network topology via three approaches N1, N2, and N3. The resulting networks are shown on the right, with color encoding of the temporal succession of nodes in the related time series from purple (start) to yellow (end), after a representation chosen in [233]. S1: periodic motion with $x_1 = \sin(\pi t)$, S2: damped trajectory with $x_2 = \sin(5t) \cdot e^{(-0.5t)}$, S3: two superposed sinusoids with $x_3 = \sin(5t) + 0.3\sin(15t)$, and S4 is defined as the x-coordinate of a Lorenz 96 system in a chaotic parameter setting. For all time series, the time interval is defined as $t = [0, 10]$ with steps of $dt = 0.02$. N1: proximity network, more precisely, an ε-recurrence network with threshold $\varepsilon = 0.1$ and time delay embedding with embedding dimension $dim = 3$ and embedding delay $\tau = 2$. N2: natural visibility graph. N3: Ordinal partition network with window size $w = 4$.

matrix of a network in which each node is a system state. Variants of the method use different thresholds for the proximity computation, such as k-nearest neighbors [172, 182, 235], adaptive nearest neighbors [172, 243], or ε-recurrence networks [172, 182, 194, 235, 244], where the neighborhood mass, number of edges or neighborhood volume are fixed, respectively [168]. Figure 4.2 shows the ε-recurrence networks obtained from four exemplary time series in the top row (N1). Each qualitatively different time series yields a distinct network topology. The periodic time series S1 is transformed to a circular shape, with each period closing one loop. The damped trajectory S2 results in a network closely connected in its center, where the later nodes from oscillation with smaller amplitudes are clustered. The two-period motion S3 translates to a circular shape with two additional embedded loops at opposite sides. Lastly, the chaotic oscillation S4 results in a network that is not entirely connected, consisting of an irregular shape and unconnected nodes. These examples illustrate that qualitatively different dynamics can yield very different network topologies while still relating to the underlying dynamical system. For instance, the networks for S1 and S3 closely resemble the phase space representation of the corresponding time series. Consequently, analysis of the recurrence-based network has been shown to allow for the

classification of qualitatively different types of dynamics in terms of measures of complexity [194, 235] and via motif analysis [245], and, therefore, facilitates the study of regime shifts in dynamics and dynamical transitions [194, 198, 246, 247]. Bifurcations can be detected via a sliding window approach, which is required because the network itself loses the temporal ordering of the nodes. Measures from the recurrence-based network have also been shown to relate to dynamical invariants, for example, unstable periodic orbits [235, 237, 238] and structural characteristics of the underlying attractor's geometry in phase space [235]. These network measures also facilitate the estimation of the largest Lyapunov exponent of the underlying system [235]. The recurrence-based approach does not require regular sampling of the time series data [172]. The method necessitates fixing a threshold ε for the recurrence, defining the upper limit to the neighborhood [243, 248], and an embedding dimension dim and the embedding delay τ. Since only a single time series is used in the analysis, its quality suffers under limited observability of time series, in other words, when said time series does not convey sufficient information on the underlying system [249]. However, the method is quite robust to noise when the observability is good [249].

Visibility graphs were introduced by Lacasa et al. in [250] for the analysis of structure in scalar, uni-variate time series inspired by the analysis of two-dimensional landscapes [168, 251]. Nodes represent states that are connected by mutual visibility over the convexity of the time series segment in between them. Variants include horizontal visibility graphs [252], which restrict visibility to states that can be seen in a horizontal direction, limited penetrable visibility graphs [253], which facilitate more noise robustness by allowing the view through some states, or parametric visibility graphs [254], which limit visibility by a specific angle. The visibility graph approach has become popular [167] due to its simplicity and lack of hyper-parameters. Figure 4.2 presents four natural visibility graphs (N2). The structure of a visibility graph is distinctly different from that of a recurrence network. Each cycle, or convex section of a time series, becomes a node cluster. Maxima in the time series become hubs in the network while separating the different clusters from each other. Visibility graphs are inherently connected networks since each node can at least "see" its neighbors. Long tails in the network result from the start and end section of the time series, which often has inherently lower visibility compared to the remainder of the structure. In the original setup of the algorithm, the graph inherits structure from the time series, but temporal information is lost. The method is thus predestined for studying structural information within the time series, as periodic time series form regular graphs, random time series form random graphs, and fractal time series form scale-free networks [250]. The method has been used to distinguish stochastic and deterministic dynamics [252], classify different types of chaos [252, 255], analyze stochastic or fractal properties of a time series as well as properties on micro- and macro states [177, 256, 257], and perform motif analysis. A slight variation that includes temporal information in the graph has been employed to test for time series irreversibility to identify nonlinear phenomena in a time series [231, 232]. In this context, variants of visibility graphs have been used to study geophysical time series [167], seismic activity [199], asymmetry of solar activity [200], and finance [258]. In the context of mechanical vibrations, small mechanical model systems in the form of Duffing oscillators in different parametric configurations have been studied using visibility graphs and horizontal visibility graphs [233]. The study indicates that while

the approach cannot be used to identify model properties directly, it may well be of use to study qualitative differences between time series, as network measures of the underlying graph can be used to distinguish different qualitative dynamics.

Transition networks translate network dynamics from a time series domain into a coarse-grained state-based domain, where nodes are connected based on temporal succession. The approaches can be divided into two subgroups: In an ordinal partition network [259], a node is defined as an ordinal partition of a time series sample, while threshold-based networks [159, 260, 261] divide the phase space into different sections, each of which becomes a node in the network. The transition network encodes transition probabilities between different system states [259]. In the process of generating the network, the two parameters "time delay" and "sample size" have to be chosen [259]. The network topology is highly sensitive to the chosen coarse-graining [172], indicating that the choice of these parameters could be related to the scale of the dynamics that will be observable. At the same time, a coarse-graining might make the method robust to noise [262]. The bottom row (N3) in Figure 4.2 shows four ordinal partition networks obtained with a sample or window size $w = 4$ and non-overlapping windows. The primary distinction between the ordinal partition networks and the networks from the preceding two methods is the significantly lower number of nodes in the ordinal partition network. The number of nodes results from the partitioning, with the upper limit $w! = 4! = 24$ due to the number of possible orderings of measurement points within a sample. The network from periodic data has the lowest number of nodes, corresponding to the lowest number of different ordinal symbols in the time series. Interestingly, the remaining networks exhibit similar structures with comparable numbers of nodes. The transition network approach can classify qualitatively different dynamics [260, 261], for example, in electrocardiogram data [223, 261] or biomedical signal processing [263]. Due to the direct encoding of time dependency, it can also help track transitions in the system behavior similar to the largest Lyapunov exponent and track bifurcations [229, 264].

While all three methods translate dynamics into network topology and encode some information on the underlying dynamics [259, 263], there are some significant differences. Of the proposed approaches, transition networks are the only ones that inherently keep time information and thus encode a sense of causality [172]. Proximity networks seem best suited to study attractor topology [229]. The inverse problem of obtaining time series from networks in the sense of classical model validation is not straightforward and a lot less studied. A random walk over a network produces a time series with similar statistical properties as the original one [182, 224]. A fully reversible, transition-based approach is proposed in [260] and [159].

Even though the descriptions in this section refer to one-dimensional time series, extensions to multivariate time series data evolve naturally by assigning vector-valued states to the individual nodes. Examples include multivariate recurrence networks [265], cross recurrence [197, 202, 206, 207], joint recurrence [266–268], and multivariate transition networks [269, 270]. In some cases, the multivariate expansion of the algorithm involves computing individual networks from each time series and connecting these networks [195], resulting in so-called multiplex networks, for example, multiplex recurrence networks [196] and multiplex visibility graphs [176, 271]. These multivariate networks have been used to study

dynamical phenomena of the system, such as synchronization [265, 266], regime changes [176, 196], and dynamical transitions [202, 207]. Other applications include coupling direction detection [197] and the distinction of direct and indirect interactions [267, 268]. Interestingly, the multi-dimensional visibility graph has also been employed for image classification [271].

4.2 Structure and dynamics in and on networks

In contrast to the methods proposed in the previous section, a second family of network models associates a node with a system component or a bounded subsystem, sometimes called agent-based models [18]. Edges encode some form of connectedness or information flow between the components. Figure 4.1 illustrates the idea of such a network using the example of an offshore wind turbine. Other examples of such a network are a snapshot of the internet at a given instant, with the nodes representing websites and the edges corresponding to links between them or species in a food web as nodes, and predator-prey relationships as the links.

In a *static network* representation such as the example of a snapshot of the internet, the structure is defined as fixed. Network analysis can provide insights into structural properties by studying the adjacency matrix $\mathbf{A}$ and answering questions like "Which is the most important node?" or "How does the structure change if a certain fraction of nodes or links are removed?" [158]. In many large real-world systems, analyzing random network models provides an acceptable initial guess for structural properties and statistical properties such as mean degree, mean excess degree, or the formation of a giant component [158]. These properties give insights into the structure of the underlying system, its vulnerability to specific attacks, and how information could spread across such a network. Interestingly, the edges of many real-world networks do not have a physical presence. For example, edges representing website links or human interactions do not fill up physical space and are therefore not mutually exclusive, as would be the connections of machine parts, where there might be limited physical space. The study of network structure in physical space is a relatively novel research area [272].

The static structural view of node connectivity described by the adjacency matrix $\mathbf{A}$ can be expanded to *dynamics on networks*, where nodes and edges have their own dynamics [173]. Examples include the food web and susceptible-infected-recovered models that study how a disease spreads through a population. Dynamics on network modeling assumes the network structure or topology to either remain fixed or the change to occur in time scales orders of magnitude slower than the dynamics of the nodes and edges. There are also examples of networks where the structure changes in time scales comparable to the nodal dynamics. One example of this type of network is an infection network, where individuals avoid contact with infected individuals and edges break. These models are called *dynamics of networks* or *adaptive networks* [173]. Dynamical network models have been used to study emergent phenomena such as synchronization in oscillator networks [44, 209, 273–279], and stability properties [208, 280].

From a network perspective, the dynamics of a single node or component i can be described as

$$\alpha\ddot{x}_i + \beta\dot{x}_i = f_{\text{int},i}(x_i) + \sum_j^N A_{ij} f_{\text{c}}(x_i, x_j) + f_{\text{ex},i}(t), \tag{4.1}$$

where the symbolic encoding is mostly the same as in Equation 2.2. The acceleration, velocity and displacement of the i-th component are given by $\ddot{x}_i, \dot{x}_i, x_i$ and $f_{\text{ex},i}(t)$ defines the external excitation. The displacement of an adjacent node j is described by x_j. The spring forces and nonlinearities $k_{\text{l}}x_i$ and $f_{\text{nl}}(x_i)$ from Equation 2.2 are combined to the node's internal dynamics $f_{\text{int},i}(x_i)$. The coupling terms $k_{\text{c}} \cdot (x_{i-1} + x_{i+1} - 2x_i)$ from Equation 2.2 are translated to the more general formulation $\sum_j^N A_{ij} f_{\text{c}}(x_i, x_j)$ with adjacency matrix $\mathbf{A}$ and coupling function $f_{\text{c}}(x_i, x_j) = k_{\text{c}}(x_j - x_i)$. α and β provide factors equivalent to mass m and damping d in Equation 2.2. Equation 4.1 represents a re-structuring of Equation 2.2, where the dynamics are split into node internal dynamics $f_{\text{int},i}(x_i)$, structural interactions $\sum_j^N A_{ij} f_{\text{c}}(x_i, x_j)$ and external excitation $f_{\text{ex},i}(t)$, instead of the structuring inertia-damping-stiffness-nonlinearities-excitation that is the common view in mechanical dynamics.

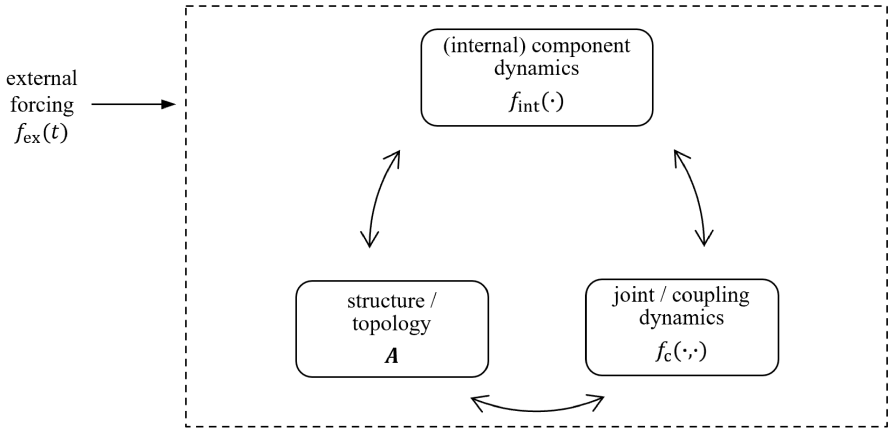

FIGURE 4.3: Four elements of structural dynamics from a network perspective. Component or internal dynamics $f_{\text{int}}(\cdot)$, structure or network topology $\mathbf{A}$, and joints described by interaction or coupling mechanisms $f_{\text{c}}(\cdot,\cdot)$ interact and might mutually influence each other. The external excitation $f_{\text{ex}}(t)$ represents control inputs and environmental factors. The overall dynamics emerge from the combination of all elements.

This new structuring offers a new, interaction-centered perspective on the dynamics of mechanical structures, illustrated in Figure 4.3. The view splits the contributions to machine dynamics into four elements: the individual part with its individual dynamics $f_{\text{int}}(\cdot)$, the structure or network topology $\mathbf{A}$, the joints described by interaction or coupling mechanisms $f_{\text{c}}(\cdot,\cdot)$, and the external excitation $f_{\text{ex}}(t)$. In this distinction, each machine component forms an individual part with its own internal dynamics. The structure defines *where* these parts are connected with each other. These connections, for example, via welts, bolts, or gears in the spatial structure of a machine, can generally be assumed as known. The interaction mechanisms describe *how* the individual parts interact with each other. The coupling between components plays an essential role in shaping the response of a system [281]. Structure, internal dynamics, and coupling dynamics mutually influence each other.

For example, the structure might limit the freedom of motion of a component, restricting its dynamics. The dynamics of a component can influence the coupling dynamics, for instance, by exciting specific dynamics within the joint. The coupling dynamics can impact the network structure, for example, if there is some slack in a connection, closing the gap may create an additional connection in the network. All these elements combined give rise to the entire network, and in this case machine, dynamics.

Agent-based network models enable the analysis of the interplay of the network structure and overall dynamics [275]. For example, [210, 211, 282] present a detailed study of system steady states in a power grid at different levels of excitation frequencies, resulting in patterns similar to eigenmodes. It has been shown that the function of a system depends strongly on the network topology [275]. At the same time, the same network topology can exhibit entirely different information flow patterns, depending on the nodal dynamics and the interaction mechanisms [283, 284], illustrating that the dynamics of the entire system are likely dependent on both dynamics and structure.

4.3 Functional networks for nonlinear mechanical vibrations

So far, the underlying network structure was assumed to be known. In the case of a snapshot of the internet, this assumption might well hold true since all link connections can be captured in measurement data. Many sciences do not have access to a direct physical network description, for example, of all connections in the brain or the intricate mechanisms in climate science. These fields rely on inferring the network structure from data. The methods of inference differ between sciences, depending on the available information. Common approaches include mutual information criteria [195], correlation measures [12, 188, 285, 286], coherence [287], and reduced auto-regressive models [288]. Despite numerous structure-inferring methods, detecting the direction of coupling between two signals remains challenging [197, 289]. Cross-recurrence methods have been proposed to resolve this issue [197].

In the application to mechanical structures, the network topology could be assumed to be known since the geometric location and connections of the machine parts seem evident, as proposed in Section 4.2. However, describing interaction mechanisms within joints is notoriously difficult (see Section 2.1), and geometric proximity does not necessarily entail close functional relationships. It has also been shown that the global system dynamics result from the structure as well as from the interaction mechanisms and nodal dynamics [283, 284]. Motivated by these considerations, a functional network approach is introduced in Publication III. The functional networks perspective combines the two previous network-based views. As in the structure-based view presented in Section 4.2, the nodes in a functional network are defined by individual system parts or machine components. Instead of using geometrical coupling to define the network connectivity, the function-based approach infers edges from time series data, related to methods presented in Section 4.1. These edges represent functional, dynamics-based rather than structural relationships between the components. This approach combines cross-recurrence-based networks, structural network analysis, and

network-based model order reduction to provide insights into the dynamic interplay of a system of oscillators, which can be used to detect localized vibrations.

The distinction between physical structure and functional interrelations is present across many disciplines [290, 291]. In neuroscience, the difference between structural (anatomical connections) and functional (resulting dynamics) connectivity is a central research point [184–186], focusing on the differences between network topology and its functional organization [247, 292, 293]. Along a similar line, the synchronization of physiological signals between a client and their caregiver is studied in [289]. Functional networks have also been employed to detect new genes and their interconnections in gene expression networks [180] and in climate science [10, 11, 294], for example, to study the relationships between the two principal branches of the Asian summer monsoon [197, 295]. In [170], the authors propose that distinguishing structural from functional connectivity is the first step to understanding emergent behavior across the disciplines.

Summary of the study
Publication III introduces a recurrence-based approach to inferring a functional network structure from time series data. The method is presented along the example of a system of coupled nonlinear Duffing oscillators. First, each oscillator becomes a node of a network. The connections within the network are inferred pairwise from oscillatory time series data obtained from the respective oscillators, following an approach proposed in [197]. The two time series are embedded in a high-dimensional cross-recurrence space, and through specific network-related measures, the coupling direction between the two components can be ascertained. The final full-sized functional network is condensed into a smaller, representative network to generate a reduced-order model. The details of the procedure are explained in Publication III. The results in Publication III indicate that the functional network picks up the symmetry within the system dynamics. Each node in the condensed network corresponds to a cluster of dynamically similar states. The edges between the nodes illustrate the relationships between the clusters, encoding the global system state. Through a sliding window approach, where small time series segments are analyzed consecutively, the propagation of a disturbance of a disturbance through the dynamical system can be tracked, revealing the interplay of components during the perturbation spreading.

Further, in-depth work
Functional networks can be employed to detect imminent localized vibrations in systems of nonlinear coupled oscillators. Localized vibrations, the high-amplitude oscillations of one machine part or a small subset of components, are potentially dangerous to the mechanical structure since vibration-induced strain might lead to component failure, see Section 2.1. This phenomenon is often challenging to predict as its occurrence depends on small parameter variations that are difficult to track during machine operation. A purely data-driven, network-based approach has the potential to enable tracking of localized vibrations during operation. The following findings are part of a publication [296], available as a preprint.
The procedure for network-based localization detection is depicted in Figure 4.4. A model system of ten forced, nonlinear oscillators with nearest-neighbor coupling is studied. As the system's symmetry is broken through the decrease of the mass m_4 of one of the oscillators, a localized vibration appears, shown in the top four panels on the right-hand side of

Figure 4.4. While the oscillations of the homogeneous system (far right) are homogeneous, the localized vibration starts to form at $m_4 = 0.903$, when its appearance depends on the initial conditions (middle panels). For m_4, the localized vibration forms independent of the initial conditions within the chosen set (left panel). By computing functional networks from overlapping ten-second samples of the time series, the co-evolution of the network with the dynamics can be tracked. The computation is performed for 100 different initial conditions for each parameter value to account for the effect of uncertain initial conditions. The resulting functional networks are analyzed for their nodal in-degree $z_{\text{in},i}$, which describes the number of links that enter each node, and the formation of strongly connected components (SCC) [297, 298] within the network. The results are presented in the bottom three panels on the right-hand side of Figure 4.4. The mean and standard deviation of the nodal in-degree $z_{\text{in},i}$ are shown, illustrating how the in-degree of the node corresponding to the localizing mass $z_{\text{in},i}$ drops even before the localized vibration is clearly discernible in the time series data. At the same time, the SCC within the functional network are tracked in the panel below, with exemplary networks shown at the bottom. The functional network splits from a single node representing the homogeneous network into several parts as the localized vibration forms, illustrating the decomposition of the system into dynamically separate units. The method seems robust against noise, small parameter uncertainties, and different time series lengths [296].

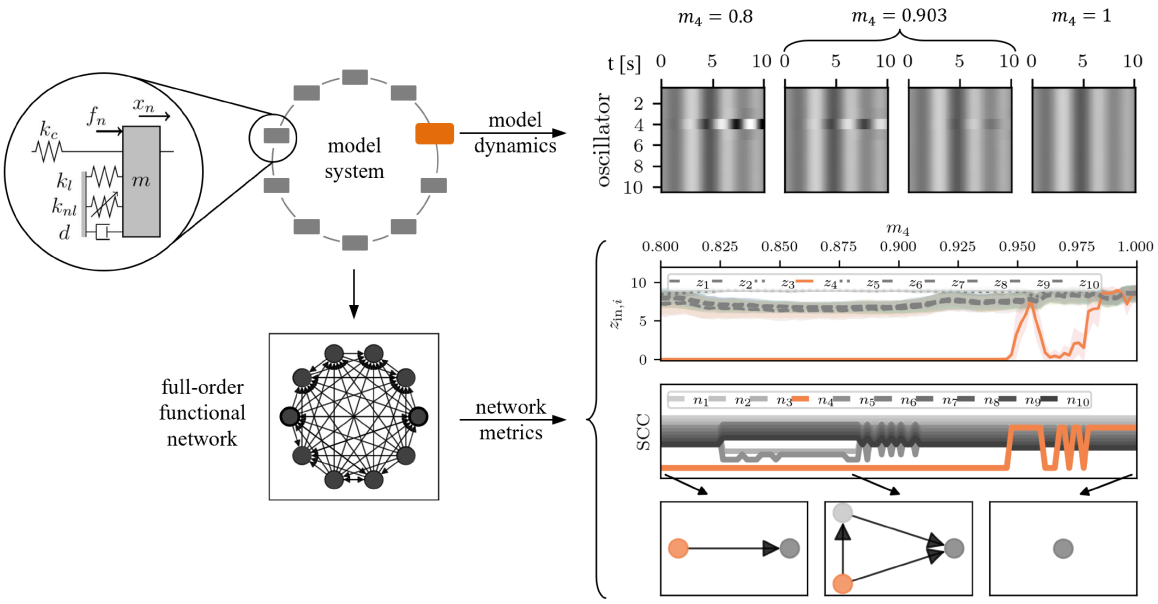

FIGURE 4.4: Network-based localization detection. The initially homogeneous model system of ten nonlinear oscillators with nearest-neighbor coupling develops localized dynamics as one of the oscillator masses, m_4, decreases. By analyzing functional networks computed from overlapping ten-second samples of the time series, the imminent localized vibration is detected even before it is clearly visible in the time series data. The first panel of network metrics shows the mean and standard deviation of each nodal in-degree $z_{\text{in},i}$ over a set of 100 initial conditions in [0, 0.01]. The second panel shows the strongly connected components (SCC) within the network, illustrating how the dynamic structure disintegrates as the localized vibration appears. The bottom panels present three exemplary networks, visualizing the topology of the reduced-order network at specific points. Figure adapted from [296].

Discussion and contribution to the field
From a machine dynamics perspective, this research provides a novel take on dynamical structural analysis. By intertwining two critical aspects of network theory, the translation of dynamics into topology and the structure-based analysis, a functional network perspective is developed. This new view presents itself as a complementary method for inferring structure from data. The approach provides a means to detect and visualize structural aspects within dynamical systems that extend beyond their physical configurations. The scheme has been applied to the detection and tracking of localizations. Although this data-driven approach offers intuitive interpretations, it presently lacks a fully formalized framework, a common scenario in complex systems science [299]. Prior research on the inter-connections of network science and dynamical systems studies highlights parallels between the inference of network structure from time series data and phase-space analysis [172] and observability and embedding techniques [300–302]. While the networks obtained in this work depart from the classical notion of a predictive model, there is potential for development in that direction. The purely data-driven approach circumvents some challenges in machine dynamics by inferring the description on a higher level, such as the coupling direction, instead of a detailed joint model. The interpretation of the results may require additional tools and methodologies, an area of active research across different scientific fields, where the analysis of mechanical vibrations can benefit from interdisciplinary exchange.
From a network science perspective, this study illustrates the inherent connection between network science and complex systems, wherein both disciplines aim to uncover the underlying principles and mechanisms of dynamics in real-world systems across various scientific domains [168, 172]. Through encoding structure and dynamics, network science reveals patterns that contribute to the interdisciplinary understanding of emergent phenomena deriving from interactions among numerous components. The resulting network is more closely aligned with a phenomenon-based description rather than serving as a comprehensive universal model, like the equations-based view in Section 2.3. Similar to the neural network approach in Chapter 3.2, the complex network approach circumvents restrictive analytical descriptions but reveals system structure from another perspective. These methods share an almost universal applicability to any system where measurement data is available and the condensation of information from a high-dimensional embedding space, while shifting the focus from traditional physics-based approaches to a phenomenological one. The following chapter provides a detailed overview of parallels between the different approaches, further discusses relations to complexity science, and gives an outlook on further research directions.

Outlook
As the network-based analysis of nonlinear dynamics of mechanical structures is a relatively novel field, there are several interesting future research directions. First, expanding the analyses to higher-dimensional and heterogeneous systems would be an interesting step, bringing the analyses closer to real-world systems. Second, the method is capable of incorporating diverse types of measurement data beyond the displacement of each node. For example, adding temperatures or velocities into the network could yield insight into the interplay of these variables. By shifting from cross-recurrence to joint-recurrence, time series with non-similar phase space dimensions can be integrated [303]. The applicability of joint

recurrence-based network analysis to systems of coupled mechanical oscillators has been studied in [304]. Third, while the study presently relies on system snapshots for temporal analysis, developing truly time-continuous methodologies, such as adaptive networks or temporal expansions, might provide further insights. This could involve introducing a "lifetime" of network edges, as outlined in [261]. Lastly, integrating different spatial or temporal scales could be achieved through strategic choices of embedding parameters or subsystem configurations, providing insight into the mechanisms behind emergent phenomena.

4.4 Publication III: Building functional networks for complex response analysis in systems of coupled nonlinear oscillators

C. Geier, M. Stender, and N. Hoffmann. "Building functional networks for complex response analysis in systems of coupled nonlinear oscillators". *Journal of Sound and Vibration* 590 (2024), p. 118544. DOI: 10.1016/j.jsv.2024.118544

Journal of Sound and Vibration 590 (2024) 118544

Contents lists available at ScienceDirect

Journal of Sound and Vibration

journal homepage: www.elsevier.com/locate/jsvi

Building functional networks for complex response analysis in systems of coupled nonlinear oscillators

Charlotte Geier [a,*], Merten Stender [b], Norbert Hoffmann [a,c]

[a] Hamburg University of Technology, Department of Mechanical Engineering, Am Schwarzenberg-Campus 1, Hamburg, 21073, Germany
[b] Chair of Cyber-Physical Systems in Mechanical Engineering, Technische Universität Berlin, Straße des 17. Juni 135, Berlin, 10623, Germany
[c] Imperial College London, Mechanical Engineering, Exhibition Road, London, SW7 2AZ, UK

ARTICLE INFO

Keywords:
Complex networks
Nonlinear dynamics
Time series analysis
Synchronization
Transient analysis
Duffing oscillators

ABSTRACT

Some aspects of engineering dynamics, such as nonlinearities and transient motion of many interconnected parts, remain difficult to handle today. To comply with increasing demands on resilience and safety, the dynamics of large machines need to be better understood. Complex network methods, already present in many scientific disciplines, provide a tool set complementary to conventional methods of system analysis. This work aims at providing a new, function-based view on mechanical systems by generating functional networks. To this end, a network algorithm is applied to sets of cyclically coupled Duffing oscillators as a common example of a complex nonlinear mechanical system. In the functional network, each node represents an oscillator while the direction of the network edges represents a functional coupling. Results show that the network method is capable of identifying dynamical transitions and synchronization between components, as well as determining the number of different states present within a system. Additionally, the time evolution of the component interactions, especially in response to a disturbance, is studied via a sliding-window approach. The results of this analysis might hopefully open new ways for a more efficient system analysis through optional sensor placement, and for effective countermeasures against unwanted dynamics through improved analysis of transient dynamics.

1. Introduction

Engineering dynamics studies large machines, which consist of many connected moving parts. The analysis of these systems is often challenging in practice [1]. Large deformations of machine parts [2], joints [3], friction [4,5], or material nonlinearities [6,7] cause nonlinear effects. These nonlinearities, as well as transient loads and motion, combined with a large number of degrees of freedom, still pose challenges to state-of-the-art system understanding and modeling approaches. At the same time, the need for lightweight structures that can withstand large and unsteady environmental loads is growing. Examples of such structures are offshore wind turbines, satellites, and space antennas. To avoid unwanted and potentially harmful vibrations, for example, in the blade of a turbine, a deeper understanding of the dynamics of these systems becomes crucial. Transfer path analysis [8] and operational deflection shape analysis [9] provide a tool set for studying the dynamics of composed structures. The accuracy of the former relies on accurate measurements and suitable sensor placement to collect appropriate data for the analysis [10]. Despite the available techniques, the identification and analysis of functional dependencies, and especially the study of transient motion, remain challenging for engineers. This work provides a complementary view of these issues in structural machine dynamics by

* Corresponding author.
E-mail address: charlotte.geier@tuhh.de (C. Geier).

https://doi.org/10.1016/j.jsv.2024.118544
Received 1 December 2023; Received in revised form 27 May 2024; Accepted 28 May 2024
Available online 30 May 2024

representing the mechanical structure as an alternative network model. Classical, geometry-based models represent these mechanical systems as components which are connected via springs and dampers based on their geometrical coupling or, in other words, their geometrical proximity. In our functional networks, each node also represents a component of the mechanical structure. In contrast to the mechanical model, the edges of the network represent functional interrelations obtained from a network-based approach. These functional interrelations are based on the dynamical interaction of the components, instead of their geometrical proximity. This approach opens the door for a variety of new network-based tools.

Network methods are popular in many fields of science, such as mathematics, physics, biology, computer science, the social sciences, medicine, and climate research [11–15]. Common examples of networks include the internet, neural networks [16], social networks [11], or power grids [17,18]. The investigation of dynamical systems as a network provides complementary tools for time series analysis [11,15] by generating a network from (measurement) time series data. This transformation from time- to network domain makes it possible to study the time series through the properties of the resulting network [19,20]. Based on this approach, network analysis has been used to identify coupling properties between different system components of a dynamical system [21–23], detect anomalies [24] and distinguish various dynamical states [25–28]. Aspects of transient motion of the system can be studied in the network domain, such as regime changes [29] and types of synchronization [28,30–33]. A detailed review of network methods for the study of dynamical systems and their possibilities can be found in [15].

In this work, network analysis with the inter-system recurrence network (ISRN) method [21] is applied to a classical toy model for a mechanical systems, a set of coupled Duffing oscillators, to generate a functional network. ISRN analysis has been used to identify the direction of links between two weakly coupled Rössler systems and to study the interrelation between two paleoclimate time series in [21], making it an appealing candidate for analyzing the functional dependencies between distinct components. The nonlinear Duffing oscillator, or sets of coupled Duffing oscillators, are a model system in many engineering applications such as forced coupled pendulums [34], alternating current electric fields [35], or vibrating bladed discs [2,36–38] which exist for example in aircraft or wind turbines [2]. The obtained functional network is then used to study functional dependencies within the mechanical system at different dynamical states, as well as the evolution of the network structure during transient processes.

The remainder of this work is structured as follows: In Section 2, the model system used in this study is presented, followed by an introduction of the applied network methods in Section 3. Section 4 includes the results for the functional network and analysis of a transient system. A discussion of the results is provided in Section 5. The paper closes with a conclusion in Section 6.

2. Coupled duffing oscillators

The Duffing oscillator is a well-known dynamical system whose dynamics have been described extensively in several works [36, 39,40]. In engineering, a single Duffing oscillator represents a common model for systems with nonlinearities due to material nonlinearities, or large deformations or motions. Example of these systems are a nonlinear pendulum [34], systems with a nonlinear spring [2] or a single blade [2,36–38]. More complex structures such as bladed disks in turbines, wind turbines, or space antennas, can be modeled by coupling several Duffing oscillators [2]. In these models, one machine component can be represented by a single oscillator. The Duffing oscillator exhibits rich dynamical behavior [36,39–41]. For specific parameter combinations, the single oscillator exhibits bi-stability [2,39], and chaotic behavior [39,40]. Correspondingly, sets of coupled oscillators may exhibit multi-stability. The bi- or multi-stability property can give rise to potentially harmful localized vibrations in coupled systems [2], where a single oscillator or a group of oscillators vibrates at a much higher amplitude than the overall system. In practice, this phenomenon can lead to system failure, for example if a turbine blade breaks due to high stress induced by high-amplitude oscillations.

A single, forced Duffing oscillator [39] is described by

$$m\ddot{x} + d\dot{x} + k_1 x + k_{\mathrm{nl}} x^3 = f(t), \tag{1}$$

where m is the model mass, d the damping coefficient, k_1 and k_{nl} the linear and nonlinear spring stiffness. The system displacement is given by x, its velocity by the time derivative $\dot{x}$ and the acceleration by $\ddot{x}$. The forcing $f(t) = F\cos(\Omega t)$ is defined as harmonic forcing with amplitude F and angular frequency Ω. The damping is defined as Rayleigh damping $d = \alpha m + \beta k_1$ with mass- and spring-proportional factors α and β, respectively. In this work, the parameter values are chosen such that the system exhibits bi-stability and the excitation frequency lies in the bi-stable regime. An overview of the parameters is given in Table 1. Fig. 1 illustrates the bi-stability behavior and hysteresis of the system for the given parameter settings. When the forcing frequency Ω is increased from zero, the amplitude $\hat{x}$ of the system response follows the path marked by red triangles and increases to $\hat{x} = 1.72$ m at $\Omega = 2.17$ rad s^{-1}, where it suddenly drops to values around $\hat{x} = 0.3$ m. On the other hand, if the forcing frequency is decreased, the amplitude follows the lower branch, marked by blue crosses, and jumps to a higher value of $\hat{x} = 1.55$ m at $\Omega = 1.89$ rad s^{-1}. The area between $1.89 < \Omega < 2.17$ rad s^{-1} defines the bi-stability region. In this work, the oscillator is excited at a frequency $\Omega = 2$ rad s^{-1} within that region, marked by a black dashed line. The right panel of Fig. 1 shows the time response of the Duffing oscillator with the given parameter settings for two different initial conditions. The initial conditions are defined as $\boldsymbol{x}_0 = [x_0, v_0]$, where x_0 is the initial displacement and v_0 is the initial velocity of the oscillator. When starting from $\boldsymbol{x}_{0,1} = [1, 0]$, the mass oscillates with a much higher amplitude than when starting at $\boldsymbol{x}_{0,2} = [0.1, 0]$.

For the purpose of studying a mechanical system made of several oscillators through a functional network, a system of $M = 5$ cyclically coupled Duffing oscillators with nearest-neighbor coupling is implemented, see Fig. 2. Similar systems are used as minimal models in engineering to model bladed disks, as described in [2,36,42]. The equation of motion for the nth oscillator is given by

$$m\ddot{x}_n + d\dot{x}_n + k_1 x_n - k_c(x_{n-1} + x_{n+1} - 2x_n) + k_{\mathrm{nl}} x_n^3 = f(t), \tag{2}$$

Table 1
Model parameters. Overview of the model parameters used in this study, unless specified otherwise.

Measure	Symbol	Unit	Value
Mass	m	kg	1
Damping prop m	α	s^{-1}	0.1
Damping prop k	β	s	0
Linear spring	k_l	N m^{-1}	1
Nonlinear spring	k_{nl}	N m^{-3}	2
Coupling spring	k_c	N m^{-1}	0.1
Forcing amplitude	F	N	1
Forcing frequency	Ω	rad s^{-1}	2

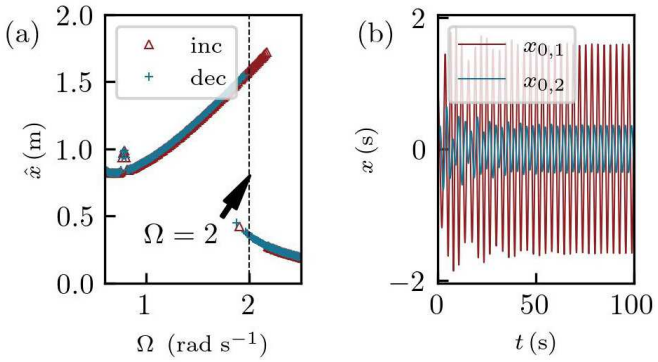

Fig. 1. Duffing oscillator with given parameter settings. The amplitude of the system response $\hat{x}$ follows two different paths for an upward- (red triangles) and downward (blue crosses) frequency sweep over the forcing frequency Ω. The bi-stability region is located at $\Omega = [1.89, 2.17]$ rad s^{-1}, where two stable solutions exist. The dashed line marks the chosen excitation frequency $\Omega = 2$ rad s^{-1}. On the right, the system responses for two different initial conditions $\boldsymbol{x}_{0,1} = [1, 0]$ (red), $\boldsymbol{x}_{0,2} = [0.1, 0]$ (blue) are shown, illustrating the dependence of the oscillation amplitude and phase on the initial conditions. (For interpretation of the references to color in this figure legend, the reader is referred to the web version of this article.)

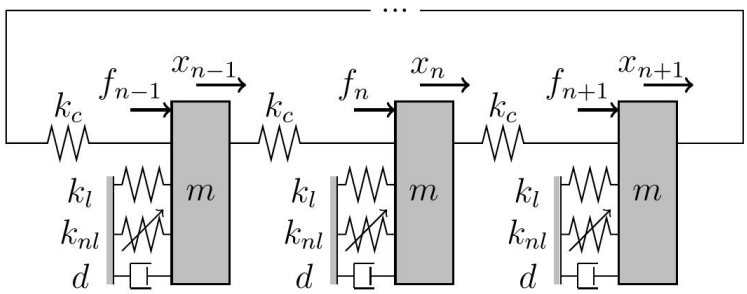

Fig. 2. Model system composed of a chain of $M = 5$ cyclically components. Each component is represented by a Duffing oscillators with nearest-neighbor coupling. The figure shows a only section of the entire model, using three oscillators to illustrate the nearest-neighbor coupling. The system is described by model masses m, the Rayleigh damping $d = \alpha m + \beta k_l$, linear and nonlinear springs k_l and k_{nl} and the connecting linear springs k_c. The displacement is given by x_n, and each mass is driven by an harmonic forcing $f_n(t) = F\cos(\Omega t)$.

where k_c describes the linear nearest-neighbor coupling spring. These types of coupled systems are known to exhibit complex dynamic behavior, such as nonlinear vibration localization [2], where a subsystem oscillates with much higher amplitude than the remainder of the system. This phenomenon is known to be caused by manufacturing imperfections (mistuning), but has also been shown to arise in fully homogeneous and symmetric structures due to bifurcations [2], as is the case for the model system at hand. The resulting high-amplitude oscillations cause a large amount of stress in the affected system components. This stress can lead to component and even system failure. Localization is therefore a potentially harmful phenomenon in the engineering context [2].

Eight different dynamical states of the five-oscillator system are studied, see Fig. 3. Each panel shows the dynamics of the entire five-oscillator system over time. Within a panel, a row represents a single oscillator of the system and the x-axis represents time. The deflection of each mass is mapped to a color bar. The first four states (a) to (d) are achieved solely by variation of the initial conditions, while the latter four (e) to (h) require variations from the system parameters in Table 1. The states in (a) and (b) show a uniform motion with all oscillators in low or high amplitude, respectively. Panels (c) and (d) show localized harmonic vibrations with one and three masses at high amplitudes, while all other masses vibrate at low amplitudes. Localized vibrations with higher periods are achieved by increasing the forcing amplitude to $F = 35$ N, see panels (e) and (f). By changing the forcing frequency from well within the bi-stability region to values at the border regions $\Omega = 1.873$ rad s^{-1} in panel (g) and $\Omega = 2.295$ rad s^{-1} in panel (h), fronts are created [43], which propagate a specific state depending on the initial conditions. The initial conditions are presented in the Appendix.

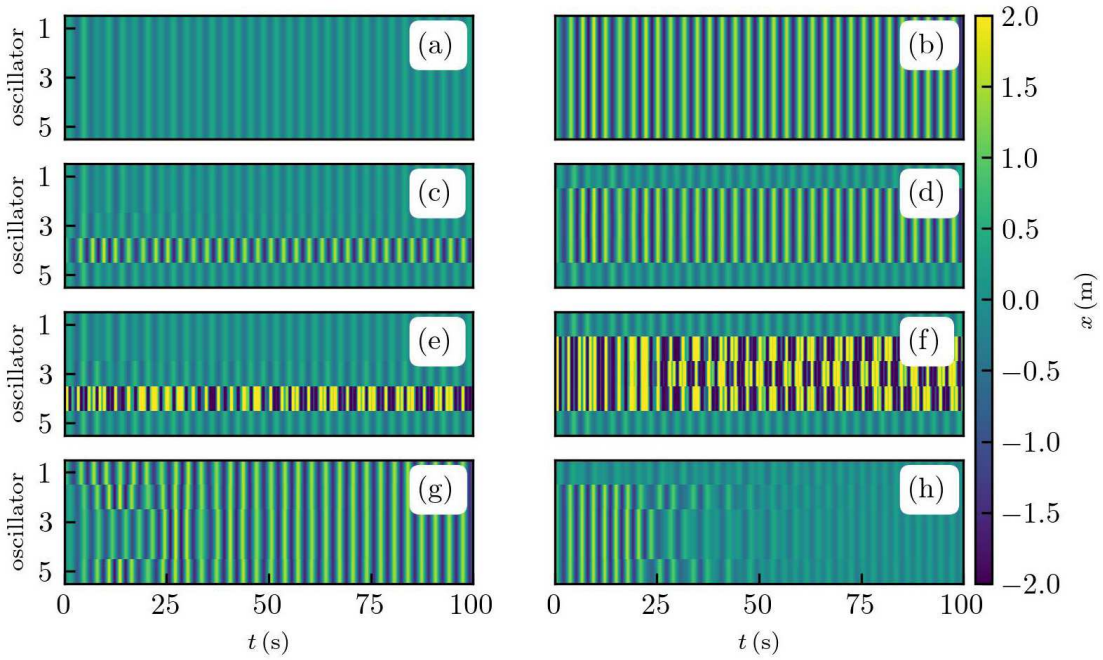

Fig. 3. Dynamics of the Duffing oscillator chain with $M = 5$ masses. The system parameters are as listed in Table 1, unless specified otherwise. (a) uniform oscillation at low amplitude, (b) uniform oscillation at high amplitude, (c) localized harmonic vibration: one oscillator with high amplitude, (d) localized harmonic vibration: three oscillators with high amplitudes, (e) localized higher-periodic oscillation: one oscillator in higher-periodic oscillation, where $F_4 = 35$ N, (f) localized higher-periodic oscillation: of three oscillators, where $F_{2,3,4} = 35$ N, (g) transient motion: front at lower end of bi-stability region, where $\Omega = 1.873$ rad s^{-1} and (h) transient motion: front at upper end of bi-stability region, where $\Omega = 2.295$ rad s^{-1}. The initial conditions $\boldsymbol{x}_{0,i}$ for the ith case are given in the Appendix. (For interpretation of the references to color in this figure legend, the reader is referred to the web version of this article.)

Although the studies in this work are limited to a homogeneous system composed of components with two states each, the approach would be equally valid for a system with components with any number of states, or even a heterogeneous system where the individual components have different numbers of states. The method focuses on the analysis of time series data, which could also be obtained from a system described by a partial differential equation, as long as a discretized time series is available.

The time series data used in the following studies is generated by integrating Eq. (2) using the integrator 'dopri5' in Python Scipy [44]. 'Dopri5' is an explicit Runge–Kutta method of order 4(5) with step size control and dense output [45]. The resulting time series have a length of $t = 100$ s and are discretized with a step size of $dt = 0.05$ s.

There is a large variety of well-established tools that can be employed to study data from complex nonlinear models. Most of these methods are based in time- or frequency domain. This work aims at building a complementary perspective, given by a functional network. This alternative view on the dynamics of a mechanical system focuses on functional dynamical relationships rather than geometrical proximity. The following section introduces the inference of functional networks based on a specific network algorithm, the inter-system recurrence network.

3. Inter-system recurrence networks and functional networks inference

In recent years, a number different methods for inferring networks from time series have been developed [15]. One group of methods are recurrence-based networks (RN) [46–50], which generate a network based on the mutual proximity of two observations in phase space. A particular recurrence-based network algorithm for the study of bi-variate data is the inter-system-recurrence network (ISRN) [15,21], which is the subject of this study. This section is dedicated to introducing the idea of RN in general and ISRN in particular, as well as an expansion of the ISRN-method to multi-variate data which is developed as part of this work to generate functional networks. An overview of the work flow for the generation of functional networks is shown in Fig. 4.

3.1. Recurrence networks

Recurrence networks are derived from recurrence plots [51]. The concept of recurrence in dynamical systems, prominent for example in recurrence quantification analysis, has developed into a well-studied field of research [52]. As an extensive amount of literature on this topic is already available, for example in [51,53], only a short introduction will be given in this section. Following the notation in [21], a recurrence plot is computed as follows. Measurements are taken from a dynamical system X at distinct times $t_i (i = 1, \dots, N^X)$. The dynamical system can be deterministic or stochastic [15]. By denoting $x_i = X(t_i)$, a time series $\{x_i\}_{i=1}^{N^X}$ is obtained. In the case of this study, the time series x_i represents the solution to a dynamical system represented by a second order differential equation. If the underlying system X is time-discrete, the time series data can be used directly. Time series data from

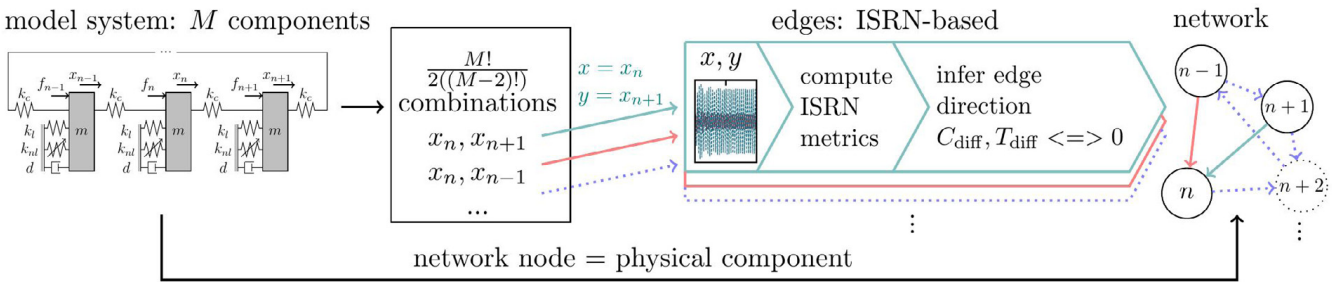

Fig. 4. Overview of the network generation process. Each of the M components of the model system becomes a node of the functional network. Here, each component is represented by a single Duffing oscillator. The direction of the edges between the nodes is determined via an iterative approach using ISRN measures. For every possible combination of two components (or, accordingly, nodes), time series measurements are obtained, an inter-system recurrence network is computed and the cross-clustering and transitivity measures are used to infer the direction of the edge between those two nodes. If $C_{\text{diff}} < -\mu, T_{\text{diff}} < -\mu$, the coupling direction is from X to Y, for $C_{\text{diff}} > \mu, T_{\text{diff}} > \mu$, it is Y to X, and for $-\mu < C_{\text{diff}} < \mu, -\mu < T_{\text{diff}} < \mu$ bi-directional coupling is defined. This process is repeated until each component has been compared with each other component, yielding $M!/(2(M-2)!)$ combinations in total. The resulting functional network is directed, but not weighted.

a time-continuous dynamical system has to be sampled with a finite frequency. A recurrence plot is defined as a matrix R^X with entries

$$R^X_{ij}(\varepsilon) = R^X(x_i, x_j|\varepsilon^X) = \Theta(\varepsilon^X - d(x_i, x_j)), \tag{3}$$

where $d(x_i, x_j) = \|x_i - x_j\|$ measures the supremum norm between two observations in phase space, Θ is the Heaviside function, and ε^X is a fixed distance measure. This threshold defines a fixed volume of the phase space, within which two observations are counted as recurrent. Alternatively, it is also possible to perform the analyses using the reconstructed phase space of the discrete time series obtained through delay embedding, at the cost of introducing two additional hyperparameters, namely the embedding dimension and the time delay. The recurrence network is obtained by interpreting the resulting recurrence matrix R^X as the adjacency matrix A^X of a network [47,49,50]. To exclude self-loops, the main diagonal of the adjacency matrix is set to zero with

$$A^X_{ij}(\varepsilon^X) = R^X_{ij}(\varepsilon^X) - \delta_{ij}, \quad \delta_{ij} = \begin{cases} 1, & i = j \\ 0, & i \neq j \end{cases}, \tag{4}$$

where δ_{ij} is the Kronecker delta. The resulting network has N^X nodes, which are connected if they lie within a fixed phase space volume ε^X of each other. Because the recurrence is defined through a fixed volume of the phase space, the network is called an ε-recurrence network. The resulting network is unweighted and undirected.

3.2. Inter-system recurrence networks

Inter-system recurrence networks [21] form an extension of the RN concept for bi-variate time series data. The following presentation follows the notation introduced in [21]. A description of the algorithm can also be found in [15]. To study the bi-variate case, a second dynamical system Y is introduced. The two dynamical systems X and Y should share the same physical units and phase space dimension to obtain physically meaningful results [15,21,51]. Applications of the inter-system recurrence theory to cases where systems do not share the same physical units or phase space are possible using specific transformation approaches [21]. However, results from these comparisons but should be interpreted carefully, as there is no mathematical foundation for the treatment of the conceptual problems that arise [21]. Analogously to the above description of a time series $\{x_i\}_{i=1}^{N^X}$ of a dynamical system X, the second dynamical system Y is measured at times $t_j (j = 1, \ldots, N^Y)$ to generate a second time series $\{y_j\}_{j=1}^{N^Y}$. The time series length and sampling frequency of the two time series $\{x_i\}_{i=1}^{N^X}$ and $\{y_j\}_{j=1}^{N^Y}$ do not need to be identical, as the method does not make use of time information directly, but leverages geometric properties of the system. Accordingly, both time series have to sample a sufficient part of the underlying attractor. For each of these time series, the corresponding adjacency matrices A^X and A^Y are obtained as defined in Eqs. (3) and (4), with fixed volumes ε^X and ε^Y of the phase space. Additionally, a cross-recurrence plot is computed as

$$CR^{XY}_{ij}(\varepsilon^{XY}) = \Theta(\varepsilon^{XY} - d(x_i, y_j)), \tag{5}$$

where $d(x_i, y_j) = \|x_i - y_j\|$ denotes the supremum norm between two observations of the two different time series. In contrast to the cross-recurrence plot, which requires two dynamical systems with identical phase space and physical units, but allows for arbitrary time series length and sampling points, an alternative method, exists. The joint recurrence plot requires identical time series length and sampling points, but allows for different phase space dimensions and physical units. The cross-recurrence matrix CR^{XY} defines the connectivity between two nodes of different networks [21]. As in an adjacency matrix, two nodes are connected if the respective entry in CR^{XY} equals one, and disconnected if the entry is zero. Due to the symmetry of the problem, the second cross-recurrence

matrix is the transpose of the first, $CR^{YX} = [CR^{XY}]^{\mathrm{T}}$. The ISRN is set up by combining the adjacency matrices A^X and A^Y derived from each time series with the cross-recurrence matrices CR^{XY} and CR^{YX} to an adjacency matrix

$$A^{\mathrm{ISRN}}(\boldsymbol{\varepsilon}) = \begin{bmatrix} A^X(\varepsilon^X) & CR^{XY}(\varepsilon^{XY}) \\ CR^{YX}(\varepsilon^{XY}) & A^Y(\varepsilon^Y) \end{bmatrix}, \tag{6}$$

where $\boldsymbol{\varepsilon} = [\varepsilon^X, \varepsilon^Y, \varepsilon^{XY}]$ comprises the fixed phase space thresholds for each individual computation. This inter-system recurrence network embodies a network with two sub-networks. The two adjacency matrices A^X and A^Y represent networks from the two individual systems, while the two cross-recurrence matrices CR^{XY} and CR^{YX} constitute the connections between the two networks.

The ISRN method requires a choice of the threshold parameters $\boldsymbol{\varepsilon}$. There are a number of studies on the determination of a suitable threshold parameter, for example in [46–48,54]. The threshold parameter ε determines the recurrence rate RR in the recurrence plot, and therefore the link density of the resulting recurrence network. For practical considerations, it is common to fix the recurrence rate instead of the threshold parameter in the context of recurrence networks [21]. Ideally, the recurrence rate is large enough such that most of the nodes in the resulting network are connected within one large component, but small enough to keep the overall connectivity small. For many systems, $RR < 0.05$ is a good choice [21]. To obtain an ISRN that represents two connected networks rather than one large network, there have to be more intra-system than inter-system connections. That is, the intra-system recurrence rates RR^X and RR^Y, defined by

$$RR = \frac{1}{N^2} \sum_i R_{ij} \tag{7}$$

have to be larger than the inter-system recurrence rate, which is given by

$$RR^{XY} = \frac{1}{N^X N^Y} \sum_{ij} CR_{ij}^{XY}, \tag{8}$$

as recommended in [21,46,48]. The inter-system recurrence rates RR^{XY} and RR^{YX} are kept identical, as the symmetry of these components is crucial to the proposed method, as described in the following section. Studies have shown that network measures depend on the choice of threshold parameter [47]. However, the method proposed in this work does not require exact quantities, but relies on the asymmetry of two network-based measures, which will be introduced in the next section. Therefore, it can be assumed that the exact choice of ε is not crucial for this method. In this work, the phase space thresholds in $\boldsymbol{\varepsilon}$ are chosen such that the recurrence rates are $RR^X = 0.03$, $RR^Y = 0.03$ and $RR^{XY} = 0.02$, based on the parameters given in [21]. The computation of the inter-system recurrence network and the related measures is performed using the pyunicorn package [55] in Python. Numerically expensive computations are performed in compiled C, C++, or FORTRAN code, rendering the computations relatively efficient. For example, computing a cross-clustering coefficient in Eq. (10) from a 2000×2000 adjacency matrix takes 0.17 s on a 12-core Intel Core i7 CPU with 2.6 GHz running Ubuntu 20.04.

3.3. Inference of functional interrelations

Two properties of the ISRN, namely the global cross-correlation coefficient C and the global cross-transitivity T, can be used to infer functional interrelations between two components X and Y [21]. A short definition and background of these two measures, based on the descriptions in [21,56], is given in this section. For more detailed information on general network properties, see [14,15]. The network measures are defined for a network $G = (V, E)$ with edges E and nodes $V = \{1, \ldots, N\}$. In the case of the ISRN, the network consists of the sub-networks V^X and V^Y. For the following description, consider a single node in sub-network V^X which is called v and two exemplary nodes of V^Y which are called p and q. The global cross-clustering coefficient C^{XY} describes the probability of a node $v \in V^X$ to have pairs of mutually connected neighbors in V^Y. It is calculated as the average over all local cross-clustering coefficients

$$C_v^{XY} = \frac{1}{k_v^{XY}(k_v^{XY} - 1)} \sum_{p,q \in V^Y} A_{vp}^{\mathrm{ISRN}} A_{pq}^{\mathrm{ISRN}} A_{qv}^{\mathrm{ISRN}}, \tag{9}$$

such that

$$C^{XY} = \langle C_v^{XY} \rangle_{v \in V^X}, \tag{10}$$

where $k_v^{XY} = \sum_{q \in V^Y} A_{vq}^{\mathrm{ISRN}}$ denotes the cross-degree. On the other hand, the cross-transitivity T^{XY} defines the probability that two nodes p, q in sub-network V^Y are connected if they are both connected to a node v in sub-network V^X. It is computed as

$$T^{XY} = \frac{\sum_{v \in V^X, p \neq q \in V^Y} A_{vp}^{\mathrm{ISRN}}\, A_{pq}^{\mathrm{ISRN}}\, A_{qv}^{\mathrm{ISRN}}}{\sum_{v \in V^X, p \neq q \in V^Y} A_{vp}^{\mathrm{ISRN}} A_{vq}^{\mathrm{ISRN}}}, \tag{11}$$

counting the number of "cross-triangles" over the number of "cross-triples". Both measures are not invariant under the permutation $X \leftrightarrow Y$, such that $C^{XY} \neq C^{YX}$ and $T^{XY} \neq T^{YX}$.

In our functional network, the direction of an edge between two nodes represents a functional relationship between the corresponding components. The basic idea of inferring a functional interrelation between two components using an ISRN is presented in [21]. In the case of uni-directional and attractive diffusive coupling from X to Y, the trajectory of Y is likely dragged towards the trajectory of X, increasing the probability of finding triangles $x - x - y$, which add to T^{YX} and C^{YX}, but not to T^{XY} and

Table 2
ISRN measures and related functional dependencies. A small threshold $\mu = 0.02$ is introduced to avoid wrong detection of coupling direction due to small asymmetries which may arise due to small system detuning or rounding.

Network measure	Functional dependency
$C_{\text{diff}} < -\mu, T_{\text{diff}} < -\mu$	X on Y
$C_{\text{diff}} > \mu, T_{\text{diff}} > \mu$	Y on X
$-\mu < C_{\text{diff}} < \mu, -\mu < T_{\text{diff}} < \mu$	Bi-directional or no dependency

C^{XY}. The opposite is true for the inverse dependency. Therefore, $T^{YX} > T^{XY}$ and $C^{YX} > C^{XY}$ is expected for a uni-directional interrelation $X \rightarrow Y$, and, accordingly, the opposite for the inverse dependency direction. For clarity, the differences are defined as $C_{\text{diff}} = C^{XY} - C^{YX}$ and $T_{\text{diff}} = T^{XY} - T^{YX}$ in this work, such that $C_{\text{diff}} > 0$ and $T_{\text{diff}} > 0$ implies a dependency of Y on X, and $C_{\text{diff}} < 0$ and $T_{\text{diff}} < 0$ implies dependency of X on Y. In the case when the two systems are not interrelated, the measures can be interpreted as arising randomly, such that $C_{\text{diff}} \approx 0$ and $T_{\text{diff}} \approx 0$. If the two systems share a symmetric bi-directional interrelation, an equal attraction between the two time series is expected, and thus $T^{YX} = T^{XY}$ and $C^{YX} = C^{XY}$, such that $C_{\text{diff}} = 0$ and $T_{\text{diff}} = 0$. Unfortunately, the method does not yield a clear distinction between the case of no interrelation and bi-directional dependency. For the purpose of this work, these ambiguous cases are always regarded as a bi-directional connection. The definition of $C_{\text{diff}} = T_{\text{diff}} = 0$ for no or bi-directional dependency is found to be too strict in the given use case, since even small detuning, for example in the natural frequencies of the two coupled systems, can lead to small asymmetries [15]. Therefore, a small threshold $\mu = 0.02$ is defined, such that $-\mu < C_{\text{diff}} < \mu, -\mu < T_{\text{diff}} < \mu$ define bi-directional or no interrelation, $C_{\text{diff}} < -\mu, T_{\text{diff}} < -\mu$ represents the X on Y- dependence case, and vice versa. A summary of the network measures and the corresponding functional dependencies can be found in Table 2.

This method of inferring the functional interrelation, or edge direction, between two dynamical systems from ISRN measures has a number of applications in literature, including the detection of coupling direction in a system of two coupled Rössler systems and paleoclimate data [21], and the study of oil-water flow states [25–27]. In this paper, the method is used in an iterative manner to generate a functional network from mechanical systems with more than two degrees of freedom. The procedure will be presented in the following section.

3.4. Generation of functional networks

Generating functional networks from a system of multiple connected components is the goal of this work. To achieve this, the method for inferring the functional interrelation between two components is applied in an iterative manner, as illustrated in Fig. 4.

The starting point in this study is a model system composed of five forced nonlinear Duffing oscillators, as introduced in Section 2. A single Duffing oscillator represents one component of the model system. Each of the M components of the dynamical system becomes a node in the functional network. To compute the connectivity of the nodes, the ISRN-based approach is taken. Every possible pairing of components is listed. By picking a pairing, for example, x_n and x_{n+1}, and defining the measured displacement time series from these components as $x_n = x$ and $x_{n+1} = y$, the ISRN analysis can be performed as described in Section 3.2. The edge direction between the two corresponding nodes n and $n+1$ is then determined according to the procedure in Section 3.3. This process is repeated until every combination of components (or nodes) has been analyzed. The resulting network has M nodes and $M!/(2((M-2)!))$ unweighted, directed edges. Per definition, there is an, either uni- or bi-directional, edge between each node and each other node.

In case of a 5-component or model system, the resulting network has five nodes, and can be described by an adjacency matrix $A^{\text{ISRN}} \in \mathbb{R}^{5\times5}$. An exemplary network is shown on the left in Fig. 5, and the corresponding adjacency matrix A^{ISRN} is given in Eq. (12). To get a clearer image of the resulting network, a network condensation is performed in a last step. Bidirectionally connected nodes that share the same in- and out-edges, such as the nodes “3” and “4” in the aforementioned graph, are combined into a single node “34”. Once all nodes are combined in this way, the edges between them are derived from the edges in the original graphs. The resulting condensed network has a number of edges $E \leq N$. For the exemplary network, the condensed version is shown on the right-hand side in Fig. 5, and the respective adjacency matrix $A^{\text{cond}} \in \mathbb{R}^{5\times5}$ is presented in Eq. (12). This visualization scheme is related to community detection algorithms [57], and allows for a better overview over the connections and symmetries within the graph.

To summarize, the networks in Fig. 5 are described by the adjacency matrices A^{ISRN} and A^{cond} as

$$A^{\text{ISRN}} = \begin{bmatrix} 0 & 1 & 1 & 1 & 1 \\ 1 & 0 & 1 & 1 & 1 \\ 0 & 0 & 0 & 1 & 1 \\ 0 & 0 & 1 & 0 & 1 \\ 0 & 0 & 0 & 0 & 0 \end{bmatrix} \rightarrow A^{\text{cond}} = \begin{bmatrix} 0 & 1 & 1 \\ 0 & 0 & 1 \\ 0 & 0 & 0 \end{bmatrix}, \tag{12}$$

where the nodes in the second matrix A^{cond} are ordered by “12”–“34”–“5”. Each of the nodes in the condensed network represents a “functional cluster”, the nodes within exhibit similar dynamical behavior. For example, the node “12” combines nodes “1” and “2” together, indicating a dynamical similarity between the two. Links, or edges, between these functional clusters represent a functional

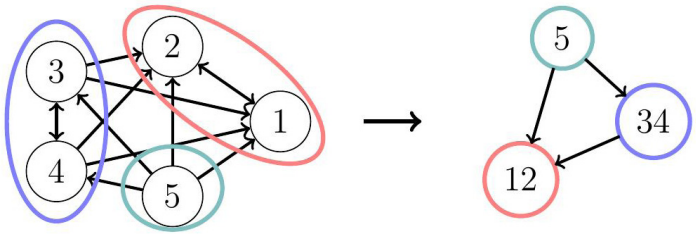

Fig. 5. Condensation of a five-dimensional network to a lower dimensional one. Bidirectionally connected nodes with identical in- and out-edges are combined into one node, allowing for a better overview of the graph structure. The corresponding adjacency matrices A^{ISRN} and A^{cond} are given in Eq. (12).

relationship between these components. Each non-zero entry in the adjacency matrix defines an edge, such that $A[i, j]$ describes an edge from node i to node j. Note that the diagonal of the adjacency matrix is always zero in this work, since self-loops, or links from one node to itself, are not allowed. Both the original and the condensed adjacency matrix are typically non-symmetric in this study, as the networks are directed. The description of the system dynamics as a functional network allows for studying a number of node–related as well as global network measures.

For example, the network size is defined by the number of nodes in the network, which is given by N for the original and by $E \leq N$ for the condensed network. Node properties can be studied in terms of in- and out-degree. The former, defined as

$$k_{\mathrm{in},p} = \sum_{q=1}^{E} A_{qp}^{\mathrm{cond}} \tag{13}$$

for the pth node, describes the number of in-links to a specific node. The out-degree represents the number of out-links from a node, and is given by

$$k_{\mathrm{out},p} = \sum_{q=1}^{E} A_{pq}^{\mathrm{cond}} \tag{14}$$

for the pth node. Each degree-measure can be summarized to a global network characteristic, the average in- or out-degree, which is defined as

$$k_{\mathrm{avg}} = 1/E \sum_{p=1}^{E} k_p, \tag{15}$$

where k can be k_{in} or k_{out}. A large number of additional network measures, such as clustering, efficiency, or average shortest path length, exist [15]. An in-depth study of these additional measures on the functional network is left for future work, as larger systems will likely make these analyses especially interesting.

4. Results

This work seeks to complement the geometry-based view of a mechanical dynamical system as a set of components and their geometric connections by a functional perspective. In our functional networks, each node represents a mechanical component, and an edge between two components indicates the functional connection between them. We thus hope to uncover a functional structure for the underlying dynamics, revealing some more insight into the inner workings of the system. Such a functional structure could yield insight into how the mechanical components interact with each other, and which of the components dominate the systems dynamics. To this end, the iterative network-based approach described in Section 3.4 is applied to time series data obtained from the model system of five cyclically coupled Duffing oscillators of Section 2. Two studies are performed: In the first study, functional networks are generated from each of the dynamical states presented in Fig. 2. Two versions of the study are performed, one using the entire time series and one discarding the transients, such that only the steady-state dynamics are considered. Thus, networks from both transient and steady-state dynamics are obtained. The second study focuses on networks from transient dynamics. The first front-like dynamics (panel (g) in Fig. 3), where an initial disturbance is propagated through the system, is investigated in more detail. To do so, consecutive smaller samples are taken from the time series, and functional networks are computed for each sample, unveiling the evolution of the functional dependencies over time. The results are shown in the following.

Fig. 6 shows the resulting networks for each of the system dynamics presented in Fig. 2. For every dynamical state, three different networks are shown. On the left-hand side, the functional network inferred from the entire time series is shown in black, and the network obtained when discarding the first 1500 time steps as transients in blue in the middle. On the right, the condensed networks obtained following the procedure described in Section 3.4 are shown in red. Where the first two networks are not identical, two condensed networks are shown.

Per definition of the method, there is an edge between each node and each other node in all networks. The functional networks differ only in direction of the edges, which can be uni- or bidirectional. In contrast, the reduced networks vary in both size E and link direction, as described by the node in- and out-degrees $\boldsymbol{k}_{\mathrm{in}}$ and $\boldsymbol{k}_{\mathrm{out}}$. Table 3 summarizes the results in terms of network measures of the condensed network.

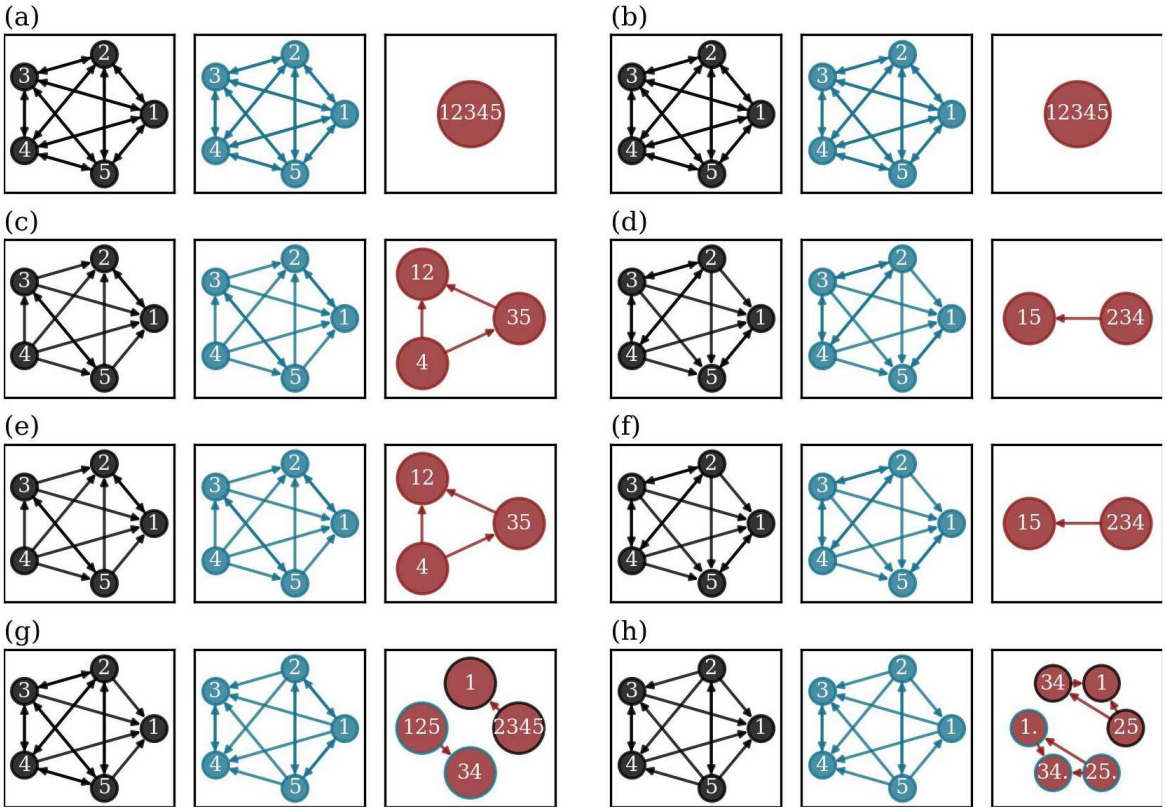

Fig. 6. Functional networks from systems of five Duffing oscillators with nearest-neighbor coupling operating in different dynamical states. For each state, the functional network generated from the entire time series is shown in black on the left, the network obtained when discarding the first 1500 time steps of each time series as transients in blue in the middle, and the smaller networks, where similar nodes are combined for clarity, as shown in red in the right panel. Images correspond to the dynamics shown in Fig. 3: Uniform oscillation with (a) low and (b) high amplitude, localized harmonic vibrations of (c) one and (d) three oscillators, localized higher-periodic vibrations of (e) one and (f) three oscillators, front like dynamics (g) one and (h) two. For the last two cases (g) and (h), where the networks with and without transients are not identical, two condensed networks as shown. The edge color of the nodes in the reduced network shows which larger network it relates to. (For interpretation of the references to color in this figure legend, the reader is referred to the web version of this article.)

Table 3
Network measures: analysis of the condensed functional networks.

Case	Size E	Node list	In-degrees $\boldsymbol{k}_{\text{in}}$	Out-degrees $\boldsymbol{k}_{\text{out}}$
(a)	1	[“12345”]	–	–
(b)	1	[“12345”]	–	–
(c)	3	[“12”, “35”, “4”]	[2, 1, 0]	[0, 1, 2]
(d)	2	[“15”, “234”]	[1, 0]	[0, 1]
(e)	3	[“12”, “35”, “4”]	[2, 1, 0]	[0, 1, 2]
(f)	2	[“15”, “234”]	[1, 0]	[0, 1]
(g.1)	2	[“1”, “2345”]	[1, 0]	[0, 1]
(g.2)	2	[“125”, “34”]	[0, 1]	[1, 0]
(h.1)	3	[“1”, “25”, “34”]	[2, 0, 1]	[0, 2, 1]
(h.2)	3	[“1”, “25”, “34”]	[1, 0, 2]	[1, 2, 0]

The top two cases (a) and (b) show functional networks generated from uniform oscillation with low and high amplitude, respectively. Both functional networks are fully connected with all bi-directional edges, resulting in a functional network of size $E_{\text{a,b}} = 1$. The corresponding condensed network has a single node “12345”, since all nodes with bi-directional links that share the same in- and out-edges get combined into one. There is no difference between the networks obtained with and without transients.

The system with a localized vibration of one oscillator at high amplitude in (c) yields a less homogeneous functional network. The functional networks generated from the full and the truncated time series are the same. Most of the edges become uni-directional, except for bi-directional edges between the nodes “1” and “2”, and “3” and “5”, which are integrated into functional clusters. Accordingly, the size of the condensed network is $E_{\text{c}} = 3$, with nodes [“12”, “35”, “4”]. The node list captures the symmetry within the system: node “4” corresponds to the component that vibrates at high amplitude, and the remaining nodes are combined in accordance with their distance to this component. The lists of in- and out-degrees encodes a functional hierarchy within the network. The node “4”, the node with the lowest in- and highest out-degree, appears as leading node with edges to “12” and “35”. An additional edge from “35” to “12” can be observed, making node “12” the one with the highest in- and lowest out-degree.

The localized vibration with three masses at high amplitudes (d) results in a slightly different functional network. Additional bi-directional edges between “2” and “4”, and “3” and “4” produce a reduced network with two nodes and size $E_{\mathrm{d}} = 2$. Two functional clusters represent the masses at high amplitude “234”, and the masses at low amplitude “15”once again capturing the symmetry within the system. In accordance with previous results, the edge between the two points from the higher to the lower amplitude, that is from “234” to “15”, as can be observed from the respective list of in- and out-degrees in Table 3.

The cases with higher-periodic motion (e) and (f) yield the same results as their counterparts in localized harmonic motion, (c) and (d). For all four cases, the inclusion or omission of the transients does not appear to have an impact on the resulting functional network.

The bottom panels (g) and (h) show the two different functional networks generated from the front-like dynamics. For all previous cases (a)–(f), dropping the transients had no impact on the result. For front 1 and front 2, the functional networks from the full time series and from the truncated time series differ. The color of the node edges indicates which time series they relate to. In Table 3, (g.1) refers to the black-edged network from the full time series, while (g.2) refers to the blue-edges network from the truncated time series. The same notation applies for the case (h). In the first case, the number and location of the bi-directional edges changes. The result are two different condensed networks with two nodes each. The functional network obtained from the full time series is described by the node list [“1”, “2345”], and in-degrees [1, 0], indicating a link from node “2345” to node “1”. The network from the truncated time series has two different nodes “125” and “34”, with an edge from “125” to “34”. Both the functional clustering of the nodes as well as the dominant link directionality change over time. In the case of the second front-like dynamics, the bi-directional edges do not change, such that the combination of nodes to functional clusters remains unchanged. The links between the nodes differ, as the different node in- and out-degrees show. While both networks share edges from “25” to “1” and “34”, the network from the full time series has an edge from “34” to “1”, which inverts its direction in the network from the truncated time series. This observation motivates a detailed study of the transient dynamics in the following.

In the second study, the analysis is performed by windowing the time series into 5 s samples, from each of which a functional network is generated. The front-like dynamics in Fig. 2(g) are generated by excitation with a frequency $\Omega = 1.873$ rad s^{-1} at the border of the bi-stability region. Only the first mass is displaced initially. Due to the particular excitation frequency at the border of the bi-stability region, the high-amplitude state propagates through the system, until all masses oscillate in synchrony at the high amplitude.

Fig. 7 shows exemplary functional networks in full and condensed form as well as the corresponding dynamics for exemplary samples during the synchronization process. It can be observed that the condensed network size $E_{\mathrm{g,t=0:75}} = 3$ is constant most of the time, but drops to $E_{\mathrm{g,t=0:125}} = 1$ as the model components synchronize. The partition into functional clusters “1”, “25” and “34”, which remains constant through the process, until all nodes merge into one functional cluster “12345” at $t = 125$. This consistent division into three parts stands in contrast to the two different partitions into two parts obtained when using a longer section of the time series. Similarly to the case with a localized mass, the network encodes the symmetry of the dynamics. Node “1” corresponds to the mass that is initially displaced, while the remaining components are divided into nodes according to their proximity to the single node. The direction of the links between the nodes changes over time, and with it the in- and out-degrees of the nodes. In Fig. 7, black arrows indicate edge directions where both measures agree, as before. In some cases, the two network measures C_{diff} or T_{diff} do not agree on the direction. The edge directions according to C_{diff} are shown in orange, the ones according to T_{diff} in blue. Only the out-degrees of the nodes will be listed in the following, counting solely the links that are indicated by both measures.

The first image for $0 < t < 5$ on the left depicts a functional network analogous to the one for the case of a single mass oscillating at high amplitude in panel (c) in Fig. 6. In the dynamics of the sample, the first mass oscillates not only with higher amplitude, but also with higher frequency, and starts pulling the other masses towards its dynamics. The edge direction in the network, encoded in the list of out-degrees $\boldsymbol{k}_{\mathrm{out,t=0}} = [2, 1, 0]$, can be interpreted as representing this fact. At $17.5 < t < 22.5$, all masses oscillate with similar, higher amplitude, but heterogeneous frequencies. The out-degrees change to $\boldsymbol{k}_{\mathrm{out,t=17.5}} = [2, 0, 0]$, indicating that the two edges pointing away from node “1” remain the same. For the edge between “25” and “34”, the two network measures do not agree on the link direction. This discrepancy can be interpreted as an indicator for the onset of change: In the next, overlapping sample $20 < t < 25$, the affected edge “25”–“34” has changed direction, resulting in new out-degrees $\boldsymbol{k}_{\mathrm{out,t=20}} = [1, 0, 2]$. The “1” to “25” link is still unchanged, while the “1” to “34” link inverts. According to the measure C_{diff}, there is a bi-directional link between “1” and “34”, probably as a result of the transition in link direction. In the dynamics of the corresponding sample, the third and fourth oscillator vibrate with the highest frequency, the other masses following with a phase lag. Oscillator 2 and 5 appear to have a slightly slower frequency than the first oscillator. In the fourth sample, the masses have almost synchronized at the high amplitude, but masses 3 and 4 are, in terms of their phase, visibly ahead of the other masses. This phenomenon is visible in the corresponding network, where the “34” node now “pulls” the other nodes, and in the out-degrees list, which now reads $\boldsymbol{k}_{\mathrm{out,t=47.5}} = [0, 1, 2]$. All edges have changed direction compared to the initial functional network on the left, inverting the functional hierarchy of model components. The fifth panel shows a transition phase, where the two networks measures only agree on a minority of link directions indicated by $\boldsymbol{k}_{\mathrm{out,t=75}} = [1, 1, 0]$. This phenomenon seems to be an expression of the transition process, as the system moves to full synchronization in the right and last panel. As expected from previous results, the corresponding functional network for uniform motion is a fully connected network with all-bidirectional edges. Accordingly, the node out-degrees are given by $\boldsymbol{k}_{\mathrm{out,t=125}} = [2, 2, 2]$. In accordance with previous explanations, the reduced network would be a single “12345”-node as shown in panels (a) and (b) of Fig. 6, but to stay consistent with the remainder of this figure, the three-wise split has been kept.

In summary, the condensed networks shown in Fig. 6, which are obtained from different global system states, encode dynamics-based, functional dependencies within the system. Functional clusters, formed by merging similar nodes of the functional network together, correspond to components with similar dynamics. Links between these clusters represent functional dependencies within

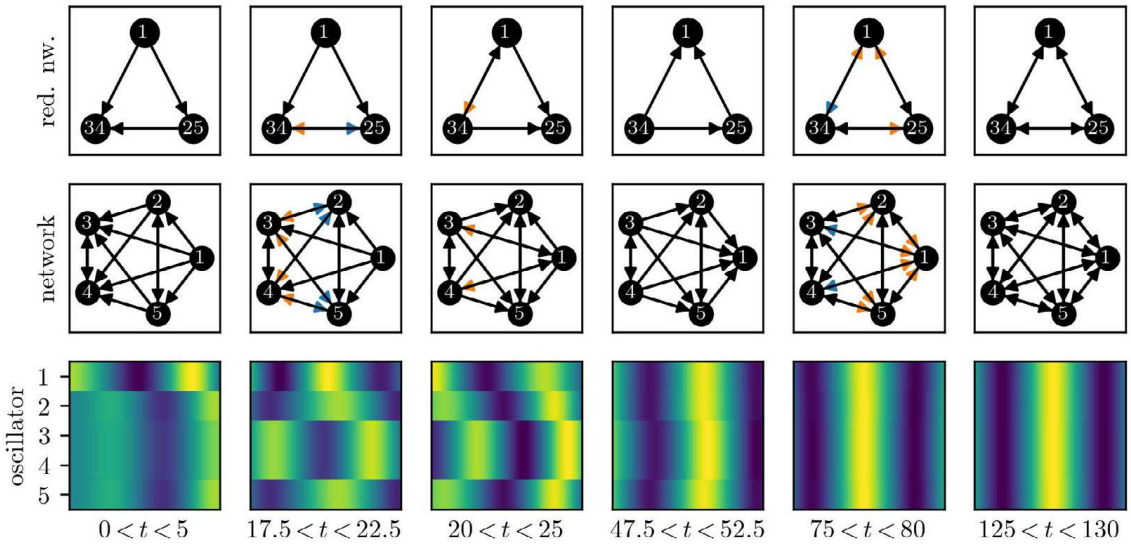

Fig. 7. Functional networks generated from time series samples of 5 s length illustrate the synchronization mechanism. The model system consists of five Duffing oscillators with nearest-neighbor coupling, excitation at frequency $\Omega = 1.873$ rad s^{-1} at the border of the bi-stability region and initial displacement of a single mass ("1"). The networks are generated as before. Black arrows indicate edges where the two metrics C_{diff} or T_{diff} agree on the direction. Where the measures do not agree, the coupling directions according to C_{diff} are shown in orange, the ones according to T_{diff} in blue. (For interpretation of the references to color in this figure legend, the reader is referred to the web version of this article.)

the system. The observation that including the transients in the data does not affect the resulting functional networks in cases (a)–(f) is likely due to the fact that these transients represent only a relatively short section of the time series data. The results indicate that the network analysis filters out dominant functional relationships over the given time period, and that the comparatively short-lived transients live on a time scale that is too small to be resolved. The data underlying cases (g) and (h) is dominated by transient motion on a larger time scale, which is captured by the analysis of even these relatively long time series sections. The second part of the analysis, which focuses on small samples of the time series in (g) at a time, resolves the functional structure on a smaller time scale. This change in the time resolution of the analysis yields different functional clusters and functional dependencies within the system, depending on the time scale to be resolved.

5. Discussion

This study uses ISRN metrics to generate functional networks to study the complex dynamics of a mechanical model system composed of nonlinear Duffing oscillators. Within the functional network, each node represents a mechanical component, and the edges correspond to functional dependencies between the respective components. Per definition of the iterative process, the resulting networks have an edge between each node, the direction of which is identified from the network metrics cross-clustering coefficient and cross-transitivity. This approach provides an alternative perspective onto multi-dimensional nonlinear systems, which focuses on function-based interrelations rather than geometrical proximity. As this study presents a novel approach at an early stage, there are still numerous compelling avenues for exploration and interesting paths to pursue.

The resulting reduced network shows the diversity of motion within a given system: In the case of uniform oscillation, there is only one distinct system state. In the case of localized vibration with one mass, there are three different types of motion: The oscillator with initial displacement is clearly in a different state than the other oscillators. The remaining oscillators are split into groups according to their proximity to the perturbed mass, based on the different time evolution in their respective transient motion. For the localized vibration with three masses, there are only two nodes in the reduced network, corresponding to the two distinct states in the time series. The functional networks make no distinction of the specific dynamics of a single oscillator, there is no difference in the results for a single-period localized vibration or a higher-periodic localized vibration. This finding is closely related to studies concerning the detection of network size from sparse measurements [58,59], or data-based reduced order modeling [60,61] and could be a starting point for further investigation. A novel reduced-order modeling approach could entail clustering degrees of freedom according to their dynamical similarity instead of the geometrical connection, as for example in the combination "35" in network (c) in Fig. 6. Perhaps the detected network size could also be a proxy for the complexity of the underlying dynamics, indicating the number of active states. The identified number of system states yields useful information on how many sensors are necessary to resolve the dynamics of the full system, as well as where to place them. For example, from network (a) in Fig. 6, it can be assumed that a single sensor placed on any of the components is sufficient to get complete measurement of the system dynamics, while for network (c), three sensors are required. This assumption is of course limited to cases such as the one presented here, where number and combination of nodes in the condensed network does not change over time.

Additionally, the presented method can track the time evolution of inter-dependencies within a system, because only a short time series is necessary for the setup of the network [21]. By exploiting this time-evolving network, the interplay of oscillators

during the synchronization process can be made visible. In the case at hand, the mechanism is not simply defined by one mass pulling the others along, but a more intricate process during which the hierarchy of oscillators changes, which ultimately leads to all masses oscillating with the high amplitude. Based on these observations, this method could represent a possibility for developing early warning strategies against dynamical transitions, which might be applied in structural health monitoring. Additionally, this approach could also help understanding the dependencies within a machine and thus form the basis for interfering with the process to avoid catastrophic events. Here, it could be possible to prevent the initial system disturbance from spreading over the entire system by simply disrupting the process or changing one of the intermediate components. For example, further studies might help to identify joints which are especially relevant for the system dynamics, such that modeling and design efforts can be focused accordingly. A possible extension to the proposed method is the distinction between direct and indirect coupling [33], similar to methods proposed in [62–64].

The results presented in this work are obtained from time series data with no added noise. For future application to real-world data, which is generally noise contaminated, the effects of noise on the functional network will be taken into account. The effects of noise on statistical features of the recurrence plot and respective analysis have been studied in detail for example in [65]. While recurrence-based analyses are generally very susceptible to noise, reliable results can still be obtained for moderate noise levels (below 20% of the standard deviation of the underlying time series), when the threshold parameter ε is chosen appropriately [15,65]. Even though detailed studies on the effect of noise on this specific recurrence-based method are still required, we are confident that our method would work for low to moderate noise levels.

6. Conclusion

In this work, an approach for inferring functional networks from data obtained from mechanical model systems is introduced, which hopes to complement conventional tools for the analysis of large multi-component systems. By assigning each physical component one network node, and connecting the nodes based on inter-system network measures cross-clustering coefficient and cross-transitivity, the functional network provides a new, function-based perspective on the dynamics of complex mechanical systems. The method is applied to a system of five Duffing oscillators with nearest-neighbor coupling operating in different dynamical states such as uniform oscillation, localized vibrations, and fronts. For each of these, a functional network is computed. By concatenating "equivalent" nodes together, a condensed network is obtained, which allows for a number of different network-based analyses. The size of the condensed network, given by the number of nodes, corresponds to the number of different dynamical states within a system. Each of the nodes within the condensed network form a functional cluster of dynamically similar components, and capture the symmetry within the system dynamics. Links between the clusters represent functional dependencies within the dynamical system. These functional relationships encode the global system state. These analyses could provide a basis for better sensor placement, insight into dynamic symmetries and thus a more efficient system analysis. The study of transient motion, or the propagation of a disturbance through the system, is made possible with a sliding-window technique. By analyzing small samples of the time series data over the course of time, the propagation of a disturbance through the dynamical system is studied. The corresponding functional networks facilitate the analysis of the transient dynamics and the interplay of the system components over time. We hope that this analysis of transient dynamics using network methods will pave the way for further studies, improved sensor placement, early warning methods, and counter-measures against potentially harmful vibrations.

CRediT authorship contribution statement

Charlotte Geier: Writing – review & editing, Writing – original draft, Visualization, Software, Methodology, Investigation, Formal analysis, Conceptualization. **Merten Stender:** Writing – review & editing, Funding acquisition. **Norbert Hoffmann:** Writing – review & editing, Supervision, Funding acquisition, Conceptualization.

Declaration of competing interest

The authors declare that they have no known competing financial interests or personal relationships that could have appeared to influence the work reported in this paper.

Data availability

Data will be made available on request.

Acknowledgments

C.G. is thankful to the DFG (German Research Foundation) for support through project number 510246309. The authors would like to thank Mathies Wedler for proof reading the article.

Appendix. Initial conditions for numerical data

See Table A.1.

Table A.1
Initial conditions for the numerical data generation presented in Section 2. The data resulting data is depicted in Fig. 3.

Case	Initial condition
(a)	$\boldsymbol{x}_{0,\mathrm{a}} = [0,0,0,0,0,0,0,0,0,0]$
(b)	$\boldsymbol{x}_{0,\mathrm{b}} = [1,1,1,1,1,0,0,0,0,0]$
(c)	$\boldsymbol{x}_{0,\mathrm{c}} = [0,0,0,1,0,0,0,0,0,0]$
(d)	$\boldsymbol{x}_{0,\mathrm{d}} = [0,1,1,1,0,0,0,0,0,0]$
(e)	$\boldsymbol{x}_{0,\mathrm{e}} = [0,0,0,0,0,0,0,0,0,0]$
(f)	$\boldsymbol{x}_{0,\mathrm{f}} = [0,0,0,0,0,0,0,0,0,0]$
(g)	$\boldsymbol{x}_{0,\mathrm{g}} = [1,0,0,0,0,0,0,0,0,0]$
(h)	$\boldsymbol{x}_{0,\mathrm{h}} = [0,1,1,1,1,0,0,0,0,0]$

References

[1] M. Stender, S. Oberst, M. Tiedemann, N. Hoffmann, Complex machine dynamics: systematic recurrence quantification analysis of disk brake vibration data, Nonlinear Dynam. 97 (4) (2019) 2483–2497, http://dx.doi.org/10.1007/s11071-019-05143-x.

[2] A. Papangelo, F. Fontanela, A. Grolet, M. Ciavarella, N. Hoffmann, Multistability and localization in forced cyclic symmetric structures modelled by weakly-coupled duffing oscillators, J. Sound Vib. 440 (1859) (2019) 202–211, http://dx.doi.org/10.1016/j.jsv.2018.10.028.

[3] M.R. Brake, The Mechanics of Jointed Structures, first ed., Springer International Publishing AG, Cham, 2018, http://dx.doi.org/10.1007/978-3-319-56818-8.

[4] S. Kruse, M. Tiedemann, B. Zeumer, P. Reuss, H. Hetzler, N. Hoffmann, The influence of joints on friction induced vibration in brake squeal, J. Sound Vib. 340 (2015) 239–252, http://dx.doi.org/10.1016/j.jsv.2014.11.016.

[5] A.T. Mathis, N.N. Balaji, R.J. Kuether, A.R. Brink, M.R.W. Brake, D.D. Quinn, A review of damping models for structures with mechanical Joints1, Appl. Mech. Rev. 72 (4) (2020) http://dx.doi.org/10.1115/1.4047707.

[6] M.S. Gadala, M.A. Dokainish, G.A. Oravas, Formulation methods of geometric and material nonlinearity problems, Internat. J. Numer. Methods Engrg. 20 (5) (1984) 887–914, http://dx.doi.org/10.1002/nme.1620200508.

[7] F. Walport, L. Gardner, E. Real, I. Arrayago, D.A. Nethercot, Effects of material nonlinearity on the global analysis and stability of stainless steel frames, J. Constr. Steel Res. 152 (2019) 173–182, http://dx.doi.org/10.1016/j.jcsr.2018.04.019.

[8] G. de Sitter, C. Devriendt, P. Guillaume, E. Pruyt, Operational transfer path analysis, Mech. Syst. Signal Process. 24 (2) (2010) 416–431, http://dx.doi.org/10.1016/j.ymssp.2009.07.011.

[9] D.J. Ewins, Modal Testing: Theory and Practice, second ed., Research Studies Press, Baldock, England, 2000.

[10] D. de Klerk, A. Ossipov, Operational transfer path analysis: Theory, guidelines and tire noise application, Mech. Syst. Signal Process. 24 (7) (2010) 1950–1962, http://dx.doi.org/10.1016/j.ymssp.2010.05.009.

[11] R. Albert, A.-L. Barabási, Statistical mechanics of complex networks, Rev. Mod. Phys. 74 (1) (2002) 47–97, http://dx.doi.org/10.1103/RevModPhys.74.47.

[12] P.B. Jain, T.T. Nguyen, R.C. Budzinski, J. Mináč, L.E. Muller, Synchronization patterns and stability of solutions in multiplex networks of nonlinear oscillators, 2023, http://dx.doi.org/10.48550/arXiv.2306.06532, arXiv preprint.

[13] L. Lacasa, R. Toral, Description of stochastic and chaotic series using visibility graphs, Phys. Rev. E 82 (3) (2010) 1078, http://dx.doi.org/10.1103/PhysRevE.82.036120.

[14] M. Newman, Networks, second ed., Oxford University Press, Oxford, 2018, http://dx.doi.org/10.1093/oso/9780198805090.001.00010.

[15] Y. Zou, R.V. Donner, N. Marwan, J.F. Donges, J. Kurths, Complex network approaches to nonlinear time series analysis, Phys. Rep. 787 (2019) 1–97, http://dx.doi.org/10.1016/j.physrep.2018.10.005.

[16] L. Astolfi, F. Cincotti, D. Mattia, M.G. Marciani, L.A. Baccala, F. de Vico Fallani, S. Salinari, M. Ursino, M. Zavaglia, L. Ding, J.C. Edgar, G.A. Miller, B. He, F. Babiloni, Comparison of different cortical connectivity estimators for high-resolution EEG recordings, Hum. Brain Mapp. 28 (2) (2007) 143–157, http://dx.doi.org/10.1002/hbm.20263.

[17] X. Zhang, S. Hallerberg, M. Matthiae, D. Witthaut, M. Timme, Fluctuation-induced distributed resonances in oscillatory networks, Science 5 (7) (2019) eaav1027, http://dx.doi.org/10.1126/sciadv.aav1027.

[18] X. Zhang, M. Timme, Fluctuation response patterns of network dynamics – An introduction, Eur. J. Appl. Math. 34 (3) (2023) 429–466, http://dx.doi.org/10.1017/S0956792522000201.

[19] M. McCullough, K. Sakellariou, T. Stemler, M. Small, Regenerating time series from ordinal networks, Chaos 27 (3) (2017) 035814, http://dx.doi.org/10.1063/1.4978743.

[20] J. Zhang, J. Sun, X. Luo, K. Zhang, T. Nakamura, M. Small, Characterizing pseudoperiodic time series through the complex network approach, Phys. D 237 (22) (2008) 2856–2865, http://dx.doi.org/10.1016/j.physd.2008.05.008.

[21] J.H. Feldhoff, R.V. Donner, J.F. Donges, N. Marwan, J. Kurths, Geometric detection of coupling directions by means of inter-system recurrence networks, Phys. Lett. A 376 (46) (2012) 3504–3513, http://dx.doi.org/10.1016/j.physleta.2012.10.008.

[22] T. Tanizawa, T. Nakamura, F. Taya, M. Small, Constructing directed networks from multivariate time series using linear modelling technique, Phys. A 512 (2018) 437–455, http://dx.doi.org/10.1016/j.physa.2018.08.137.

[23] M.A. Kramer, U.T. Eden, S.S. Cash, E.D. Kolaczyk, Network inference - with confidence - from multivariate time series, Phys. Rev. E 79 (6) (2009) 528, http://dx.doi.org/10.1103/PhysRevE.79.061916.

[24] A. Gozolchiani, K. Yamasaki, O. Gazit, S. Havlin, Pattern of climate network blinking links follows El Niño events, Europhys. Lett. 83 (2) (2008) 28005, http://dx.doi.org/10.1209/0295-5075/83/28005.

[25] Z.-K. Gao, X.-W. Zhang, N.-D. Jin, N. Marwan, J. Kurths, Multivariate recurrence network analysis for characterizing horizontal oil-water two-phase flow, Phys. Rev. E 88 (3) (2013) 032910, http://dx.doi.org/10.1103/PhysRevE.88.032910.

[26] Z.-K. Gao, Y.-X. Yang, Q. Cai, S.-S. Zhang, N.-D. Jin, Multivariate weighted recurrence network inference for uncovering oil-water transitional flow behavior in a vertical pipe, Chaos 26 (6) (2016) 063117, http://dx.doi.org/10.1063/1.4954271.

[27] Z.-K. Gao, Y.-X. Yang, L.-S. Zhai, W.-D. Dang, J.-L. Yu, N.-D. Jin, Multivariate multiscale complex network analysis of vertical upward oil-water two-phase flow in a small diameter pipe, Sci. Rep. UK 6 (2016) 20052, http://dx.doi.org/10.1038/srep20052.

[28] L. Lacasa, V. Nicosia, V. Latora, Network structure of multivariate time series, Sci. Rep. UK 5 (2015) 15508, http://dx.doi.org/10.1038/srep15508.

[29] D. Eroglu, N. Marwan, M. Stebich, J. Kurths, Multiplex recurrence networks, Phys. Rev. E 97 (1) (2018) 1, http://dx.doi.org/10.1103/PhysRevE.97.012312.

[30] M.C. Romano, M. Thiel, J. Kurths, I.Z. Kiss, J.L. Hudson, Detection of synchronization for non-phase-coherent and non-stationary data, Europhys. Lett. 71 (3) (2005) 466–472, http://dx.doi.org/10.1209/epl/i2005-10095-1.

[31] J.H. Feldhoff, R.V. Donner, J.F. Donges, N. Marwan, J. Kurths, Geometric signature of complex synchronisation scenarios, Europhys. Lett. 102 (3) (2013) 30007, http://dx.doi.org/10.1209/0295-5075/102/30007.
[32] M. Jachan, K. Henschel, J. Nawrath, A. Schad, J. Timmer, B. Schelter, Inferring direct directed-information flow from multivariate nonlinear time series, Phys. Rev. E 80 (1 Pt 1) (2009) 011138, http://dx.doi.org/10.1103/PhysRevE.80.011138.
[33] J. Zhang, J. Zhou, M. Tang, H. Guo, M. Small, Y. Zou, Constructing ordinal partition transition networks from multivariate time series, Sci. Rep. UK 7 (1) (2017) 7795, http://dx.doi.org/10.1038/s41598-017-08245-x.
[34] G. Terrones, D.W. McLaughlin, E.A. Overman, A.J. Pearlstein, Stability and bifurcation of spatially coherent solutions of the damped-driven NLS equation, SIAM J. Appl. Math. 50 (3) (1990) 791–818, http://dx.doi.org/10.1137/0150046.
[35] D.J. Kaup, A.C. Newell, Theory of nonlinear oscillating dipolar excitations in one-dimensional condensates, Phys. Rev. B 18 (10) (1978) 5162–5167, http://dx.doi.org/10.1103/PhysRevB.18.5162.
[36] F. Fontanela, Solitons in Cyclic and Symmetric Structures (Ph.D. thesis), Imerial College London, 2018.
[37] T. Hoffmann, L. Panning-von Scheidt, J. Wallaschek, Analysis of contacts in friction damped turbine blades using dimensionless numbers, J. Eng. Gas Turb. Power 141 (12) (2019) http://dx.doi.org/10.1115/1.4044481.
[38] T. Hoffmann, L. Panning-von Scheidt, J. Wallaschek, Measured and simulated forced response of a rotating turbine disk with asymmetric and cylindrical underplatform dampers, J. Eng. Gas Turb. Power 142 (5) (2020) http://dx.doi.org/10.1115/1.4045337.
[39] I. Kovacic, M.J. Brennan, The Duffing Equation: Nonlinear Oscillators and Their Phenomena, first ed., John Wiley & Sons, Ltd., Chichester West Sussex U.K. and Hoboken N.J., 2011, http://dx.doi.org/10.1002/97804709778590.
[40] Y. Ueda, Survey of regular and chaotic phenomena in the forced duffing oscillator, Chaos Solitons Fractals 1 (3) (1991) 199–231, http://dx.doi.org/10.1016/0960-0779(91)90032-5.
[41] M. Stender, N. Hoffmann, bSTAB: an open-source software for computing the basin stability of multi-stable dynamical systems, Nonlinear Dynam. 107 (2) (2022) 1451–1468, http://dx.doi.org/10.1007/s11071-021-06786-5.
[42] Y.S. Kivshar, M. Peyrard, Modulational instabilities in discrete lattices, Phys. Rev. A 46 (6) (1992) 3198–3205, http://dx.doi.org/10.1103/PhysRevA.46.3198.
[43] A. Papangelo, N. Hoffmann, A. Grolet, M. Stender, M. Ciavarella, Multiple spatially localized dynamical states in friction-excited oscillator chains, J. Sound Vib. 417 (2018) 56–64, http://dx.doi.org/10.1016/j.jsv.2017.11.056.
[44] P. Virtanen, R. Gommers, T.E. Oliphant, M. Haberland, T. Reddy, D. Cournapeau, E. Burovski, P. Peterson, W. Weckesser, J. Bright, S.J. van der Walt, M. Brett, J. Wilson, K.J. Millman, N. Mayorov, A.R.J. Nelson, E. Jones, R. Kern, E. Larson, C.J. Carey, İ. Polat, Y. Feng, E.W. Moore, J. VanderPlas, D. Laxalde, J. Perktold, R. Cimrman, I. Henriksen, E.A. Quintero, C.R. Harris, A.M. Archibald, A.H. Ribeiro, F. Pedregosa, P. van Mulbregt, SciPy 1.0 Contributors, SciPy 1.0: Fundamental Algorithms for Scientific Computing in Python, Nature Methods 17 (2020) 261–272, http://dx.doi.org/10.1038/s41592-019-0686-2.
[45] E. Hairer, G. Wanner, S.P.N. rsett, Solving Ordinary Differential Equations I, vol. 8, Springer Berlin Heidelberg, Berlin, Heidelberg, 1993, http://dx.doi.org/10.1007/978-3-540-78862-1.
[46] J.F. Donges, J. Heitzig, R.V. Donner, J. Kurths, Analytical framework for recurrence-network analysis of time series, Phys. Rev. E 85 (4) (2012) 1, http://dx.doi.org/10.1103/PhysRevE.85.046105.
[47] R.V. Donner, Y. Zou, J.F. Donges, N. Marwan, J. Kurths, Recurrence networks—a novel paradigm for nonlinear time series analysis, New J. Phys. 12 (3) (2010) 033025, http://dx.doi.org/10.1088/1367-2630/12/3/033025.
[48] R.V. Donner, Y. Zou, J.F. Donges, N. Marwan, J. Kurths, Ambiguities in recurrence-based complex network representations of time series, Phys. Rev. E 81 (1 Pt 2) (2010) 015101, http://dx.doi.org/10.1103/PhysRevE.81.015101.
[49] R.V. Donner, M. Small, J.F. Donges, N. Marwan, Y. Zou, R. Xiang, J. Kurths, Recurrence-based time series analysis by means of complex network methods, Int. J. Bifurcation Chaos 21 (04) (2011) 1019–1046, http://dx.doi.org/10.1142/S0218127411029021.
[50] N. Marwan, J.F. Donges, Y. Zou, R.V. Donner, J. Kurths, Complex network approach for recurrence analysis of time series, Phys. Lett. A 373 (46) (2009) 4246–4254, http://dx.doi.org/10.1016/j.physleta.2009.09.042.
[51] N. Marwan, C.M. Romano, M. Thiel, J. Kurths, Recurrence plots for the analysis of complex systems, Phys. Rep. 438 (5–6) (2007) 237–329, http://dx.doi.org/10.1016/j.physrep.2006.11.001.
[52] N. Marwan, K.H. Kraemer, Trends in recurrence analysis of dynamical systems, Eur. Phys. J. Spec. Top. 232 (1) (2023) 5–27, http://dx.doi.org/10.1140/epjs/s11734-022-00739-8.
[53] N. Marwan, A historical review of recurrence plots, Eur. Phys. J. Spec. Top. 164 (1) (2008) 3–12, http://dx.doi.org/10.1140/epjst/e2008-00829-1.
[54] D. Eroglu, N. Marwan, S. Prasad, J. Kurths, Finding recurrence networks' threshold adaptively for a specific time series, Nonlinear Proc. Geophys. 21 (6) (2014) 1085–1092, http://dx.doi.org/10.5194/npg-21-1085-2014.
[55] J.F. Donges, J. Heitzig, B. Beronov, M. Wiedermann, J. Runge, Q.Y. Feng, L. Tupikina, V. Stolbova, R.V. Donner, N. Marwan, H.A. Dijkstra, J. Kurths, Unified functional network and nonlinear time series analysis for complex systems science: The pyunicorn package, Chaos 25 (11) (2015) 113101, http://dx.doi.org/10.1063/1.4934554.
[56] J.F. Donges, H.C.H. Schultz, N. Marwan, Y. Zou, J. Kurths, Investigating the topology of interacting networks, Eur. Phys. J. B 84 (4) (2011) 635–651, http://dx.doi.org/10.1140/epjb/e2011-10795-8.
[57] F.D. Malliaros, M. Vazirgiannis, Clustering and community detection in directed networks: A survey, Phys. Rep. 533 (4) (2013) 95–142, http://dx.doi.org/10.1016/j.physrep.2013.08.002.
[58] G. Börner, H. Haehne, J. Casadiego, M. Timme, Revealing system dimension from single-variable time series, Chaos 33 (7) (2023) http://dx.doi.org/10.1063/5.0156448.
[59] H. Haehne, J. Casadiego, J. Peinke, M. Timme, Detecting hidden units and network size from perceptible dynamics, Phys. Rev. Lett. 122 (15) (2019) 158301, http://dx.doi.org/10.1103/PhysRevLett.122.158301.
[60] C. Geier, M. Stender, N. Hoffmann, Data-driven reduced order modeling for mechanical oscillators using koopman approaches, Front. Appl. Math. Statist. 9 (2023) http://dx.doi.org/10.3389/fams.2023.1124602.
[61] S.L. Brunton, J.L. Proctor, J.N. Kutz, Discovering governing equations from data by sparse identification of nonlinear dynamical systems, Proc. Natl. Acad. Sci. USA 113 (15) (2016) 3932–3937, http://dx.doi.org/10.1073/pnas.1517384113.
[62] J. Nawrath, M.C. Romano, M. Thiel, I.Z. Kiss, M. Wickramasinghe, J. Timmer, J. Kurths, B. Schelter, Distinguishing direct from indirect interactions in oscillatory networks with multiple time scales, Phys. Rev. Lett. 104 (3) (2010) 038701, http://dx.doi.org/10.1103/PhysRevLett.104.038701.
[63] Y. Zou, M.C. Romano, M. Thiel, N. Marwan, J. Kurths, Inferring indirect coupling by means of recurrences, Int. J. Bifurcation Chaos 21 (04) (2011) 1099–1111, http://dx.doi.org/10.1142/S0218127411029033.
[64] A. Groth, Visualization of coupling in time series by order recurrence plots, Phys. Rev. E 72 (4 Pt 2) (2005) 046220, http://dx.doi.org/10.1103/PhysRevE.72.046220.
[65] M. Thiel, M. Romano, J. Kurths, R. Meucci, E. Allaria, F. Arecchi, Influence of observational noise on the recurrence quantification analysis, Phys. D 171 (3) (2002) 138–152, http://dx.doi.org/10.1016/S0167-2789(02)00586-9.

5 Towards novel perspectives on nonlinear machine dynamics

This chapter discusses and contextualizes the various methodologies presented throughout this work. Different perspectives on system analysis are compared, specifically focusing on prior assumptions, model interpretability, and applicability in data-based methods. Parallels and differences of the approaches and resulting model perspectives are highlighted, placing them in the broader field of complexity science. This discussion is structured into four sections: The first section is concerned with the methodological framework, comparing the different procedures presented throughout this work. The resulting models are analyzed in the second paragraph, concentrating on model interpretability and perspectives. The third paragraph provides an embedding into the sciences beyond mechanical vibrations, presenting mixed methods and the relation to complexity science. The final passage gives an outlook on future research directions.

Methodological frameworks: procedures and methods
Across the various methods introduced in this work, an overarching principle emerges: the route from low-dimensional input data via high-dimensional embedding spaces to low-dimensional, human-interpretable outputs. The low-dimensional input is given by a single, one-dimensional time series in Section 3.1.1 and Section 4.1, parameter-sparse measurement data in Section 3.2.1, and full-scale oscillatory information in Section 4.3. High-dimensional embeddings are facilitated by the delay embedding into a Hankel matrix in Section 3.1.1, mapping into a multi-layer deep neural network in Section 3.2.1, and cross-recurrence-based analysis in Sections 4.1 and 4.3. Three different approaches to information condensation, via singular value decomposition in Section 3.1.1, information mapping in Section 3.2.1, and network condensation via strongly connected components in Section 4.3, result in three different perspectives on the underlying system, namely an ordinary differential equation, a state map, and a reduced-order network, respectively.
Each modeling approach brings different prior assumptions on the underlying system with it: From the fixed model form in the HAVOK algorithm in Section 3.1.1, to the fixed model dimensions in the neural network-based procedure in Section 3.2.1, to the fixed structuring of the system into different parts, or measurement sections, in Section 4.3. Consequently, each method comes with its own set of hyper-parameters and tuning requirements, which are discussed in the respective sections.
Additionally, this work has presented different ideas for dealing with data sparsity and reduced-order modeling, both of which could be employed individually and outside of the context of the given case study. Time delay embedding, as seen in the setup of the Hankel matrix in Section 3.1.1, is a well-established method for reconstructing the phase space of

a dynamical system from a one-dimensional time series data, dating back to the seminal work by Takens [306]. While delay embedding addresses data sparsity in space, the data augmentation procedure sketched out in Section 3.2.1 focuses on data sparsity in parameter space. With the singular value decomposition of the Hankel matrix, a pooling layer in the convolutional neural network, and the strongly connected components of the functional network, three different takes on reduced-order modeling have been illustrated. Each approach underlines a different aspect of the high-dimensional model during the reduction. The singular value decomposition simultaneously provides a low-rank approximation and a system-specific model basis. It can therefore be interpreted as a generalization of the Fourier transform, which provides a generic basis [4]. This approach yields a reduction in dynamical complexity. Similarly, the Max Pooling Layer in the convolutional neural network takes the maximum value of the high-dimensional data within a given sliding window, down-sampling the complexity of the high-dimensional pattern. The strongly connected components provide a dimensionality reduction on two levels, first by condensing the high-dimensional cross-recurrence plot into a coupling direction via the cross-clustering and cross-transitivity coefficients, and second by coarse-graining physical space via the clustering of closely related system components.

Resulting models: perspectives and interpretability
Each method offers a distinct view of a dynamical system via a separate model type. Models in this work range from "classical" representations such as linear ordinary differential equations in Section 3.1.1 via maps of a user-defined system state in Section 3.2.1 to different network descriptions, for example of functional component inter-dependencies, in Chapter 4. The order in which the methods are named reflects the transition from first principles of physics towards more phenomenon-based descriptions.
The equation-based model might intuitively appear as the most interpretable because of its amenability to analysis with conventional, well-tested methods. However, this assumption can be treacherous, since the model does not necessarily capture all of the dynamic properties of the underlying system, as has been explored in Section 3.1.1. Still, this perspective remains perhaps the most familiar one to the reader. It is, in theory, the most generalizable of the three, capturing system properties such as its stability, while also encompassing predictive capabilities.
While the neural network in itself is not accessible for human interpretation, the resulting state map provides a low-threshold description of the underlying system state that is interpretable even without a deeper mathematical understanding. However, this machine learning-based model does not generalize, it can only be queried for the task it was trained to perform. In this case, the neural network can classify system states, but cannot predict future system behavior in terms of time series data. Through the user-defined definition of the system state, this approach allows for the analysis of states beyond the classical stability- or dynamics-based descriptions, broadening the view for more human-intuitive ideas.
The network-based descriptions provide different views on the underlying system while paving the way for network-based analysis of mechanical systems. The functional network-based approach offers a view between the translation of dynamics into network topology and the static or dynamic network perspective. These models provide insight into the

hitherto largely neglected phenomenon of functional connectivity in mechanical structures. The condensed network description gives an intuition on the number of dynamically distinct components within a given system, describes their interrelationships via arrows, and can even be leveraged for detecting dynamical transitions, as illustrated in Section 4.3.

Beyond mechanical structures: mixed methods and complexity science
The different approaches presented in this work can be merged to combine their advantages or to adapt them to a specific use case. Examples of combinations of physics-based and machine learning techniques, such as PINNs [151–153], or equation learning with neural networks, such as autoencoders [102] or SINDy-reinforcement learning [106], have already been introduced in Section 3.2. Other methods use network-based insights to build more efficient machine learning models, for example, by leveraging the network structure of the underlying system in a reservoir computer [307] or by using network methods to describe symmetries in a reservoir computer [308]. Graph neural networks combine deep learning and structure-based methods to obtain generalizing, interpretable models from data represented in graph form [81, 309, 310]. These examples illustrate the ongoing strive for novel perspectives and innovative methods in dynamical systems science.

The methods in this work are, in principle, applicable to any dynamical system and often originate at least in part from other disciplines. This interdisciplinarity is one of the pillars of complexity science, which studies the qualitatively novel macroscopic behavior that emerges from the collective dynamics of individual components [173]. The origin of complexity science is often attributed to Anderson's seminal work in 1972 [57], where the popular statement "the whole is more than the sum of its parts" was coined. A detailed introduction to the field is given in [9, 16, 17, 311]. Complexity science provides a counterpart to the reductionist idea by stating that the dynamics at a higher level cannot be explained simply by the governing laws at a lower level [9]. The notion of scales in time and space in this context is highly important, as different levels of abstraction of the same system might exhibit different dynamical phenomena [9, 17, 312], and it is therefore crucial to identify the relevant scale for a given problem. Notions of symmetry breaking, such as the mass variation that leads to a localized vibration, as a driving factor in the emergence of complex dynamics, are common factors [17, 57], as is the search for structure and patterns at different levels [311]. Common applications of complex models include biological networks, the human brain, social networks, the internet, and the climate [173]. The relation of this work to complexity science is underlined by the parallels of the approaches to applications in completely different fields: The social sciences study similar phenomena using a different terminology [169], such as collective human decision-making [15], biology models the interaction of alive agents such as the collective dynamics of fish swarms [13, 181], and complex adaptive systems are concerned with the trans-disciplinary study of interactions of intelligent agents [18]. All these methods study the interactions of many interacting components or agents and the dynamics that arise from their interplay.

Outlook: Future research directions
The network science-based analysis of the nonlinear dynamics of mechanical structures is a mostly undiscovered field and thus contains vast potential for future work. Here, three of them will be highlighted: The development of a rigorous framework for the description

of mechanical systems in network form, which contains uncertainty quantification, noise treatment, and model quantification, the introduction of true time-continuity beyond the analysis of time series samples in a sliding window fashion, and the combination of spatial and dynamical analyses at a more fundamental level, for example, by generating adaptive networks from measurement data.

This discussion highlights the interconnectedness of scientific methodologies as data-based descriptions, facilitating phenomenon-focused modeling that can be applied trans-disciplinary. Motivated by the idea that patterns might only be recognizable across scientific disciplines and in the spirit of complexity science, this work hopes to encourage interdisciplinary exchange on modeling techniques and perspectives.

6 Conclusion

This work has explored the dynamics of large-scale mechanical systems with numerous interacting components from multiple points of view on the way to developing a network perspective. Starting with a description of the phenomena and challenges in the nonlinear dynamics of mechanical structures, Chapter 2 moves on to the "classical", physics-based modeling approaches in structural dynamics. The default lumped-mass modeling scheme is presented, and additional viewpoints are derived from it. These different representations illustrate the power of distinct perspectives such as equations, recurrence plots, and bifurcation diagrams to yield insights about various aspects of the same dynamical system. Motivated by this demonstration, the remaining chapters focus on developing novel perspectives and modeling schemes.

Data-driven perspectives in terms of statistical and machine learning are presented in Chapter 3, highlighting the trade-off between interpretability and generalizability that is often present in modeling methods. Two case studies pose practical examples of the applications of statistical and machine learning methods to the dynamics of mechanical structures. The first study uses equation learning to distill a linear state space model from synthetic data. While the resulting model is, in principle, amenable to analysis with state-of-the-art methods, the study demonstrates that the model is limited in representing nonlinearities. The second study uses neural network-based techniques to learn a mapping of user-defined system states over specified sets of parameters. The generated state map provides a new approach to a well-known description, the bifurcation analysis, and extends the concept to user-defined states not limited to system stability.

Chapter 4 develops different network techniques and answers the first research question with a definite "Yes, a network perspective can yield additional insights into the nonlinear dynamics of mechanical structures, and it can do so on different levels." First, the classification of qualitatively different dynamics and tracking of the transitions between them is facilitated by translating time series data into network topology. Second, the importance of specific components and connections within a mechanical structure can be analyzed by interpreting its components and physical connections as a network. Third, a functional network description captures the dynamical interplay of system components beyond their geometrical proximity, reveals symmetries in the dynamics, and can track transitions in the global system dynamics. These data-driven approaches appear unhindered by transients, nonlinearities, and minor parameter uncertainties.

The discussion in Chapter 5 connects the different methods and models and highlights the advantages of interdisciplinary approaches for describing nonlinear dynamical systems. This chapter provides the answer to the second and third research question by explaining the benefits of the different, increasingly unconventional descriptions. The model focuses on a specific property of the underlying system, such as a user-defined state of a functional interrelation, instead of incorporating every detail into a single model. At the same time, it provides a more holistic approach for the combined analysis of structure and dynamics.

The findings in this work each provide their own contribution to a better design, analysis and operation of mechanical systems, from providing methods for data-based system identification, via strategies for inferring state mappings and analyses from data, to approaches to uncover functional relationships within data. The results of this thesis will hopefully motivate further research endeavors, which may offer new perspectives and a deeper understanding not only of the nonlinear dynamics of mechanical systems but of dynamical systems in general.

Bibliography

[1] L. Faulkner and J. L. Earl. *Handbook of machinery dynamics*. CRC Press, 2000.

[2] W. Skolaut. *Maschinenbau: Ein Lehrbuch für das ganze Bachelor-Studium*. Springer-Verlag, 2018.

[3] M. Stender, S. Oberst, M. Tiedemann, and N. Hoffmann. "Complex machine dynamics: systematic recurrence quantification analysis of disk brake vibration data". *Nonlinear Dynamics* 97.4 (2019), pp. 2483–2497. DOI: 10.1007/s11071-019-05143-x.

[4] S. L. Brunton and J. N. Kutz. *Data-driven science and engineering: Machine learning, dynamical systems, and control*. Second edition. Cambridge: Cambridge University Press, 2022.

[5] A. Martin and F. Thouverez. "Dynamic analysis and reduction of a cyclic symmetric system subjected to geometric Nonlinearities". *Journal of Engineering for Gas Turbines and Power* 141.4 (2019). DOI: 10.1115/1.4041001.

[6] C. Touzé, A. Vizzaccaro, and O. Thomas. "Model order reduction methods for geometrically nonlinear structures: a review of nonlinear techniques". *Nonlinear Dynamics* 105.2 (2021), pp. 1141–1190. DOI: 10.1007/s11071-021-06693-9.

[7] M. Stender, M. Di Bartolomeo, F. Massi, and N. Hoffmann. "Revealing transitions in friction-excited vibrations by nonlinear time-series analysis". *Nonlinear Dynamics* 98.4 (2019), pp. 2613–2630. DOI: 10.1007/s11071-019-04987-7.

[8] M. R. Brake. *The Mechanics of Jointed Structures*. Cham: Springer International Publishing, 2018. DOI: 10.1007/978-3-319-56818-8.

[9] M. Mitchell. *Complexity: A guided tour*. Oxford University Press paperback. Oxford and New York: Oxford university press, 2011.

[10] J. F. Donges, Y. Zou, N. Marwan, and J. Kurths. "Complex networks in climate dynamics". *The European Physical Journal Special Topics* 174.1 (2009), pp. 157–179. DOI: 10.1140/epjst/e2009-01098-2.

[11] J. F. Donges, Y. Zou, N. Marwan, and J. Kurths. "The backbone of the climate network". *EPL (Europhysics Letters)* 87.4 (2009), p. 48007. DOI: 10.1209/0295-5075/87/48007.

[12] A. Gozolchiani, K. Yamasaki, O. Gazit, and S. Havlin. "Pattern of climate network blinking links follows El Niño events". *EPL (Europhysics Letters)* 83.2 (2008), p. 28005. DOI: 10.1209/0295-5075/83/28005.

[13] O. Artime and M. de Domenico. "From the origin of life to pandemics: emergent phenomena in complex systems". *Philosophical Transactions. Series A, Mathematical, Physical, and Engineering Sciences* 380.2227 (2022), p. 20200410. DOI: 10.1098/rsta.2020.0410.

[14] W. Wang, R. Escobedo, S. Sanchez, Z. Han, C. Sire, and G. Theraulaz. "Collective phases and long-term dynamics in a fish school model with burst-and-coast swimming". *Preprint* (2024). DOI: 10.1101/2024.05.26.595998.

[15] J. Holehouse and H. Pollitt. "Non-equilibrium time-dependent solution to discrete choice with social interactions". *PloS one* 17.5 (2022), e0267083. DOI: 10.1371/journal.pone.0267083.

[16] R. Solé, C. P. Kempes, B. Corominas-Murtra, M. de Domenico, A. Kolchinsky, M. Lachmann, E. Libby, S. Saavedra, E. Smith, and D. Wolpert. "Fundamental constraints to the logic of living systems". *Interface Focus* 14.5 (2024), p. 20240010. DOI: 10.1098/rsfs.2024.0010.

[17] D. C. Krakauer. "Symmetry-simplicity, broken symmetry-complexity". *Interface Focus* 13.3 (2023), p. 20220075. DOI: 10.1098/rsfs.2022.0075.

[18] J. H. Holland. *Signals and boundaries: Building blocks for complex adaptive systems*. Cambridge, Massachusetts: The MIT Press, 2014.

[19] S. L. Brunton and J. N. Kutz. *Data-driven science and engineering: Machine learning, dynamical systems, and control*. Second edition. Cambridge: Cambridge University Press, 2022.

[20] N. Marwan. "A historical review of recurrence plots". *The European Physical Journal Special Topics* 164.1 (2008), pp. 3–12. DOI: 10.1140/epjst/e2008-00829-1.

[21] S. Quaegebeur, T. Vadcard, and F. Thouverez. "A new numerical path to retrieve isolated branches on large scale nonlinear mechanical systems". *Nonlinear Dynamics* (2024). DOI: 10.1007/s11071-024-10369-5.

[22] B. Besselink, U. Tabak, A. Lutowska, N. van de Wouw, H. Nijmeijer, D. J. Rixen, M. E. Hochstenbach, and W. Schilders. "A comparison of model reduction techniques from structural dynamics, numerical mathematics and systems and control". *Journal of Sound and Vibration* 332.19 (2013), pp. 4403–4422. DOI: 10.1016/j.jsv.2013.03.025.

[23] C. Huang, K. Duraisamy, and C. Merkle. "Component-Based Reduced Order Modeling of Large-Scale Complex Systems". *Frontiers in Physics* 10 (2022). DOI: 10.3389/fphy.2022.900064.

[24] D. de Klerk, D. J. Rixen, and S. N. Voormeeren. "General Framework for Dynamic Substructuring: History, Review and Classification of Techniques". *AIAA Journal* 46.5 (2008), pp. 1169–1181. DOI: 10.2514/1.33274.

[25] M. Kreutz, F. Trainotti, V. Gimpl, and D. J. Rixen. "On the robust experimental multi-degree-of-freedom identification of bolted joints using frequency-based substructuring". *Mechanical Systems and Signal Processing* 203 (2023), p. 110626. DOI: 10.1016/j.ymssp.2023.110626.

[26] J. Craig. "Coupling of substructures for dynamic analyses - An overview". *41st Structures, Structural Dynamics, and Materials Conference and Exhibit, Atlanta, GA, U.S.A.* (2000). DOI: 10.2514/6.2000-1573.

[27] M. Krack and J. Gross. *Theory of Harmonic Balance: In: Harmonic Balance for Nonlinear Vibration Problems*. Springer, Cham, 2019. DOI: 10.1007/978-3-030-14023-6_2.

[28] Y. Chen, L. Hou, R. Lin, J. Song, T. Y. Ng, and Y. Chen. "A harmonic balance method combined with dimension reduction and FFT for nonlinear dynamic simulation". *Mechanical Systems and Signal Processing* 221 (2024), p. 111758. DOI: 10.1016/j.ymssp.2024.111758.

[29] G. Kerschen, J.-c. Golinval, A. F. Vakakis, and L. A. Bergman. "The Method of Proper Orthogonal Decomposition for Dynamical Characterization and Order Reduction of Mechanical Systems: An Overview". *Nonlinear Dynamics* 41.1-3 (2005), pp. 147–169. DOI: 10.1007/s11071-005-2803-2.

[30] Y. C. Liang, H. P. Lee, S. P. Lim, W. Z. Lin, K. H. Lee, and C. G. Wu. "Proper orthogonal decomposition and its applications - Part I: Theory". *Journal of Sound and Vibration* 252.3 (2002), pp. 527–544. DOI: 10.1006/jsvi.2001.4041.

[31] S. H. Strogatz. *Nonlinear dynamics and chaos: With applications to physics, biology, chemistry and engineering*. Second edition. Boulder (Colorado): Westview Press, 2015.

[32] S. L. Brunton, M. Budišić, E. Kaiser, and J. N. Kutz. "Modern Koopman Theory for Dynamical Systems". *SIAM Review* 64.2 (2022), pp. 229–340. DOI: 10.1137/21M1401243.

[33] M. Stender, M. Tiedemann, D. Spieler, D. Schoepflin, N. Hoffmann, and S. Oberst. "Deep learning for brake squeal: Brake noise detection, characterization and prediction". *Mechanical Systems and Signal Processings* 149 (2021), p. 107181. DOI: https://doi.org/10.1016/j.ymssp.2020.107181.

[34] F. Walport, L. Gardner, E. Real, I. Arrayago, and D. A. Nethercot. "Effects of material nonlinearity on the global analysis and stability of stainless steel frames". *Journal of Constructional Steel Research* 152 (2019), pp. 173–182. DOI: 10.1016/j.jcsr.2018.04.019.

[35] M. S. Gadala, M. A. Dokainish, and G. A. Oravas. "Formulation methods of geometric and material nonlinearity problems". *International Journal for Numerical Methods in Engineering* 20.5 (1984), pp. 887–914. DOI: 10.1002/nme.1620200508.

[36] J. González-Carbajal, D. García-Vallejo, J. Domínguez, and E. Freire. "The role of dynamic friction in the appearance of periodic oscillations in mechanical systems". *Nonlinear Dynamics* 112.24 (2024), pp. 21587–21603. DOI: 10.1007/s11071-024-10162-4.

[37] A. Papangelo, F. Fontanela, A. Grolet, M. Ciavarella, and N. Hoffmann. "Multistability and localization in forced cyclic symmetric structures modelled by weakly-coupled Duffing oscillators". *Journal of Sound and Vibration* 440.1859 (2019), pp. 202–211. DOI: 10.1016/j.jsv.2018.10.028.

[38] A. Bhattu, Y.-C. Lo, G. Zara, P. Hippold, D. Fochler, o. Groß, M. Brake, M. Krack, and E. Ferhatoglu. "Effects of Nonunique Residual Traction on the Non-repeatability of the Dynamics of Jointed Structures" (2024), pp. 65–69. DOI: 10.1007/978-3-031-69409-7_11.

[39] B. Niedergesäß, A. Papangelo, A. Grolet, A. Vizzaccaro, F. Fontanela, L. Salles, A. J. Sievers, and N. Hoffmann. "Experimental observations of nonlinear vibration localization in a cyclic chain of weakly coupled nonlinear oscillators". *Journal of Sound and Vibration* 497 (2021), p. 115952. DOI: 10.1016/j.jsv.2021.115952.

[40] A. Papangelo, N. Hoffmann, A. Grolet, M. Stender, and M. Ciavarella. "Multiple spatially localized dynamical states in friction-excited oscillator chains". *Journal of Sound and Vibration* 417 (2018), pp. 56–64. DOI: 10.1016/j.jsv.2017.11.056.

[41] F. Fontanela. "Solitons in cyclic and symmetric structures". PhD thesis. 2018.

[42] A. Chandrashaker, S. Adhikari, and M. I. Friswell. "Quantification of Vibration Localization in Periodic Structures". *Journal of Vibration and Acoustics* 138.2 (2016). DOI: 10.1115/1.4032032.

[43] P. W. Anderson. "Absence of Diffusion in Certain Random Lattices". *Physical Review* 109.5 (1958), pp. 1492–1505. DOI: 10.1103/PhysRev.109.1492.

[44] M. Thümler, S. G. M. Srinivas, M. Schröder, and M. Timme. "Synchrony for weak coupling in the complexified Kuramoto model". *Physical Review Letters* 130.18 (2023), p. 187201. DOI: 10.1103/PhysRevLett.130.187201.

[45] J. P. Noël and G. Kerschen. "Nonlinear system identification in structural dynamics: 10 more years of progress". *Mechanical Systems and Signal Processing* 83 (2017), pp. 2–35. DOI: 10.1016/j.ymssp.2016.07.020.

[46] M. Brake, C. W. Schwingshackl, and P. Reuß. "Observations of variability and repeatability in jointed structures". *Mechanical Systems and Signal Processing* 129 (2019), pp. 282–307. DOI: 10.1016/j.ymssp.2019.04.020.

[47] A. T. Mathis, N. N. Balaji, R. J. Kuether, A. R. Brink, M. R. W. Brake, and D. D. Quinn. "A review of damping models for structures with mechanical joints". *Applied Mechanics Reviews* 72.4 (2020). DOI: 10.1115/1.4047707.

[48] S. Kruse, M. Tiedemann, B. Zeumer, P. Reuss, H. Hetzler, and N. Hoffmann. "The influence of joints on friction induced vibration in brake squeal". *Journal of Sound and Vibration* 340 (2015), pp. 239–252. DOI: 10.1016/j.jsv.2014.11.016.

[49] S. Schafhirt and M. Muskulus. "Decoupled simulations of offshore wind turbines with reduced rotor loads and aerodynamic damping". *Wind Energy Science* 3.1 (2018), pp. 25–41. DOI: 10.5194/wes-3-25-2018.

[50] M. Krack. "Systems with Contact Nonlinearities". *Exploiting the Use of Strong Nonlinearity in Dynamics and Acoustics. CISM International Centre for Mechanical Sciences*. Ed. by O. Gendelman and A. Vakakis. Vol. 613. Cham: Springer, 2024, pp. 235–272. DOI: 10.1007/978-3-031-56902-9_7.

[51] S. Bograd, P. Reuss, A. Schmidt, L. Gaul, and M. Mayer. "Modeling the dynamics of mechanical joints". *Mechanical Systems and Signal Processing* 25.8 (2011), pp. 2801–2826. DOI: 10.1016/j.ymssp.2011.01.010.

[52] M. R. Brake. "The role of epistemic uncertainty of contact models in the design and optimization of mechanical systems with aleatoric uncertainty". *Nonlinear Dynamics* 77.3 (2014), pp. 899–922. DOI: 10.1007/s11071-014-1350-0.

[53] M. Tiedemann, S. Kruse, and N. Hoffmann. "Dominant damping effects in friction brake noise, vibration and harshness: the relevance of joints". *Proceedings of the Institution of Mechanical Engineers, Part D: Journal of Automobile Engineering* 229.6 (2015), pp. 728–734. DOI: 10.1177/0954407014536378.

[54] B. A. Wernitz and N. P. Hoffmann. "Recurrence analysis and phase space reconstruction of irregular vibration in friction brakes: Signatures of chaos in steady sliding". *Journal of Sound and Vibration* 331.16 (2012), pp. 3887–3896. DOI: 10.1016/j.jsv.2012.04.003.

[55] S. Oberst and J. Lai. "Chaos in brake squeal noise". *Journal of Sound and Vibration* 330.5 (2011), pp. 955–975. DOI: 10.1016/j.jsv.2010.09.009.

[56] S. Oberst and J. Lai. "A statistical approach to estimate the Lyapunov spectrum in disc brake squeal". *Journal of Sound and Vibration* 334 (2015), pp. 120–135. DOI: 10.1016/j.jsv.2014.06.025.

[57] P. W. Anderson. "More is different". *Science* 177.4047 (1972), pp. 393–396. DOI: 10.1126/science.177.4047.393.

[58] M. Stender and N. Hoffmann. "bSTAB: an open-source software for computing the basin stability of multi-stable dynamical systems". *Nonlinear Dynamics* 107.2 (2022), pp. 1451–1468. DOI: 10.1007/s11071-021-06786-5.

[59] P. J. Menck, J. Heitzig, N. Marwan, and J. Kurths. "How basin stability complements the linear-stability paradigm". *Nature Physics* 9.2 (2013), pp. 89–92. DOI: 10.1038/nphys2516.

[60] E. Denimal, J.-J. Sinou, S. Nacivet, and L. Nechak. "Squeal analysis based on the effect and determination of the most influential contacts between the different components of an automotive brake system". *International Journal of Mechanical Sciences* 151 (2019), pp. 192–213. DOI: 10.1016/j.ijmecsci.2018.10.054.

[61] H. Ouyang, Q. Cao, J. E. Mottershead, and T. Treyde. "Vibration and squeal of a disc brake: Modelling and experimental results". *Proceedings of the Institution of Mechanical Engineers, Part D: Journal of Automobile Engineering* 217.10 (2003), pp. 867–875. DOI: 10.1243/095440703769683270.

[62] H. Ouyang, W. Nack, Y. Yuan, and F. Chen. "Numerical analysis of automotive disc brake squeal: a review". *International Journal of Vehicle Noise and Vibration* 1.3/4 (2005), p. 207. DOI: 10.1504/IJVNV.2005.007524.

[63] T. Butlin and J. Woodhouse. "Sensitivity of friction-induced vibration in idealised systems". *Journal of Sound and Vibration* 319.1-2 (2009), pp. 182–198. DOI: 10.1016/j.jsv.2008.05.034.

[64] T. Butlin and J. Woodhouse. "Friction-induced vibration: Quantifying sensitivity and uncertainty". *Journal of Sound and Vibration* 329.5 (2010), pp. 509–526. DOI: 10.1016/j.jsv.2009.09.026.

[65] J.-J. Sinou. "Transient non-linear dynamic analysis of automotive disc brake squeal – On the need to consider both stability and non-linear analysis". *Mechanics Research Communications* 37.1 (2010), pp. 96–105. DOI: 10.1016/j.mechrescom.2009.09.002.

[66] N. Gräbner, M. Tiedemann, U. von Wagner, and N. Hoffmann. "Nonlinearities in Friction Brake NVH - Experimental and Numerical Studies". *SAE Technical Paper 2014-01-2511* (2014). DOI: 10.4271/2014-01-2511.

[67] M. Nouby, D. Mathivanan, and K. Srinivasan. "A combined approach of complex eigenvalue analysis and design of experiments (DOE) to study disc brake squeal". *International Journal of Engineering, Science and Technology* 1.1 (2010). DOI: 10.4314/ijest.v1i1.58084.

[68] G. de Sitter, C. Devriendt, P. Guillaume, and E. Pruyt. "Operational transfer path analysis". *Mechanical Systems and Signal Processing* 24.2 (2010), pp. 416–431. DOI: 10.1016/j.ymssp.2009.07.011.

[69] D. J. Ewins. "The effects of detuning upon the forced vibrations of bladed disks". *Journal of Sound and Vibration* 9.1 (1969), pp. 65–79. DOI: 10.1016/0022-460X(69)90264-8.

[70] D. de Klerk and A. Ossipov. "Operational transfer path analysis: Theory, guidelines and tire noise application". *Mechanical Systems and Signal Processing* 24.7 (2010), pp. 1950–1962. DOI: 10.1016/j.ymssp.2010.05.009.

[71] K. Champion, B. Lusch, J. N. Kutz, and S. L. Brunton. "Data-driven discovery of coordinates and governing equations". *Proceedings of the National Academy of Sciences of the United States of America* 116.45 (2019), pp. 22445–22451. DOI: 10.1073/pnas.1906995116.

[72] L. Ljung. "Perspectives on system identification". *Annual Reviews in Control* 34.1 (2010), pp. 1–12. DOI: 10.1016/j.arcontrol.2009.12.001.

[73] K. Worden and Kerschen, G. and Vakakis, A.F. and Golinval, J.C. "Nonlinear system identification in structural dynamics: A short (and biased) history". *25th International Modal Analysis Conference, Orlando* (2007).

[74] M. Stender, S. Oberst, and N. Hoffmann. "Recovery of Differential Equations from Impulse Response Time Series Data for Model Identification and Feature Extraction". *Vibration* 2.1 (2019), pp. 25–46. DOI: 10.3390/vibration2010002.

[75] R. M. Rosenberg. "The normal modes of nonlinear n-degree-of-freedom systems". *Journal of Applied Mechanics* 29.1 (1962), pp. 7–14. DOI: 10.1115/1.3636501.

[76] S. W. Shaw and C. Pierre. "Non-linear normal modes and invariant manifolds". *Journal of Sound and Vibration* 150.1 (1991), pp. 170–173. DOI: 10.1016/0022-460X(91)90412-D.

[77] S. W. Shaw and C. Pierre. "Normal modes for non-linear vibratory systems". *Journal of Sound and Vibration* 164.1 (1993), pp. 85–124. DOI: 10.1006/jsvi.1993.1198.

[78] N. Boivin, C. Pierre, and S. W. Shaw. "Non-linear normal modes, invariance, and modal dynamics approximations of non-linear systems". *Nonlinear Dynamics* 8.3 (1995), pp. 315–346. DOI: 10.1007/BF00045620.

[79] J.-P. Eckmann, S. O. Kamphorst, and D. Ruelle. "Recurrence Plots of Dynamical Systems". *EPL (Europhysics Letters)* 4.9 (1987), pp. 973–977. DOI: 10.1209/0295-5075/4/9/004.

[80] N. Marwan, M. C. Romano, M. Thiel, and J. Kurths. "Recurrence plots for the analysis of complex systems". *Physics Reports* 438.5-6 (2007), pp. 237–329. DOI: 10.1016/j.physrep.2006.11.001.

[81] P. W. Battaglia, J. B. Hamrick, V. Bapst, A. Sanchez-Gonzalez, V. Zambaldi, M. Malinowski, A. Tacchetti, D. Raposo, A. Santoro, R. Faulkner, C. Gulcehre, F. Song, A. Ballard, J. Gilmer, G. Dahl, A. Vaswani, K. Allen, C. Nash, V. Langston, C. Dyer, N. Heess, D. Wierstra, P. Kohli, M. Botvinick, O. Vinyals, Y. Li, and R. Pascanu. "Relational inductive biases, deep learning, and graph networks". *ArXiv preprint* (2018). DOI: 10.48550/arXiv.1806.01261.

[82] S. L. Brunton, J. L. Proctor, and J. N. Kutz. "Discovering governing equations from data by sparse identification of nonlinear dynamical systems". *Proceedings of the National Academy of Sciences of the United States of America* 113.15 (2016), pp. 3932–3937. DOI: 10.1073/pnas.1517384113.

[83] I. Goodfellow, Y. Bengio, and A. Couville. *Deep Learning*. Adaptive Computation and Machine Learning Series. Cambridge, Mass.: MIT Press Ltd, 2017.

[84] J. N. Kutz and S. L. Brunton. "Parsimony as the ultimate regularizer for physics-informed machine learning". *Nonlinear Dynamics* 107.3 (2022), pp. 1801–1817. DOI: 10.1007/s11071-021-07118-3.

[85] M. Didonna, M. Stender, A. Papangelo, F. Fontanela, M. Ciavarella, and N. Hoffmann. "Reconstruction of Governing Equations from Vibration Measurements for Geometrically Nonlinear Systems". *Lubricants* 7.8 (2019), p. 64. DOI: 10.3390/lubricants7080064.

[86] J.-N. Juang and R. S. Pappa. "An eigensystem realization algorithm for modal parameter identification and model reduction". *Journal of Guidance, Control, and Dynamics* 8.5 (1985), pp. 620–627. DOI: 10.2514/3.20031.

[87] J. Bongard and H. Lipson. "Automated reverse engineering of nonlinear dynamical systems". *Proceedings of the National Academy of Sciences of the United States of America* 104.24 (2007), pp. 9943–9948. DOI: 10.1073/pnas.0609476104.

[88] M. Schmidt and H. Lipson. "Distilling free-form natural laws from experimental data". *Science* 324.5923 (2009), pp. 81–85. DOI: 10.1126/science.1165893.

[89] R. Tibshirani. "Regression Shrinkage and Selection Via the Lasso". *Journal of the Royal Statistical Society Series B: Statistical Methodology* 58.1 (1996), pp. 267–288. DOI: 10.1111/j.2517-6161.1996.tb02080.x.

[90] J.-C. Loiseau and S. L. Brunton. "Constrained sparse Galerkin regression". *Journal of Fluid Mechanics* 838 (2018), pp. 42–67. DOI: 10.1017/jfm.2017.823.

[91] J.-C. Loiseau. "Data-driven modeling of the chaotic thermal convection in an annular thermosyphon". *Theoretical and Computational Fluid Dynamics* 34.4 (2020), pp. 339–365. DOI: 10.1007/s00162-020-00536-w.

[92] N. M. Mangan, S. L. Brunton, J. L. Proctor, and J. N. Kutz. "Inferring Biological Networks by Sparse Identification of Nonlinear Dynamics". *IEEE Transactions on Molecular, Biological and Multi-Scale Communications* 2.1 (2016), pp. 52–63. DOI: 10.1109/TMBMC.2016.2633265.

[93] L. Guo, X. Yang, Z. Zheng, N. Riemer, and C. W. Tessum. "Uncertainty Quantification in Reduced–Order Gas–Phase Atmospheric Chemistry Modeling Using Ensemble SINDy". *Journal of Geophysical Research: Machine Learning and Computation* 1.4 (2024). DOI: 10.1029/2024JH000358.

[94] X. Yang, L. Guo, Z. Zheng, N. Riemer, and C. W. Tessum. "Atmospheric Chemistry Surrogate Modeling With Sparse Identification of Nonlinear Dynamics". *Journal of Geophysical Research: Machine Learning and Computation* 1.2 (2024). DOI: 10.1029/2024JH000132.

[95] R. Supekar, B. Song, A. Hastewell, G. P. T. Choi, A. Mietke, and J. Dunkel. "Learning hydrodynamic equations for active matter from particle simulations and experiments". *Proceedings of the National Academy of Sciences of the United States of America* 120.7 (2023), e2206994120. DOI: 10.1073/pnas.2206994120.

[96] X. Wen, U. Oberhofer, L. R. Gorjão, G. Yalcin, V. Hagenmeyer, and B. Schäfer. "Identifying complex dynamics of power grid frequency". *Tackling Climate Change with Machine Learning Workshop at ICLR* (2024), pp. 408–414. DOI: 10.1145/3632775.3661944.

[97] A. A. Klishin, J. Bakarji, J. N. Kutz, and K. Manohar. "Statistical Mechanics of Dynamical System Identification". *ArXiv preprint* (2024). DOI: 10.48550/arXiv.2403.01723.

[98] A. Somacal, Y. Barrera, L. Boechi, M. Jonckheere, V. Lefieux, D. Picard, and E. Smucler. "Uncovering differential equations from data with hidden variables". *Physical Review E* 105.5-1 (2022), p. 054209. DOI: 10.1103/PhysRevE.105.054209.

[99] E. Kaiser, J. N. Kutz, and S. L. Brunton. "Sparse identification of nonlinear dynamics for model predictive control in the low-data limit". *Proceedings of the Royal Society A: Mathematical, Physical and Engineering Sciences* 474.2219 (2018), p. 20180335. DOI: 10.1098/rspa.2018.0335.

[100] D. A. Messenger and D. M. Bortz. "Weak SINDy: Galerkin-based data-driven model selection". *Multiscale Modeling & Simulation: A SIAM Interdisciplinary Journal* 19.3 (2021), pp. 1474–1497. DOI: 10.1137/20M1343166.

[101] S. H. Rudy, S. L. Brunton, J. L. Proctor, and J. N. Kutz. "Data-driven discovery of partial differential equations". *Science Advances* 3.4 (2017), e1602614. DOI: 10.1126/sciadv.1602614.

[102] J. Bakarji, K. Champion, J. Nathan Kutz, and S. L. Brunton. "Discovering governing equations from partial measurements with deep delay autoencoders". *Proceedings of the Royal Society A: Mathematical, Physical and Engineering Sciences* 479.2276 (2023). DOI: 10.1098/rspa.2023.0422.

[103] D. Voina, S. Brunton, and J. N. Kutz. "Deep generative modeling for identification of noisy, non-stationary dynamical systems". *ArXiv preprint* (2024). DOI: 10.48550/arXiv.2410.02079.

[104] G. Martius and C. H. Lampert. "Extrapolation and learning equations". *ArXiv preprint* (2016). DOI: 10.48550/arXiv.1610.02995.

[105] S. Sahoo, C. Lampert, and G. Martius. "Learning equations for extrapolation and control". *Proceedings of the 35th International Conference on Machine Learning*. Ed. by J. Dy and A. Krause. Vol. 80. PMLR, 2018, pp. 4442–4450.

[106] N. Zolman, U. Fasel, J. N. Kutz, and S. L. Brunton. "SINDy-RL: interpretable and efficient model-based reinforcement learning". *ArXiv preprint* (2024). DOI: 10.48550/arXiv.2403.09110.

[107] B. O. Koopman. "Hamiltonian systems and transformation in Hilbert space". *Proceedings of the National Academy of Sciences of the United States of America* 17.5 (1931), pp. 315–318. DOI: 10.1073/pnas.17.5.315.

[108] I. Mezić and A. Banaszuk. "Comparison of systems with complex behavior". *Physica D: Nonlinear Phenomena* 197.1-2 (2004), pp. 101–133. DOI: 10.1016/j.physd.2004.06.015.

[109] I. Mezić. "Spectral properties of dynamical systems, model reduction and decompositions". *Nonlinear Dynamics* 41.1-3 (2005), pp. 309–325. DOI: 10.1007/s11071-005-2824-x.

[110] S. L. Brunton, B. W. Brunton, J. L. Proctor, E. Kaiser, and J. N. Kutz. "Chaos as an intermittently forced linear system". *Nature Communications* 8.1 (2017), p. 19. DOI: 10.1038/s41467-017-00030-8.

[111] P. J. Schmid. "Dynamic mode decomposition of numerical and experimental data". *Journal of Fluid Mechanics* 656 (2010), pp. 5–28. DOI: 10.1017/S0022112010001217.

[112] C. W. Rowley, I. Mezić, S. Bagheri, P. Schlatter, and D. S. Henningson. "Spectral analysis of nonlinear flows". *Journal of Fluid Mechanics* 641 (2009), pp. 115–127. DOI: 10.1017/S0022112009992059.

[113] J. N. Kutz, S. L. Brunton, B. W. Brunton, and J. L. Proctor. *Dynamic Mode Decomposition*. Philadelphia, PA: Society for Industrial and Applied Mathematics, 2016. DOI: 10.1137/1.9781611974508.

[114] M. Kamb, E. Kaiser, S. L. Brunton, and J. N. Kutz. "Time-Delay Observables for Koopman: Theory and Applications". *SIAM Journal on Applied Dynamical Systems* 19.2 (2020), pp. 886–917. DOI: 10.1137/18M1216572.

[115] H. Arbabi and I. Mezić. "Ergodic Theory, Dynamic Mode Decomposition, and Computation of Spectral Properties of the Koopman Operator". *SIAM Journal on Applied Dynamical Systems* 16.4 (2017), pp. 2096–2126. DOI: 10.1137/17M1125236.

[116] B. Lusch, J. N. Kutz, and S. L. Brunton. "Deep learning for universal linear embeddings of nonlinear dynamics". *Nature Communications* 9.1 (2018), p. 4950. DOI: 10.1038/s41467-018-07210-0.

[117] D. Aristoff, J. Copperman, N. Mankovich, and A. Davies. "Featurizing Koopman mode decomposition for robust forecasting". *The Journal of Chemical Physics* 161.6 (2024). DOI: 10.1063/5.0220277.

[118] T. Lu, J. Feng, J. Su, Y. Han, and Q. Guo. "System identification based on sparse approximation of Koopman operator". *The European Physical Journal Special Topics* (2024). DOI: 10.1140/epjs/s11734-024-01264-6.

[119] I. Mezić. "Analysis of fluid flows via spectral properties of the Koopman operator". *Annual Review of Fluid Mechanics* 45.1 (2013), pp. 357–378. DOI: 10.1146/annurev-fluid-011212-140652.

[120] S. E. Otto and C. W. Rowley. "Koopman operators for estimation and control of dynamical systems". *Annual Review of Control, Robotics, and Autonomous Systems* 4.1 (2021), pp. 59–87. DOI: 10.1146/annurev-control-071020-010108.

[121] J. H. Tu, C. W. Rowley, D. M. Luchtenburg, S. L. Brunton, and J. Nathan Kutz. "On dynamic mode decomposition: Theory and applications". *Journal of Computational Dynamics* 1.2 (2014), pp. 391–421. DOI: 10.3934/jcd.2014.1.391.

[122] S. Das and D. Giannakis. "Delay-Coordinate Maps and the Spectra of Koopman Operators". *Journal of Statistical Physics* 175.6 (2019), pp. 1107–1145. DOI: 10.1007/s10955-019-02272-w.

[123] K. P. Champion, S. L. Brunton, and J. N. Kutz. "Discovery of Nonlinear Multiscale Systems: Sampling Strategies and Embeddings". *SIAM Journal on Applied Dynamical Systems* 18.1 (2019), pp. 312–333. DOI: 10.1137/18M1188227.

[124] Y. Lan and I. Mezić. "Linearization in the large of nonlinear systems and Koopman operator spectrum". *Physica D: Nonlinear Phenomena* 242.1 (2013), pp. 42–53. DOI: 10.1016/j.physd.2012.08.017.

[125] D. Dylewsky, E. Kaiser, S. L. Brunton, and J. N. Kutz. "Principal component trajectories for modeling spectrally continuous dynamics as forced linear systems". *Physical Review E* 105.1-2 (2022), p. 015312. DOI: 10.1103/PhysRevE.105.015312.

[126] M. A. Khodkar, P. Hassanzadeh, and A. Antoulas. "A Koopman-based framework for forecasting the spatiotemporal evolution of chaotic dynamics with nonlinearities modeled as exogenous forcings". *ArXiv preprint* (2019). DOI: 10.48550/arXiv.1909.00076.

[127] C. Geier, M. Stender, and N. Hoffmann. "Data-driven reduced order modeling for mechanical oscillators using Koopman approaches". *Frontiers in Applied Mathematics and Statistics* 9 (2023). DOI: 10.3389/fams.2023.1124602.

[128] D. E. Rumelhart, G. E. Hinton, and R. J. Williams. "Learning representations by back-propagating errors". *Nature* 323.6088 (1986), pp. 533–536. DOI: 10.1038/323533a0.

[129] Y. LeCun, B. Boser, J. Denker, D. Henderson, R. Howard, W. Hubbard, and L. Jackel. "Handwritten digit recognition with a back-propagation network". *Advances in Neural Information Processing Systems*. Ed. by D. Touretzky. Vol. 2. Morgan-Kaufmann, 1989.

[130] Y. LeCun, Y. Bengio, and G. Hinton. "Deep learning". *Nature* 521.7553 (2015), pp. 436–444. DOI: 10.1038/nature14539.

[131] G. E. Hinton, S. Osindero, and Y.-W. Teh. "A fast learning algorithm for deep belief nets". *Neural Computation* 18.7 (2006), pp. 1527–1554. DOI: 10.1162/neco.2006.18.7.1527.

[132] Y. Bengio, P. Lamblin, D. Popovici, and H. Larochelle. "Greedy Layer-Wise Training of Deep Networks". *Advances in Neural Information Processing Systems*. Ed. by B. Schölkopf, J. Platt, and T. Hoffman. Vol. 19. MIT Press, 2006.

[133] Y. Lecun, L. Bottou, Y. Bengio, and P. Haffner. "Gradient-based learning applied to document recognition". *Proceedings of the IEEE* 86.11 (1998), pp. 2278–2324. DOI: 10.1109/5.726791.

[134] G. Hinton, L. Deng, D. Yu, G. Dahl, A.-r. Mohamed, N. Jaitly, A. Senior, V. Vanhoucke, P. Nguyen, T. Sainath, and B. Kingsbury. "Deep Neural Networks for Acoustic Modeling in Speech Recognition: The Shared Views of Four Research Groups". *IEEE Signal Processing Magazine* 29.6 (2012), pp. 82–97. DOI: 10.1109/MSP.2012.2205597.

[135] Waibel, A., Hanazawa, T., Hinton, G., Shikano, K., & Lang, K. J. "Phoneme recognition using time-delay neural networks". *Backpropagation*. Ed. by Y. Chauvin and D. E. Rumelhart. New York, NY: Psychology Press, 1995, pp. 35–61.

[136] Taigman, Yaniv and Yang, Ming and Ranzato, Marc'Aurelio and Wolf, Lior. "DeepFace: Closing the Gap to Human-Level Performance in Face Verification". *Proceedings of the IEEE Conference on Computer Vision and Pattern Recognition (CVPR)*. 2014.

[137] S. Hochreiter. "Long Short-term Memory". *Neural Computation* 9.8 (1997), pp. 1735–1780.

[138] P. R. Vlachas, W. Byeon, Z. Y. Wan, T. P. Sapsis, and P. Koumoutsakos. "Data-driven forecasting of high-dimensional chaotic systems with long short-term memory networks". *Proceedings of the Royal Society A: Mathematical, Physical and Engineering Sciences* 474.2213 (2018), p. 20170844. DOI: 10.1098/rspa.2017.0844.

[139] A. Wikner, J. Harvey, M. Girvan, B. R. Hunt, A. Pomerance, T. Antonsen, and E. Ott. "Stabilizing machine learning prediction of dynamics: Novel noise-inspired regularization tested with reservoir computing". *Neural Networks : the Official Journal of the International Neural Network Society* 170 (2024), pp. 94–110. DOI: 10.1016/j.neunet.2023.10.054.

[140] H. Jaeger. "The "echo state" approach to analysing and training recurrent neural networks – with an erratum note. 148.34 (2001): 13". *Bonn, Germany: German National Research Center for Information Technology GMD Technical Report* 148.34 (2001), p. 13.

[141] M. Yadav, S. Chauhan, M. D. Shrimali, and M. Stender. "Predicting multi-parametric dynamics of an externally forced oscillator using reservoir computing and minimal data". *Nonlinear Dynamics* (2024). DOI: 10.1007/s11071-024-10720-w.

[142] J. Pathak, B. Hunt, M. Girvan, Z. Lu, and E. Ott. "Model-free prediction of large spatiotemporally chaotic systems from data: a reservoir computing approach". *Physical Review Letters* 120.2 (2018), p. 024102. DOI: 10.1103/PhysRevLett.120.024102.

[143] A. Mardt, L. Pasquali, H. Wu, and F. Noé. "VAMPnets for deep learning of molecular kinetics". *Nature Communications* 9.1 (2018), p. 5. DOI: 10.1038/s41467-017-02388-1.

[144] Z. C. Lipton. "The mythos of model interpretability". *Queue* 16.3 (2018), pp. 31–57. DOI: 10.1145/3236386.3241340.

[145] M. Wedler, M. Stender, M. Klein, and N. Hoffmann. "Machine learning simulation of one-dimensional deterministic water wave propagation". *Ocean Engineering* 284 (2023), p. 115222. DOI: 10.1016/j.oceaneng.2023.115222.

[146] S. Ehlers, M. Klein, A. Heinlein, M. Wedler, N. Desmars, N. Hoffmann, and M. Stender. "Machine learning for phase-resolved reconstruction of nonlinear ocean wave surface elevations from sparse remote sensing data". *Ocean Engineering* 288 (2023), p. 116059. DOI: 10.1016/j.oceaneng.2023.116059.

[147] K. Lee and K. T. Carlberg. "Model reduction of dynamical systems on nonlinear manifolds using deep convolutional autoencoders". *Journal of Computational Physics* 404 (2020), p. 108973. DOI: 10.1016/j.jcp.2019.108973.

[148] F. J. Gonzalez and M. Balajewicz. "Deep convolutional recurrent autoencoders for learning low-dimensional feature dynamics of fluid systems". *ArXiv prepint* (2018). DOI: 10.48550/arXiv.1808.01346.

[149] J. Bakarji and D. M. Tartakovsky. "Data-driven discovery of coarse-grained equations". *Journal of Computational Physics* 434 (2021), p. 110219. DOI: 10.1016/j.jcp.2021.110219.

[150] C. Rudin. "Stop Explaining Black Box Machine Learning Models for High Stakes Decisions and Use Interpretable Models Instead". *Nature Machine Intelligence* 1.5 (2019), pp. 206–215. DOI: 10.1038/s42256-019-0048-x.

[151] S. Ehlers, N. A. Wagner, A. Scherzl, M. Klein, N. Hoffmann, and M. Stender. "Data Assimilation and Parameter Identification for Water Waves Using the Nonlinear Schrödinger Equation and Physics-Informed Neural Networks". *Fluids* 9.10 (2024), p. 231. DOI: 10.3390/fluids9100231.

[152] M. Raissi, P. Perdikaris, and G. E. Karniadakis. "Physics informed deep learning (Part I): data-driven solutions of nonlinear partial cifferential equations". *ArXiv preprint* (2017). DOI: 10.48550/arXiv.1711.10561.

[153] M. Raissi, P. Perdikaris, N. Ahmadi, and G. E. Karniadakis. "Physics-informed neural networks and extensions". *ArXiv preprint* (2024). DOI: 10.48550/arXiv.2408.16806.

[154] G. Y. Bingöl, G., O. A. Soysal, and E. Günay. "Model reduction of dynamical systems with a novel data-driven approach: The RC-HAVOK algorithm". *Chaos (Woodbury, N.Y.)* 34.8 (2024). DOI: 10.1063/5.0207907.

[155] M. Thévenot, J.-F. Brunel, F. Brunel, M. Bigerelle, M. Stender, N. Hoffmann, and P. Dufrénoy. "In situ tracker for brake squeal prediction". *Preprint* (2024). DOI: 10.21203/rs.3.rs-4144253/v1.

[156] S. M. Lundberg and S.-I. Lee. "A unified approach to interpreting model predictions". *Advances in Neural Information Processing Systems*. Ed. by I. Guyon, U. Von Luxburg, S. Bengio, H. Wallach, R. Fergus, S. Vishwanathan, and R. Garnett. Vol. 30. Curran Associates, Inc, 2017.

[157] C. Geier, S. Hamdi, T. Chancelier, P. Dufrénoy, N. Hoffmann, and M. Stender. "Machine learning-based state maps for complex dynamical systems: applications to friction-excited brake system vibrations". *Nonlinear Dynamics* 111.24 (2023), pp. 22137–22151. DOI: 10.1007/s11071-023-08739-6.

[158] M. Newman. *Networks*. Oxford University Press, 2018.

[159] A. H. Shirazi, G. Reza Jafari, J. Davoudi, J. Peinke, M. Reza Rahimi Tabar, and M. Sahimi. "Mapping stochastic processes onto complex networks". *Journal of Statistical Mechanics: Theory and Experiment* 2009.07 (2009), P07046. DOI: 10.1088/1742-5468/2009/07/P07046.

[160] J. B. Kruskal. "On the Shortest Spanning Subtree of a Graph and the Traveling Salesman Problem". *Proceedings of the American Mathematical Society* 7.1 (1956), p. 48. DOI: 10.2307/2033241.

[161] P. Erdős and A. Rényi. "On random graphs." *Publications Mathematiques* 6 (1959), pp. 290–297.

[162] P. Erdős and A. Rényi. "On the evoluation of random graphs". *Publications Mathematiques Inst. Hung. Acad. Sci* 5 (1960), pp. 17–61.

[163] R. M. May. "Will a large complex system be stable?" *Nature* 238.5364 (1972), pp. 413–414. DOI: 10.1038/238413a0.

[164] M. R. Gardner and W. R. Ashby. "Connectance of Large Dynamic (Cybernetic) Systems: Critical Values for Stability". *Nature* 228.5273 (1970), p. 784. DOI: 10.1038/228784a0.

[165] D. J. Watts and S. H. Strogatz. “Collective dynamics of small world networks”. *Nature* 393 (1998), pp. 440–442.

[166] R. Albert and A.-L. Barabási. “Statistical mechanics of complex networks”. *Reviews of Modern Physics* 74.1 (2002), pp. 47–97. DOI: 10.1103/RevModPhys.74.47.

[167] R. V. Donner and J. F. Donges. “Visibility graph analysis of geophysical time series: Potentials and possible pitfalls”. *Acta Geophysica* 60.3 (2012), pp. 589–623. DOI: 10.2478/s11600-012-0032-x.

[168] Y. Zou, R. V. Donner, N. Marwan, J. F. Donges, and J. Kurths. “Complex network approaches to nonlinear time series analysis”. *Physics Reports* 787 (2019), pp. 1–97. DOI: 10.1016/j.physrep.2018.10.005.

[169] C. A. Hidalgo. “Disconnected, fragmented, or united? a trans-disciplinary review of network science”. *Applied Network Science* 1.1 (2016), p. 6. DOI: 10.1007/s41109-016-0010-3.

[170] L. Turnbull, M.-T. Hütt, A. A. Ioannides, S. Kininmonth, R. Poeppl, K. Tockner, L. J. Bracken, S. Keesstra, L. Liu, R. Masselink, and A. J. Parsons. “Connectivity and complex systems: learning from a multi-disciplinary perspective”. *Applied Network Science* 3.1 (2018), p. 11. DOI: 10.1007/s41109-018-0067-2.

[171] P. Holme and J. Saramäki. “Temporal Networks”. *Physics Reports* 519.3 (2012), pp. 97–125. DOI: 10.1016/j.physrep.2012.03.001.

[172] R. V. Donner, M. Small, J. F. Donges, N. Marwan, Y. Zou, R. Xiang, and J. Kurths. “Recurrence-based time series analysis by means of complex network methods”. *International Journal of Bifurcation and Chaos* 21.04 (2011), pp. 1019–1046. DOI: 10.1142/S0218127411029021.

[173] T. Gross and H. Sayama, eds. *Adaptive Networks*. Berlin, Heidelberg: Springer Berlin Heidelberg, 2009. DOI: 10.1007/978-3-642-01284-6.

[174] J. Falk, E. Eichler, K. Windt, and M.-T. Hütt. “Collective patterns and stable misunderstandings in networks striving for consensus without a common value system”. *Scientific Reports* 12.1 (2022), p. 3028. DOI: 10.1038/s41598-022-06880-7.

[175] C. R. Sampson, M. A. Porter, and J. G. Restrepo. “Oscillatory and excitable dynamics in an opinion model with group opinions”. *ArXiv preprint* (2024). DOI: 10.48550/arXiv.2408.13336.

[176] L. Lacasa, V. Nicosia, and V. Latora. “Network structure of multivariate time series”. *Scientific Reports* 5 (2015), p. 15508. DOI: 10.1038/srep15508.

[177] M. Stephen, C. Gu, and H. Yang. “Visibility graph based time series analysis”. *PloS one* 10.11 (2015), e0143015. DOI: 10.1371/journal.pone.0143015.

[178] A. Lesne. “Complex networks: from graph theory to biology”. *Letters in Mathematical Physics* 78.3 (2006), pp. 235–262. DOI: 10.1007/s11005-006-0123-1.

[179] M. Müller-Linow, C. C. Hilgetag, and M.-T. Hütt. “Organization of excitable dynamics in hierarchical biological networks”. *PLoS Computational Biology* 4.9 (2008), e1000190. DOI: 10.1371/journal.pcbi.1000190.

[180] M. Zanin, J. M. Alcazar, J. V. Carbajosa, M. G. Paez, D. Papo, P. Sousa, E. Menasalvas, and S. Boccaletti. "Parenclitic networks: uncovering new functions in biological data". *Scientific Reports* 4 (2014), p. 5112. DOI: 10.1038/srep05112.

[181] W. Wang, R. Escobedo, S. Sanchez, Z. Han, C. Sire, and G. Theraulaz. "Collective phases and long-term dynamics in a fish school model with burst-and-coast swimming". *Preprint* (2024). DOI: 10.1101/2024.05.26.595998.

[182] L. Hou, M. Small, and S. Lao. "Dynamical Systems Induced on Networks Constructed from Time Series". *Entropy* 17.12 (2015), pp. 6433–6446. DOI: 10.3390/e17096433.

[183] J. A. Dunne. "Food Webs." *Encyclopedia of Complexity and Systems Science 1.* Vol. 1, pp. 3661–3682.

[184] A. Messé, M.-T. Hütt, P. König, and C. C. Hilgetag. "A closer look at the apparent correlation of structural and functional connectivity in excitable neural networks". *Scientific Reports* 5 (2015), p. 7870. DOI: 10.1038/srep07870.

[185] H. Gast and Y. Assaf. "Weighting the structural connectome: Exploring its impact on network properties and predicting cognitive performance in the human brain". *Network Neuroscience (Cambridge, Mass.)* 8.1 (2024), pp. 119–137. DOI: 10.1162/netn_a_00342.

[186] B. Avila, P. Augusto, D. Phillips, T. Gili, M. Zimmer, and H. A. Makse. "Symmetries and synchronization from whole-neural activity in C. elegans connectome: Integration of functional and structural networks". *ArXiv preprint* (2024). DOI: 10.48550/arXiv.2409.02682.

[187] L. Astolfi, F. Cincotti, D. Mattia, M. G. Marciani, L. A. Baccala, F. de Vico Fallani, S. Salinari, M. Ursino, M. Zavaglia, L. Ding, J. C. Edgar, G. A. Miller, B. He, and F. Babiloni. "Comparison of different cortical connectivity estimators for high-resolution EEG recordings". *Human Brain Mapping* 28.2 (2007), pp. 143–157. DOI: 10.1002/hbm.20263.

[188] A. B. El-Yaagoubi, M. K. Chung, and H. Ombao. "Statistical inference for dependence networks in topological data analysis". *Frontiers in Artificial Intelligence* 6 (2023). DOI: 10.3389/frai.2023.1293504.

[189] F. Strozzi, E. Gutiérrez, F. Bono, K. Poljansek, and J. Zaldívar. *From complex networks to time series analysis end viceversa: Application to metabolic networks.* Vol. 23947. Luxembourg: Office for Official Publications of the European Communities, 2009.

[190] P. Trzaskoma, S. Jung, A. Pękowska, C. H. Bohrer, X. Wang, F. Naz, S. Dell'Orso, W. D. Dubois, A. Olivera, S. V. Vartak, Y. Zhao, S. Nayak, A. Overmiller, M. I. Morasso, V. Sartorelli, D. R. Larson, C. C. Chow, R. Casellas, and J. J. O'Shea. "3D chromatin architecture, BRD4, and Mediator have distinct roles in regulating genome-wide transcriptional bursting and gene network". *Science Advances* 10.32 (2024). DOI: 10.1126/sciadv.adl4893.

[191] A. Segura-Ortiz, J. García-Nieto, J. F. Aldana-Montes, and I. Navas-Delgado. "Multi-objective context-guided consensus of a massive array of techniques for the inference of gene regulatory networks". *Computers in Biology and Medicine* 179 (2024), p. 108850. DOI: 10.1016/j.compbiomed.2024.108850.

[192] X. C. Li, V. Srinivasan, I. Laiker, N. Misunou, N. Frankel, L. F. Pallares, and J. Crocker. "TF-high-evolutionary: in vivo mutagenesis of gene regulatory networks for the study of the genetics and evolution of the drosophila regulatory genome". *Molecular biology and evolution* 41.8 (2024). DOI: 10.1093/molbev/msae167.

[193] G. A. Wachs-Lopes and P. S. Rodrigues. "Analyzing natural human language from the point of view of dynamic of a complex network". *Expert Systems with Applications* 45 (2016), pp. 8–22. DOI: 10.1016/j.eswa.2015.09.020.

[194] J. F. Donges, R. V. Donner, K. Rehfeld, N. Marwan, M. H. Trauth, and J. Kurths. "Identification of dynamical transitions in marine palaeoclimate records by recurrence network analysis". *Nonlinear Processes in Geophysics* 18.5 (2011), pp. 545–562. DOI: 10.5194/npg-18-545-2011.

[195] J. F. Donges, H. C. H. Schultz, N. Marwan, Y. Zou, and J. Kurths. "Investigating the topology of interacting networks". *The European Physical Journal B* 84.4 (2011), pp. 635–651. DOI: 10.1140/epjb/e2011-10795-8.

[196] D. Eroglu, N. Marwan, M. Stebich, and J. Kurths. "Multiplex Recurrence Networks". *Physical Review E* 97.1 (2018), p. 1. DOI: 10.1103/PhysRevE.97.012312.

[197] J. H. Feldhoff, R. V. Donner, J. F. Donges, N. Marwan, and J. Kurths. "Geometric detection of coupling directions by means of inter-system recurrence networks". *Physics Letters A* 376.46 (2012), pp. 3504–3513. DOI: 10.1016/j.physleta.2012.10.008.

[198] N. Marwan, J. F. Donges, Y. Zou, R. V. Donner, and J. Kurths. "Complex network approach for recurrence analysis of time series". *Physics Letters A* 373.46 (2009), pp. 4246–4254. DOI: 10.1016/j.physleta.2009.09.042.

[199] A. Ramírez-Rojas, E. L. Flores-Márquez, and C. A. Vargas. "Visibility graph analysis of the seismic activity of three areas of the cocos plate mexican subduction where the last three large earthquakes (M 7) occurred in 2017 and 2022". *Entropy (Basel, Switzerland)* 25.5 (2023). DOI: 10.3390/e25050799.

[200] Y. Zou, R. V. Donner, N. Marwan, M. Small, and J. Kurths. "Long-term changes in the north–south asymmetry of solar activity: a nonlinear dynamics characterization using visibility graphs". *Nonlinear Processes in Geophysics* 21.6 (2014), pp. 1113–1126. DOI: 10.5194/npg-21-1113-2014.

[201] K. Taira and A. G. Nair. "Network-based analysis of fluid flows: Progress and outlook". *Progress in Aerospace Sciences* 131 (2022), p. 100823. DOI: 10.1016/j.paerosci.2022.100823.

[202] Z.-K. Gao, Y.-X. Yang, Q. Cai, S.-S. Zhang, and N.-D. Jin. "Multivariate weighted recurrence network inference r uncovering oil-water transitional flow behavior in a vertical pipe". *Chaos (Woodbury, N.Y.)* 26.6 (2016), p. 063117. DOI: 10.1063/1.4954271.

[203] Z.-K. Gao, Y.-X. Yang, P.-C. Fang, N.-D. Jin, C.-Y. Xia, and L.-D. Hu. "Multi-frequency complex network from time series for uncovering oil-water flow structure". *Scientific Reports* 5 (2015), p. 8222. DOI: 10.1038/srep08222.

[204] Z.-K. Gao, Y.-X. Yang, P.-C. Fang, Y. Zou, C.-Y. Xia, and M. Du. "Multiscale complex network for analyzing experimental multivariate time series". *EPL (Europhysics Letters)* 109.3 (2015), p. 30005. DOI: 10.1209/0295-5075/109/30005.

[205] "Multivariate multiscale complex network analysis of vertical upward oil-water two-phase flow in a small diameter pipe". *Scientific Reports* 6 (2016), p. 20052. DOI: 10.1038/srep20052.

[206] Z.-K. Gao, X.-W. Zhang, N.-D. Jin, R. V. Donner, N. Marwan, and J. Kurths. "Recurrence networks from multivariate signals for uncovering dynamic transitions of horizontal oil-water stratified flows". *EPL (Europhysics Letters)* 103.5 (2013), p. 50004. DOI: 10.1209/0295-5075/103/50004.

[207] Z.-K. Gao, X.-W. Zhang, N.-D. Jin, N. Marwan, and J. Kurths. "Multivariate recurrence network analysis for characterizing horizontal oil-water two-phase flow". *Physical Review E* 88.3 (2013), p. 032910. DOI: 10.1103/PhysRevE.88.032910.

[208] C. Alvares and S. Banerjee. "How Network Topology Affects the Strength of Dangerous Power Grid Perturbations". *ArXiv preprint* (2024). DOI: 10.48550/arXiv.2401.00552.

[209] J. Park and B. Kahng. "Hybrid synchronization with continuous varying exponent in decentralized power grid". *ArXiv preprint* (2024). DOI: 10.48550/arXiv.2407.07312.

[210] X. Zhang, Cheng Ma, and and Marc Timme. "Dynamic Vulnerability in Oscillatory Networks and Power Grids". *ArXiv preprint* (2019).

[211] "Fluctuation-induced distributed resonances in oscillatory networks". *Science Advances* 5.7 (2019), eaav1027. DOI: 10.1126/sciadv.aav1027.

[212] X. Zhang and M. Timme. "Fluctuation response patterns of network dynamics – An introduction". *European Journal of Applied Mathematics* 34.3 (2023), pp. 429–466. DOI: 10.1017/S0956792522000201.

[213] M. Kim and F. Radicchi. "Shortest-path percolation on random networks". *Physical Review Letters* 133.4 (2024), p. 047402. DOI: 10.1103/PhysRevLett.133.047402.

[214] R. Carvalho, L. Buzna, F. Bono, E. Gutiérrez, W. Just, and D. Arrowsmith. "Robustness of trans-European gas networks". *Physical Review E* 80.1 (2009), p. 016106. DOI: 10.1103/PhysRevE.80.016106.

[215] R. V. Donner, Y. Zou, J. F. Donges, N. Marwan, and J. Kurths. "Recurrence networks—a novel paradigm for nonlinear time series analysis". *New Journal of Physics* 12.3 (2010), p. 033025. DOI: 10.1088/1367-2630/12/3/033025.

[216] L. Lacasa and R. Toral. "Description of stochastic and chaotic series using visibility graphs". *Physical Review E* 82.3 (2010), p. 1078. DOI: 10.1103/PhysRevE.82.036120.

[217] N. Marwan and N. Wessel, H. Stepan, J. Kurths. "Recurrence based complex network analysis of cardiovascular variability data to predict pre-eclampsia". *Proc. Int. Symp. Nonlinear Theory its Appl., NOLTA2010, Krakow* (2010), pp. 585–588.

[218] G. M. Ramírez Ávila, A. Gapelyuk, N. Marwan, H. Stepan, J. Kurths, T. Walther, and N. Wessel. "Classifying healthy women and preeclamptic patients from cardiovascular data using recurrence and complex network methods". *Autonomic Neuroscience : Basic & Clinical* 178.1-2 (2013), pp. 103–110. DOI: 10.1016/j.autneu.2013.05.003.

[219] N. P. Subramaniyam and J. Hyttinen. "Analysis of nonlinear dynamics of healthy and epileptic EEG signals using recurrence based complex network approach". *2013 6th International IEEE/EMBS Conference on Neural Engineering (NER)* (2013), pp. 605–608. DOI: 10.1109/NER.2013.6696007.

[220] N. P. Subramaniyam, J. F. Donges, and J. Hyttinen. "Signatures of chaotic and stochastic dynamics uncovered with ϵ -recurrence networks". *Proceedings of the Royal Society A: Mathematical, Physical and Engineering Sciences* 471.2183 (2015), p. 20150349. DOI: 10.1098/rspa.2015.0349.

[221] E. J. Ngamga, S. Bialonski, N. Marwan, J. Kurths, C. Geier, and K. Lehnertz. "Evaluation of selected recurrence measures in discriminating pre-ictal and inter-ictal periods from epileptic EEG data". *Physics Letters A* 380.16 (2016), pp. 1419–1425. DOI: 10.1016/j.physleta.2016.02.024.

[222] Z.-K. Gao, Y.-X. Yang, W.-D. Dang, Q. Cai, Z. Wang, N. Marwan, S. Boccaletti, and J. Kurths. "Reconstructing multi-mode networks from multivariate time series". *EPL (Europhysics Letters)* 119.5 (2017), p. 50008. DOI: 10.1209/0295-5075/119/50008.

[223] C. W. Kulp, J. M. Chobot, H. R. Freitas, and G. D. Sprechini. "Using ordinal partition transition networks to analyze ECG data". *Chaos (Woodbury, N.Y.)* 26.7 (2016), p. 073114. DOI: 10.1063/1.4959537.

[224] M. McCullough, K. Sakellariou, T. Stemler, and M. Small. "Regenerating time series from ordinal networks". *Chaos (Woodbury, N.Y.)* 27.3 (2017), p. 035814. DOI: 10.1063/1.4978743.

[225] G. Górski, G. Litak, R. Mosdorf, and A. Rysak. "Two phase flow bifurcation due to turbulence: transition from slugs to bubbles". *The European Physical Journal B* 88 (2015), p. 239. DOI: 10.1140/epjb/e2015-60245-8.

[226] Z. Gao and N. Jin. "Flow-pattern identification and nonlinear dynamics of gas-liquid two-phase flow in complex networks". *Physical Review E* 79.6 Pt 2 (2009), p. 066303. DOI: 10.1103/PhysRevE.79.066303.

[227] R. Mosdorf and G. Górski. "Detection of two-phase flow patterns using the recurrence network analysis of pressure drop fluctuations". *International Communications in Heat and Mass Transfer* 64 (2015), pp. 14–20. DOI: 10.1016/j.icheatmasstransfer.2015.02.014.

[228] J. F. Donges, R. V. Donner, M. H. Trauth, N. Marwan, H.-J. Schellnhuber, and J. Kurths. "Nonlinear detection of paleoclimate-variability transitions possibly related to human evolution". *Proceedings of the National Academy of Sciences of the United States of America* 108.51 (2011), pp. 20422–20427. DOI: 10.1073/pnas.1117052108.

[229] M. McCullough, M. Small, T. Stemler, and H. H.-C. Iu. "Time lagged ordinal partition networks for capturing dynamics of continuous dynamical systems". *Chaos (Woodbury, N.Y.)* 25.5 (2015), p. 053101. DOI: 10.1063/1.4919075.

[230] C.-F. Schleussner, D. V. Divine, J. F. Donges, A. Miettinen, and R. V. Donner. "Indications for a North Atlantic ocean circulation regime shift at the onset of the Little Ice Age". *Climate Dynamics* 45.11-12 (2015), pp. 3623–3633. DOI: 10.1007/s00382-015-2561-x.

[231] L. Lacasa, A. Nuñez, É. Roldán, J. M. R. Parrondo, and B. Luque. "Time series irreversibility: a visibility graph approach". *The European Physical Journal B* 85.6 (2012). DOI: 10.1140/epjb/e2012-20809-8.

[232] J. F. Donges, R. V. Donner, and J. Kurths. "Testing time series irreversibility using complex network methods". *EPL (Europhysics Letters)* 102.1 (2013), p. 10004. DOI: 10.1209/0295-5075/102/10004.

[233] L. Cherouny. "Characterization of low-dimensional nonlinear mechanical systems by means of complex network methods". Master Thesis. Hamburg: Hamburg University of Technology, 2024.

[234] R. V. Donner, Y. Zou, J. F. Donges, N. Marwan, and J. Kurths. "Recurrence networks – a novel paradigm for nonlinear time series analysis". *New Journal of Physics* 12.3 (2010), p. 033025. DOI: 10.1088/1367-2630/12/3/033025.

[235] R. V. Donner, J. Heitzig, J. F. Donges, Y. Zou, N. Marwan, and J. Kurths. "The geometry of chaotic dynamics — a complex network perspective". *The European Physical Journal B* 84.4 (2011), pp. 653–672. DOI: 10.1140/epjb/e2011-10899-1.

[236] J. Liu, S.-T. Shi, and J.-C. Zhao. "Comparison study of typical algorithms for reconstructing time series from the recurrence plot of dynamical systems". *Chinese Physics B* 22.1 (2013), p. 010505. DOI: 10.1088/1674-1056/22/1/010505.

[237] J. Zhang and M. Small. "Complex network from pseudoperiodic time series: topology versus dynamics". *Physical Review Letters* 96.23 (2006), p. 238701. DOI: 10.1103/PhysRevLett.96.238701.

[238] J. Zhang, J. Sun, X. Luo, K. Zhang, T. Nakamura, and M. Small. "Characterizing pseudoperiodic time series through the complex network approach". *Physica D: Nonlinear Phenomena* 237.22 (2008), pp. 2856–2865. DOI: 10.1016/j.physd.2008.05.008.

[239] M. Small, J. Zhang, and X. Xu. "Transforming Time Series into Complex Networks". *Complex Sciences. Complex 2009. Lecture Notes of the Institute for Computer Sciences, Social Informatics and Telecommunications Engineering, vol 5* 5 (2009), pp. 2078–2089. DOI: 10.1007/978-3-642-02469-6_84.

[240] Y. Yang and H. Yang. "Complex network-based time series analysis". *Physica A: Statistical Mechanics and its Applications* 387 (2008), pp. 1381–1386.

[241] J. P. Zbilut and C. L. Webber. "Embeddings and delays as derived from quantification of recurrence plots". *Physics Letters A* 171.3-4 (1992), pp. 199–203. DOI: 10.1016/0375-9601(92)90426-M.

[242] N. Marwan, N. Wessel, U. Meyerfeldt, A. Schirdewan, and J. Kurths. "Recurrence-plot-based measures of complexity and their application to heart-rate-variability data". *Physical Review E* 66.2 Pt 2 (2002), p. 026702. DOI: 10.1103/PhysRevE.66.026702.

[243] D. Eroglu, N. Marwan, S. Prasad, and J. Kurths. "Finding recurrence networks' threshold adaptively for a specific time series". *Nonlinear Processes in Geophysics* 21.6 (2014), pp. 1085–1092. DOI: 10.5194/npg-21-1085-2014.

[244] J. F. Donges, J. Heitzig, R. V. Donner, and J. Kurths. "Analytical framework for recurrence-network analysis of time series". *Physical Review E* 85.4 (2012), p. 1. DOI: 10.1103/PhysRevE.85.046105.

[245] X. Xu, J. Zhang, and M. Small. "Superfamily phenomena and motifs of networks induced from time series". *Proceedings of the National Academy of Sciences of the United States of America* 105.50 (2008), pp. 19601–19605. DOI: 10.1073/pnas.0806082105.

[246] Y. Shimada, T. Kimura, and T. Ikeguchi. "Analysis of Chaotic dynamics using measures of complex network theory". *Artificial Neural Networks - ICANN 2008. ICANN 2008. Lecture Notes in Computer Science, vol 5163.* Berlin, Heidelberg: Springer, 2008.

[247] C. Zhou, L. Zemanová, G. Zamora, C. C. Hilgetag, and J. Kurths. "Hierarchical organization unveiled by functional connectivity in complex brain networks". *Physical Review Letters* 97.23 (2006), p. 238103. DOI: 10.1103/PhysRevLett.97.238103.

[248] R. V. Donner, Y. Zou, J. F. Donges, N. Marwan, and J. Kurths. "Ambiguities in recurrence-based complex network representations of time series". *Physical Review E* 81.1 Pt 2 (2010), p. 015101. DOI: 10.1103/PhysRevE.81.015101.

[249] L. L. Portes, A. N. Montanari, D. C. Correa, M. Small, and L. A. Aguirre. "The reliability of recurrence network analysis is influenced by the observability properties of the recorded time series". *Chaos (Woodbury, N.Y.)* 29.8 (2019), p. 083101. DOI: 10.1063/1.5093197.

[250] L. Lacasa, B. Luque, F. Ballesteros, J. Luque, and J. C. Nuño. "From time series to complex networks: the visibility graph". *Proceedings of the National Academy of Sciences of the United States of America* 105.13 (2008), pp. 4972–4975. DOI: 10.1073/pnas.0709247105.

[251] D. O'Sullivan and A. Turner. "Visibility graphs and landscape visibility analysis". *International Journal of Geographical Information Science* 15.3 (2001), pp. 221–237. DOI: 10.1080/13658810151072859.

[252] B. Luque, L. Lacasa, F. Ballesteros, and J. Luque. "Horizontal visibility graphs: exact results for random time series". *Physical Review E* 80 (4 2009), p. 046103. DOI: 10.1103/PhysRevE.80.046103.

[253] T. Zhou, N.-D. Jin, Z.-K. Gao, and Y.-B. Luo. "Limited penetrable visibility graph for establishing complex network from time series". *Acta Physica Sinica* 61.3 (2012), p. 030506. DOI: 10.7498/aps.61.030506.

[254] I. V. Bezsudnov and A. A. Snarskii. "From the time series to the complex networks: The parametric natural visibility graph". *Physica A: Statistical Mechanics and its Applications* 414 (2014), pp. 53–60. DOI: 10.1016/j.physa.2014.07.002.

[255] L. Lacasa and R. Toral. "Description of stochastic and chaotic series using visibility graphs". *Physical Review E* 82.3 (2010), p. 1078. DOI: 10.1103/PhysRevE.82.036120.

[256] L. Lacasa, B. Luque, J. Luque, and J. C. Nuño. "The visibility graph: A new method for estimating the Hurst exponent of fractional Brownian motion". *Europhysics Letters* 86.3 (2009), p. 30001. DOI: 10.1209/0295-5075/86/30001.

[257] X.-H. Ni, Z.-Q. Jiang, and W.-X. Zhou. "Degree distributions of the visibility graphs mapped from fractional Brownian motions and multifractal random walks". *Physics Letters A* 373.42 (2009), pp. 3822–3826. DOI: 10.1016/j.physleta.2009.08.041.

[258] C. Mari and C. Baldassari. "Optimization of mixture models on time series networks encoded by visibility graphs: an analysis of the US electricity market". *Computational Management Science* 20.1 (2023). DOI: 10.1007/s10287-023-00460-4.

[259] M. Small. "Complex networks from time series: Capturing dynamics". *IEEE International Symposium on Circuits and Systems (ISCAS), Beijing, China* (2013), pp. 2509–2512. DOI: 10.1109/ISCAS.2013.6572389.

[260] A. S. L. O. Campanharo, M. I. Sirer, R. D. Malmgren, F. M. Ramos, and L. A. N. Amaral. "Duality between time series and networks". *PloS one* 6.8 (2011), e23378. DOI: 10.1371/journal.pone.0023378.

[261] T. Weng, J. Zhang, M. Small, R. Zheng, and P. Hui. "Memory and betweenness preference in temporal networks induced from time series". *Scientific Reports* 7 (2017), p. 41951. DOI: 10.1038/srep41951.

[262] C. S. Daw, C. E. A. Finney, and E. R. Tracy. "A review of symbolic analysis of experimental data". *Review of Scientific Instruments* 74.2 (2003), pp. 915–930. DOI: 10.1063/1.1531823.

[263] M. H. McCullough. "Nonlinear time series analysis using ordinal networks with select applications in biomedical signal processing". *Bulletin of the Australian Mathematical Society* 100.1 (2019), pp. 170–172. DOI: 10.1017/S0004972719000480.

[264] G. Nicolis, A. G. Cantu, and C. Nicolias. "Dynamical aspects of interaction networks". *International Journal of Bifurcation and Chaos* 15.11 (2005), pp. 3467–3480. DOI: 10.1142/S0218127405014167.

[265] M. C. Romano, M. Thiel, J. Kurths, I. Z. Kiss, and J. L. Hudson. "Detection of synchronization for non-phase-coherent and non-stationary data". *Europhysics Letters (EPL)* 71.3 (2005), pp. 466–472. DOI: 10.1209/epl/i2005-10095-1.

[266] J. H. Feldhoff, R. V. Donner, J. F. Donges, N. Marwan, and J. Kurths. "Geometric signature of complex synchronisation scenarios". *EPL (Europhysics Letters)* 102.3 (2013), p. 30007. DOI: 10.1209/0295-5075/102/30007.

[267] J. Nawrath, M. C. Romano, M. Thiel, I. Z. Kiss, M. Wickramasinghe, J. Timmer, J. Kurths, and B. Schelter. "Distinguishing direct from indirect interactions in oscillatory networks with multiple time scales". *Physical Review Letters* 104.3 (2010), p. 038701. DOI: 10.1103/PhysRevLett.104.038701.

[268] Y. Zou, M. C. Romano, M. Thiel, N. Marwan, and J. Kurths. "Inferring indirect coupling by means of recurrences". *International Journal of Bifurcation and Chaos* 21.04 (2011), pp. 1099–1111. DOI: 10.1142/S0218127411029033.

[269] A. Groth. "Visualization of coupling in time series by order recurrence plots". *Physical Review E* 72.4 (2005), p. 046220. DOI: 10.1103/PhysRevE.72.046220.

[270] J. Zhang, J. Zhou, M. Tang, H. Guo, M. Small, and Y. Zou. "Constructing ordinal partition transition networks from multivariate time series". *Scientific Reports* 7.1 (2017), p. 7795. DOI: 10.1038/s41598-017-08245-x.

[271] T. Wen, H. Chen, and K. H. Cheong. "Visibility graph for time series prediction and image classification: a review". *Nonlinear Dynamics* 110.4 (2022), pp. 2979–2999. DOI: 10.1007/s11071-022-08002-4.

[272] M. Pósfai, B. Szegedy, I. Bačić, L. Blagojević, M. Abért, J. Kertész, L. Lovász, and A.-L. Barabási. "Impact of physicality on network structure". *Nature Physics* 20.1 (2024), pp. 142–149. DOI: 10.1038/s41567-023-02267-1.

[273] S. V. Nagpal, G. G. Nair, S. H. Strogatz, and F. Parise. "Synchronization in random networks of identical phase oscillators: A graphon approach". *ArXiv preprint* (2024). DOI: 10.48550/arXiv.2403.13998.

[274] A. Pavlov, E. Steur, and N. van de Wouw. "Nonlinear integral coupling for synchronization in networks of nonlinear systems". *Automatica* 140 (2022), p. 110202. DOI: 10.1016/j.automatica.2022.110202.

[275] J. Niehues, S. Yanchuk, R. Berner, J. Kurths, F. Hellmann, and M. Anvari. "Resonant solitary states in complex networks". *New Journal of Physics* 26.11 (2024), p. 113016. DOI: 10.1088/1367-2630/ad8b63.

[276] I. León, R. Muolo, S. Hata, and H. Nakao. "Higher-order interactions induce anomalous transitions to synchrony". *Chaos (Woodbury, N.Y.)* 34.1 (2024). DOI: 10.1063/5.0176748.

[277] M. S. Anwar, S. N. Jenifer, P. Muruganandam, D. Ghosh, and T. Carletti. "Synchronization in adaptive higher-order networks". *Physical Review E* 110.6 (2024), p. 064305. DOI: 10.1103/PhysRevE.110.064305.

[278] S. Ansarinasab, F. Parastesh, F. Ghassemi, K. Rajagopal, S. Jafari, and J. Kurths. "Optimized multi-variable coupling can improve synchronization in complex networks". *Nonlinear Dynamics* 112.20 (2024), pp. 18491–18500. DOI: 10.1007/s11071-024-09934-9.

[279] Y. Qin, A. M. Nobili, D. S. Bassett, and F. Pasqualetti. "Vibrational stabilization of cluster synchronization in oscillator networks". *IEEE Open Journal of Control Systems* 2 (2023), pp. 439–453. DOI: 10.1109/OJCSYS.2023.3331195.

[280] C. Nauck, M. Lindner, N. Molkenthin, J. Kurths, E. Schöll, J. Raisch, and F. Hellmann. "Predicting instability in complex oscillator networks: limitations and potentials of network Measures and Machine Learning". *ArXiv preprint* (2024). DOI: 10.48550/arXiv.2402.17500.

[281] G. Börner, M. Schröder, M. Thümler, and M. Timme. "Perturbation-response dynamics of coupled nonlinear systems". *Chaos (Woodbury, N.Y.)* 34.10 (2024). DOI: 10.1063/5.0223294.

[282] X. Zhang and M. Timme. "Fluctuation response patterns of network dynamics – An introduction". *European Journal of Applied Mathematics* 34.3 (2023), pp. 429–466. DOI: 10.1017/S0956792522000201.

[283] U. Harush and B. Barzel. "Dynamic patterns of information flow in complex networks". *Nature Communications* 8.1 (2017), p. 2181. DOI: 10.1038/s41467-017-01916-3.

[284] C. Hens, U. Harush, S. Haber, R. Cohen, and B. Barzel. "Spatiotemporal signal propagation in complex networks". *Nature Physics* 15.4 (2019), pp. 403–412. DOI: 10.1038/s41567-018-0409-0.

[285] M. A. Kramer, U. T. Eden, S. S. Cash, and E. D. Kolaczyk. "Network inference - with confidence - from multivariate time series". *Physical Review E* 79.6 (2009), p. 528. DOI: 10.1103/PhysRevE.79.061916.

[286] M. Nagy, Z. Akos, D. Biro, and T. Vicsek. "Hierarchical group dynamics in pigeon flocks". *Nature* 464.7290 (2010), pp. 890–893. DOI: 10.1038/nature08891.

[287] M. Jachan, K. Henschel, J. Nawrath, A. Schad, J. Timmer, and B. Schelter. "Inferring direct directed-information flow from multivariate nonlinear time series". *Physical Review E* 80.1 Pt 1 (2009), p. 011138. DOI: 10.1103/PhysRevE.80.011138.

[288] T. Tanizawa, T. Nakamura, F. Taya, and M. Small. "Constructing directed networks from multivariate time series using linear modelling technique". *Physica A: Statistical Mechanics and its Applications* 512 (2018), pp. 437–455. DOI: 10.1016/j.physa.2018.08.137.

[289] F. Hasselman, L. den Uil, R. Koordeman, P. de Looff, and R. Otten. "The geometry of synchronization: quantifying the coupling direction of physiological signals of stress between individuals using inter-system recurrence networks". *Frontiers in Network Physiology* 3 (2023). DOI: 10.3389/fnetp.2023.1289983.

[290] S. Boccaletti, V. Latora, Y. Moreno, M. Chavez, and D. Hwang. "Complex networks: Structure and dynamics". *Physics Reports* 424.4-5 (2006), pp. 175–308. DOI: 10.1016/j.physrep.2005.10.009.

[291] T. Stankovski, T. Pereira, P. V. E. McClintock, and A. Stefanovska. "Coupling functions: Universal insights into dynamical interaction mechanisms". *Reviews of Modern Physics* 89.4 (2017). DOI: 10.1103/RevModPhys.89.045001.

[292] E. Bullmore and O. Sporns. "Complex brain networks: graph theoretical analysis of structural and functional systems". *Nature Reviews. Neuroscience* 10.3 (2009), pp. 186–198. DOI: 10.1038/nrn2575.

[293] C. Zhou, L. Zemanová, G. Zamora-López, C. C. Hilgetag, and J. Kurths. "Structure–function relationship in complex brain networks expressed by hierarchical synchronization". *New Journal of Physics* 9.6 (2007), p. 178. DOI: 10.1088/1367-2630/9/6/178.

[294] A. A. Tsonis and P. J. Roebber. "The architecture of the climate network". *Physica A: Statistical Mechanics and its Applications* 333 (2004), pp. 497–504. DOI: 10.1016/j.physa.2003.10.045.

[295] N. Marwan and J.H. Feldhoff, R.V. Donner, J.F. Donges, J. Kurths. "Detection of coupling directions with intersystem recurrence networks". *International Symposium on Nonlinear Theory and its Applications* (2012), pp. 231–234.

[296] Geier, Charlotte and Hoffmann, Norbert. "Exploring localization in nonlinear oscillator systems through network-based predictions". *ArXiv preprint* (2024). DOI: https://doi.org/10.48550/arXiv.2407.05497.

[297] R. Tarjan. "Depth-first search and linear graph algorithms". *SIAM Journal on Computing* 1.2 (1972), pp. 146–160. DOI: 10.1137/0201010.

[298] E. Nuutila and E. Soisalon-Soininen. "On finding the strongly connected components in a directed graph". *Information Processing Letters* 49.1 (1994), pp. 9–14. DOI: 10.1016/0020-0190(94)90047-7.

[299] S. Thurner, R. A. Hanel, and P. Klimek. *Introduction to the theory of complex systems*. Oxford: Oxford university press, 2018.

[300] B. J. Lünsmann, C. Kirst, and M. Timme. "Transition to reconstructibility in weakly coupled networks". *PloS one* 12.10 (2017), e0186624. DOI: 10.1371/journal.pone.0186624.

[301] G. Börner, H. Haehne, J. Casadiego, and M. Timme. "Revealing system dimension from single-variable time series". *Chaos (Woodbury, N.Y.)* 33.7 (2023). DOI: 10.1063/5.0156448.

[302] H. Haehne, J. Casadiego, J. Peinke, and M. Timme. "Detecting Hidden Units and Network Size from Perceptible Dynamics". *Physical Review Letters* 122.15 (2019), p. 158301. DOI: 10.1103/PhysRevLett.122.158301.

[303] N. Marwan and K. H. Kraemer. "Trends in recurrence analysis of dynamical systems". *The European Physical Journal Special Topics* 232.1 (2023), pp. 5–27. DOI: 10.1140/epjs/s11734-022-00739-8.

[304] K. Maharjan. "Inference of coupling properties of coupled Duffing oscillators using recurrence analysis". Research Project Thesis. Hamburg: Hamburg University of Technology, 2024.

[305] C. Geier, M. Stender, and N. Hoffmann. "Building functional networks for complex response analysis in systems of coupled nonlinear oscillators". *Journal of Sound and Vibration* 590 (2024), p. 118544. DOI: 10.1016/j.jsv.2024.118544.

[306] F. Takens. "Detecting strange attractors in turbulence". *Dynamical Systems and Turbulence Warwick 1980: proceedings of a symposium held at the University of Warwick 1979/80*, pp. 366–381.

[307] K. Srinivasan, N. Coble, J. Hamlin, T. Antonsen, E. Ott, and M. Girvan. "Parallel machine learning for forecasting the dynamics of complex networks". *Physical Review Letters* 128.16 (2022), p. 164101. DOI: 10.1103/PhysRevLett.128.164101.

[308] T. L. Carroll and L. M. Pecora. "Network structure effects in reservoir computers". *Chaos (Woodbury, N.Y.)* 29.8 (2019), p. 083130. DOI: 10.1063/1.5097686.

[309] M. D. Cranmer, R. Xu, P. Battaglia, and S. Ho. "Learning Symbolic Physics with Graph Networks". *ArXiv preprint* (2019). DOI: 10.48550/arXiv.1909.05862.

[310] F. Scarselli and Gori, M., Tsoi, A. C., Hagenbuchner, M., & Monfardini, G. "The graph neural network model". *IEEE Transactions on Neural Networks 2009*. Vol. 1. 2009, pp. 61–80.

[311] J. P. Crutchfield. "Between order and chaos". *Nature Physics* 8.1 (2012), pp. 17–24. DOI: 10.1038/nphys2190.

[312] S. Kauffman. "The large scale structure and dynamics of gene control circuits: an ensemble approach". *Journal of Theoretical Biology* 44.1 (1974), pp. 167–190. DOI: 10.1016/S0022-5193(74)80037-8.